

Forschungsbericht 2017-01

**Design and Performance Analysis of  
Three-Dimensional Air Intakes for Su-  
personic Combustion Ramjet Engines**

Andreas K. Flock

Deutsches Zentrum für Luft- und Raumfahrt  
Institut für Aerodynamik und  
Strömungstechnik  
Abteilung Über- und  
Hyperschalltechnologien  
Köln

ISSN 1434-8454  
ISRN DLR-FB--2017-01

ISRN DLR-FB--2017-01

A. K. Flock



DLR Deutsches Zentrum  
für Luft- und Raumfahrt

## D93

Simultaneously published as doctoral thesis at the Faculty of Aerospace Engineering and Geodesy of the University of Stuttgart.  
Erscheint gleichzeitig als Dissertation an der Fakultät für Luft- und Raumfahrttechnik und Geodäsie der Universität Stuttgart.



*Herausgeber* Deutsches Zentrum  
für Luft- und Raumfahrt e. V.  
Bibliotheks- und  
Informationswesen  
D-51170 Köln  
Porz-Wahnheide  
Linder Höhe  
D-51147 Köln

*Telefon* (0 22 03) 6 01 - 44 44  
*Telefax* (0 22 03) 6 01 - 47 47

Als Manuskript gedruckt.  
Abdruck oder sonstige Verwendung  
nur nach Absprache mit dem DLR gestattet.

ISSN 1434-8454

*Hypersonics, Air-Breathing Propulsion, Scramjet, Analytical Intake Design, Supersonic Diffusor, Intake Starting*

Andreas K. FLOCK

Institute of Aerodynamics and Flow Technology within DLR, Supersonic and Hypersonic Technologies Department, Köln, Germany

### **Design and Performance Analysis of Three-Dimensional Air Intakes for Supersonic Combustion Ramjet Engines**

*Doctoral Thesis University of Stuttgart*

*DLR-Forschungsbericht 2017-1, 2017, 153 pages, 105 figures, 14 tables, 119 references, 33.00 € plus taxes*

The Supersonic Combustion Ramjet (SCRamjet) engine is an efficient propulsion device for supersonic and hypersonic velocities. The present work focuses on the SCRamjet air intake which serves as the engine's compressor. First, an analytical intake design tool was developed to generate so called streamline traced intake geometries. Second, the starting behavior of hypersonic air intakes was investigated experimentally in a blow down wind tunnel with a three-dimensional intake model with planar surfaces. A semi-empirical estimate was developed to predict intake starting of three-dimensional intake geometries. Third, the three-dimensional intake was further investigated experimentally and results were compared to numerical simulations. Finally, the performance of the three-dimensional intake was compared to the performance of different streamline traced intakes, designed with the analytical tool. Overall, the specific impulse of the streamline traced intakes was approximately 10 % higher compared to the three-dimensional intake configuration.

*Hyperschall, Luftatmender Antrieb, Scramjet, Analytische Einlaufauslegung, Überschall-diffusor, Einlauf-Startverhalten*

*(Published in English)*

Andreas K. FLOCK

Institut für Aerodynamik und Strömungstechnik des DLR, Abteilung Über- und Hyperschalltechnologien, Köln

### **Auslegung und Leistungscharakterisierung von dreidimensionalen Lufteinläufen für SCRamjet Antriebe**

*Dissertation Universität Stuttgart*

*DLR-Forschungsbericht 2017-1, 2017, 153 Seiten, 105 Bilder, 14 Tabellen, 119 Literaturstellen, 33,00 € zzgl. MwSt.*

Der Supersonic Combustion Ramjet (SCRamjet)-Motor ist ein effizienter Antrieb für den Über- und Hyperschallflug. Die vorliegende Arbeit konzentriert sich auf den Lufteinlauf, welcher als Kompressor dient. Zuerst wurde ein analytisches Einlaufauslegungsverfahren entwickelt, um so genannte „Streamline-Traced“ Geometrien zu generieren. Als nächstes wurde das Startverhalten von Hyperschalleinläufen anhand eines dreidimensionalen Rampen-Einlaufmodells experimentell in einem Windkanal untersucht. Eine halb-empirische Abschätzung wurde entwickelt um das Startverhalten von dreidimensionalen Einlaufgeometrien vorherzusagen. Weiterhin wurde der Rampen-Einlauf experimentell näher untersucht und Ergebnisse wurden mit numerischen Simulationen verglichen. Zuletzt wurden die Leistungsparameter des Rampen-Einlaufs mit denen von „Streamline-Traced“ Einläufen verglichen. Insgesamt war der spezifische Impuls der „Streamline-Traced“ Einläufe etwa 10% höher verglichen mit den Rampeneinläufen.



# **Forschungsbericht 2017-01**

## **Design and Performance Analysis of Three-Dimensional Air Intakes for Su- personic Combustion Ramjet Engines**

Andreas K. Flock

Deutsches Zentrum für Luft- und Raumfahrt  
Institut für Aerodynamik und  
Strömungstechnik  
Abteilung Über- und  
Hyperschalltechnologien  
Köln

153 Seiten  
105 Bilder  
14 Tabellen  
119 Literaturstellen



DLR

Deutsches Zentrum  
für Luft- und Raumfahrt



# **Design and Performance Analysis of Three-Dimensional Air Intakes for Supersonic Combustion Ramjet Engines**

A thesis accepted by the Faculty of Aerospace Engineering and Geodesy of the University of Stuttgart in partial fulfillment of the requirements for the degree of Doctor of Engineering Sciences (Dr.-Ing.)

by

**Andreas K. Flock**

born in Schweinfurt, Germany

Main Referee: Prof. Dr.-Ing. Ewald Krämer  
Co-Referee: Prof. Dr.-Ing. Herbert Olivier (RWTH Aachen, Germany)  
Date of Defense: 18. November 2016

Institute of Aerodynamics and Gas Dynamics

University of Stuttgart

2017





## Preface

I conducted the present work within the Supersonic and Hypersonic Technology Department of the Institute of Aerodynamics and Flow Technology at the German Aerospace Center (DLR) Köln. For the opportunity to conduct this work, the outstanding working conditions, and the scientific advice I sincerely thank Dr. Ali Gülhan. Furthermore, I thank Prof. Dr. Ewald Krämer for being my main referee, and Prof. Dr. Herbert Olivier for being my co-referee. I am convinced that the expertise of both was essential during the preparation of this manuscript.

Next, I would like to thank the entire Supersonic and Hypersonic Technology Department for the great working atmosphere and inspiring discussions held during various opportunities. In particular I would like to thank Marco Schmors and Michael Kosbow for the technical support and advice during the wind tunnel experiments; Dr. Burkard Esser for advice on computer related issues and high temperature effects; Sergej Blem, Dr. Patrick Gruhn, Dr. Dirk Herrmann, and Dr. Oliver Hohn for discussions on air breathing propulsion. Finally, I would like to thank Matthias Koslowski, Dominik Neeb, Dr. Johannes Riehmer, and Dominik Saile for the vivid discussions, great advices, and fruitful comments made in the context of this work and beyond.

I also would like to thank the German Research Foundation (DFG) for the funding of the project. As English is not my first language I depended on various editors, which all added to the quality of the manuscript. In this context I would like to thank: Nicolas DeLouise, Sam Duckitt, Dr. Abhinav Krishna, Dr. Siddarth Krishnamoorthy, Angela Pavuk, Amit Roghelia, Jessica Thompson, and Kyle Zienin.

Finally, and most importantly, I would like to thank my family and friends, for the granted motivation during the past few years. In particular I would like to thank my parents, who not only supported me during my time at DLR but during my entire life. Last, I would like to thank Antonia for being great!

Köln, November 2016

Andreas Flock



# Contents

<b>Preface</b>	<b>3</b>
<b>Contents</b>	<b>5</b>
<b>List of Figures</b>	<b>9</b>
<b>List of Tables</b>	<b>13</b>
<b>Nomenclature</b>	<b>15</b>
<b>Abstract</b>	<b>19</b>
<b>Kurzfassung – German Abstract</b>	<b>21</b>
<b>1 Introduction</b>	<b>23</b>
1.1 Framework – Research Training Group 1095 . . . . .	23
1.2 Supersonic Combustion Ramjet Engine . . . . .	23
1.2.1 General Description . . . . .	23
1.2.2 Fields of Application . . . . .	25
1.2.3 Flight Demonstrators . . . . .	25
1.3 SCRamjet Intakes . . . . .	27
1.3.1 Intake Design . . . . .	28
1.3.2 Intake Performance Parameters . . . . .	28
1.3.3 Intake Starting . . . . .	30
1.4 Objective of Current Work . . . . .	30
<b>2 Current Scientific Knowledge</b>	<b>32</b>
2.1 Intake Design . . . . .	32
2.1.1 Compression Flow Field . . . . .	32
2.1.2 Truncation Effects . . . . .	33
2.1.3 Streamline Tracing . . . . .	35
2.1.4 Viscous Effects . . . . .	35
2.2 Performance Determination . . . . .	37
2.2.1 Experimental . . . . .	37
2.2.2 Numerical . . . . .	37
2.3 Intake Starting . . . . .	38
2.3.1 General Research . . . . .	38
2.3.2 Self-Starting Intake Configurations . . . . .	40
<b>3 Aerodynamic Theory</b>	<b>41</b>
3.1 Fundamentals . . . . .	41
3.1.1 Standard Atmosphere . . . . .	41
3.1.2 Gas Properties . . . . .	41
3.1.3 Quasi One-Dimensional Flow . . . . .	41
3.1.4 Oblique and Normal Shock Relations . . . . .	42

3.2	Axisymmetric Compression Flow Fields . . . . .	43
3.2.1	Taylor McColl Equations . . . . .	43
3.2.2	Method of Characteristics . . . . .	44
3.3	Boundary Layer Flow . . . . .	45
3.3.1	Boundary Layer Equations . . . . .	45
3.3.2	Approximate Solution: Approach with Integral Method . . . . .	46
3.3.3	Walz' Integral Method: Rechenverfahren II . . . . .	49
<b>4</b>	<b>Intake Design Tool</b>	<b>51</b>
4.1	Overview . . . . .	51
4.2	Compression Flow Field . . . . .	51
4.2.1	Busemann Flow Field . . . . .	52
4.2.2	Reversed Nozzle Flow Field . . . . .	53
4.3	Truncation Effects . . . . .	54
4.3.1	Leading Edge Truncation Effects . . . . .	54
4.3.2	Rear Side Truncation Effects . . . . .	55
4.4	Streamline Tracing Algorithm . . . . .	56
4.5	Viscous Effects . . . . .	57
4.6	Performance Parameters Calculation . . . . .	59
<b>5</b>	<b>Intake Starting Prediction</b>	<b>62</b>
5.1	Empirical Relation . . . . .	62
5.2	Semi-Empirical Relation . . . . .	62
<b>6</b>	<b>Experimental Apparatus and Numerical Methods</b>	<b>66</b>
6.1	Intake Models . . . . .	66
6.1.1	3D-GRK Intake . . . . .	66
6.1.2	Streamline Traced Intake 1 – ST1 . . . . .	68
6.1.3	Streamline Traced Intake 2 – ST2 . . . . .	68
6.1.4	Streamline Traced Intake 3 – ST3 . . . . .	70
6.2	Blow Down Wind Tunnel H2K . . . . .	72
6.3	Complementary Measurement Equipment . . . . .	72
6.3.1	Pressure Data Recording . . . . .	72
6.3.2	Mach Number Determination . . . . .	73
6.3.3	Schlieren Imaging . . . . .	74
6.3.4	Throttle System . . . . .	74
6.3.5	Temperature Data Recording . . . . .	75
6.4	Numerical Simulation . . . . .	76
6.4.1	DLR-TAU Software System . . . . .	76
6.4.2	Mesh Generation . . . . .	76
6.4.3	Mesh Analysis . . . . .	76
6.5	One-Dimensional Post-Analysis . . . . .	77
6.5.1	Combustion Chamber Model . . . . .	79
6.5.2	Nozzle Model . . . . .	80
6.6	Averaging . . . . .	80
6.6.1	Conventional Averaging . . . . .	81
6.6.2	Stream-Thrust Averaging . . . . .	81
<b>7</b>	<b>Results</b>	<b>83</b>
7.1	Validation of Approach to Truncation Effects . . . . .	83
7.1.1	Leading Edge Truncation . . . . .	83

7.1.2	Rear Side Truncation . . . . .	88
7.2	Validation of Approach to Viscous Effects . . . . .	92
7.2.1	Busemann Flow . . . . .	93
7.2.2	Reversed Nozzle Flow . . . . .	94
7.3	Comparison of Busemann Flow and Reversed Nozzle Flow . . . . .	96
7.3.1	Geometry . . . . .	96
7.3.2	Leading Edge Truncation . . . . .	98
7.3.3	Rear Side Truncation . . . . .	98
7.3.4	Viscous Effects . . . . .	98
7.3.5	Superimposed: Leading Edge Truncation and Viscous Effects . . . . .	101
7.3.6	Evaluation and Summary . . . . .	101
7.4	Streamline Traced Intakes . . . . .	103
7.4.1	ST1 Intake . . . . .	103
7.4.2	ST2 Intake . . . . .	105
7.4.3	ST3 Intake . . . . .	107
7.4.4	Summary . . . . .	109
7.5	Starting Experiments . . . . .	111
7.5.1	Mach Number Influence . . . . .	111
7.5.2	Cowl Geometry Influence . . . . .	112
7.5.3	Angle of Attack Influence . . . . .	112
7.5.4	In the Context of Kantrowitz Theory . . . . .	114
7.6	3D-GRK Intake . . . . .	116
7.6.1	Back Pressure Influence . . . . .	116
7.6.2	Mass Flow Measurement . . . . .	116
7.6.3	CFD Analysis . . . . .	117
7.6.4	Extrapolation to Flight Condition . . . . .	122
7.7	Comparison: 3D-GRK and Streamline Traced Intakes . . . . .	122
7.7.1	Design Approach . . . . .	122
7.7.2	Geometry . . . . .	123
7.7.3	Intake Performance . . . . .	123
7.7.4	Summary . . . . .	126
<b>8</b>	<b>Conclusion</b>	<b>127</b>
8.1	Summary . . . . .	127
8.2	Outlook . . . . .	129
<b>A</b>	<b>Appendix</b>	<b>131</b>
A.1	Overview of Flow Conditions . . . . .	131
A.2	Integral Method – Rechenverfahren II . . . . .	132
A.3	Calibration Curves . . . . .	134
A.4	Mesh Analysis – Additional Plots . . . . .	136
A.5	Viscous Effects – Axisymmetric Contour Plots . . . . .	137
A.6	ST Configurations – Cross-Stream Parameters . . . . .	139
A.7	3D-GRK Configuration – Cross-Stream Parameters . . . . .	140
A.8	Comparison of Flight and Wind Tunnel Conditions . . . . .	141
	<b>Bibliography</b>	<b>143</b>
	<b>Index</b>	<b>151</b>
	<b>Curriculum Vitae</b>	<b>153</b>



## List of Figures

1.1	Schematic cross section of SCRamjet engine along with certain terminology. . . . .	24
1.2	Estimated maximum specific impulse for hydrogen combustion of various jet propulsion systems. . . . .	24
1.3	X43A sketch. . . . .	26
1.4	Artistic rendering of X51 vehicle along with booster and interstage. . . . .	26
1.5	SR71 aircraft (left) and Lockheed-Martin concept image of SR72 aircraft (right). . . . .	30
2.1	Top: Schematic of classical Busemann flow; bottom: Schematic of leading edge truncation effects on Busemann flow. . . . .	33
2.2	Top: Schematic of classical Busemann flow; bottom: Schematic of rearside truncation effects on Busemann flow along with Control Volume (CV) for stream thrust analysis. . . . .	34
2.3	Top: Schematic of classical Busemann flow; bottom: Schematic of viscous effects in uncorrected Busemann contour. . . . .	36
2.4	Top: Schematic of classical Busemann flow; bottom: Schematic of viscous effects in corrected Busemann contour. . . . .	36
2.5	Schematic of fully and partially enclosed intakes. . . . .	39
2.6	Kantrowitz diagram for $1/CR_i$ and $CR_i$ along with isentropic limit and empirical relations. . . . .	39
3.1	Schematic of flow across a normal (left) and oblique shock (right). . . . .	42
3.2	Schematic of classical Busemann flow. . . . .	43
3.3	Sketch of characteristic mesh along with streamline traced contour (left) and close-up of three points (right). . . . .	45
4.1	Flow chart of design steps of the three-dimensional intake generation tool. . . . .	52
4.2	Control volume of figure 2.2 reprinted for analysis of truncated portion of Busemann intake. . . . .	55
4.3	Schematic of streamline tracing within a compression flow field. . . . .	56
4.4	Different perspectives of streamline traced Busemann intake; geometry designed for $M_\infty = 8$ , $\Pi_{st} = 45$ , $\delta = 3$ deg. . . . .	56
4.5	Mach number contour plots of the streamline traced Busemann intake for the analytical (left) and Euler solution (right); geometry designed for $M_\infty = 8$ , $\Pi_{st} = 45$ , $\delta = 0$ . . . . .	57
4.6	Probability density function and cumulative distribution function of the Berkowitz data set, along with analytical function, $tp(A)$ . . . . .	58
4.7	Displacement thicknesses for different boundary layer states along with edge pressure distribution plotted against the free stream distance ( $T_w = 500$ K). . . . .	59
4.8	Wall pressures of leading edge truncated Busemann intake, designed for $M_\infty = 8$ , $\Pi_{st} = 43$ , $\delta = 4$ deg. . . . .	60
5.1	Kantrowitz plot with empirical starting relation, that allows adjustment via $C_1$ -constant. . . . .	63
5.2	Schlieren images of started and unstarted 3D-GRK intake flow along with sketched shock positions and possible separation region in internal flow path. . . . .	63
5.3	Sketch of various diffuser flows. . . . .	64
5.4	Kantrowitz plot with lines of constant total pressure and semi-empirical limit. . . . .	65
6.1	Different perspectives of the 3D-GRK intake; dimensions are in millimeter. . . . .	67

6.2	Internal contraction ratio, plotted against the distance from the intake leading edge to the cowl closure location. . . . .	67
6.3	Top and cross sectional view of intake configuration along with throttle and wind tunnel mount. . . . .	68
6.4	Different perspectives of the streamline traced intake ST1; dimensions are in millimeter. . . . .	69
6.5	Different perspectives of the streamline traced intake ST2; dimensions are in millimeter. . . . .	69
6.6	Mach number contour plot extracted from axisymmetric CFD simulation for ST3 configuration. . . . .	71
6.7	Different perspectives of the streamline traced intake ST3; dimensions are in millimeter. . . . .	71
6.8	Schematic set-up of the H2K wind tunnel (left) along with characteristic diagram (right). . . . .	72
6.9	Rake with pitot and static pressure tubes. . . . .	73
6.10	Schematic of double-pass schlieren apparatus used during H2K wind tunnel experiments. . . . .	74
6.11	Settling chamber and throttle as attached to the 3D-GRK intake model to measure mass flow and simulate back pressure. . . . .	75
6.12	Starting mesh for 3D-GRK intake configuration. . . . .	76
6.13	Starting mesh for axisymmetric Busemann intake configuration. . . . .	77
6.14	Influence of mesh size on pressure and temperature in intake exit plane at $x = 0.722$ m. . . . .	78
6.15	Influence of mesh size on pressure in axisymmetric SCRamjet configuration. . . . .	78
6.16	Sample intake exit plane. . . . .	81
7.1	Mach number contour plot extracted from CFD for 4 deg leading edge truncation. . . . .	84
7.2	Busemann intake contours along with wall pressure plots for increasing leading edge truncation; all intakes designed for $M_\infty = 8$ and $\Pi_{st} = 43$ . . . . .	84
7.3	Cross-stream pressure and Mach number of leading edge truncated Busemann intakes at outlet plane; all intakes designed for $M_\infty = 8$ and $\Pi_{st} = 43$ . . . . .	85
7.4	Mass- and stream-thrust-averaged parameters and maximum temperature of leading edge truncated Busemann intakes; all intakes designed for $M_\infty = 8$ and $\Pi_{st} = 43$ . . . . .	85
7.5	Reversed nozzle intake contours along with wall pressure plots for increasing leading edge truncation; all intakes designed for $M_\infty = 8$ and $\Pi_{st} = 43$ . . . . .	86
7.6	Cross-stream pressure and Mach number of leading edge truncated reversed nozzle intakes at outlet plane; all intakes designed for $M_\infty = 8$ and $\Pi_{st} = 43$ . . . . .	87
7.7	Mass- and stream-thrust-averaged parameters and maximum temperature of leading edge truncated reversed nozzle intakes; all intakes designed for $M_\infty = 8$ and $\Pi_{st} = 43$ . . . . .	87
7.8	Mach number contour plot extracted from CFD for largest amount of rear side truncation. . . . .	88
7.9	Busemann intake contours along with wall pressure plots for increasing rear side truncation; all intakes designed for $M_\infty = 8$ , $\delta = 0$ , and $\Pi_{st} = 43$ . . . . .	89
7.10	Cross-stream pressure and Mach number of rear side truncated Busemann intakes at outlet plane; all intakes designed for $M_\infty = 8$ , $\delta = 0$ , and $\Pi_{st} = 43$ . . . . .	89
7.11	Mass- and stream-thrust-averaged parameters and maximum temperature of rear side truncated Busemann intakes; all intakes designed for $M_\infty = 8$ , $\delta = 0$ , and $\Pi_{st} = 43$ . . . . .	90
7.12	Reversed nozzle intake contours along with wall pressure plots for increasing rear side truncation; all intakes designed for $M_\infty = 8$ , $\delta = 0$ , and $\Pi_{st} = 43$ . . . . .	91
7.13	Cross-stream pressure and Mach number of rear side truncated reversed nozzle intakes at outlet plane; all intakes designed for $M_\infty = 8$ , $\delta = 0$ , and $\Pi_{st} = 43$ . . . . .	91
7.14	Mass- and stream-thrust-averaged parameters and maximum temperature of rear side truncated reversed nozzle intakes; all intakes designed for $M_\infty = 8$ , $\delta = 0$ , and $\Pi_{st} = 43$ . . . . .	92
7.15	Busemann intake contours for Mach 8 case with and without viscous correction. . . . .	93
7.16	Normalized pressures for Mach 8 Busemann configurations with and without viscous correction plotted against $x$ -coordinate. . . . .	93



7.17	Normalized pressures extracted from Busemann intakes for various Mach numbers plotted against $x$ -coordinate. . . . .	94
7.18	Reversed nozzle contours for Mach 8 reference case with and without viscous correction. . . . .	95
7.19	Normalized pressures for Mach 8 reversed nozzle configurations with and without viscous correction plotted against $x$ -coordinate. . . . .	95
7.20	Normalized pressures extracted from reversed nozzle flows for various Mach numbers plotted against $x$ -coordinate. . . . .	96
7.21	Geometry overview of Busemann and reversed nozzle geometry for Mach 8 condition. . . . .	97
7.22	Intake performance parameters for leading edge truncation. . . . .	97
7.23	Intake performance parameters for rear side truncation. . . . .	99
7.24	Intake performance parameters for Mach number variation. . . . .	100
7.25	Intake performance parameters for leading edge truncation with viscous correction. . . . .	102
7.26	Wall pressure, averaged pressure, and Mach number contour plot extracted from CFD for ST1 intake configuration for on-design condition. . . . .	104
7.27	CFD-schlieren plot and averaged variables extracted from internal portion of ST1 intake configuration for on-design condition. . . . .	104
7.28	Normalized pressure on cross sectional planes of ST1, ST2, and ST3 configuration for Mach 8, extracted from CFD at $x = 0.722$ m. . . . .	105
7.29	Wall pressure, averaged pressure, and Mach number contour plot extracted from CFD for ST2 intake configuration for on-design condition. . . . .	106
7.30	CFD-schlieren plot and averaged variables extracted from internal portion of ST2 intake configuration for on-design condition. . . . .	106
7.31	CFD-schlieren plot and averaged variables extracted from internal portion of ST2 intake configuration for Mach 7 off-design condition. . . . .	108
7.32	CFD-schlieren plot and averaged variables extracted from internal portion of ST2 intake configuration for Mach 6 off-design condition. . . . .	108
7.33	Normalized pressure on cross sectional planes of ST2 configuration for different Mach numbers, extracted from CFD at $x = 0.722$ m. . . . .	109
7.34	Wall pressure, averaged pressure, and Mach number contour plot extracted from CFD for ST3 intake configuration for on-design condition. . . . .	110
7.35	CFD-schlieren plot and averaged variables extracted from internal portion of ST3 intake configuration for on-design condition. . . . .	110
7.36	Starting behavior for different free stream Mach numbers and different cowl geometries. . . . .	111
7.37	Schlieren images of unstarted, started, and plateau case for $M_\infty = 7$ and the v-shaped cowl configuration. . . . .	112
7.38	Influence of pitch angle ( $\alpha$ ) variation on starting behavior of intake; yaw angle was kept zero. . . . .	113
7.39	Influence of yaw angle ( $\beta$ ) and of simultaneous pitch and yaw angle on intake starting for v-shaped lip at Mach 7. . . . .	114
7.40	Self-starting limits of the 3D-GRK intake configurations plotted in the Kantrowitz diagram. . . . .	115
7.41	Self-developed semi-empirical relation in comparison with self-starting intake configurations plotted in the Kantrowitz diagram. . . . .	115
7.42	Intake exit pressure, averaged at rake, plotted against throttle ratio (throttle closed for increasing throttle ratio) for the three different self-starting configurations. . . . .	116
7.43	Measured captured mass flow and intake exit velocity for different intake configurations. . . . .	117
7.44	Close-up of captured mass flow and intake exit velocity for Mach 6 configuration. . . . .	118
7.45	Numerical and experimental results of Mach 7, v-cowl configuration. . . . .	118
7.46	Numerical and experimental results of Mach 7, s-cowl configuration. . . . .	119
7.47	Numerical and experimental results of Mach 6, v-cowl configuration. . . . .	119

7.48	Static and pitot pressure, as well as Mach number for the Mach 7, v-cowl configuration, at $x = 0.722$ m. . . . .	120
7.49	Static and pitot pressure, as well as Mach number for the Mach 7, s-cowl configuration, at $x = 0.722$ m. . . . .	121
7.50	Static and pitot pressure, as well as Mach number for the Mach 6, v-cowl configuration, at $x = 0.722$ m. . . . .	121
7.51	Normalized pressure on cross sectional planes, extracted from CFD at $x = 0.722$ m. . . . .	122
7.52	Geometrical overview of streamline traced intakes and v-cowl 3D-GRK intake. . . . .	123
7.53	Stream-thrust-averaged variables for 3D-GRK and streamline traced intakes, extracted for Mach 8; data for internal portion of intakes. . . . .	125
7.54	Specific impulse from figure 1.2 replotted along with various intake configurations and close-up near Mach 8 region of streamline traced intake configurations. . . . .	126
A.1	Influence of mesh size on wall pressure. . . . .	136
A.2	Influence of mesh size on average pressure (left) and average temperature (right). . . . .	136
A.3	Axisymmetric Busemann contour plots without truncation. . . . .	137
A.4	Axisymmetric reversed nozzle contour plots without truncation. . . . .	138
A.5	Normalized temperature on cross sectional planes of ST1, ST2, and ST3 configuration for Mach 8, extracted from CFD at $x = 0.722$ m. . . . .	139
A.6	Mach number on cross sectional planes of ST1, ST2, and ST3 configuration for Mach 8, extracted from CFD at $x = 0.722$ m. . . . .	139
A.7	Normalized temperature on cross sectional planes, extracted from CFD at $x = 0.722$ m. . . . .	140
A.8	Mach number on cross sectional planes, extracted from CFD at $x = 0.722$ m. . . . .	140
A.9	Comparison of numerical data for Wind Tunnel (WT) and Flight Condition (FC). . . . .	141

## List of Tables

1.1	Overview of the HIFiRE flights. . . . .	27
6.1	Approximate mesh sizes for three-dimensional and axisymmetric cases. . . . .	77
7.1	Design parameters for leading edge truncated Busemann intakes with $p_3$ -adjustment; all intakes designed for $M_\infty = 8$ and $\Pi_{st} = 43$ . . . . .	84
7.2	Design parameters for leading edge truncated reversed nozzle intakes with $p_3$ -adjustment; all intakes designed for $M_\infty = 8$ and $\Pi_{st} = 43$ . . . . .	86
7.3	Design parameters for Busemann intakes truncated at their rear-side; all intakes designed for $M_\infty = 8$ , $\delta = 0$ , and $\Pi_{st} = 43$ . . . . .	88
7.4	Design parameters for reversed nozzle intakes truncated at their rear-side; all intakes designed for $M_\infty = 8$ , $\delta = 0$ , and $\Pi_{st} = 43$ . . . . .	91
7.5	Design parameters for Busemann intakes with viscous correction; all intakes designed for $\Pi_{st} = 43$ and flight along constant dynamic pressure trajectory. . . . .	94
7.6	Design parameters for reversed nozzle intakes with viscous correction; all intakes designed for $\Pi_{st} = 43$ and flight along constant dynamic pressure trajectory. . . . .	96
7.7	Stream-thrust-averaged data extracted from CFD at intake throat ( $x = 0.65$ m) compared to tool predictions for ST1, ST2, and ST3 on-design conditions. . . . .	104
7.8	Overview of investigated angle of attack configurations. . . . .	113
7.9	Captured mass flow for different configurations measured with attached throttle. . . . .	117
7.10	Mass capture ratios for various intake configurations; data extracted from CFD for flight conditions. . . . .	124
A.1	Overview of different flight conditions along a trajectory with constant dynamic pressure ( $q_\infty = 0.53$ bar). . . . .	131
A.2	Overview of different wind tunnel test conditions. . . . .	131



## Nomenclature

$A$	area	$m^2$
$a$	speed of sound	$m/s$
$c_f$	friction coefficient	
$c_H$	Stanton number, $\alpha/c_p/\rho/v$	
$c_p$	specific heat at const. pressure	$J/kg/K$
$c_v$	specific heat at const. density	$J/kg/K$
$CR$	contraction ratio	
$D$	diameter	$m$
$e$	specific internal energy	$m^2/s^2$
$e_\nu, f_\nu, g_\nu$	auxiliary variables	
$F, \vec{F}$	force, force vector	$N$
$g$	gravity constant	$N/kg$
$H$	shape factor	
$h$	altitude, height	$m$
$h$	specific enthalpy	$m^2/s^2$
$I$	specific impulse	$s$
$k$	thermal conductivity	$J/s/m/K$
$L$	length	$m$
$LHV$	lower heating value	$J/kg$
$\hat{n}$	mass ratio	
$\dot{m}$	mass flow rate	$kg/s$
$M$	Mach number, $V/a$	
$MCR$	mass capture ratio	
$\vec{n}$	surface normal vector	
$p$	pressure	$N/m^2$
$\dot{Q}$	heat flow	$J/s$
$\dot{q}$	specific heat flow	$J/s/m^2$
$q$	dynamic pressure	$N/m^2$
$R$	specific gas constant	$J/kg/K$
$\mathcal{R}$	recovery factor	
$r$	radial coordinate	$m$
$Re$	Reynolds number, $\rho V x/\mu$	
$s$	Reynolds analogy factor	
$T$	temperature	$K$
$tp$	transition parameter	
$TR$	throttle ratio	
$u, v, w$	$x, y, z$ velocity	$m/s$
$U$	normalized velocity	
$\vec{v}$	velocity, vector notation	$m/s$
$V$	absolute velocity = $ \vec{v} $	$m/s$
$x, y, z$	spatial coordinates	$m$
$y^+$	non-dimensional wall distance	
$Z$	thickness parameter	
$\alpha$	Busemann: flow angle	$deg$

## Nomenclature

---

$\alpha$	heat transfer coefficient	J/s/m <sup>2</sup> /K
$\alpha, \beta$	pitch, yaw angle	deg
$\beta$	shock angle	deg
$\gamma$	ratio of specific heats	
$\delta$	truncation angle	deg
$\delta_1$	displacement thickness	m
$\delta_2$	momentum thickness	m
$\delta_{0.99}$	boundary layer thickness	m
$\varphi$	equivalence ratio	
$\eta$	efficiency	
$\Theta$	temperature ratio	
$\theta$	deflection angle	deg
$\theta$	Busemann: angle of fan-like lines	deg
$\theta$	Method of Characteristics: flow angle	deg
$\mu$	dynamic viscosity	kg/s/m
$\mu$	Mach angle	deg
$\Pi$	pressure ratio	
$\rho$	density	kg/m <sup>3</sup>
$\tau$	shear stress	N/m <sup>2</sup>
$\Omega$	sample variable	

## Subscripts

3	intake exit position
adj	adjusted
cc	combustion chamber
char	characteristic
cl	cowl closure
corr	corrected
d	drag
e	boundary layer edge location
emp	empirical
H	hydraulic
i	internal portion
$i$	index variable
isent	isentropic
Kantr	Kantrowitz
KE	kinetic energy
m	modified
mav	mass-averaged
n	normal direction
norm	normalized
o	overall portion
p	pressure portion
pit	pitot
r	radial direction
rec	recovery
sp	specific
st	static
sta	stream-thrust-averaged

stoi	stoichometric
t, tot	total
th	throat
trans	transitional
v	viscous portion
w	wall
$\infty$	free stream condition

### Abbreviations

3D-GRK	three-dimensional intake configuration of research training group
AoA	Angle of Attack
AUS	AUStralia
BM	BuseMann
CAD	Computer Aided Design
CFD	Computational Fluid Dynamics
DLR	German Aerospace Center
DNS	Direct Numerical Simulation
EXP	EXPerimental/EXPeriment
FC	Flight Condition
H2K	Hypersonic blow down wind tunnel at DLR Cologne
HIFiRE	Hypersonic International Flight Research and Experimentation
inv	inviscid
LES	Large Eddy Simulation
LHV	Lower Heating Value
M7v	Mach 7 condition with v-shaped cowl
M7s	Mach 7 condition with straight cowl
M6v	Mach 6 condition with v-shaped cowl
MAV	Mass AVeraged
MDO	Multidisciplinary Design Optimization
MOC	Method Of Characteristics
NASA	National Aeronautics and Space Administration
NASP	National AeroSpace Plane
PSI	Pressure Systems Inc.
RANS	Reynolds-Averaged Navier-Stokes
REST	Rectangular to Elliptical Shape Transition
RV2	RechenVerfahren II – Walz' integral method
revN	reversed Nozzle
s-cowl	straight cowl geometry
SST	Shear-Stress Transport
SSTO	Single Stage To Orbit
ST	Streamline Traced
STA	Stream-Thrust-Averaged
TR	Throttle Ratio
TMK	Trisonic wind tunnel at DLR Cologne
US	United States
v-cowl	v-shaped cowl geometry
VC	Viscous Correction
vis	viscous
w/wo	with/without

## Nomenclature

---

WT            Wind Tunnel



## Abstract

The Supersonic Combustion Ramjet (SCRamjet) engine is an efficient propulsion device for supersonic and hypersonic velocities. The SCRamjet uses air from the surrounding atmosphere for the combustion process and therefore no oxidizer has to be carried on board. Furthermore, with higher velocities the ram compression increases and no compressor stage with rotating parts is needed. Thus, at supersonic and hypersonic velocities the SCRamjet engine becomes more efficient when compared to rocket or jet engines. The present work focuses on the SCRamjet air intake which serves as the engine's compressor and is a crucial component. More specifically different topics related to analytical intake design and to general performance characterization of three-dimensional SCRamjet intakes were examined.

First, an analytical intake design tool was developed. To start, an axisymmetric Busemann or reversed nozzle flow was truncated at the leading edge or rear end. The changes caused by the truncation were modeled analytically. Then, from the axisymmetric flow field, streamlines were traced to generate a fully three-dimensional geometry. Along the individual streamlines the boundary layer displacement thickness was calculated with an integral method. This served two purposes: First, the geometry was widened with the displacement thickness to counteract additional contraction by the viscous boundary layer. Second, friction drag was calculated. The analytical results of axisymmetric and fully three-dimensional configurations were validated with numerical simulations. Numerical results were within 3% and 8% of the analytical predictions for inviscid and viscous flows, respectively.

Second, the starting behavior of hypersonic air intakes was investigated experimentally in a blow down wind tunnel with a three-dimensional intake model (3D-GRK) with planar surfaces. Influence of intake cowl, free stream Mach number and angle of attack on intake starting were investigated. The self-starting configurations were all within the critical region of the Kantrowitz diagram, where intake starting should not occur according to Kantrowitz theory. In particular, the straight cowl in comparison to the v-shaped cowl allowed for more overboard spillage, therefore improving the starting characteristics. The increase in free stream Mach number raised the internal contraction ratio, at which intakes were still self-starting. Angle of attack effects were twofold: On the one hand, for positive pitch angle and no yaw deflection, intake starting was enhanced. On the other hand, for negative pitch angle or yaw deflection, starting was delayed. The experimental data were used to develop correlations to better predict intake starting. The correlations were within the critical region of the Kantrowitz plot and agreed with the experimental data and with data collected from literature.

Third, the 3D-GRK intake was further investigated experimentally and results were compared to numerical simulations. Experimental and numerical results agreed to within the uncertainty of the measurements and only minor displacements near regions with separated flow were detected. To simulate pressure peaks stemming from the combustion process a throttle was attached to the intake model. The intake behavior under back pressure was investigated and the captured mass flow was measured. Captured mass flow, operating pressure ratio, and maximum sustainable pressure ratio before unstart all decreased as free stream Mach number was lowered. The ratio of maximum sustainable pressure to operating pressure, however, was constant at around 4:1. To yield performance parameters at flight condition, the numerical simulations were extrapolated to flight condition. During extrapolation, the change in performance was below 2%, therefore practically negligible.

Finally, the performance of the 3D-GRK intake configurations was compared to performance of different streamline traced intakes. The streamline traced configurations consisted of continuously curved surfaces, which generated portions of isentropic compression. The 3D-GRK intake, in contrast, consisted of planar surfaces, and its performance, i.e. compression efficiency or total pressure recovery, was therefore lower. After post-processing with one-dimensional combustor and nozzle tools the streamline traced

configurations had specific impulses of about 3200 s, 2700 s, and 2300 s for free stream Mach numbers of 6, 7, and 8, respectively. For the same Mach numbers specific impulse of the 3D-GRK configuration was approximately 300 s lower.

## Kurzfassung – German Abstract

Der Supersonic Combustion Ramjet (SCRamjet)-Motor ist ein effizienter Antrieb für den Über- und Hyperschallflug. Der SCRamjet nutzt Luft aus der Atmosphäre zur Verbrennung und muss daher keinen Oxidator mit sich führen. Weiterhin steigt die Staustrahlkompression mit höheren Geschwindigkeiten und eine Verdichterstufe mit drehenden Teilen ist nicht mehr nötig. Deswegen ist der SCRamjet im Über- und Hyperschallflug effizienter, verglichen mit Raketen- oder Strahltriebwerken. Die vorliegende Arbeit konzentriert sich auf den Lufteinlauf, welcher als Kompressor dient und eine wichtige Triebwerkskomponente ist. Im Detail wurden verschiedene Themen in Zusammenhang mit analytischer Einlaufauslegung und genereller Leistungscharakterisierung von dreidimensionalen Triebwerkseinläufen untersucht.

Zuerst wurde ein analytisches Einlaufauslegeverfahren entwickelt. Dafür wurden zunächst axialsymmetrische Busemann- oder umgekehrte Düsenströmungsfelder an der Spitze oder am Heck gekürzt. Die Veränderungen, welche durch die Kürzung verursacht wurden, wurden analytisch modelliert. In dem axialsymmetrischen Strömungsfeld wurden dann Stromlinien verfolgt und eine dreidimensionale Geometrie erzeugt. Entlang jeder einzelnen Stromlinie wurde die Grenzschichtverdrängungsdicke mit einem Integralverfahren berechnet. Dies hatte zwei Gründe: Erstens wurde die Geometrie mit der Verdrängungsdicke geweitet, um der durch die Grenzschicht verursachten Kontraktion entgegenzuwirken. Zweitens wurde der Reibungswiderstand berechnet. Die analytischen Ergebnisse für axialsymmetrische und dreidimensionale ("Streamline-Traced") Konfigurationen wurden mit numerischen Simulationen validiert. Die numerischen und analytischen Ergebnisse lagen in reibungsfreien Fällen nur maximal 3% und in reibungsbehafteten Fällen nur maximal 8% auseinander.

Als nächstes wurde das Startverhalten von Hyperschalleinläufen anhand eines dreidimensionalen Einlaufmodells (3D-GRK) experimentell in einem Windkanal untersucht. Der Einfluss der Einlauf-Haubengeometrie, der Anströmmachzahl und des Anstellwinkels auf das Startverhalten wurden untersucht. Die selbststartenden Konfigurationen lagen alle innerhalb des kritischen Gebiets des Kantrowitz-Diagramms, in welchem laut Kantrowitz Einläufe nicht selbststartend sein sollten. Die gerade Haube verursachte einen größeren Verlustmassenstrom im Vergleich zu der v-förmigen und verbesserte so das Startverhalten. Mit steigender Anströmmachzahl erhöhte sich die Innenkontraktion, bei der die Einläufe selbststartend waren. Der Einfluss des Anstellwinkels war wie folgt: Das Starten wurde zum einen durch positive Nick- und Gierwinkel nahe Null verbessert, zum anderen durch negative Nick- oder Gierwinkel verschlechtert. Die experimentellen Daten wurden verwendet, um Korrelationen zu entwickeln, welche das Startverhalten besser vorhersagen können. Die Korrelationen lagen innerhalb des kritischen Gebiets des Kantrowitz-Diagramms und stimmten mit den experimentellen und aus der Literatur recherchierten Daten überein.

Weiterhin wurde der 3D-GRK-Einlauf experimentell näher untersucht und Ergebnisse wurden mit numerischen Simulationen verglichen. Experimentelle und numerische Ergebnisse stimmten innerhalb der Messungenauigkeit überein, wobei nur kleinere Verschiebungen in der Nähe von Ablösegebieten existierten. Um Druckschwankungen aus einem Verbrennungsprozess zu simulieren, wurde eine Drossel an das Einlaufmodell angefügt. Damit wurden das Einlaufverhalten unter Gegendruck und der gefangene Massenstrom gemessen. Sowohl der Massenstrom, das Druckverhältnis als auch das maximal mögliche Druckverhältnis nahmen mit sinkender Machzahl ab. Das Verhältnis von maximal möglichem zu normalem Druckverhältnis hingegen war mit 4:1 in etwa konstant. Um Leistungsparameter bei Flugbedingungen zu ermitteln, wurden die numerischen Simulationen auf Flugbedingungen extrapoliert. Die Extrapolation beeinflusste die Ergebnisse nur marginal (<2%).

Zuletzt wurden die Leistungsparameter des 3D-GRK-Einlaufs mit denen von Streamline-Traced (ST)-Einläufen verglichen. Die ST-Einläufe hatten kontinuierlich gewölbte Oberflächen, welche zum Teil

eine isentrope Kompression ermöglichten. Im Gegensatz dazu hatte der 3D-GRK-Einlauf ebene Oberflächen und seine Leistung, d.h. die Kompressionseffizienz oder der Totaldruckrückgewinn, waren deswegen niedriger. Nachdem die Einlaufparameter mit eindimensionalen Brennkammer- und Düsenauslegungsverfahren weiter analysiert wurden, ergaben sich für die ST-Einläufe spezifische Impulse von jeweils 3200 s für Mach 6, 2700 s für Mach 7 und 2300 s für Mach 8. Für die gleichen Machzahlen lagen die spezifischen Impulse des 3D-GRK-Einlaufs etwa 300 s niedriger.

# 1 Introduction

## 1.1 Framework – Research Training Group 1095

The current dissertation is embedded into the Research Training Group 1095 [112, 40], as the subproject A3 labeled *Design and Characterization of a 3D SCRamjet Inlet*. The overall program objective was to investigate the SCRamjet engine as a possible propulsion system for future space transport applications. Therefore, three groups were built according to the following structure:

- Group A focused on the SCRamjet intake and flow phenomena related to it.
- Group B focused on the SCRamjet combustor and supersonic combustion process.
- Group C focused on the SCRamjet nozzle design as well as overall system aspects.

Apart from the German Aerospace Center, three universities participated in the Research Training Group, namely the RWTH Aachen University, the Technical University of Munich, and the University of Stuttgart, which had the lead in the program. The program started in the spring of 2005 and ended in 2014 with a closing symposium in March at the University of Stuttgart.

It should be noted that even though some groups worked more independently at certain institutions, in general there was a high need for collaboration throughout the program and therefore throughout the locations. To ensure this collaboration, workshops were held once a year, which allowed program members to present their current results and hold discussions regarding their program status. To increase the collaboration and the international attention, so called *Summer Schools* were held sequentially at the four different institutions and recognized experts from the field of SCRamjet research were invited. The goal was twofold; to receive input from professionals via presentations on their current research, and to exchange opinions and perspectives during individual discussions amongst program members.

## 1.2 Supersonic Combustion Ramjet Engine

The present section gives a short overview of the SCRamjet engine in general as well as of possible applications that could benefit from it. Finally, important flight demonstrators are discussed.

### 1.2.1 General Description

A Supersonic Combustion Ramjet, or SCRamjet engine, is an air breathing jet engine for supersonic or hypersonic speeds. The same cycle phases – compression, combustion, expansion – are present as in conventional air breathing jet engines. However, since ram compression is sufficient no rotating compressor and thus no turbine are used. Therefore, SCRamjet engines are normally mechanically simpler compared to their lower speed counterparts such as the turbojet or turbofan engines. Their internal shape and the design of the flow path determine engine performance. At low Mach numbers ram compression is weak and thrust declines to insufficient levels. Therefore, supplementary devices, such as rocket engines or hybrid engine cycles, are needed to bring a SCRamjet aircraft to an adequate take over speed.

Figure 1.1 shows a sketch of a SCRamjet vehicle along with certain terminology. In contrast to conventional turbofan engines, the SCRamjet engine is highly integrated into the aircraft. The three main components are the air intake, the combustion chamber, and the exhaust nozzle. Incoming air is compressed by the contraction of the air intake and guided into the combustion chamber where, at supersonic

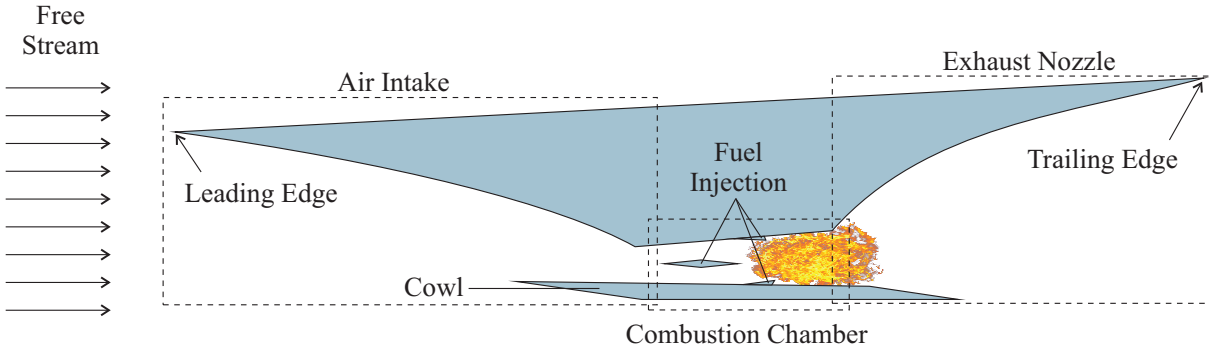


Figure 1.1: Schematic cross section of SCRamjet engine along with certain terminology.

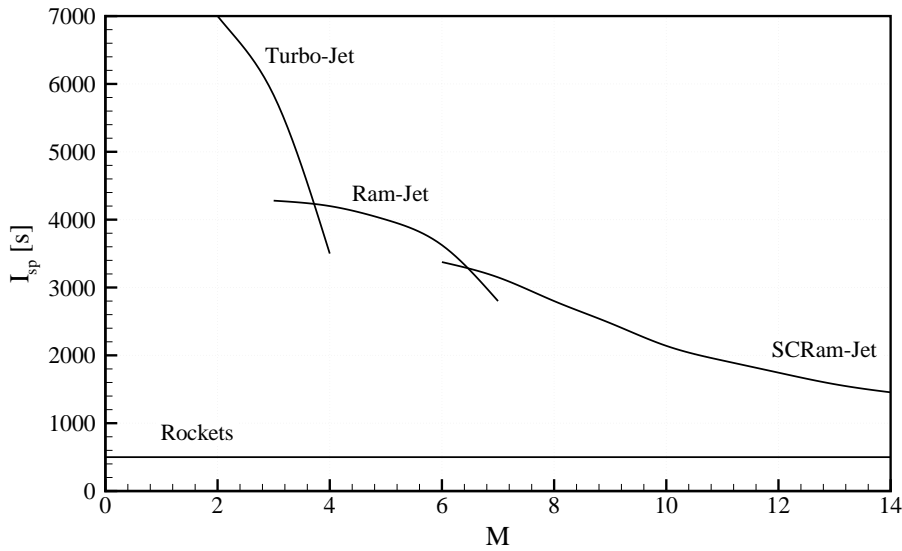


Figure 1.2: Estimated maximum specific impulse for hydrogen combustion of various jet propulsion systems; image adapted from [29].

speeds, fuel and air are mixed and burned. The exhaust gas is then accelerated through the nozzle. Minor components are the leading and trailing edges, or the intake cowl and fuel injection system.

Since SCRamjet engines use air from the atmosphere for combustion, no oxidizer has to be carried along, which reduces overall vehicle weight and increases efficiency. The specific impulse relates the engine's thrust  $F$  to the amount of fuel consumed  $\dot{m}_{\text{fuel}}$  and earth's gravity  $g$ :

$$I_{\text{sp}} = \frac{F}{g\dot{m}_{\text{fuel}}}, \tag{1.1}$$

and is a parameter to measure and compare engine efficiency [47, p.111]. In figure 1.2 estimated specific impulse is plotted against Mach number for different air-breathers as well as rocket engines. In contrast to rocket engines, which have a constant specific impulse,  $I_{\text{sp}}$  of air breathing engines varies with Mach number and it is evident that especially for high supersonic velocities ( $> 4$ ) ram compression is superior compared to rocket or turbo-jet engines. Extensive literature with overviews of SCRamjet engine systems exists and can be consulted for further information [47, 28, 29, 91].

### 1.2.2 Fields of Application

#### *Access to Space*

One field of application for SCRamjet engines are launch vehicles that lift payloads through the earth's atmosphere into low earth orbit. Since air breathing engines have considerably higher specific impulse and efficiency compared to rocket engines [47], a significant effort was made during the National Aerospace-Plane (NASP, 1983 – 1995) program to design a Single Stage To Orbit (SSTO) vehicle [11, 90] that was capable of running in SCRamjet mode for a certain Mach number range. However, the effort at the time was too large, partially due to the fact that multi stage to orbit has advantages over SSTO, but also due to SCRamjet technology not being advanced enough compared to rocket technology, and thus no flight vehicle was built. Nevertheless, the incentive of air breathing assisted space access is still an active field of research. Currently there are ongoing studies which investigate the replacement of the second stage of a multi-stage to orbit vehicle with an air breathing SCRamjet engine [81].

The present project and the entire research training group (section 1.1) are also embedded in the context of space access. Furthermore, AIAA's International Space Planes and Hypersonic Systems conference that was held in 2015 for the twentieth time, features extensive discussion and research on SCRamjet systems as means for space access, underlining the wide interest in this topic.

#### *Military Usage*

A country's military is most likely the first user of SCRamjet powered vehicles to operate on a regular basis. The increase in speed that aircraft gain by switching to ram powered operation is encouraged by the better efficiency of the ram engine cycle at higher Mach numbers. The SR71 blackbird, for example, had a ramjet flow path in addition to the turbojet engine, which was used in greater proportion with increasing Mach number. This led to a decrease in fuel flow rate from 38,000 to 36,000 pounds per hour while accelerating from Mach 3.0 to 3.15, due to the more efficient ramjet cycle [65, p.119]. Furthermore, various applications of ramjet missiles [12] already exist, and an evolution to a SCRamjet powered missile would be a natural step. The interest and participation of the United States Air Force and other defense contractors in the X51A and the HIFiRE programs (section 1.2.3) support this argument, and it is noted that a substantial amount of military-featured research would be classified.

#### *Hypersonic Transport*

In the long term, the SCRamjet engine cycle will also be of use for the civil sector, by reducing travel times, most likely after a substantial amount of flight hours have been accumulated during operation in the previous two sectors. Among others the LAPCAT [102, 94], FAST 20XX [93], and HEXAFLY [103] programs investigate this topic.

### 1.2.3 Flight Demonstrators

#### *X43A*

The X43A, or Hyper X vehicle (figure 1.3) is a SCRamjet flight demonstrator by the National Aeronautics and Space Administration (NASA) and a direct descendant of the earlier NASP and X15 flight programs [78, 63]. It was developed in a Multidisciplinary Design Optimization (MDO) loop [18, 19] for hypersonic flight and was the first SCRamjet to deliver positive thrust and acceleration during a controlled flight. While the first flight attempt in 2001 failed, the second and third flight in 2004 were successful and achieved Mach numbers of 6.83 and 9.68, respectively, making it the fastest air breathing vehicle to date.

The vehicle was air launched from a B52 bomber and further accelerated to hypersonic speed by a Pegasus rocket booster. After booster separation the intake cowl opened and hydrogen fuel was injected.

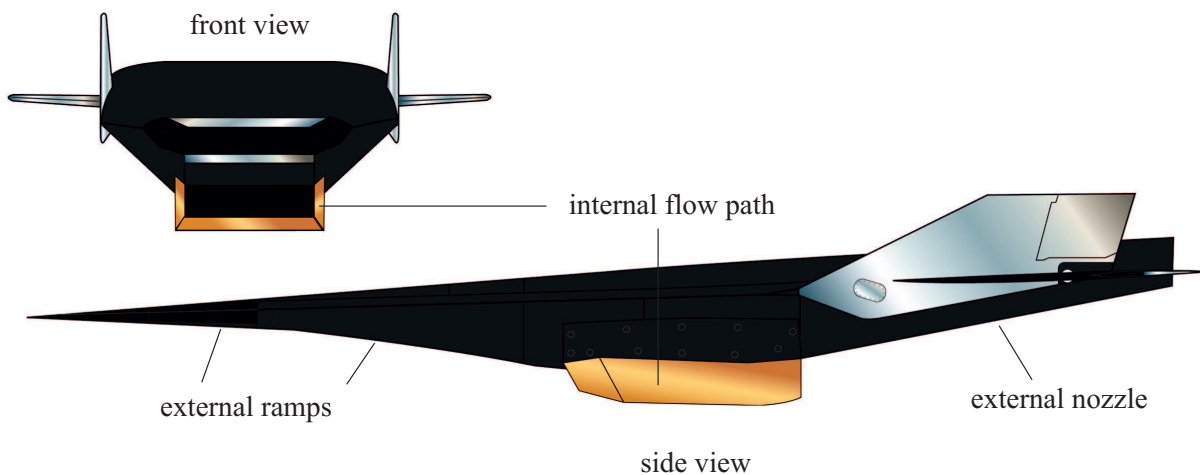


Figure 1.3: X43A sketch (<http://www.dfrc.nasa.gov/Gallery/Graphics/X-43A/>).

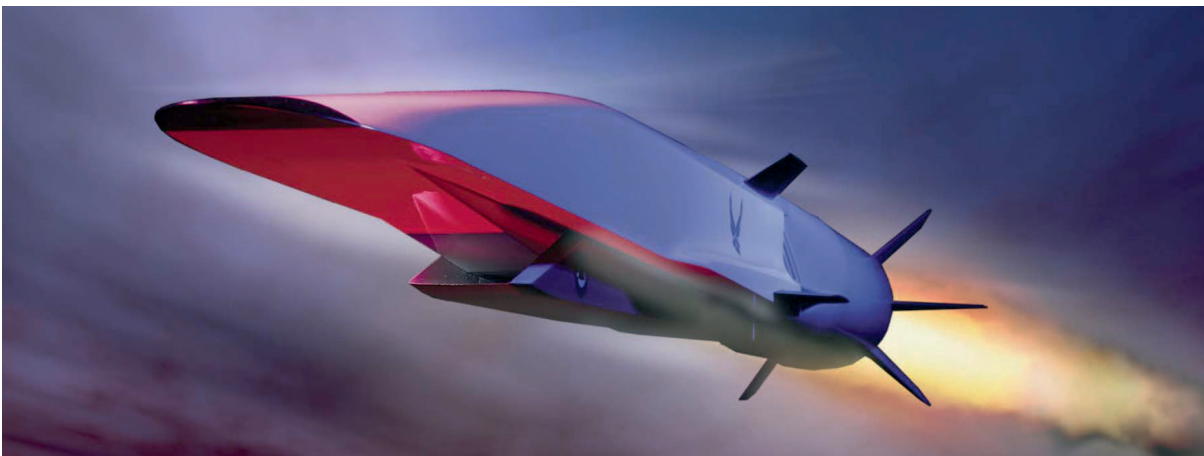


Figure 1.4: Artistic rendering of X51 vehicle along with booster and interstage ([https://commons.wikimedia.org/wiki/File:X-51A\\_Waverider.jpg](https://commons.wikimedia.org/wiki/File:X-51A_Waverider.jpg)).

Silane was added to assure ignition and turned off once the engine started successfully. The SCRamjet flow path was two-dimensional and consisted of the external parts and inner portion in which combustion occurred. Dynamic pressure during flight was  $\approx 0.5$  bar and the fuel flow lasted for 10 seconds. After engine shut-down post flight maneuvers were performed in which the vehicle made a controlled hypersonic glide.

### X51A

The X51A vehicle (figure 1.4) is a flight demonstrator of the HyTech program, led by the United States Air Force, with support of various defense contractors [45]. It is a direct descendant of X43A, but uses hydrocarbon fuel and ethylene to support ignition. Also launched from a B52 bomber, it is accelerated by a booster to a take over speed of about Mach 4.8. During operation, dynamic pressure was larger than for the Hyper X vehicle at  $\approx 1.0$  bar [72, 73]. The vehicle airframe was derived from a wave rider geometry while the engine flow path, that was built by Pratt and Whitney Rocketdyne, was two-dimensional. Between 2010 and 2013 there were four flights, while malfunctions, often related to the fins and once to an unstart of the intake, occurred during the initial three. The final flight in May 2013 was fully successful and the vehicle accelerated from Mach 4.8 to 5.1 during a 210 seconds flight. Post flight maneuvers were performed to test hypersonic glide capabilities after engine shut down.



**Table 1.1: Overview of the HIFiRE flights; table adapted from [21].**

HIFiRE #	led by	topic	launch date
0	AUS	Software development	March 2009
1	US	Transition measurements on cone	March 2010
2	US	SCRamjet combustor study	April 2012
3	AUS	Axisymmetry, ducted SCRamjet	Sept. 2012
4	AUS/US	Hypersonic glider maneuverability during sounding rocket flight	2017 <sup>†</sup>
5	US	Transition on elliptical cone	April 2012 <sup>*</sup>
6	US	Related to HIFiRE 4, but with SCRamjet flow path (no combustion)	2017 <sup>†</sup>
7	AUS/US	Ethylene combustion in three-dimensional SCRamjet flow path at Mach 7	March 2015 <sup>*</sup>
8	AUS/US	Sustained SCRamjet powered flight for 30 seconds at Mach 7	2018 <sup>†</sup>

<sup>†</sup> estimated launch dates; could be subject to change

<sup>\*</sup> flight attempt failed; will be repeated

### *HIFiRE*

The Hypersonic International Flight Research and Experimentation (HIFiRE) program investigates key aspects of hypersonic flight and is a joint cooperation between the United States and Australia. It consists of nine flights, the first of which (HIFiRE 0) was launched in 2009 and the last of which (HIFiRE 8) is planned to be launched in 2018. As of 2016, this program is still on going. In table 1.1 the flights are summarized, and it can be seen that at the beginning of the program experiments focused on basic topics such as hypersonic transition [57, 55] or supersonic combustion [53]. Towards the end of the program experiments are deeper specialized on hypersonic maneuverability and SCRamjet engine demonstration leading to HIFiRE 8: a sustained SCRamjet powered flight with ethylene fuel for 30 seconds.

There are two main differences to the previous X43A and X51A programs: First, all flights are launched with sounding rockets, and therefore for the sustained SCRamjet flight an additional pointing maneuver is necessary to readjust the vehicle horizontally. Second, the SCRamjet flow path is three-dimensional, as can be seen from the streamline traced and Rectangular to Elliptical Shape Transition (REST) intakes, that are used for HIFiRE 6 and 7, respectively [17, 86].

### **1.3 SCRamjet Intakes**

The SCRamjet intake serves as the compressor within its engine cycle while the intake shape is responsible for the entire ram compression. The intake can be regarded as the component that increases pressure and temperature of the free stream to levels sufficiently high for combustion. Pressure and temperature of 0.5 bar and 1000 K are reported in the literature as a priori estimates for hydrogen combustion with air [47, 98]. Pressure mainly influences combustion time and temperature affects ignition delay [84]. Therefore, during intake design the focus is on minimizing total pressure losses and guaranteeing stable operation along the flight path.

The intake is a critical component because it is located at the interface to the free stream and thus all

subsequent components depend on its proper functionality. Furthermore, the intake is a scene to various flow phenomena, such as laminar-turbulent boundary layer transition, shock boundary layer interaction or leading edge heating, that partially make up their own fields of research. Since the intake shape needs to integrate itself into the aircraft's geometry, usually a trade off has to be made between the optimum aerodynamic design, manufacturing restrictions, practicality, or the like. Various literature exists that gives different perspectives on the topics of supersonic diffusers [48, 24] and hypersonic intakes [13, 114].

### 1.3.1 Intake Design

If considering an intake as a black box, there are two interfaces. The first one is the interface to the free stream. It is dependent on variables such as Mach number and the dynamic pressure or altitude along a given trajectory and can usually be considered as given. The second one is the interface to the isolator and combustor section. The intake black box is enclosed by boundary conditions such as state of the intake wall or geometrical restrictions. The work of the intake designer is then to meet all requirements while maximizing intake efficiency and maintaining a high degree of flexibility.

A general distinction between two-dimensional and three-dimensional intakes can be made [14], while three-dimensional intakes have several advantages. First, they compress the flow field in all three dimensions and thus usually have less wetted surface area per unit mass flow through the intake. Second, as reported in [95], they show superior performance characteristics, even at off-design conditions, when compared to optimized two-dimensional ramp intakes. Third, as reported by Hirschel [49, p.311] shock boundary layer interactions occurring in three-dimensional space are frequently more tolerable than in two-dimensional. He noted that two-dimensional flow separations, such as on airfoils, are often times unsteady, while three-dimensional flow separations, such as on delta wings, can be macroscopically steady. Finally, two-dimensional configurations are more sensitive to angle of yaw.

Furthermore, one can distinguish between an analytical intake design approach and a more practical one, such as a parameter study supported by CFD, as reported by previous researchers within the research training group [50, 84]. Note that nowadays experimental investigations come in to play at later moments, due to the better development of numerical tools and increased costs for wind tunnel operation and model manufacturing. Several arguments are in favor of the analytical design approach. First, once a design tool is developed, in a relatively short amount of time an intake performance overview becomes available due to the numerically less expensive analytical computations. Second, requirements from the combustion chamber or trajectory can directly be considered during the design. Third, the intake design tool can be embedded in overall engine tools to quickly perform engine optimized parameter studies. Finally, with an analytical approach one remains more flexible to late changes in requirements.

Due to the above reasoning and the requirement of a three-dimensional intake design within the research training group, the focus of the present work is on the development of an analytical design tool for three-dimensional hypersonic intakes. A detailed report with the present state status on analytical intake design is given in section 2.1. Nevertheless, the great amount of research in that topic and the advancement from two-dimensional intake flow paths during the X43A and X51A studies to three-dimensional SCRamjet configurations (HIFiRE 7 & 8), stress the importance of the approach.

### 1.3.2 Intake Performance Parameters

Understanding of intake characteristics and flow can be gained by various means. Via qualitative information, such as the shock structure within an intake, or a schlieren image acquired during a wind tunnel run, general trends can be observed and effects can be compared relative to each other. Furthermore, local information such as wall pressure distribution or pitot pressure measurements can be extracted to study certain effects in more detail. Finally, overall intake behavior is best described by one-dimensional parameters, which are usually extracted at the intake exit plane. Those performance parameters are very

useful for two reasons. First, they quantify an intake's performance and allow for a comparison between different intakes. Second, they serve as a common denominator when the intake component is tailored back into a SCRamjet engine system analysis. Intake performance parameters, for example, can serve as boundary conditions to the combustion chamber or can be further processed in one-dimensional tools to calculate overall engine efficiency and performance.

In the further context some intake performance parameters are summarized. According to Smart [99], *static pressure ratio*, or sometimes referred to as compression ratio  $\Pi_{st}$ , is a so called capability parameter and describes the average pressure at the intake exit divided by free stream static pressure. A higher static pressure ratio increases combustion rate while ignition delay is less affected [84].

*Static temperature ratio*  $\Theta_{st}$  describes average static temperature at the intake exit normalized with free stream static temperature. Static temperature and pressure ratio are strongly coupled and an increase in one will normally lead to an increase of the other.

*Total pressure recovery* or total pressure ratio  $\Pi_{tot}$  is the average total pressure at the intake exit divided by free stream total pressure and is always  $< 1$  due to shock and viscous losses within the intake flow. Total pressure recovery is a measure for the efficiency of the compression process. An increase in compression ratio will normally lead to a decrease in total pressure recovery.

*Total temperature ratio*  $\Theta_{tot}$  relates total temperature at the intake exit and entrance and is a measure of heat transfer into or from the vehicle structure. For cooled intake walls  $\Theta_{tot} < 1$  holds, while a first approximation of  $\Theta_{tot} \approx 1$  can often be used as a practical assumption.

*Mass capture ratio*  $MCR$  relates mass flow through the intake to the mass flow through the capture area. Thus  $MCR < 1$  indicates that an intake is spilling air and does not capture the full air stream. Mass capture ratio is an important parameter to calculate nominal thrust parameters.

The parameters above are sufficient for any engine cycle analysis. Nevertheless, the following parameters are important for a better understanding of the intake flow. *Intake exit Mach number*,  $M_{ex}$  or  $M_3$ , can directly be calculated from static and total temperature ratio.

*Overall contraction ratio*  $CR_o$  is the capture area divided by the smallest cross sectional, or throat area of an intake. It is a geometrical feature rather than a performance parameter, but should always be given along with intake compression ratio. Similarly, *internal contraction ratio*  $CR_i$  is the cross sectional area at the beginning of the internal portion of an intake, divided by the throat area. It is also a geometrical feature, but has great impact on the starting behavior of an intake and can be used to estimate starting characteristics via empirical or analytical relations.

*Maximum sustainable static pressure ratio* before intake unstart  $\Pi_{st,max}$  is an important parameter to determine thresholds for stable intake operation.

*Maximum static temperature ratio*  $\Theta_{st,max}$  at the intake exit plane has a strong influence on ignition delay [84], because hotter locations can trigger ignition. The difference between static and maximum temperature ratio can be regarded as a measure for flow non-uniformity.

Finally, with total pressure recovery and free stream Mach number another compression efficiency parameter can be calculated, namely *kinetic energy efficiency*:

$$\eta_{KE} = 1 - \frac{2}{(\gamma - 1) M_\infty^2} \left( (\Pi_{tot})^{\frac{1-\gamma}{\gamma}} - 1 \right). \quad (1.2)$$

The variable  $\gamma$  describes the heat capacity ratio of the fluid. Kinetic energy efficiency is less dependent on free stream Mach number than total pressure recovery.

The performance parameters above will frequently be used throughout the context of this work. The list does not claim to be complete and further information on intake performance quantification can be found in the literature [16, 114, 98].



**Figure 1.5:** SR71 aircraft (left – <http://bilder.4ever.eu/luftfahrt/jagdflugzeug/lockheed-sr-71-blackbird-155931>) and Lockheed-Martin concept image of SR72 aircraft (right – <http://www.extremetech.com/wp-content/uploads/2013/11/SR-72.jpg>).

### 1.3.3 Intake Starting

The flow through a SCRamjet intake can either be subsonic or supersonic while the latter is the condition desired and is referred to as started intake flow. Intake starting behavior is a performance characteristic that attracts special attention during intake design. Not only is it important to successfully start an intake once a vehicle reaches take over speeds, it is also important to know the limitations and flight conditions that might unstart an intake. Figure 1.5 shows an image of the reconnaissance aircraft SR71 and a design concept of the follow-up aircraft SR72, that has not been built to this date. Note that the SR71 possessed two turbo ramjet engines, while the SR72 is proposed to contain SCRamjet cycles. However, the problem of intake starting occurs thereof independently. An unstarted intake not only causes a loss in thrust and introduces the complicated task of engine restart, but it can also affect the aerodynamic stability or operability when more than one engine is installed as seen in figure 1.5. The SR71 for example encountered severe handling problems once one intake unstarted [65], due to the other one causing a high yaw moment that had to be balanced by the rudder. Ultimately an intake unstart and fail to restart can even lead to a loss of the vehicle, as reported for one flight of the X51A [73].

Furthermore, great interest throughout the community has been present over the years, ranging from early work on supersonic diffusers [77, 56] to more recent studies that include empirical relations to predict intake starting [105, 99] and focus on three-dimensional geometries [54, 74]. A detailed report with present state status of starting mechanisms is given in section 2.3. Nevertheless, it is emphasized up front that starting behavior of three-dimensional intakes is still an open topic and that options to improve intake starting are still being investigated.

## 1.4 Objective of Current Work

The current work is encompassed by the design guidelines of the research training group, which were a flight at a Mach number and altitude of 8 and 30 km, respectively. For the chosen design point, static pressure and temperature were constant at 1170 Pa and 226 K, respectively, and dynamic pressure, calculated via:

$$q_{\infty} = \frac{1}{2} \rho_{\infty} V_{\infty}^2, \quad (1.3)$$

was 0.53 bar. To yield a static pressure of 0.5 bar in the combustor, the intake design pressure ratio at Mach 8 was 43. No fore-body compression was considered and a central strut fuel injector was to be used at the combustion chamber entrance. Detailed flight conditions and derived wind tunnel conditions are listed in the appendix (section A.1).

The main objective was the development of an analytical intake design tool and its validation. The tool

should be capable of generating an intake shape and analytically estimating intake performance. Furthermore, it should allow for a change in requirements or boundary conditions during a design process. If possible, CFD should be excluded from the design process to decrease the run time of the tool. Nevertheless, numerical simulations should be used for the validation of the analytical results.

Another objective was to better understand the performance characteristics of SCRamjet intakes and to develop a relation to better predict intake starting. Therefore, an already existing intake model, which was developed during the early phase of the research training group, should be further investigated experimentally in the hypersonic wind tunnel H2K. The focus of the experimental work should be on the intake starting behavior. The impact of different variables on intake starting should be investigated and with the gained experience an analytical relation to predict intake starting should be developed. Furthermore, experimental results should be compared with numerical simulations, to prove the applicability of the computational tools to three-dimensional SCRamjet intake configurations.

The final objective was to contrast the new design methodology to the one used for the already existing intake model. Furthermore, performance of the two classes of intakes should be compared relative to one another at the design point and at off-design conditions. In this context intake performance parameters should be used in a one-dimensional engine analysis to determine overall efficiency and to better understand the influence of intake performance on the overall engine system.

## 2 Current Scientific Knowledge

This section presents an overview of the current literature. It first focuses on analytical intake design and then on experimental and numerical performance estimation. Finally, the topic of intake starting is discussed and reviewed.

### 2.1 Intake Design

Smart [96] analytically investigated two-dimensional ramp intakes for Mach numbers ranging from 4 – 10, via the oblique shock relations. The intakes represented on-design configurations and for a constant pressure ratio the total pressure recovery generally increased with the number of oblique shocks. Viscous effects were not taken into account. Häberle [44] designed a two-dimensional intake with boundary layer bleed using the oblique shock relations for the ramps on the external portion of the intake. The internal shape and the isolator were widened in the vertical direction to account for the boundary layer thickness. Regions between shocks within the isolator were modeled with the method of characteristics, while viscous effects were not captured analytically. The boundary layer bleed reduced the size of the separation region but had only minor influence on intake performance. A three-dimensional ramp intake was designed by Reinartz and Gaisbauer [83]. The intake flow was first investigated numerically to estimate performance parameters and suitable sensor locations for a subsequent wind tunnel model. The intake model was then complemented with a combustion chamber and nozzle. Subsequently, the full engine model was successfully tested in a short duration facility [40], in which ignition of the hydrogen-air mixture was accomplished.

Hohn [50] and Riehmer [84] designed a three-dimensional intake, which is also a subject of this study and is explained in greater detail in section 6.1.1, via a parameter analysis and the aid of Computational Fluid Dynamics (CFD). Various parameters of the three-dimensional contour were varied and the geometry was subsequently analyzed numerically to yield a performance estimate. A design loop was performed and finished once the required intake exit conditions were reached. No analytical performance estimate could be made, but practical constraints, such as intake length or exit shape, were successfully considered. Furthermore, Hohn [50] generated streamline traced intakes from existing tools and pointed out their advantages.

In the remainder of this section the general approach to three-dimensional intake design, with an analytical performance estimate is given, along with selected specific approaches from the literature. The general four steps can be summarized as follows. First, a compression flow field, such as Busemann flow or reversed nozzle flow, needs to be calculated analytically. Second, because those flow fields are usually long and therefore heavy, they need to be truncated. Third, after placing a desired cross sectional shape in the flow field perpendicular to the free stream, streamlines can be traced that confine the outer hull of a three-dimensional intake geometry. Finally, because the flow fields mentioned above are valid for inviscid flow only, viscous effects need to be considered.

#### 2.1.1 Compression Flow Field

The axisymmetric compression flow field is the core of the three-dimensional design approach. There are two options to describe it analytically. On the one hand there are the Taylor McColl equations that result in Busemann flow [23, 68], which consists of an isentropic compression and a conical shock at the intake exit. On the other hand there is the method of characteristics, which usually describes expanding nozzle flow [2] that is fully isentropic. The nozzle flow can be reversed to a compressing flow field, which is

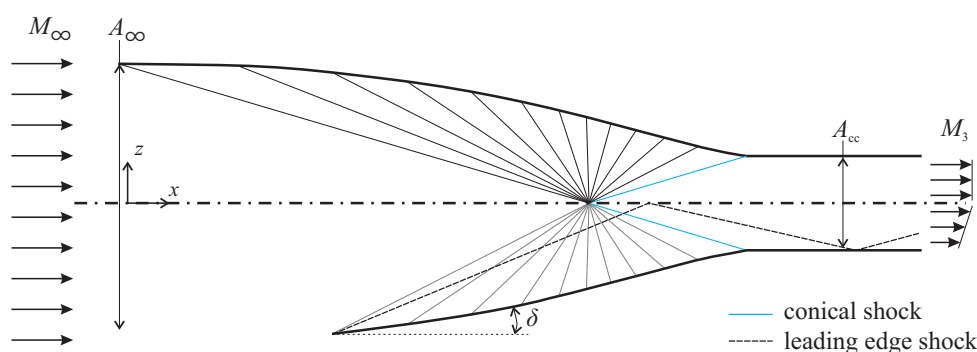


**Figure 2.1: Top: Schematic of classical Busemann flow; bottom: Schematic of leading edge truncation effects on Busemann flow.**

also referred to as reversed nozzle flow. The Taylor McColl equations and method of characteristics are described in greater detail in section 3. There is no definite tendency that favors one flow field over the other, and there are groups with a Busemann flow [116, 54, 106] or a reversed nozzle flow [92, 95] as the underlying compression flow field.

A Busemann flow field is used for the description of the following truncation and viscous effects, and it is shortly described via figure 2.1 (top). The free stream is isentropically compressed through lines of constant pressure, temperature, and Mach number (iso-lines) and the flow field is terminated by a single conical shock. Along the iso-lines, the velocity and its direction are known, and therefore the intake contour can be calculated by tracing one streamline up- or downstream. A deeper introduction to Busemann flow is given in section 3.2.1.

### 2.1.2 Truncation Effects

In the present work, truncation effects are divided into leading edge and rear side truncation effects. Generally, due to the truncation of the geometry, the intake shape is no longer similar to its non-truncated counterpart. Therefore, the flow fields will no longer be self-similar and the flow variables are different from the non-truncated, classical flow field. Consequently, for fixed design conditions, i.e.  $M_\infty$  and  $\Pi_{st}$ , a truncated geometry's shape does not fall onto a classical one.

#### *Leading Edge Truncation*

While Busemann and reversed nozzle intakes show excellent performance characteristics due to the isentropic compression, they tend to become excessively long, and therefore skin friction drag and weight increases. Furthermore, their compression starts gradually, and therefore a 0 deg inflow would have to be ensured. Since there are manufacturing limitations on how sharp the leading edges can be, and because a 0 deg leading edge would be prone to flow separation at angle of attack, Busemann and reversed nozzle intakes are usually truncated at the leading edge. A schematic of a truncated Busemann flow is shown at the bottom of figure 2.1, and it is noted that the general effect is also valid for reversed nozzle flow.

When truncating the flow field, an oblique shock forms at the leading edge. This oblique shock interferes with the iso-lines of the isentropic compression and travels down the isolator, while the compression efficiency decreases with increasing truncation. Furthermore, the outflow is no longer homogeneous. Usually, a trade-off has to be made between the benefit of isentropic compression or reduced skin friction while considering manufacturing restrictions and the expected range of angle of attack. Truncation angles between 2 deg and 6 deg are usually sufficient to reduce the intake length to an acceptable degree.

The truncation effect was also investigated in a numerical study for inviscid flows by Zhao [118], up to truncation angles of  $\delta = 6$  deg. Zhao reported that with increasing truncation angle, a stronger oblique

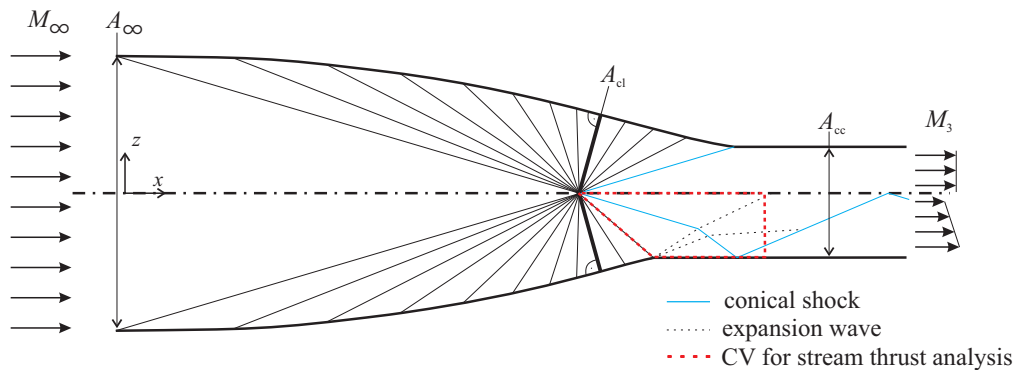


**Figure 2.2: Top: Schematic of classical Busemann flow; bottom: Schematic of rear side truncation effects on Busemann flow along with Control Volume (CV) for stream thrust analysis.**

shock emanates from the leading edge and distorts the flow field. Furthermore, the intake efficiency decreases with increasing truncation angle.

Ogawa et al. [75] verified this result for inviscid cases and extended the study to viscous applications. They set the intake exit radius to 0.1 m. At a Mach number, static pressure, and temperature of 8, 1197 Pa and 227 K, respectively, they observed that due to viscosity the Busemann intake performance, given as the total pressure recovery, generally dropped. With increasing leading edge truncation however, they found that the total pressure recovery has a weak maximum at around 2 deg. Another approach Ogawa proposed to reduce intake length was stunting, which is equal to contracting the intake in the free stream direction, thus changing the geometry. During stunting the overall contraction ratio remained constant, and for large amounts of stunting, they observed a Mach disk where the tip of the conical shock would normally stand. No results on different Mach or Reynolds numbers were reported.

### *Rear Side Truncation*

By truncating the classical Busemann and reversed nozzle contour at the rear side, intake length can be further reduced. A schematic of a truncated Busemann contour is displayed on the bottom of figure 2.2, and it is noted that the general effects are also valid for reversed nozzle flow. The impact on length reduction is not as distinct as for the leading edge truncation. However, the leading edge truncation causes an oblique shock at the highest Mach number, hence high shock losses. Therefore, it can be favorable to limit the leading edge truncation to a certain degree and achieve the desired length reduction by a combination of both: leading edge and rear side truncation. The structure of the iso-lines, thus isentropic compression, is terminated earlier and an expansion at the beginning of the isolator further disturbs the flow field. Consequently, the flow through the isolator is no longer homogeneous. If a certain geometry is truncated, the compression is usually less than for the non-truncated geometry.

Even though the rear side truncation complicates an analytical formulation of the flow field, truncating the intake at the rear side has other advantages: By truncating the intake at the rear side, the internal contraction ratio, which is the ratio of cowl closure cross sectional area  $A_{cl}$  to combustion chamber area  $A_{cc}$  decreases. The role of internal contraction ratio is discussed in section 2.3, but generally an intake shows improved starting characteristics for decreasing internal contraction. Furthermore, in certain cases the non-uniform flow through the combustor could improve fuel mixing and decrease ignition and combustion times, due to local regions of high temperature.

No investigations dedicated solely on rear side truncation are available. However, Veillard [110] proposed a so called strong shock principle, which resembles a truncation at the rear. Therein, instead of a weak shock, a strong oblique shock was used at the rear portion of a Busemann flow field. This ultimately truncated the geometry and resulted in improved starting behavior.



### 2.1.3 Streamline Tracing

The streamline tracing approach is a powerful means to generate fully three-dimensional geometries from two-dimensional or axisymmetric flow fields. Related research areas are for example wave raider geometries [82, 20], which show superior lift to drag ratios and which can be designed from axisymmetric flow fields. Furthermore, the streamline tracing approach was used to design three-dimensional nozzle geometries [67, 85]. In the SCRamjet intake community a lot of work on streamline tracing with regard to intake generation was documented by Billig [13, 15]. Billig emphasized the flexibility which can be gained by applying a streamline tracing approach. Furthermore, the integration of the engine flow path into the aircraft structure can be facilitated.

Streamline tracing can be performed with any desired shape, such as circular [54], elliptical [43] or quadratic [116, 12]. In all cases one portion of the cross section is placed near the center of the compression flow field. Thus, geometries with large leading edge sweep are generated. Furthermore, the approach was extended to include a shape transformation from rectangular/quadratic to elliptical/circular [92, 95] cross-stream shape. Thereto, streamlines were traced for geometries with different cross sections and finally the different flow paths were morphed into one geometry with a weighing function. The morphed geometries had similar performance to the unchanged geometries and improved integration into the vehicle structure.

### 2.1.4 Viscous Effects

In the Reynolds number range considered ( $< 50 \cdot 10^6 \text{m}^{-1}$ ), a viscous and inviscid solution to the Busemann or reversed nozzle flow differ significantly from each other. Generally, a boundary layer is forming at the leading edge and grows under the influence of the edge properties known from the inviscid flow field. However, due to the displacement effect of the boundary layer, the compression region is further contracted and the properties themselves change. This has an effect on the boundary layer development, which again is felt by the core flow. This effect is sketched on the bottom of figure 2.3 for a Busemann flow field, and it is noted that the general effect is also valid for reversed nozzle flow.

Generally, the effective contraction of the Busemann contour is increased by the additional displacement of the boundary layer, and the pressure and temperature are higher than predicted analytically. Furthermore, the fan-like flow field is disturbed, and depending on the case, the flow through the isolator could be no longer uniform. This effect depends on Reynolds number and becomes more severe with decreasing Reynolds number.

One approach is to calculate the displacement thickness of the viscous boundary layer. With the displacement thickness, the intake contour can be widened, and a corrected contour is obtained, that has a lower internal as well as overall contraction ratio. The key objective is to protect the inviscid core flow from the additional contraction of the boundary layer, as displayed schematically in figure 2.4.

Wie and Mölder [116] used the edge pressure distribution that is known from the analytical compression flow field as input to a boundary layer code to calculate the displacement thickness. Corrected geometries were investigated numerically for axisymmetric cases and viscous simulations matched the analytical prediction. For a classical contour, without truncation, they observed an expansion near the leading edge due to the initial widening of the flow. This is another reason for truncation the flow at the leading edge. Smart [95] used a finite difference boundary layer code to account for viscous effects. The viscous correction was performed for the on-design conditions and laminar-turbulent transition was triggered in the boundary layer tool at a fixed location downstream of the leading edge. For an axisymmetric spike intake Matthews et al. [62] calculated viscous properties with a turbulent flat plate correlation and the reference temperature method. They were able to properly predict intake performance analytically, and emphasized that isolator skin friction had to be considered to properly match analytical and experimental data.

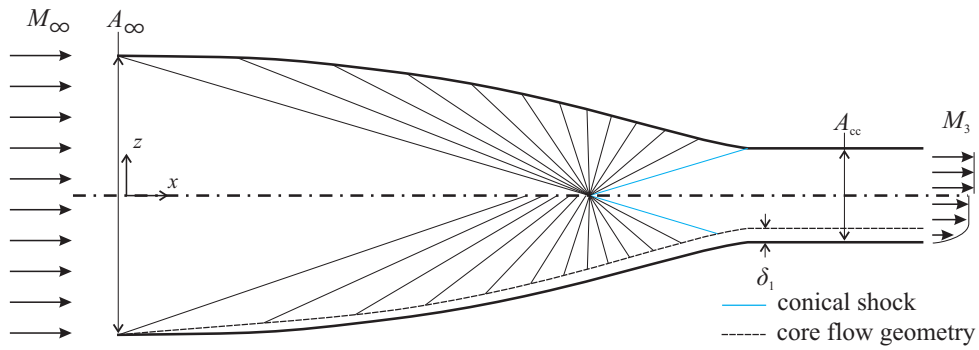


**Figure 2.3: Top: Schematic of classical Busemann flow; bottom: Schematic of viscous effects in uncorrected Busemann contour.**

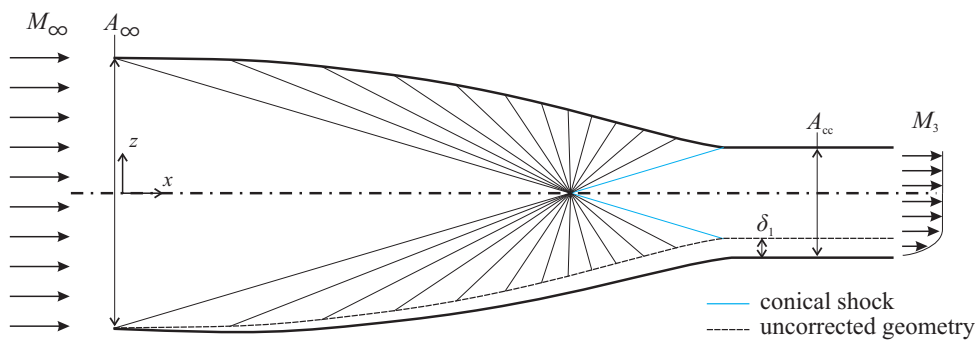


**Figure 2.4: Top: Schematic of classical Busemann flow; bottom: Schematic of viscous effects in corrected Busemann contour.**

## 2.2 Performance Determination

Pre-flight performance estimates of a hypersonic vehicle can be gathered via analytical, experimental, and numerical tools. Since the analytical portion was treated in the context of intake design (section 2.1), in the following paragraphs the focus is put on experimental and numerical means.

### 2.2.1 Experimental

Experiments on the aerothermal behavior of hypersonic vehicles are usually performed in supersonic and hypersonic wind tunnels, which can roughly be divided into short duration and longer duration facilities. In general, higher test duration time and free stream enthalpy both increase the operational costs. Furthermore, there are technological limitations such as temperature restrictions on materials, or pressure restrictions on critical wind tunnel components. Therefore, longer duration tunnels usually operate in cold flow test conditions, meaning that they duplicate flight Mach and Reynolds number rather than flight velocity. Normally, tunnels which additionally duplicate flight velocity tend to have shorter test duration times.

Hohn [50] investigated the influence of angle of attack on intake wall pressure. The model was mounted with the cowl pointing upwards. When the nose was pitched upwards so that the ramp shock decreased in strength, wall pressures decreased. Stephen et al. [104] reported hysteretic behavior during intake start and unstart, while varying angle of attack in the range of  $-5$  deg to  $15$  deg. Jacobsen et al. [54] used schlieren images to determine whether an intake was started or not and various others acquired the shock train structure in the internal portion of a two-dimensional intake configuration [41, 44]. Furthermore, wall pressure and heat transfer as well as oil film measurements can reveal more detailed information of the flow field. For instance, wall pressure was successfully used by Chan et al. [25] to determine whether combustion and ignition occurs. Durant et al. [32] performed heat transfer measurements on a generic SCRamjet fore-body in quiet and noisy flow environment and observed that transition is delayed for quiet flow. Note that in some intake configurations, such as the X43A engine [78], the boundary layer was tripped to force transition and eventually turbulence at a discrete location. Even though turbulent flow increases skin friction and heat transfer, it can withstand a higher adverse pressure gradient before separation. Finally, at the intake exit in-stream parameters such as static and pitot pressure, and thus Mach number, are often times measured with a rake to determine intake performance [44, 84]. Pinckney [80] for example improved a conventional static pressure probe by smoothing the transition section between the probe tip and downstream end to reduce probe length. In some cases, additional devices such as a throttle are added to the intake to measure mass flow, or to impose a back pressure on the intake exit [108].

### 2.2.2 Numerical

With the increase in computing power, large scale simulations, such as Large Eddy or in certain regions Direct Numerical Simulations (LES/DNS), become more feasible in hypersonic flows. Within the research training group, for example, Konopka [58, 59] investigated the film cooling effect of supersonic flow by means of LES and Atak [7] investigated unsteady phenomena, such as shock wave boundary layer interactions, with a discontinuous Galerkin method on large scale grids. In the current work Reynolds-Averaged Navier-Stokes (RANS) simulations were performed with the DLR-TAU code (see section 6.4). Therefore, in the further context focus is put on similar approaches.

Riehmer et al. [85] validated different CFD codes with wind tunnel experiments for a SCRamjet engine model. Note that their intake model was also used for experiments in the present work. They obtained good agreement between numerical results and wind tunnel data and repeated the simulations for flight conditions to yield numerical flight data. Furthermore, during the design of the axisymmetric SCRamjet demonstrator vehicle SCRAMSPACE [22], CFD was extensively utilized. Grainger et al. for example investigated the starting behavior of the axisymmetric air intake [42], and they showed that it could

be started successfully with bleed holes. On a similar configuration Peterson et al. performed CFD studies with hybrid LES-RANS and RANS-only solvers on fuel-air mixing within the intake [79]. They showed that fuel injection in the expansion region of the intake results in the greatest amount of fuel penetration and that the RANS simulation had problems resolving shear layer vortices. Baurle et al. further post-processed CFD intake data for usage in one-dimensional design tools [9]. They stressed that stream-thrust-averaged variables need to be used once performance parameters extracted from CFD solutions are used for cycle analysis, because they conserve mass, momentum and energy. Finally, Holden et al. performed experiments at the CUBRC lens facilities on turbulent boundary layers of axisymmetric cone-flare and double cone configurations that were subsequently compared to RANS solutions of different CFD solvers [51, 52]. While attached flow was generally simulated correctly with CFD, boundary layer separation lengths and especially heat transfer within and downstream of the separation region differed, in some cases significantly, from the experiments. More information on the blind test comparison can be found on the CUBRC website ([http://www.cubrc.org/index.php?option=com\\_content&view=article&id=121&Itemid=64](http://www.cubrc.org/index.php?option=com_content&view=article&id=121&Itemid=64)). This stresses the importance of validating numerical results with certain configurations investigated in wind tunnel experiments.

## 2.3 Intake Starting

### 2.3.1 General Research

As mentioned before intake unstart can lead to a severe reduction in mass flow or overall engine performance, and can affect the vehicle aerodynamic stability. In figure 2.5 a fully enclosed and a partially enclosed intake are displayed, while in a first approximation the fully enclosed intake can be regarded as the internal portion of the partially enclosed intake. The flow through a convergent duct can be modeled most simply by isentropic flow, and the largest area ratio physically possible is described by:

$$CR_{\text{isentr}} = \frac{A}{A_{\text{th}}} = \frac{1}{M} \left[ \frac{2}{\gamma + 1} \left( 1 + \frac{\gamma - 1}{2} M^2 \right) \right]^{\frac{\gamma + 1}{2(\gamma - 1)}}. \quad (2.1)$$

If the fully enclosed intake is initially unstarted, a normal shock stands in front of the diffuser. According to Oswatitsch [77] and Kantrowitz and Donaldson [56] the normal shock is going to be swallowed by the intake, if the subsonic flow behind the shock is accelerated just to  $M = 1$  at the intake throat. If the contraction is increased, the normal shock will not be swallowed but detach from the intake to allow a spillage air stream around the intake to account for the lower mass flow through the intake. If the contraction ratio is decreased the shock will be swallowed and the intake starts.

This behavior is widely referred to as the Kantrowitz criterion and is given by:

$$CR_{\text{Kanttr}} = \frac{A_{\text{cl}}}{A_{\text{th}}} = \left( \frac{(\gamma + 1)M_{\text{cl}}^2}{(\gamma - 1)M_{\text{cl}}^2 + 2} \right)^{0.5} \left( \frac{(\gamma + 1)M_{\text{cl}}^2}{2\gamma M_{\text{cl}}^2 - (\gamma - 1)} \right)^{\frac{1}{\gamma - 1}}. \quad (2.2)$$

If the Mach number approaches infinity, the contraction ratio reaches a constant limit:

$$\lim_{M \rightarrow \infty} CR_{\text{Kanttr}} = \left( \frac{(\gamma + 1)}{(\gamma - 1)} \right)^{0.5} \left( \frac{(\gamma + 1)}{2\gamma} \right)^{\frac{1}{\gamma - 1}} = 1.666, \quad (2.3)$$

which means that according to the Kantrowitz theory, no intake with a contraction ratio larger than 1.666 is self-starting.

The Kantrowitz criterion and the isentropic limit are plotted in figure 2.6, along with empirical relations that are explained in the further context. The figure is frequently referred to as Kantrowitz plot and can be drawn with  $1/CR_i$  or  $CR_i$  as the dependent variable. Three regions are present in the Kantrowitz plot. First, for low contraction ratios ( $CR_i < CR_{\text{Kanttr}}$ ) intakes will be self-starting according to Kantrowitz.

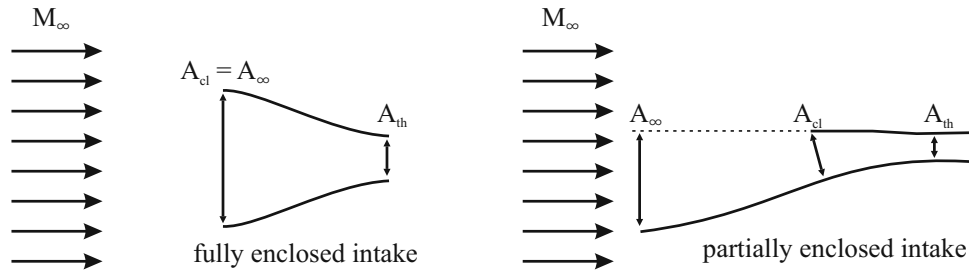


Figure 2.5: Schematic of fully and partially enclosed intakes.

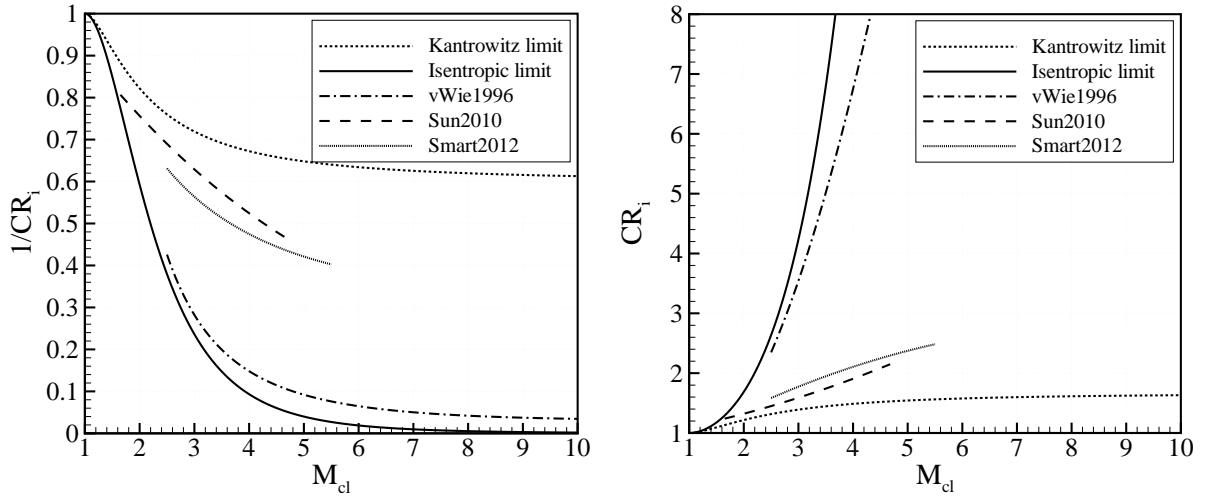


Figure 2.6: Kantrowitz diagram for  $1/CR_i$  and  $CR_i$  along with isentropic limit and empirical relations.

Second, for large contraction ratios ( $CR_i > CR_{isentr}$ ) the contraction is too large for an intake to work physically. Third, for moderate contraction ratios ( $CR_{Kanttr} < CR_i < CR_{isentr}$ ) intakes are not self-starting according to Kantrowitz, but can work once successfully started. In the further context this region is referred to as critical region.

Various authors published research on the intake starting process and stressed that especially three-dimensional intakes tend to be self-starting at contraction ratios higher than predicted by Kantrowitz. Sun [105] proposed a quadratic, empirical relation between the contraction ratio and  $M_{cl}$  to predict intake starting in the Mach number range between  $1.65 < M_{cl} < 4.68$ :

$$CR_{Sun} = 0.933 - \frac{1}{6.87}M_{cl} + \frac{1}{40.9}M_{cl}^2. \quad (2.4)$$

Therefore, different self-starting intakes taken from experiments found in the literature, were plotted in the Kantrowitz diagram and then quadratically approximated (see dashed line in figure 2.6). Similarly, Smart [99] proposed a quadratic fit to data of various three-dimensional intakes which predicts slightly larger contraction ratios. The correlation is valid for  $2.5 < M_{cl} < 5.5$  (figure 2.6). Both relations fall well within the critical region where starting should not occur according to Kantrowitz theory.

Van Wie et al. [115] investigated intake starting behavior with a generic two-dimensional model of an internal intake. They observed hard and soft versions of intake unstart, depending on the specific configuration of their generic model, which had variable geometry and therefore an adjustable internal contraction ratio, but were not able in all cases to discern the causal effects of hard and soft unstarts. From their data they introduced an empirical limit for the highest contraction ratios possible, similar to

the isentropic limit, but taking into account viscous effects and shock losses (see dashed-dotted line in figure 2.6). The relation is valid for  $2.5 < M_{cl} < 10$  and is given by:

$$\frac{1}{CR_{vanWie}} = 0.05 - \frac{0.52}{M_{cl}} + \frac{3.65}{M_{cl}^2}. \quad (2.5)$$

Finally, Mölder, Tahir and Timofeev published numerous articles on intake starting [69, 107, 110]. They studied different ways of promoting intake starting, such as overboard spillage, overspeeding, permeable walls, or by employing unsteady effects. A general approach was to first articulate the intake geometry into the region where the intake will self-start and then change the geometry via movable parts towards the isentropic limit. Their paper on intake starting, presented at the 2008 AIAA Space Planes Conference, gives a good overview of the different techniques and mechanisms [107].

### 2.3.2 Self-Starting Intake Configurations

In this section experimental starting data are extracted from the literature, which fulfills the following criteria: First, the intake had to be started or re-started from a blocked condition after the tunnel flow was fully developed. This prevented any enhancements of the unsteady effects during wind tunnel start and excluded any experiments conducted in short duration facilities such as shock or expansion tubes. Second, an estimate of the Mach number at the cowl closure location needed to be given. Third, intake configurations with boundary layer bleed were excluded since they make a proper calculation of the internal contraction ratio difficult. All configurations fall within the critical region of the Kantrowitz plot.

Various starting experiments were performed by Smart et al. [97, 101, 100] on three-dimensional intakes with Rectangular to Elliptical Shape Transition (REST-intakes). Tests were performed in blow down wind tunnels down to Mach numbers of 4, and mostly fixed geometry intakes were investigated. Mach number at the cowl closure position was estimated from CFD. An intake was determined to be self-starting once it re-started after being blocked to an unstart with a throttle attached to the intake exit. For the low Mach number tests (Mach 4) the intake only started by the addition of bleed holes on the cowl side and side walls [101]. For the Mach 12 intake configuration [100], the Mach number at the cowl closure position was assumed to be equal to the geometry investigated earlier [97].

During a test campaign in a blow down wind tunnel at Virginia Tech, Jacobsen [54] investigated the starting behavior of a streamline traced Busemann intake. The model was equipped with a movable cowl and after tunnel-start the internal contraction was decreased by moving the cowl downstream until the intake started. At a free stream Mach number of 4 the intake started for  $CR_i = 1.59$ . Jacobsen estimated the Mach number at the cowl closure position to be 3.

Goldberg and Hefner [41] performed starting experiments in a Mach 6 blow down wind tunnel with a two-dimensional model without external compression. Thus, the Mach number at the cowl closure was approximately equal to the free stream Mach number. The intake cowl could be rotated to modify the internal contraction and flaps at the cowl's trailing edge were used to block off the flow and determine self-starting capabilities. Reynolds number had a minor effect and wall cooling enhanced starting.

In a blow down wind tunnel Emami et al. [33] investigated the unstart and restart qualities of a two-dimensional intake model with a single ramp as external compression. Together with the free stream Mach number (6) and deflection angle (11 deg) the Mach number at the cowl closure could be estimated. The intake cowl could be rotated around the throat location, thus internal contraction ratio could be varied. Once the intake unstarted, the restart position – therefore internal contraction – could be detected by opening the intake cowl. They observed that with thinner boundary layers entering the internal portion of the intake, intake starting could be improved.

## 3 Aerodynamic Theory

### 3.1 Fundamentals

In the following subsections, selected topics in aerodynamics that are utilized throughout this work are presented shortly. A more comprehensive introduction into aerodynamics can be found in the literature [2, 4].

#### 3.1.1 Standard Atmosphere

The standard atmosphere was approximated according to the 1976 U.S. Standard Atmosphere report [71]. Temperature depended on altitude, and an exponential relation for pressure was used. Thus, for a given altitude pressure and temperature were known. Further information can be found in [5, chap.3]

#### 3.1.2 Gas Properties

An ideal gas is defined by:

$$p = \rho RT, \quad (3.1)$$

while the specific gas constant  $R$  is a known property of the gas. When the specific heat capacities at constant specific volume  $c_v$  and pressure  $c_p$  can be considered as constant, the gas is called a calorically perfect gas. The speed of sound of a calorically perfect gas can be expressed as:

$$a = \sqrt{\frac{\gamma p}{\rho}} = \sqrt{\gamma RT}, \quad (3.2)$$

and the latter expression states that it is a function of temperature only.

Viscosity  $\mu$  was modeled with Sutherland's law and a linear relation for temperatures lower than 120 K was used [1, p.4].

#### 3.1.3 Quasi One-Dimensional Flow

In quasi one-dimensional flow it is assumed that flow properties are uniform and depend on only one local coordinate, usually the  $x$ -variable. Furthermore, the cross sectional area is assumed to vary with the local coordinate and thus a general relationship between the Mach number and cross sectional area can be derived as:

$$\left(\frac{A}{A^*}\right)^2 = \frac{1}{M^2} \left(\frac{2}{\gamma+1} \left(1 + \frac{\gamma-1}{2} M^2\right)\right)^{\frac{\gamma+1}{\gamma-1}}. \quad (3.3)$$

If the assumption of adiabatic flow is applicable, the following equation allows for the calculation of the temperature within the flow, assuming the free stream conditions are known:

$$h_t = \text{const.} = c_p T \left(1 + \frac{\gamma-1}{2} M^2\right) = c_p T + \frac{V^2}{2}. \quad (3.4)$$

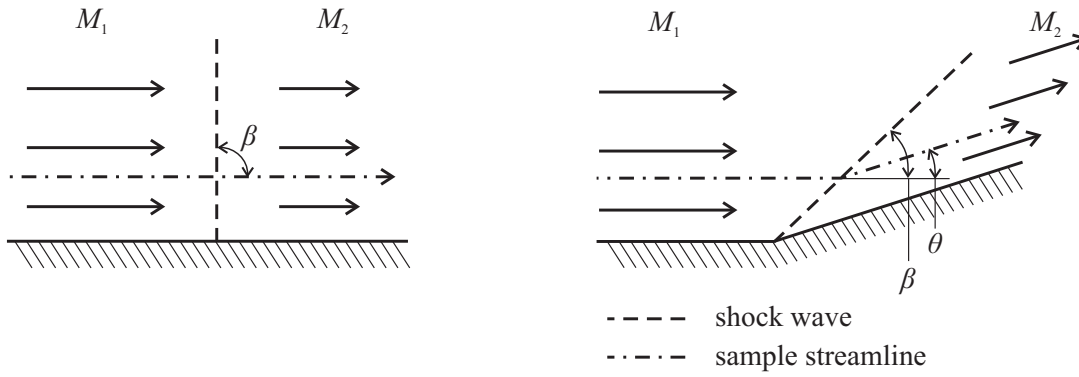


**Figure 3.1: Schematic of flow across a normal (left) and oblique shock (right).**

Especially in nozzle flows, the assumption of isentropic flow is often used and together with the equation of state, (3.1), further flow properties can be calculated:

$$T^\gamma p^{1-\gamma} = \text{constant}. \tag{3.5}$$

In internal flows, the previous equations can become quite powerful for calculating general trends. However, one has to keep in mind the applicability of quasi one-dimensional flow and that certain flow phenomena, such as viscous effects or non-uniformity due to three-dimensional geometries are hard to capture analytically.

### 3.1.4 Oblique and Normal Shock Relations

A normal shock is equivalent to an oblique shock with a shock angle of 90 deg. Properties with the subscripts 1 and 2 denote conditions upstream and downstream of the shock, while the subscripts n and t denote directions normal and tangential to the shock wave, respectively. For a better understanding, in figure 3.1 a schematic of the flow profile is given.

$$M_{n,1} = M_1 \sin(\beta) \tag{3.6}$$

$$M_{n,2}^2 = \frac{1 + \frac{\gamma-1}{2} M_{n,1}^2}{\gamma M_{n,1}^2 - \frac{\gamma-1}{2}} \tag{3.7}$$

$$\frac{p_2}{p_1} = 1 + \frac{2\gamma}{\gamma + 1} (M_{n,1}^2 - 1) \tag{3.8}$$

$$\frac{\rho_2}{\rho_1} = \frac{(\gamma + 1) M_{n,1}^2}{2 + (\gamma - 1) M_{n,1}^2} \tag{3.9}$$

The Mach number after the shock wave can finally be calculated with:

$$M_2 = \frac{M_{n,2}}{\sin(\beta - \theta)}. \tag{3.10}$$



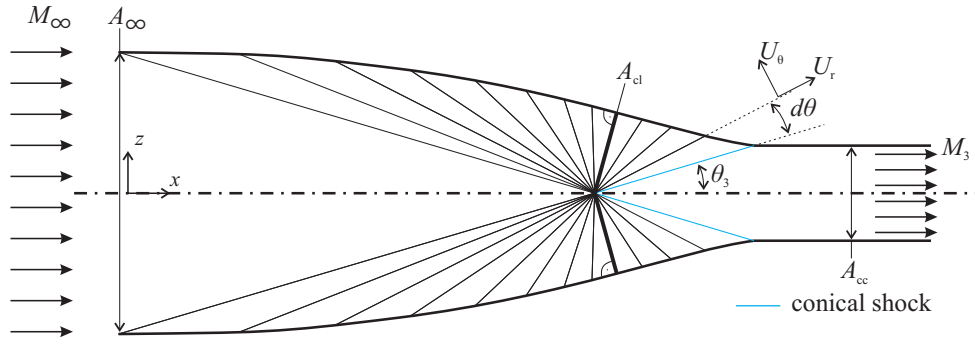


**Figure 3.2: Schematic of classical Busemann flow.**

The relationship between Mach number  $M_1$ , deflection angle  $\theta$ , and shock wave angle  $\beta$  is given as:

$$\tan(\theta) = 2 \cot(\beta) \frac{M_1^2 (\sin(\beta))^2 - 1}{M_1^2 (\gamma + \cos(2\beta)) + 2}. \quad (3.11)$$

It is noted, that equation (3.11) has to be solved iteratively with for example Newton's method [6, p. 292], if Mach number or shock wave angle is the unknown property.

## 3.2 Axisymmetric Compression Flow Fields

The compression flow field is the core element during the intake design process. In the present work a Busemann flow and a reversed nozzle flow designed with the method of characteristics were studied. If those flow fields are considered without any truncation or viscous effects, they will be referred to as classical. Both flow fields start out with a zero degree inflow and an isentropic compression. While the Busemann flow is terminated by a conical shock wave, the reversed nozzle flow is purely isentropic, and therefore the efficiency is usually slightly higher. The outflow of both flow fields is homogeneous. For both flows the assumptions are inviscid, axisymmetric and irrotational.

### 3.2.1 Taylor McColl Equations

A general sketch of a classical Busemann intake is shown in figure 3.2. The uniform free stream is deflected gradually and compressed isentropically through an array of fan-like lines that focus around one point. This point is the tip of a conical shock, after which the air flow is again uniform and parallel to the free stream. Along the fan-like lines, the flow properties ( $p, T, M$ ) are constant and therefore these lines are referred to as iso-lines in the further context. With the isentropic compression and the shock wave occurring at the lowest Mach number, the Busemann intake shows excellent performance characteristic, while at the same time the flow field can be described analytically.

The change in flow properties throughout the isentropic compression can be calculated with the Taylor McColl equations:

$$U_r'^2 (U_r + U_r'') = \frac{\gamma - 1}{2} (1 - U_r^2 - U_r'^2) (U_r'' + U_r' \cot(\theta) + 2U_r), \text{ and} \quad (3.12a)$$

$$U_r' = U_\theta. \quad (3.12b)$$

One and two primes describe the first and second derivatives with respect to  $\theta$ , respectively. The  $r$  and  $\theta$  direction describe the radial and tangential direction, respectively and  $\theta$  is the angle of a fan-like line

to the free stream as denoted in figure 3.2. The velocities  $U_i$  are normalized to the maximum velocity that would be reached when expanding the flow isentropically to  $T = 0$  K and are functions of  $\theta$  only. The iso-line which is perpendicular to the Busemann contour is labeled as the cowl closure position (cl) which will be further explained in section 4.4. Equation (3.12) can be integrated, starting at  $\theta_3$  with increments of  $d\theta$  with for example a Runge Kutta method [6].

With

$$\sqrt{U_r^2 + U_\theta^2} = U = \sqrt{\frac{(\gamma - 1)M^2}{2 + (\gamma - 1)M^2}}, \quad (3.13)$$

the normalized velocity is related to the Mach number, while the pressure, temperature and density can be calculated by the energy equation (3.4), the relation for isentropic flow (3.5), and the equation of state (3.1). To this point, the exact size of the Busemann intake is not defined, and dimensions can be given as fraction of an arbitrary length scale. Note, that this is applicable for inviscid flow only. In viscous flows intake scale has an influence on Reynolds number and consequently Busemann flow fields become scale and Reynolds number dependent. Furthermore, the pressure and temperature along the iso-lines can be given as fractions of arbitrary free stream properties,  $p_\infty$  and  $T_\infty$ .

### 3.2.2 Method of Characteristics

Flow through a supersonic nozzle is described by the method of characteristics, which calculates a characteristic mesh as displayed schematically in figure 3.3. If the nozzle is reversed a compression flow field can be calculated analytically. In the present section, the theory for the method of characteristic for axisymmetric flow will be explained. Important literature with more detailed information is [117, 26, 2].

Characteristic directions can be defined with the flow angle  $\theta$  and Mach angle  $\mu$ :

$$\left(\frac{dr}{dx}\right)_{\text{char}} = \tan(\theta \pm \mu). \quad (3.14)$$

The  $\pm$  sign describes right and left running characteristics, respectively and therefore, along a right running, or  $C_-$  characteristic, the following compatibility equations hold:

$$\frac{dr}{dx} = \tan(\theta - \mu), \text{ and} \quad (3.15)$$

$$d\theta + \cot \mu \frac{dV}{V} - \frac{\sin \theta \sin \mu}{\sin(\theta - \mu)} \frac{dr}{r} = 0. \quad (3.16)$$

Along a left running, or  $C_+$  characteristic, the following compatibility equations hold:

$$\frac{dr}{dx} = \tan(\theta + \mu), \text{ and} \quad (3.17)$$

$$d\theta - \cot \mu \frac{dV}{V} + \frac{\sin \theta \sin \mu}{\sin(\theta + \mu)} \frac{dr}{r} = 0. \quad (3.18)$$

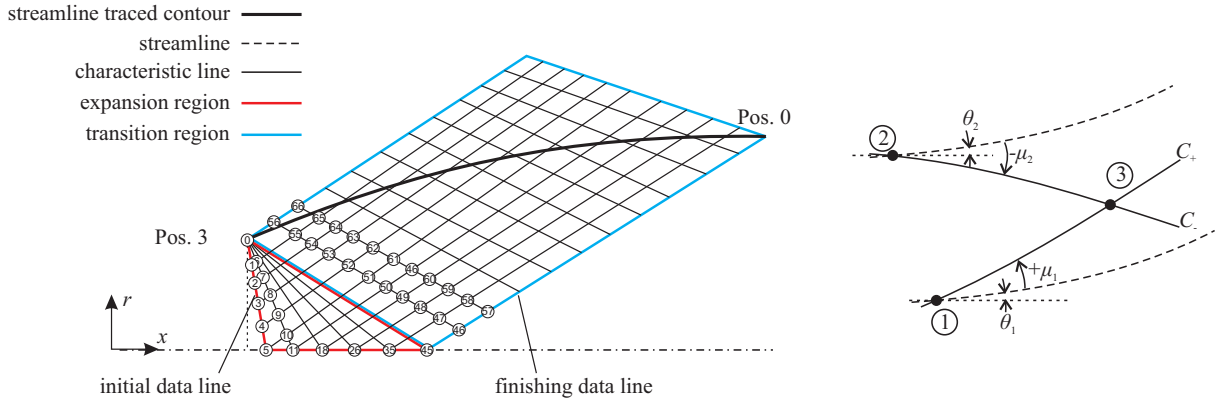


**Figure 3.3: Sketch of characteristic mesh along with streamline traced contour (left) and close-up of three points (right).**

### 3.3 Boundary Layer Flow

#### 3.3.1 Boundary Layer Equations

The boundary layer equations can be derived from the Navier-Stokes equations, written here for steady, two-dimensional flow in the  $x - y$ -plane, where the normal stress terms were neglected [4]:

$$\frac{\partial \rho u}{\partial x} + \frac{\partial \rho v}{\partial y} = 0, \quad (3.19)$$

$$\rho u \frac{\partial u}{\partial x} + \rho v \frac{\partial u}{\partial y} = -\frac{\partial p}{\partial x} + \frac{\partial}{\partial y} \left( \mu \left( \frac{\partial v}{\partial x} + \frac{\partial u}{\partial y} \right) \right), \quad (3.20)$$

$$\rho u \frac{\partial v}{\partial x} + \rho v \frac{\partial v}{\partial y} = -\frac{\partial p}{\partial y} + \frac{\partial}{\partial x} \left( \mu \left( \frac{\partial v}{\partial x} + \frac{\partial u}{\partial y} \right) \right), \text{ and} \quad (3.21)$$

$$\rho u \frac{\partial (e + V^2/2)}{\partial x} + \rho v \frac{\partial (e + V^2/2)}{\partial y} = \frac{\partial}{\partial x} \left( k \frac{\partial T}{\partial x} \right) + \frac{\partial}{\partial y} \left( k \frac{\partial T}{\partial y} \right) - \frac{\partial (up)}{\partial x} - \frac{\partial (vp)}{\partial y} + \frac{\partial}{\partial x} \left( \mu v \left( \frac{\partial v}{\partial x} + \frac{\partial u}{\partial y} \right) \right) + \frac{\partial}{\partial y} \left( \mu u \left( \frac{\partial v}{\partial x} + \frac{\partial u}{\partial y} \right) \right). \quad (3.22)$$

In equations (3.20) through (3.22)  $V$ ,  $e$ , and  $k$  are the absolute velocity, specific internal energy, and thermal conductivity of the fluid, respectively.

In addition to two-dimensional flow the following assumptions lead to the boundary layer equations:

- $x$ -axis points along the body surface
- boundary layer thickness is small compared to geometry of the body ( $\delta_{0.99} \ll L$ )
- high temperature effects are neglected

It is noted, that the body surface may be curved, but that the local curvature radius has to be large compared to the boundary layer thickness. Then centrifugal forces are negligible. After an order of magnitude

analysis, the Navier-Stokes equations simplify into the boundary layer equations for compressible flow:

$$\text{Continuity: } \frac{\partial \rho u}{\partial x} + \frac{\partial \rho v}{\partial y} = 0 \quad (3.23)$$

$$x\text{-momentum: } \rho u \frac{\partial u}{\partial x} + \rho v \frac{\partial u}{\partial y} = -\frac{\partial p}{\partial x} + \frac{\partial}{\partial y} \left( \mu \frac{\partial u}{\partial y} \right) \quad (3.24)$$

$$y\text{-momentum: } \frac{\partial p}{\partial y} = 0 \quad (3.25)$$

$$\text{Energy: } \rho u \frac{\partial h}{\partial x} + \rho v \frac{\partial h}{\partial y} = u \frac{\partial p}{\partial x} + \mu \left( \frac{\partial u}{\partial y} \right)^2 + \frac{\partial}{\partial y} \left( k \frac{\partial T}{\partial y} \right) \quad (3.26)$$

Pressure perpendicular to the wall is constant (equation (3.25)) and therefore only dependent on the axial distance,  $p = f(x)$ . This pressure  $p_e(x)$  is usually imposed as a known boundary condition at the edge of the boundary layer. Equations (3.23), (3.24) and (3.26), together with the equation of state (3.1) and the expression for a calorically perfect gas,  $h = c_p T$ , yield five expressions, for the five unknowns:  $u$ ,  $v$ ,  $\rho$ ,  $T$  and  $h$ . To solve the system of equations an initial condition, as well as conditions at the wall and boundary layer edge are needed. For a detailed derivation and discussion of the boundary layer equations from the Navier-Stokes equations please refer to the literature [89, 113, 3, 88].

If drag forces at the wall become too large and slow down the flow to the point where  $(\partial u / \partial y)_{\text{wall}} \leq 0$ , the viscous boundary layer is no longer attached to the wall but separates. When separation occurs the underlying assumptions of the boundary layer theory, such as vanishing velocity perpendicular to the wall, no longer apply. Therefore, the boundary layer equations, and parameters calculated therewith, are no longer valid [89, p. 113]. For instance, heating rates and total drag forces usually increase once the flow separates. Since turbulent boundary layers have higher momentum exchange perpendicular to the wall, their velocity profiles are fuller, thus cause higher drag forces. Nevertheless, due to the higher momentum exchange they separate later than laminar boundary layers. If a positive pressure gradient is present ( $\partial p / \partial x > 0$ ), such as in compressing intake flows, separation is favored. Furthermore, Reynolds number, Mach number, and wall temperature influence separation within a flow field. This is aggravated by the difficulty to predict separation analytically and numerically. Therefore, boundary layer separation deserves special attention during the analysis of compressing viscous flows.

### 3.3.2 Approximate Solution: Approach with Integral Method

The boundary layer equations are non-linear, partial differential equations. For certain boundary conditions, they can be simplified into linear equations, and exact closed form analytical solutions can be obtained. However, for arbitrary boundary conditions, exact solutions can only be obtained via numerical methods, such as for example a finite difference approach. On the other hand, if an approximate solution of the boundary layer equations is sufficient enough for the application, an integral method can be used [111, 60, 113]. Integral methods fulfill the boundary layer equations over the whole boundary layer region, rather than at each individual point within the boundary layer. They therefore allow calculating variables that are characteristic for the whole boundary layer region, such as the displacement, or momentum thickness.

In the following, the integral equations for compressible boundary layers are described in a general manner as presented in [111, pp. 78]. The continuity, (3.23), and  $x$ -momentum equation, (3.24), are multiplied with  $u^{\nu+1} / (\nu + 1)$  and  $u^\nu$  respectively, while  $\nu$  is an arbitrary natural number. Next, the two

equations are added to each other:

$$\frac{\rho u}{\nu+1} \frac{\partial u^{\nu+1}}{\partial x} + \frac{\rho v}{\nu+1} \frac{\partial u^{\nu+1}}{\partial y} + \frac{u^{\nu+1}}{\nu+1} \left( \frac{\partial \rho u}{\partial x} + \frac{\partial \rho v}{\partial y} \right) = -u^{\nu} \left( \frac{dp}{dx} - \frac{\partial \tau}{\partial y} \right), \quad (3.27)$$

while  $\tau$  is the shear-stress in  $x$ -direction. After further simplification the following form is obtained:

$$\frac{1}{\nu+1} \left( \frac{\partial \rho u^{\nu+2}}{\partial x} + \frac{\partial \rho v u^{\nu+1}}{\partial y} \right) = -u^{\nu} \left( \frac{dp}{dx} - \frac{\partial \tau}{\partial y} \right). \quad (3.28)$$

Equation (3.28) is integrated from the wall ( $y = 0$ ) to the boundary layer edge ( $y = \delta$ ), while the boundary layer edge depends on the  $x$ -coordinate, therefore  $\delta = \delta(x)$ .

$$\frac{1}{\nu+1} \left( \int_0^{\delta(x)} \frac{\partial}{\partial x} \rho u^{\nu+2} dy + \rho v u^{\nu+1} \Big|_0^{\delta(x)} \right) = -\frac{dp}{dx} \int_0^{\delta(x)} u^{\nu} dy + \int_0^{\delta(x)} u^{\nu} \frac{\partial \tau}{\partial y} dy \quad (3.29)$$

The first part on the left side of equation (3.29) can be modified as:

$$\int_0^{\delta(x)} \frac{\partial}{\partial x} \rho u^{\nu+2} dy = \frac{\partial}{\partial x} \int_0^{\delta(x)} \rho u^{\nu+2} dy - \rho_e u_e^{\nu+2} \frac{d\delta(x)}{dx}, \quad (3.30)$$

while the second part on the left side of equation (3.29), together with the continuity equation, (3.23), leads to:

$$\begin{aligned} \rho v u^{\nu+1} \Big|_0^{\delta(x)} &= \rho_e v_e u_e^{\nu+1} - 0 \\ &= u_e^{\nu+1} \left( - \int_0^{\delta(x)} \frac{\partial(\rho u)}{\partial x} dy \right) \\ &= u_e^{\nu+1} \left( - \frac{\partial}{\partial x} \int_0^{\delta(x)} \rho u dy + \rho_e u_e \frac{d\delta(x)}{dx} \right). \end{aligned} \quad (3.31)$$

The subscript  $e$  denotes the condition at the edge of the boundary layer. After reassembling equation (3.29) the following term is obtained, where the spatial derivatives of the boundary layer edge distance cancel out:

$$\begin{aligned} \frac{\partial}{\partial x} \int_0^{\delta(x)} \rho u^{\nu+2} dy - \rho_e u_e^{\nu+2} \frac{d\delta(x)}{dx} - u_e^{\nu+1} \frac{\partial}{\partial x} \int_0^{\delta(x)} \rho u dy + \rho_e u_e^{\nu+2} \frac{d\delta(x)}{dx} = \\ \left( - \frac{dp}{dx} \int_0^{\delta(x)} u^{\nu} dy + \int_0^{\delta(x)} u^{\nu} \frac{\partial \tau}{\partial y} dy \right) (\nu+1). \end{aligned} \quad (3.32)$$

Finally, the following equation is derived:

$$\frac{df_{\nu}}{dx} + f_{\nu} \left( 2 + \nu + \frac{g_{\nu}}{f_{\nu}} - M_e^2 \right) \frac{du_e/dx}{u_e} + e_{\nu} = 0, \quad (3.33)$$

with the auxiliary variables,  $e_{\nu}$ ,  $f_{\nu}$  and  $g_{\nu}$ :

$$e_{\nu} = (\nu+1) \int_0^{\delta(x)} \left( \frac{u}{u_e} \right)^{\nu} \frac{\partial}{\partial y} \left( \frac{\tau}{\rho_e u_e^2} \right) dy, \quad (3.34)$$

$$f_\nu = \int_0^{\delta(x)} \frac{\rho u}{\rho_e u_e} \left( 1 - \left( \frac{u}{u_e} \right)^{\nu+1} \right) dy, \text{ and} \quad (3.35)$$

$$g_\nu = (\nu + 1) \int_0^{\delta(x)} \frac{\rho u}{\rho_e u_e} \left( \left( \frac{u}{u_e} \right)^{\nu-1} \frac{\rho_e}{\rho} - 1 \right) dy. \quad (3.36)$$

Various values of  $\nu$  lead to various versions of the integral equation for the boundary layer [111]. For  $\nu = 0$  the momentum integral equation is derived:

$$\frac{d\delta_2}{dx} + \frac{\delta_2}{u_e} \left( 2 + \frac{\delta_1}{\delta_2} - M_e^2 \right) \frac{du_e}{dx} - \frac{\tau_w}{\rho_e u_e^2} = 0 \quad (3.37)$$

The auxiliary variables match the negative skin friction coefficient  $c_{f,Walz}$  as formulated by Walz, the boundary layer momentum thickness  $\delta_2$  and the boundary layer displacement thickness  $\delta_1$ , respectively.

$$e_0 = \int_0^{\delta(x)} \frac{\partial}{\partial y} \left( \frac{\tau}{\rho_e u_e^2} \right) dy = -\frac{\tau_w}{\rho_e u_e^2} = -c_{f,Walz} = -\frac{1}{2} c_f \quad (3.38)$$

$$f_0 = \int_0^{\delta(x)} \frac{\rho u}{\rho_e u_e} \left( 1 - \left( \frac{u}{u_e} \right) \right) dy = \delta_2 \quad (3.39)$$

$$g_0 = \int_0^{\delta(x)} \frac{\rho u}{\rho_e u_e} \left( \frac{\rho_e u_e}{\rho u} - 1 \right) dy = \delta_1 \quad (3.40)$$

As it can be seen from equation (3.38) Walz defined the skin friction coefficient differently from the norm in modern literature.

For the boundary layer analysis, one edge-property, as well as the free-stream conditions should be given. With the assumptions of inviscid and adiabatic core-flow the remaining edge-properties can be calculated via:

$$T_e^\gamma p_e^{1-\gamma} = T_\infty^\gamma p_\infty^{1-\gamma}, \quad (3.41)$$

$$c_p T_e + \frac{u_e^2}{2} = c_p T_\infty + \frac{u_\infty^2}{2}, \text{ and} \quad (3.42)$$

$$M_e = \frac{u_e}{\sqrt{\gamma R T_e}}. \quad (3.43)$$

Therefore, in equation (3.37) only the variables  $\delta_1$ ,  $\delta_2$  and  $c_f$  are unknown a priori. However, if information on the velocity and temperature profiles would be available, expressions for the displacement thickness and skin friction at the wall can be calculated and equation (3.37) can be transformed into an ordinary differential equation.

Walz directly related the temperature profile to the velocity profile with the following polynomial ex-

pression:

$$\frac{T}{T_e} = \left( \frac{T_w}{T_e} \right) + \left( \frac{T_{\text{rec}} - T_w}{T_e} \right) \frac{u}{u_e} + \left( -\mathcal{R} \frac{\gamma - 1}{2} M_e^2 \right) \left( \frac{u}{u_e} \right)^2, \quad (3.44)$$

where  $\mathcal{R}$  is the recovery factor, and the recovery temperature is defined by:

$$T_{\text{rec}} = T_e \left( 1 + \mathcal{R} \frac{\gamma - 1}{2} M_e^2 \right). \quad (3.45)$$

A common way in the literature is, to assume a 1-parameter velocity profile, where the normalized velocity,  $u/u_e$ , is dependent on the  $y$ -variable, the Reynolds number  $Re_{\delta_2}$ , and one further parameter, the shape factor  $H$ :

$$\frac{u}{u_e} = f \left( \frac{y}{\delta_2}, Re_{\delta_2}, H \right). \quad (3.46)$$

With the profiles for the temperature and velocity, expressions for the displacement thickness and the skin friction can be calculated, which then depend on the two remaining unknowns – namely the momentum thickness  $\delta_2$ , and the additional parameter  $H$ . To solve for the two unknowns, equation (3.37) is taken and one other equation needs to be introduced.

The additional parameter,  $H$ , and the corresponding additional equation are a feature of each individual integration method and therefore discussed in the following section.

### 3.3.3 Walz' Integral Method: Rechenverfahren II

The integral method described by Walz in [111, chap. 4] is a one-parameter method, applicable to compressible, laminar or turbulent flow. The integral method uses the momentum integral equation, (3.37), and as the additional equation the energy integral equation, which can be obtained by setting  $\nu = 1$  in equation (3.33):

$$\frac{d\delta_3}{dx} + \frac{\delta_3}{u_e} \left( 3 + 2 \frac{\delta_4}{\delta_3} - M_e^2 \right) \frac{du_e}{dx} - \frac{2}{\rho_e u_e^3} \int_0^{u_e} \tau du = 0. \quad (3.47)$$

The German term Walz used for his integral method is Rechenverfahren II and therefore the shortcut RV2 can be found throughout the present work. For the energy integral equation, the auxiliary variables,  $e_1, f_1, g_1$ , are:

$$e_1 = -2 \frac{1}{\rho_e u_e^3} \int_0^{u_e} \tau du, \quad (3.48)$$

$$f_1 = \int_0^{\delta(x)} \frac{\rho u}{\rho_e u_e} \left( 1 - \left( \frac{u}{u_e} \right)^2 \right) dy = \delta_3, \text{ and} \quad (3.49)$$

$$g_1 = 2 \int_0^{\delta(x)} \frac{\rho u}{\rho_e u_e} \left( \frac{\rho_e}{\rho} - 1 \right) dy = 2\delta_4, \text{ respectively,} \quad (3.50)$$

and are known with the assumed velocity and boundary layer profiles (3.44, 3.46). As the velocity profile, Walz used Hartree-profiles [46] for laminar, and empirical relations for turbulent flows, respectively.

The objective is to solve for the two unknowns  $\delta_2(x)$  and  $H(x)$  with the two integral equations (3.37)

and (3.47). Therefore, the variable  $\delta_2$  is transformed into the thickness parameter  $Z$  via:

$$\delta_2 Re_{\delta_2}^n = Z, \quad (3.51)$$

where:

$$Re_{\delta_2} = \frac{\rho_e u_e \delta_2}{\mu_w}, \quad (3.52)$$

and the variable  $n = 1$  for the laminar and  $n = 0.268$  for the turbulent case, respectively. Next, the integral momentum equation, (3.37), can be transformed into:

$$\frac{dZ}{dx} + Z \frac{du_e/dx}{u_e} F_1 - F_2 = 0, \quad (3.53)$$

while the expressions for  $F_1$  and  $F_2$  are listed in detail in the appendix. For axisymmetric flows, equation (3.53) is complemented by the influence of the radial coordinate,  $r$ :

$$\frac{dZ}{dx} + Z \left( \frac{du_e/dx}{u_e} F_1 + (1+n) \frac{dr/dx}{r} \right) - F_2 = 0. \quad (3.54)$$

Equation (3.47) transforms into:

$$\frac{dH^*}{dx} + H^* \frac{du_e/dx}{u_e} F_3 - \frac{F_4}{Z} = 0, \quad (3.55)$$

while  $H^*$  is directly related to the shape factor  $H$ . Again the detailed expressions for  $F_3$ ,  $F_4$  and  $H^*$  are given in the appendix.

The correlation between the variables ( $F_1$ ,  $F_2$ ,  $F_3$ ,  $F_4$ ,  $H^*$ ) and the shape factor ( $H$ ) is a special feature of the individual integral method by Walz [111], and the specific equations for laminar and turbulent flow are listed in the appendix (section A.2) and in [111, pp. 230]. Finally, equations (3.53) and (3.55) can be integrated numerically to obtain values for the shape factor  $H$  and the momentum thickness  $\delta_2$ . Other global variables, such as the displacement thickness  $\delta_1$  or the drag coefficient  $c_f$  can be subsequently calculated. Note that the boundary layer thickness  $\delta_{0.99}$  can not be directly calculated.



## 4 Intake Design Tool

### 4.1 Overview

To design a three-dimensional intake and to analytically predict its performance was one core-task of the present work. Thereto, as explained in [37] and shown in figure 4.1, the following steps were performed:

1. A compression flow field was generated, which was axisymmetric and which could be described analytically (section 3.2). A Busemann or a reversed nozzle flow field generated with the method of characteristics, was used.
2. The amount of leading edge and of rear side truncation had to be specified. The truncation angle  $\delta$ , and the internal contraction ratio  $CR_i = A_{cl}/A_{th} = A_{cl}/A_{cc}$ , were used as measures. To properly capture the performance parameters analytically, for the leading edge truncation the pressure at the intake exit needed to be adjusted, while for the rear side truncation a stream-thrust analysis had to be performed.
3. A cross sectional geometry had to be selected, which was either the capture area or the intake exit area. This geometry needed to be put on top of the axisymmetric flow field and streamlines had to be traced forward or backward. The streamlines formed the outer contour of the inviscid intake geometry. When skipping the streamline tracing procedure and only adding information about the intake diameter, an axisymmetric geometry could be extracted from the tool.
4. Finally, for each streamline the boundary layer displacement thickness needed to be calculated to take into account the additional contraction by the viscous boundary layer. The displacement thickness was then added to the streamline in radial direction, thus the three-dimensional geometry was widened.

To automate and simplify the design process of a three-dimensional SCRamjet intake, a FORTRAN (f95) computer program was written. The Intel FORTRAN Composer XE2011 was used for compiling on windows operating systems, while the GNU FORTRAN compiler was used on Unix based systems. The program could be controlled within the command window or terminal. Thus it was possible to execute the program within a python script, and feed in the desired input via the *stdin*, and write out the resulting output via the *stdout*. This feature enabled automated generation of various intake geometries, and drastically reduced work effort otherwise needed to manually set up the configurations. In the subsequent context the implemented formulation of the design tool is explained in more detail.

### 4.2 Compression Flow Field

The two axisymmetric compression flow fields, discussed in this section, were equal in the way, that their governing equations had to be integrated numerically. Considering the intake flow field, integration started at the rear end of the intake and marched upstream. As displayed in figure 4.1, two design parameters such as free stream Mach number and pressure ratio ( $M_\infty, \Pi_{st}$ ), free stream and exit Mach number ( $M_\infty, M_{cc}$ ), or the like needed to be defined to describe the classical compression flow field.

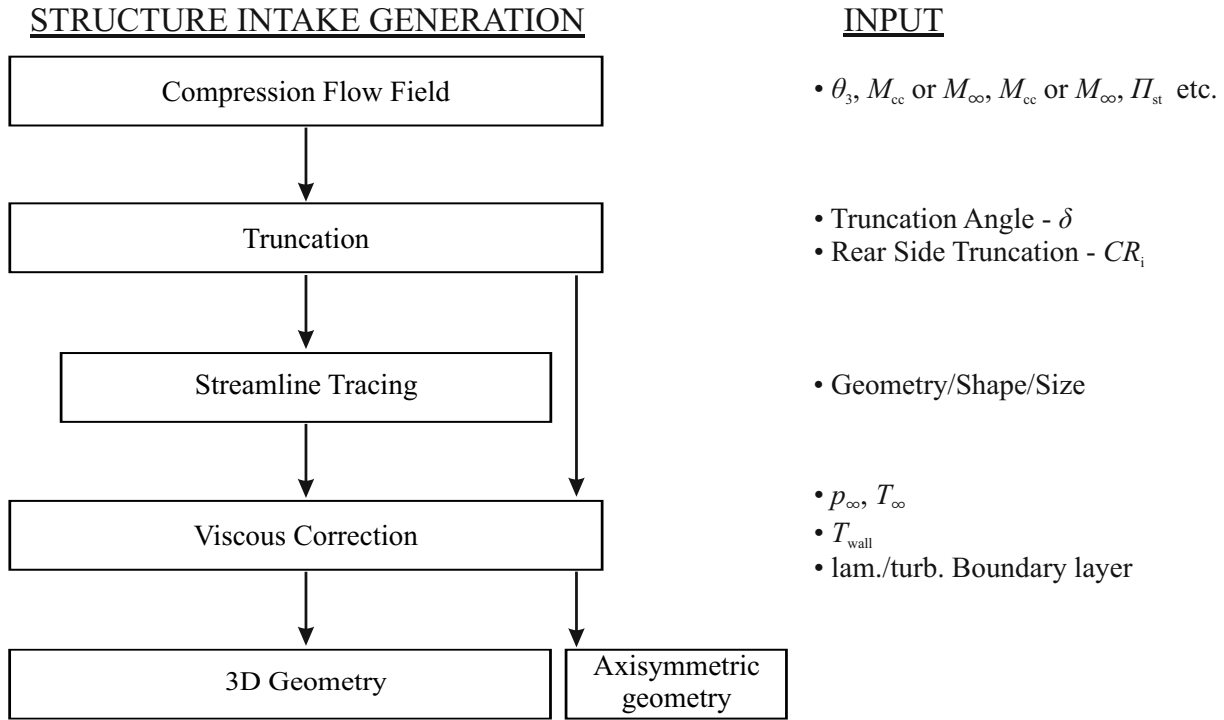


**Figure 4.1: Flow chart of design steps of the three-dimensional intake generation tool.**

#### 4.2.1 Busemann Flow Field

To calculate the Busemann flow field, the following steps had to be performed:

1. Define a desired exit Mach number  $M_3 = M_{cc}$  and characteristic angle  $\theta_3$  at the intake exit.
2. From the conditions at position 3 downstream of the conical shock, calculate the conditions upstream of the shock (position 2), with the oblique shock relations (section 3.1.4).
3. Starting at position 2, integrate equation (3.12) along  $\theta$  with  $d\theta$  increments. At each iso-line the variables  $p$ ,  $T$ , and  $M$  depend on the independent variable  $\theta$  only.
4. The integration is finished once the flow angle, defined by  $\cos^{-1}(U_r/U) - \theta$ , is zero. Note that the normalized velocity  $U$  is always positive, while the radial velocity  $U_r$  needs to be used with its corresponding sign.
5. To calculate an actual contour trace along a streamline starting either at the free stream side or the combustor side. As stated earlier, this contour is given as a fraction of an arbitrary length scale and can be scaled to a desired size.

Note that the characteristic angle  $\theta_3$  as an input variable seemed rather impractical and thus more practical input variables, such as the free stream Mach number  $M_\infty$  were favored. Since there was no solution to the Taylor McColl equations with the free stream and exit Mach numbers as the input variables, the steps above were automatically repeated until converged conditions were reached. Furthermore, by assuming no heat loss ( $h_t = \text{const.}$ ) throughout the intake flow, a temperature ratio  $\Theta_{st}$  was directly defined via:

$$\Theta_{st} = \frac{T_3}{T_\infty} = \frac{1 + 0.5(\gamma - 1)M_\infty^2}{1 + 0.5(\gamma - 1)M_3^2}. \quad (4.1)$$

Other sets of input parameters, such as the definition of the free stream Mach number and the static pressure ratio ( $M_\infty$  and  $\Pi_{st}$ ), or the definition of the free stream Mach number and the overall contraction

ratio ( $M_\infty$  and  $CR_o$ ), could be defined by replacing the exit Mach number  $M_3$  with the desired input variable and iterate until the desired values were reached. Generally, the classical Busemann flow field was defined once two of the previously mentioned input variables were fixed. Throughout this work free stream Mach number and intake pressure ratio were usually taken as input variables. To define the precise intake dimension and design point, one had to further define a length scale parameter and the free stream conditions  $p_\infty$  and  $T_\infty$ .

#### 4.2.2 Reversed Nozzle Flow Field

Figure 3.3 displays the initial and finishing data line of the characteristic mesh, which itself is divided into an expansion region and a transition region. The order in which new points were calculated was according to the numbering of the circled points in figure 3.3 (left). From two points ① and ② with known flow properties, a third point could be constructed as displayed in figure 3.3 (right). Equations (3.15) and (3.17) could be transformed into algebraic equations for the new coordinate of the data point ③:

$$x_3 = \frac{r_2 - r_1 - \tan(\bar{\theta}_{23} - \bar{\mu}_{23})x_2 + \tan(\bar{\theta}_{13} + \bar{\mu}_{13})x_1}{\tan(\bar{\theta}_{13} + \bar{\mu}_{13}) - \tan(\bar{\theta}_{23} - \bar{\mu}_{23})}, \text{ and} \quad (4.2a)$$

$$r_3 = r_1 + (x_3 - x_1) \tan(\bar{\theta}_{13} + \bar{\mu}_{13}). \quad (4.2b)$$

With equations (3.16) and (3.18) the new flow angle and velocity could be calculated:

$$U_3 = \frac{U_1 \bar{Q}_{13} + U_2 \bar{Q}_{23} + \bar{F}_{13} \frac{(r_3 - r_1)}{\bar{r}_{13}} + \bar{G}_{23} \frac{(r_3 - r_2)}{\bar{r}_{23}} + \theta_2 - \theta_1}{\bar{Q}_{13} + \bar{Q}_{23}}, \text{ and} \quad (4.3a)$$

$$\theta_3 = \theta_1 + \bar{Q}_{13} (U_3 - U_1) - \bar{F}_{13} \frac{(r_3 - r_1)}{\bar{r}_{13}}. \quad (4.3b)$$

The additional variables  $\bar{Q}_{i3}$ ,  $\bar{F}_{i3}$  and  $\bar{G}_{i3}$  were defined as:

$$\bar{Q}_{i3} = \frac{\cot(\bar{\mu}_{i3})}{\bar{U}_{i3}}, \quad \bar{F}_{i3} = \frac{\sin(\bar{\theta}_{i3}) \sin(\bar{\mu}_{i3})}{\sin(\bar{\theta}_{i3} + \bar{\mu}_{i3})}, \quad \bar{G}_{i3} = \frac{\sin(\bar{\theta}_{i3}) \sin(\bar{\mu}_{i3})}{\sin(\bar{\theta}_{i3} - \bar{\mu}_{i3})}. \quad (4.4)$$

To maintain a higher accuracy during the numerical integration, averaged variables  $\bar{\theta}_{i3}$ ,  $\bar{\mu}_{i3}$ ,  $\bar{U}_{i3}$  and  $\bar{r}_{i3}$  were calculated via:

$$(\bar{\cdot})_{i3} = \frac{1}{2} ((\cdot)_i + (\cdot)_3), \quad (4.5)$$

and were updated until data point ③ converged.

The procedure to calculate the entire reversed nozzle flow field is described by the steps below:

1. A desired throat Mach number  $M_3$  and free stream Mach number  $M_\infty$  had to be defined at positions 3 and 0, respectively.
2. To calculate the expansion region, it was iterated for a new point with the axis of symmetry and the starting line as the initial conditions using the characteristic equations; the expansion region is fully defined once the Mach number on the symmetry line reaches the desired free stream value  $M_\infty$ .

3. To calculate the transition region, the characteristic line connecting the last point on the symmetry line and the initial point were taken as the initial condition, and new sets of data points were calculated until the flow angle at the intake exit became zero.
4. To calculate an actual contour, one had to trace along a streamline starting at position 3 and march towards position 0; as stated earlier, this contour was given as a fraction of an arbitrary length scale and could be scaled to a desired size.

### 4.3 Truncation Effects

Truncation effects influence the classical compression flow field, because they modify the classical contour into one that is no longer geometrically similar. In the present section the approach to quantify these influences is explained for the leading edge and rear side truncation. Generally the methods are applicable to Busemann flow as well as reversed nozzle flow.

#### 4.3.1 Leading Edge Truncation Effects

Leading edge truncation effects were studied up to truncation angles of 7 deg in steps of 1 deg. The oblique shock at the leading edge was assumed to be planar, and with the truncation angle taken as the deflection angle the change in flow properties across the shock was calculated. Leading edge truncation created a flow inconsistency, because the truncated intake was no longer geometrically similar to its classical counterpart. The analytically calculated mass flow at the rear (position 3) was unaffected of the truncation. The analytically calculated mass flow at the entrance, however, changed due to the truncation and was no longer equal to the exiting mass flow, which is non-physical. In numerical simulations the mass flow through the intake contour was constant, and the flow inconsistency transformed into an intake exit pressure different from the one predicted analytically. This different intake exit pressure will be referred to as adjusted intake exit pressure. As the deflection angles and the induced shock losses at the leading edge were low, the temperature increase of an isentropic process was approximately equal to the temperature increase caused by an oblique shock. Thus, temperature was less affected, which was confirmed in numerical simulations where the temperature from CFD results matched the analytical value.

Therefore, the following approach was used to calculate the adjusted intake exit pressure. The mass flow through the intake was constant and could be written as:

$$\rho_{\infty} V_{\infty} A_{\infty} = \rho_3 V_3 A_3. \quad (4.6)$$

Using the equation of state and the Mach number relation equation (4.6) could be transformed into:

$$\frac{p_{\infty} A_{\infty} M_{\infty}}{\sqrt{T_{\infty}}} = \frac{p_3 A_3 M_3}{\sqrt{T_3}}. \quad (4.7)$$

Since free stream properties and temperature as well as Mach number at the intake exit were known, equation (4.7) could be rearranged to yield an expression for an adjusted pressure:

$$p_{3,\text{adj}} = p_{\infty} \frac{A_{\infty}}{A_3} \frac{M_{\infty}}{M_3} \sqrt{\frac{T_3}{T_{\infty}}}. \quad (4.8)$$

Note that for leading edge truncation an empirical procedure was also developed to modify the intake geometry and to account for the change in flow properties. For this refer to [37, sec. II.B.1] in the context of *half-stretching*.

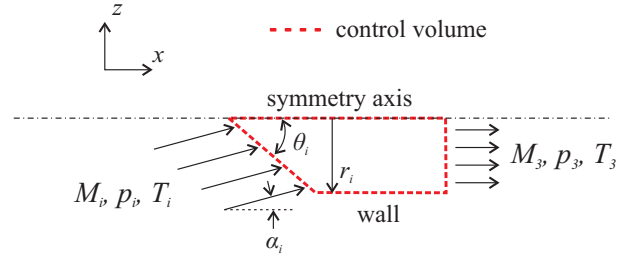


**Figure 4.2:** Control volume of figure 2.2 reprinted for analysis of truncated portion of Busemann intake; image from [38].

### 4.3.2 Rear Side Truncation Effects

The rear side truncation was measured with the internal contraction ratio  $CR_i$ . For the Mach 8 reference condition intakes were truncated at the rear until a maximum length reduction of  $6 \times h_{cc}$  was reached. This corresponded to a minimum internal contraction ratio of 1.6 and 1.0 for the Busemann and reversed nozzle case, respectively. Rear side truncation was varied between the default internal contraction ratio and the minimum value in steps of 0.2.

When truncating the intake at the rear side, the isentropic compression is not brought to a complete end, and pressures usually come out lower than in the corresponding classical counterpart. In the present work a stream-thrust analysis was used to calculate stream-thrust-averaged values for rear side truncated intakes. The control volume of a rear side truncated intake (figure 2.2) is reprinted in figure 4.2 while the subscripts  $i$  and  $3$  describe the inflow and exit locations of the control volume. The mass flow through the control volume is constant and was calculated via:

$$\dot{m}_i = \int (\rho_i \vec{v}_i \cdot \vec{n}_i) dA_i = \int (\rho_3 \vec{v}_3 \cdot \vec{n}_3) dA_3 = \dot{m}_3, \quad (4.9)$$

while the density  $\rho$  and velocity  $v$  were calculated from the equation of state for an ideal gas and the definition of Mach number, respectively. Since total enthalpy is constant, the energy equation was valid:

$$h_{t,i} = c_p T_i \left( 1 + \frac{\gamma - 1}{2} M_i^2 \right) = c_p T_3 \left( 1 + \frac{\gamma - 1}{2} M_3^2 \right) = h_{t,3}. \quad (4.10)$$

The third equation used was the momentum equation, which in vector form is:

$$\vec{F}_i = \int ((\vec{v}_i \cdot \vec{n}_i) \rho_i \vec{v}_i + p_i \vec{n}_i) dA_i = \int ((\vec{v}_3 \cdot \vec{n}_3) \rho_3 \vec{v}_3 + p_3 \vec{n}_3) dA_3 = \vec{F}_3. \quad (4.11)$$

Since the flow is axisymmetric the velocity components perpendicular to the free stream canceled out and equation 4.11 became the scalar term:

$$F_{x,i} = \dot{m}_i V_i \cos(\alpha_i) + p_i A_i \sin(\theta_i) = \dot{m}_3 V_3 + p_3 A_3 = F_{x,3}. \quad (4.12)$$

Therefore, with equations (4.9), (4.10) and (4.12), as well as the equation of state and the expression for the Mach number it was possible to solve for the five unknowns:  $M_3$ ,  $V_3$ ,  $p_3$ ,  $\rho_3$ , and  $T_3$ , which represent one-dimensional, so-called stream-thrust-averaged variables. It is noted that solving the three equations for velocity led to a quadratic equation, which had two results – usually subsonic and supersonic velocities. In the present case the supersonic solution was used. For a more detailed discussion about stream-thrust analysis in general refer to the cited literature [27, 9, 87].

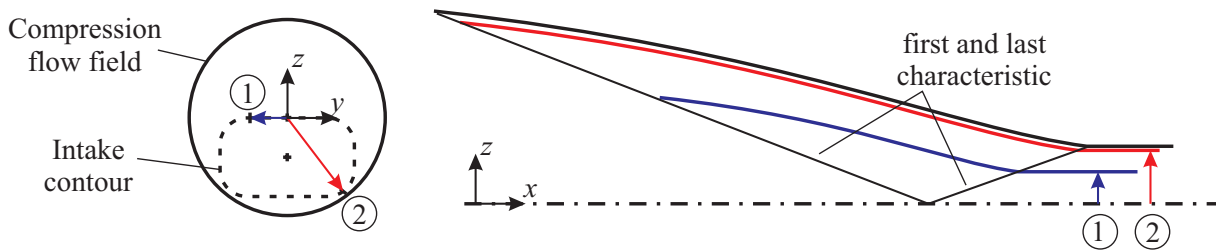


Figure 4.3: Schematic of streamline tracing within a compression flow field.

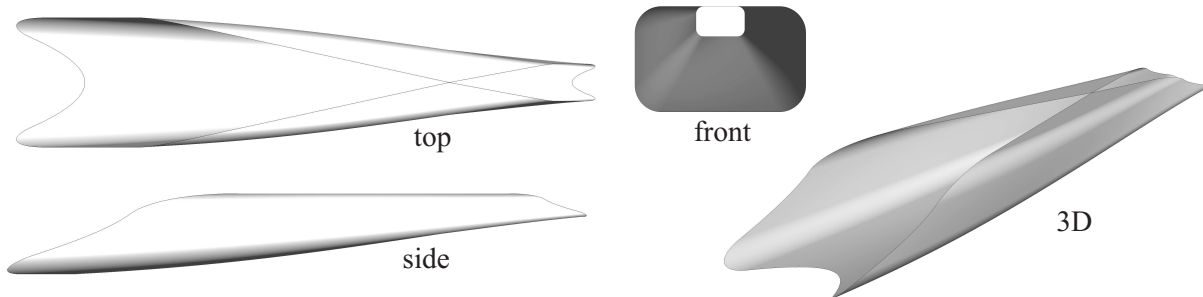


Figure 4.4: Different perspectives of streamline traced Busemann intake; geometry designed for  $M_\infty = 8$ ,  $\Pi_{st} = 45$ ,  $\delta = 3$  deg.

#### 4.4 Streamline Tracing Algorithm

The underlying compression flow field for the streamline tracing algorithm was either a Busemann flow field or a reversed axisymmetric nozzle, designed with the method of characteristics. The methodology is described based on figure 4.3 with a Busemann flow field as reference case but can readily be applied to reversed nozzle flows. An arbitrary intake cross sectional shape is projected into the compression flow field, perpendicular to the free stream direction. In figure 4.3 for example, a rectangular shape with rounded corners was used. Along the cross sectional shape a sufficient number of points had to be placed and along each point, a streamline was traced, as indicated by the sample points ① and ②.

The streamlines spanned a three-dimensional intake contour, and different perspectives of a sample geometry are displayed in figure 4.4. On the front view, the cross sectional geometry is visible, and the capture area as well as intake exit area are geometrically similar. Another characteristic was that automatically a swept back cowl configuration was obtained, simply by placing part of the cross sectional geometry near the origin ( $y, z = 0$ ) as indicated in figure 4.3. Furthermore, in contrast to the 3D-GRK intake, which still contained planar surfaces, the surfaces of streamline traced intakes were curved. The continuously curved surface enhanced gradual compression of the intake flow.

Finally, a comment is made on the influence of streamline tracing on the actual flow throughout the intake. Since on every streamline the flow properties are defined by their governing equations, a contour plot with the analytical solution can be established, as done in figure 4.5 with a Busemann flow for instance. This analytical solution is valid for inviscid flow, and for a classical flow field precisely matches a CFD Euler solution of the corresponding geometry (4.5 – right) [38]. It is emphasized that the inherently axisymmetric flow through a classical Busemann flow field is not disturbed by applying the streamline tracing algorithm, rather the values along each streamline give the exact solution. This was not only a strength of the usage of streamline tracing for creating SCRamjet intake geometries. It emphasized that the axisymmetric flow field, which served as the foundation, needed to be fully understood and properly described. Finally, this reinforced the investigation of the previously described leading edge and rear side truncation and viscous effects.

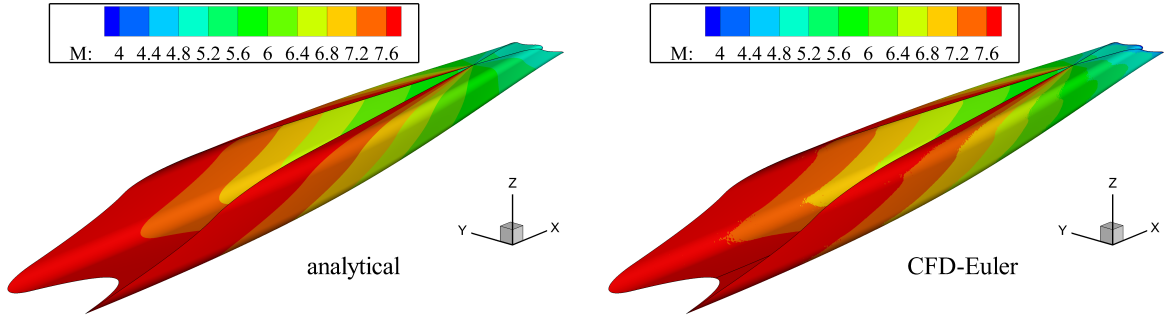


**Figure 4.5: Mach number contour plots of the streamline traced Busemann intake for the analytical (left) and Euler solution (right); geometry designed for  $M_\infty = 8$ ,  $\Pi_{st} = 45$ ,  $\delta = 0$ ; image from [38].**

#### 4.5 Viscous Effects

To address viscous effects the boundary layer displacement thickness was added to the inviscid contour to widen the intake geometry and to counteract the additional contraction of the viscous boundary layer. Walz' integral method was used (section 3.3.3) to calculate the displacement thickness, while the pressure distribution and intake contour were known from the compression flow field and served as boundary conditions. In this work a constant wall temperature was applied. The integral method could be applied to laminar or turbulent flow, while transition could be triggered in the integral method at a single point. To model transition in a broader region rather than at a single point the following approach was added to the integral method.

The data set of Berkowitz [10] contains approximately 150 transition locations collected from free flight data. More specifically, Berkowitz restricted the data to sphere-cone geometries in which transition onset was detected near zero angle of attack. In figure 4.6 (left) the probability density function of the transition locations is plotted against  $Re_{\delta_2}/M_e$ . The chart gives a general idea of where transition is going to occur, based on the Reynolds number formed with the momentum thickness divided by the boundary layer edge Mach number. For the transition modeling it was concluded that for  $Re_{\delta_2}/M_e < 56$ , the flow will always be laminar, while for  $Re_{\delta_2}/M_e > 461$  it will always be turbulent. Somewhere in between flow transitioned from laminar to turbulent and therefore the transition region was defined by  $56 < (Re_{\delta_2}/M_e)_{trans} < 461$ . By integrating the probability density function, the cumulative distribution function can be calculated and is plotted in figure 4.6 (right). The cumulative distribution function was regarded as a measure for how much the flow transitioned from laminar to turbulent. To model the data collected by Berkowitz, a transition parameter  $tp$  was developed and adjusted to the discrete data points of the cumulative distribution function via the parameter  $n$ , as described by:

$$tp(A) = \frac{1}{2} \left( \sin \left( \frac{f(A) - A_{\min}}{A_{\max} - A_{\min}} \pi - \frac{\pi}{2} \right) + 1 \right), \text{ and} \quad (4.13a)$$

$$f(A) = -\frac{|A - A_{\max}|^n}{(A_{\max} - A_{\min})^n} + A_{\max}, \text{ with} \quad (4.13b)$$

$$A = \frac{Re_{\delta_2}}{M_e}, \quad A_{\min} = 56, \quad A_{\max} = 461, \text{ and} \quad n = 3. \quad (4.13c)$$

With the transition parameter the laminar boundary layer could be gradually transitioned into a turbulent

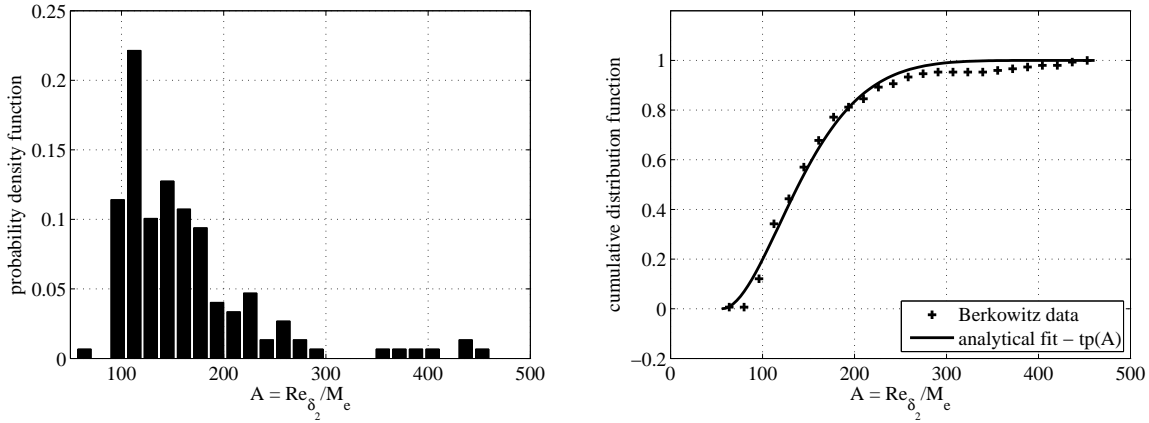


**Figure 4.6: Probability density function and cumulative distribution function of the Berkowitz data set [10], along with analytical function,  $tp(A)$ ; image from [38].**

one.

Since the integral method also calculated the skin friction coefficient, the viscous drag along the intake contour could also be calculated via:

$$F_{d,v} = \int \underbrace{c_{f,Walz} \rho_e V_e^2}_{\tau_w} dA. \quad (4.14)$$

As example in figure 4.7 the edge pressure distribution of a Busemann flow field, which was designed for Mach 8 flight and a static pressure ratio of 43 is displayed. Free stream pressure and temperature were 1170 Pa and 226 K, respectively. The intake length was approximately one meter, and the intake throat was located at the origin of the  $x$ -axis. The contour was not truncated and the continuous isentropic compression is clearly visible. Note that the pressure jump due to the final conical shock was not displayed because it was not considered in the viscous correction. Furthermore, a fully laminar, a fully turbulent, and the transitional boundary layer displacement thickness are plotted. For the laminar case the integral method predicted separation at  $\approx -0.1$  m, where the displacement thickness was set to zero. However, due to the very high Reynolds number at that station ( $Re_{\delta_2}/M_e$ ) it is unlikely that the flow would be laminar, and therefore the predicted laminar separation was irrelevant. Note that the laminar boundary layer is drastically stabilized by the cold wall boundary condition ( $T_w = 500$  K) and that for higher wall temperatures separation would occur further upstream. At the leading edge the fully turbulent boundary layer displacement thickness was lower than the fully laminar one, but exceeded the laminar boundary layer at  $x > -0.85$  m. A turbulent boundary layer is fuller and therefore its displacement thickness, relative to its boundary layer thickness, can be lower than in a laminar boundary layer at low values of Reynolds number [49, pp. 223]. The displacement thickness with gradual transition, based on the data set of Berkowitz [10], showed a monotonic growth from laminar to turbulent. The fully turbulent boundary layer thickness and the transitional case matched each other at  $x > -0.45$  m only by coincidence. The turbulent displacement thickness looked qualitatively similar to the results Smart [95, Fig. 11] obtained with his finite difference method.

The corrected Busemann and reversed nozzle geometries were further investigated with CFD and the numerical modeling is explained in detail in 6.4. Since a fully turbulent wall condition was used during CFD simulations, the boundary layer displacement thickness for a fully turbulent wall was used for widening the intake geometries.



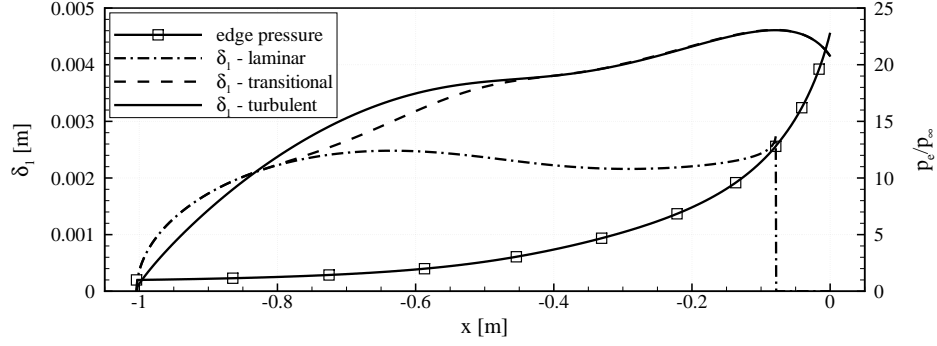


**Figure 4.7: Displacement thicknesses for different boundary layer states along with edge pressure distribution plotted against the free stream distance ( $T_w = 500$  K); image from [38].**

#### 4.6 Performance Parameters Calculation

From the analytical description of the compression flow field all major performance parameters ( $\Pi_{st}$ ,  $\Pi_{tot}$ ,  $\Theta_{st}$ , etc.) could be calculated for inviscid flow. Furthermore, the viscous correction provided additional information on boundary layer properties, which were used to calculate performance parameters for viscous flow. This additionally underlines the importance of the viscous correction. Only the intake flow path was considered in the present analysis, while the outer aircraft structure was neglected. Thus, the performance parameters calculated below resemble uninstalled properties.

Friction drag in  $x$ -direction was calculated via the wall shear stress known from the integral method:

$$F_{x,v} = \int \tau_w \cos(\alpha) dA, \quad (4.15)$$

with the flow angle  $\alpha$  known from the intake flow field. Pressure drag in  $x$ -direction was calculated analogously via:

$$F_{x,p} = \int p_{w,adj} \sin(\alpha) dA. \quad (4.16)$$

After comparing analytical to numerical wall pressures best agreement was obtained, when the wall pressure was adjusted to the exit pressure  $p_{3,adj}$  (see figure 4.8 for the representative 4 deg truncated Busemann intake case). The adjusted wall pressure was calculated via:

$$p_{w,adj} = (p_w - p_1) \frac{p_{3,adj}}{p_3} + p_1, \quad (4.17)$$

while position 1 and 3 were immediately downstream of the leading edge shock and at the intake exit, respectively. With a momentum balance in  $x$ -direction, which also considered friction drag:

$$F_x = F_{x,v} + F_{x,p} = (\dot{m}V_\infty + p_\infty A_\infty) - (\dot{m}V_{3,v} + p_{3,adj} A_3), \quad (4.18)$$

the intake exit velocity  $V_{3,v}$  could be calculated. This velocity was valid for viscous flow and was lower compared to its counterpart valid for inviscid flow. If no heat loss into the wall ( $h_t = const.$ ) was assumed, the temperature at the intake exit was calculated via:

$$T_{3,v} = \frac{1}{c_p} \left( h_t - \frac{V_{3,v}^2}{2} \right). \quad (4.19)$$

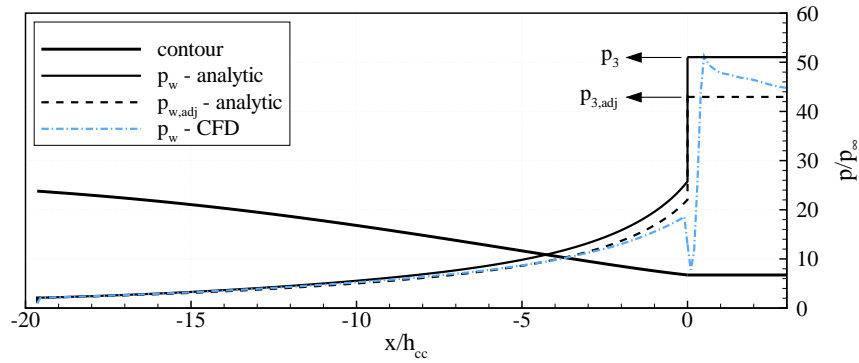


**Figure 4.8:** Wall pressures of leading edge truncated Busemann intake, designed for  $M_\infty = 8$ ,  $\Pi_{st} = 43$ ,  $\delta = 4$  deg.

With the exit temperature and velocity the exit Mach number was calculated by:

$$M_{3,v} = \frac{V_{3,v}}{\sqrt{\gamma R T_{3,v}}}. \quad (4.20)$$

Total pressure recovery, kinetic energy efficiency and other intake performance parameters were then updated with the modified properties and were valid for viscous flow.

For more accurate results heat losses into the intake wall could also be considered in the analysis. For this purpose total enthalpy was reduced by the wall heat losses. Thus, in equation (4.19) specific free stream enthalpy was reduced by  $\Delta\dot{Q}/\dot{m}_\infty$ :

$$T_{3,v} = \frac{1}{c_p} \left( h_{t,\infty} - \frac{\Delta\dot{Q}}{\dot{m}_\infty} - \frac{V_{3,v}^2}{2} \right). \quad (4.21)$$

Therefore, wall heat losses further decreased intake exit temperature, and increased exit Mach number and total pressure recovery, as those parameters were influenced by the reduction of total enthalpy.

The estimate of wall heat losses was made via Reynolds analogy, described in [30, 31]. The Stanton number was related to the skin friction coefficient via:

$$c_H = \frac{1}{2s} c_f, \quad (4.22)$$

while the Reynolds analogy factor  $s$  was set to 0.825 for a fully turbulent wall [31]. Together with equation (3.38) the specific wall heat loss was then calculated via:

$$\dot{q}_w = \frac{\tau_w c_p}{V_{e,s}} (T_{rec} - T_w) \quad (4.23)$$

Similar to skin friction,  $\dot{q}_w$  was integrated along the intake surface to calculate the magnitude of heat flux into the wall.

To conclude, the need for viscous correction was driven by two main objectives. First, the boundary layer displacement thickness needed to be calculated, with which the geometry could be modified to maintain the structure of the inviscid core flow. Second, friction drag needed to be considered in the momentum balance to calculate performance parameters applicable to viscous flow. Friction drag was only known due to the viscous correction. With Reynolds analogy wall heat losses could be considered during the performance analysis to yield more accurate results.

Note that with the above information on the axisymmetric flow field, an estimate on the  $x$ -drag force of three-dimensional streamline traced intakes could be made. Via equation (4.18) and information on

the capture and intake exit area as well as mass flow through the intake, the total drag force can be calculated. The ratio of viscous to pressure drag forces should be approximately equal to the underlying axisymmetric flow field.

## 5 Intake Starting Prediction

Two approaches to predict intake starting are presented: First, a fully empirical approach, similar to the ones presented in section 2.3; second, a semi-empirical approach, in which the assumptions of the Kantrowitz theory were modified.

### 5.1 Empirical Relation

Influenced by the work of Smart [99], and Sun and Zhang [105] another empirical relation to predict intake starting was developed. The relation should incorporate Mach number independency for large Mach numbers and allow for self adjustment by the user. Therefore, the requirements are summarized as follows:

1. For  $M \rightarrow 1$ , the contraction ratio should approach 1.
2. For  $M \rightarrow \infty$ , the contraction ratio should approach a constant value ( $> 1.666$ ).
3. The contraction ratio should be larger than the values from the Kantrowitz criterion, but lower than the maximum contraction ratios for isentropic flow.
4. The relation should be adjustable to allow for calibration to certain classes of intakes.

The expression:

$$CR_{\text{empirical}} = \frac{CR_{\text{Kantrowitz}}}{C_1 + CR_{\text{Kantrowitz}}(1 - C_1)}, \quad (5.1)$$

with the constant  $C_1$ , fulfilled the requirements. In figure 5.1 the empirical relation is plotted for different constants in the Kantrowitz plot. For  $C_1 = 1$  the empirical relation merged into the Kantrowitz line and for increasing  $C_1$ 's stretched into the critical region. Overall it resembled the shape and therefore trends of the Kantrowitz line. At low supersonic Mach numbers  $CR_{\text{empirical}}$  approached 1, but also intersected the isentropic relation. Therefore, low Mach number cases should be observed carefully when applying this relation. In general the method allowed for flexible adjustment of the starting limit to certain classes of intake geometries. Furthermore, it enabled interpolation between known data points while conserving the shape and therefore trend of the Kantrowitz line.

### 5.2 Semi-Empirical Relation

The problem of predicting intake starting was re-approached from the physical perspective, with Kantrowitz theory as the starting position. As seen in the introduction, the theory is a conservative limit for intake starting, especially for three-dimensional flow configurations. Nevertheless, the slope of the Kantrowitz line resembles the general trends correctly. Since the deficiency of Kantrowitz theory is most distinct for three-dimensional cases, the initial assumption of one-dimensional flow was reconsidered. Furthermore, the assumption of a normal shock in front of the intake is less realistic due to the three-dimensional flow field near the cowl closure location. Therefore, it has been assumed that a strong oblique or curved shock was present near the cowl closure and needed to be swallowed by the intake for starting. This reasoning was supported by figure 5.2, which shows schlieren images of unstarted (left) and started (right) intake flow, acquired during a previous study on intake starting [36]. For the started

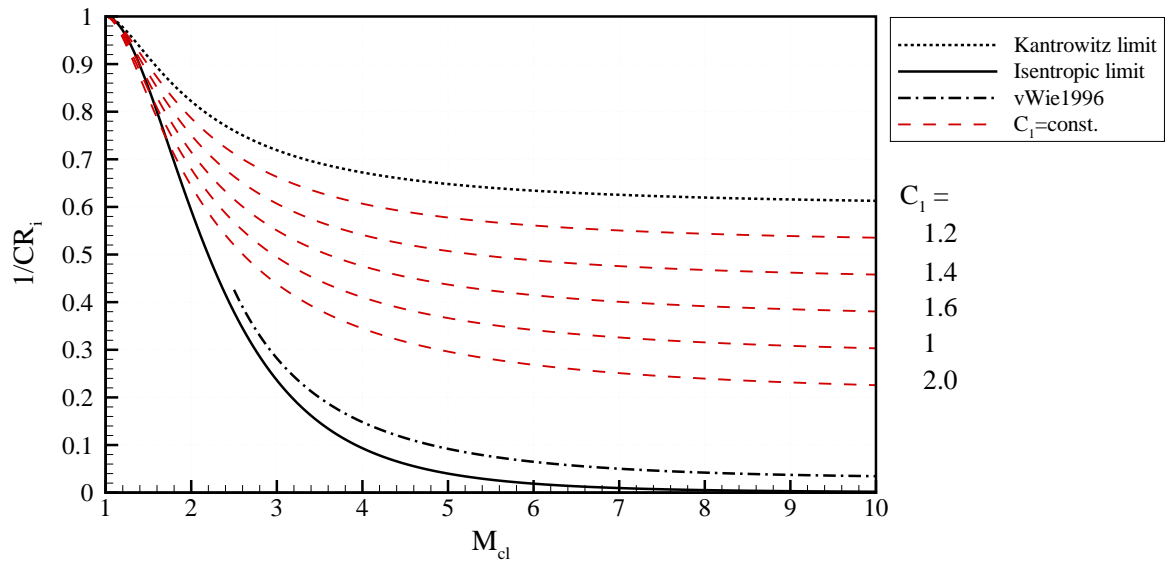


Figure 5.1: Kantrowitz plot with empirical starting relation, that allows adjustment via  $C_1$ -constant.

condition the ramp shock was clearly visible and no strong shock with subsonic downstream portion was present. However, the unstarted flow field showed a strong oblique shock which interacted with the ramp shock, therefore causing increased air flow losses, or spillage, across the intake cowl. Furthermore, an estimate of the extension of the oblique shock into the internal flow path was sketched, with a separation zone at the entrance of the fully enclosed intake portion.

With the above discussion the following reasoning was made. Figure 5.3 shows isentropic flow through schematic diffusers with equal free stream conditions. Due to a shock wave, the total pressure on the right hand side and in the middle was lower than on the left hand side. In the Kantrowitz-case this total pressure reduction is due to the shock losses across the normal shock (figure 5.3–middle). Note that the flows through the diffusers are regarded as isentropic, and the only source of reduced total pressure is due to the shock waves. The diffuser on the left can withstand the highest contraction before choking, thus  $A_m^* > A^*$ . Furthermore, the process of total pressure loss was adiabatic and no mass was lost, thus  $h_t = const.$  and  $\dot{m} = const.$  for all configurations.

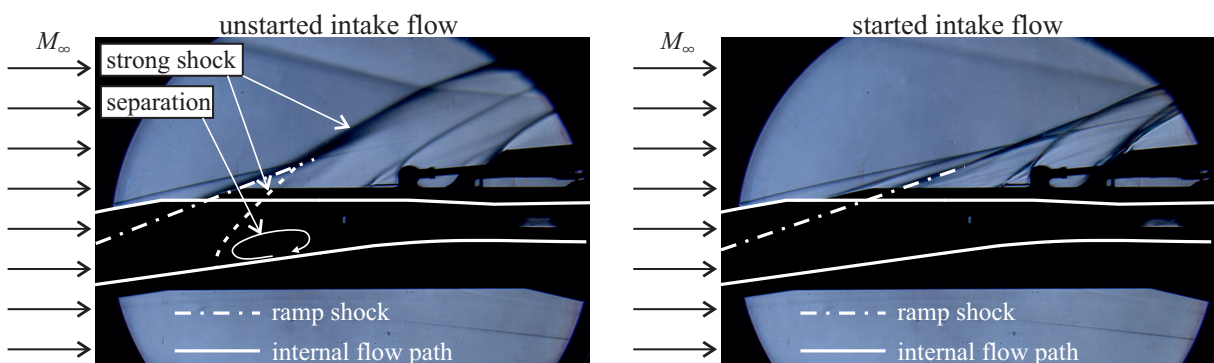


Figure 5.2: Schlieren images of started and unstarted 3D-GRK intake flow along with sketched shock positions and possible separation region in internal flow path; image adapted from [36].

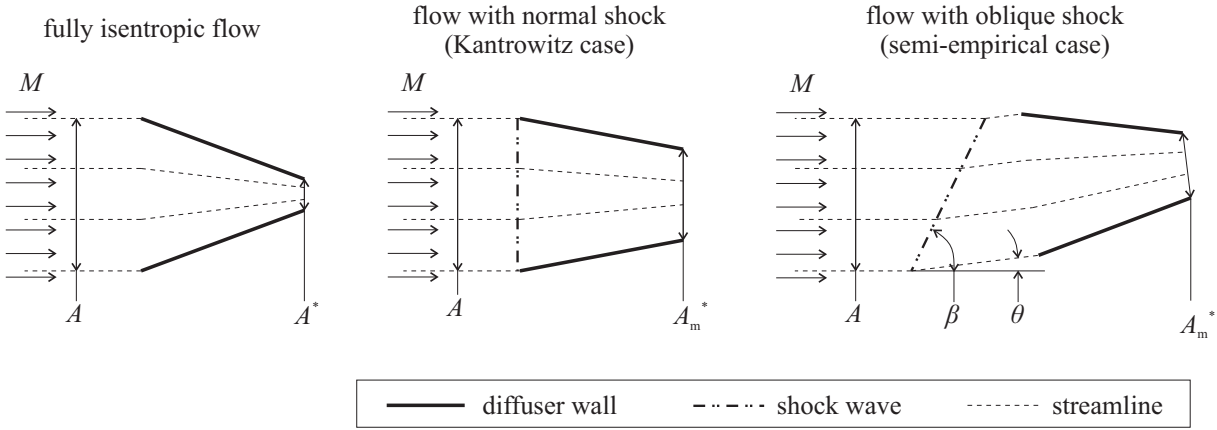


Figure 5.3: Sketch of various diffuser flows.

Therefore, for the diffuser throat, at which the Mach number is one, the following holds:

$$\rho^* A^* a^* = \rho_m^* A_m^* a_m^*. \quad (5.2)$$

With the assumption of an adiabatic process it could be shown that the temperatures, and thus local speeds of sound, at the diffuser throats were equal:

$$h_t = const. \Rightarrow T^* \left( 1 + \frac{\gamma - 1}{2} M^* \right) = T_m^* \left( 1 + \frac{\gamma - 1}{2} M_m^* \right). \quad (5.3)$$

Thus, the following equation related the throat area ratio to the density and pressure ratios, via the equation of state:

$$\frac{A^*}{A_m^*} = \frac{\rho_m^*}{\rho^*} = \frac{p_m^*}{p^*}. \quad (5.4)$$

Total pressure was calculated via:

$$p_t = p \left( 1 + \frac{\gamma - 1}{2} M^2 \right)^{\frac{\gamma}{\gamma - 1}}, \quad (5.5)$$

and because the Mach number at the diffuser throat was one, total and static pressure could be related for the diffuser configurations:

$$\frac{p_m^*}{p^*} = \frac{p_{t,m}^*}{p_t^*}. \quad (5.6)$$

Together with equation (5.4) this yields an expression that relates the throat areas to their difference in free stream total pressure:

$$\frac{A^*}{A_m^*} = \frac{p_{t,m}^*}{p_t^*}. \quad (5.7)$$

This expression could be further modified to relate the contraction ratios of the configurations and the total pressure loss by:

$$\frac{A}{A_m^*} = \frac{A}{A^*} \frac{p_{t,m}^*}{p_t^*}. \quad (5.8)$$

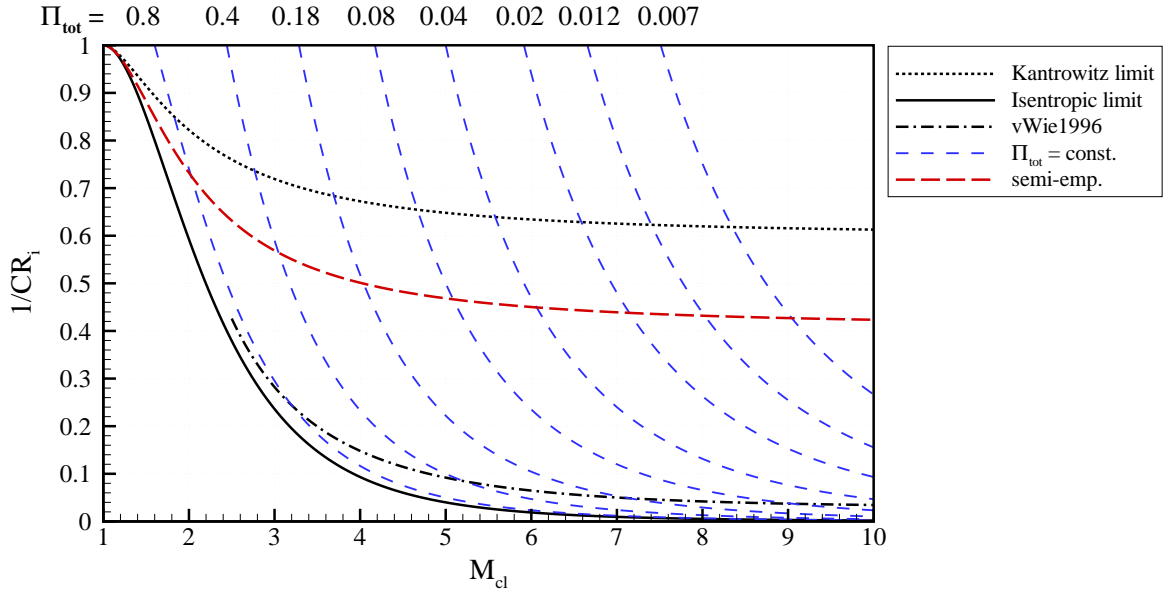


**Figure 5.4: Kantrowitz plot with lines of constant total pressure and semi-empirical limit.**

Thus, for the assumption of a constant total pressure loss, the isentropic limit could simply be modified via:

$$CR_m = CR_{isentr} \times \Pi_{tot}, \quad (5.9)$$

while the total pressure loss is given by  $(1 - \Pi_{tot})$ . Note that the above derivation can also be found in the related research area of shock swallowing within supersonic wind tunnels [48, pp.34]. With equation (5.9) lines of constant total pressure ratio could be added to the Kantrowitz diagram (figure 5.4). The intersections between the Kantrowitz line and the lines of constant total pressure corresponded to the total pressure loss due to a normal shock, which increased with Mach number. Lines within the critical region corresponded to flow that experienced less total pressure loss, while the isentropic line resembled the limit for  $\Pi_{tot} \rightarrow 1$ . The lines of constant total pressure loss for which  $CR_m < CR_{Kanttr}$  holds, denoted cases in which total pressure loss exceeded the losses due to a normal shock, for example by additional viscous losses in the boundary layer.

To develop the semi-empirical relation the shock which needed to be swallowed during intake starting was assumed to be oblique, as depicted schematically in figure 5.2. Thereto, the oblique shock angle  $\beta_{max}$  was used and could be expressed as a function of Mach number. Note that  $\beta_{max}$  was not the largest shock angle to occur, but was rather the shock angle related to the largest deflection possible  $\theta_{max}$ , before the shock detached. To calculate  $\beta_{max}$ , for one Mach number, equation (3.11) had to be solved for the largest  $\theta$  to occur numerically. With  $\beta_{max}$  being a function of Mach number and maximum shock angle  $\theta_{max}$ , a total pressure loss could be calculated, with which a modified starting limit was obtained:

$$CR_{semi-emp} = CR_{isentr} \times \Pi_{tot}(\beta_{max}(\theta_{max}, M)). \quad (5.10)$$

This relation is plotted in figure 5.4.

## 6 Experimental Apparatus and Numerical Methods

In this chapter the numerically and experimentally investigated intake models are described in detail. Next, the experimental apparatus is described, namely the blow down wind tunnel H2K and additional measurement equipment. Thereafter, the numerical tools along with the used meshes and computational domains are discussed. Finally, a one-dimensional post-analysis of an entire SCRamjet flow path, and further post-processing techniques are explained.

### 6.1 Intake Models

#### 6.1.1 3D-GRK Intake

During the second phase of the research training group, a three-dimensional intake was designed iteratively with a CFD parameter study by Hohn [50] and Riehm [84]. The configuration was part of a conceptual study for a flight experiment and the scale of the model was 1 : 1. During the design, various parameters such as the angle of the main ramp or the side walls were varied until desired conditions were reached: namely a static pressure ratio of 43 at a flight Mach number and altitude of 8 and 30 km, respectively. No optimization algorithm was used, but modifications were embedded manually. Furthermore, the intake was part of an entire SCRamjet configuration, which was designed and investigated during the second phase of the Research Training Group [85].

Different perspectives of the intake along with important dimensions are displayed in figure 6.1. The overall length of the intake was 0.75 m, while at 0.722 m a rake was positioned, which will be explained in more detail shortly. The throat was located at 0.65 m. The edge of the upper part of the intake was located at 0.55 m. On top of this edge, a moving cowl was positioned, which was manufactured in two ways: a v-shape and a straight (s) geometry (top view, figure 6.1). The distance from the leading edge to the tip of the cowl was determined as  $x_{lip}$  and could be varied between 0.54 m and 0.39 m. Thereby the internal contraction ratio also varied between 1.28 and 2.56 (see figure 6.2). The main ramp was inclined to an angle of 8 deg, while each side wall converged with 7 deg. The sweep angle at the leading edge started out with 45 deg, and increased gradually.

Along the ramp side and on the cowl side, there were 39 static pressure probes distributed on the symmetry plane ( $x - z$ -plane). Furthermore, at both positions  $Q1$  and  $Q2$ , there were six pressure probes installed to measure any asymmetry within the flow. In the movable cowl, 4 pressure probes were installed. Depending on how far downstream the cowl was located, the pressure ports further downstream were blocked off by the non-movable part of the intake starting at 0.55 m. A detailed overview over the exact position of the pressure probes is given in [50, pp. 238].

To further investigate the intake model in the H2K wind tunnel, a more extensive set-up was added to the intake model; a CAD image of the entire wind tunnel configuration is displayed in figure 6.3. In this figure, only the v-shaped cowl is displayed. Its axial location was controlled by an hydraulic cylinder. Following the intake, an adapter was mounted, which morphed the intake exit shape from a rectangle to a circle. Before entering a settling chamber, the flow passed a honeycomb mesh. Finally, the air stream exited through a conical throttle, which was used to impose a back pressure on the intake or allowed for the captured air stream to be measured. The throttle is explained in more detail in section 6.3.4.



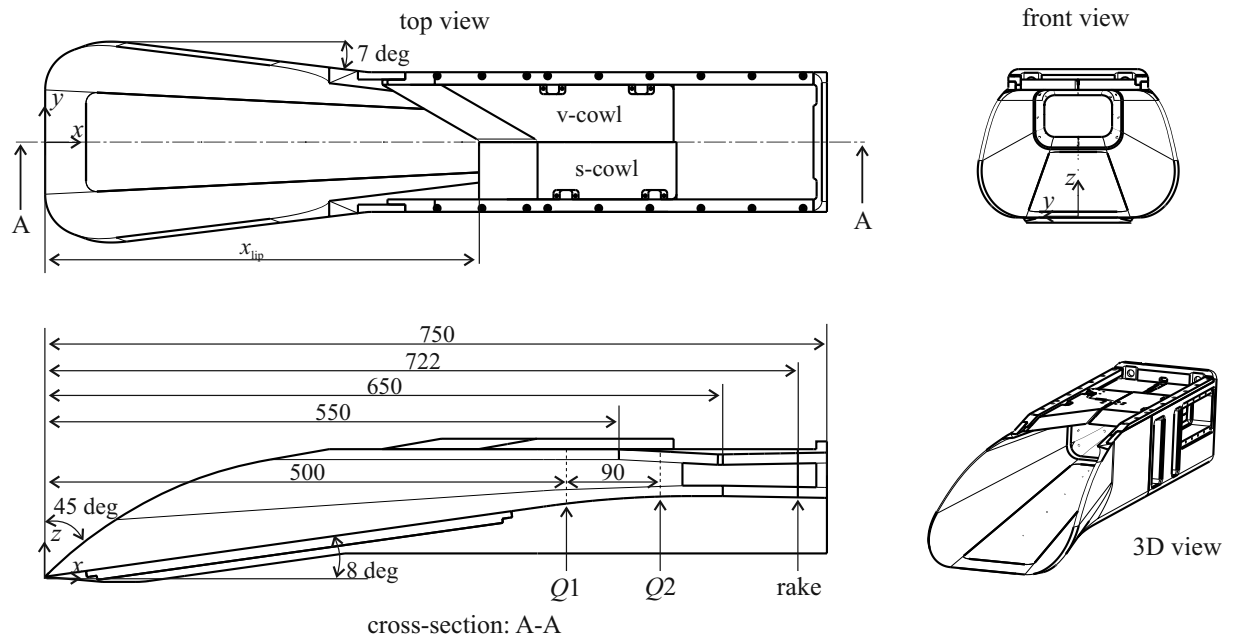


Figure 6.1: Different perspectives of the 3D-GRK intake; dimensions are in millimeter.

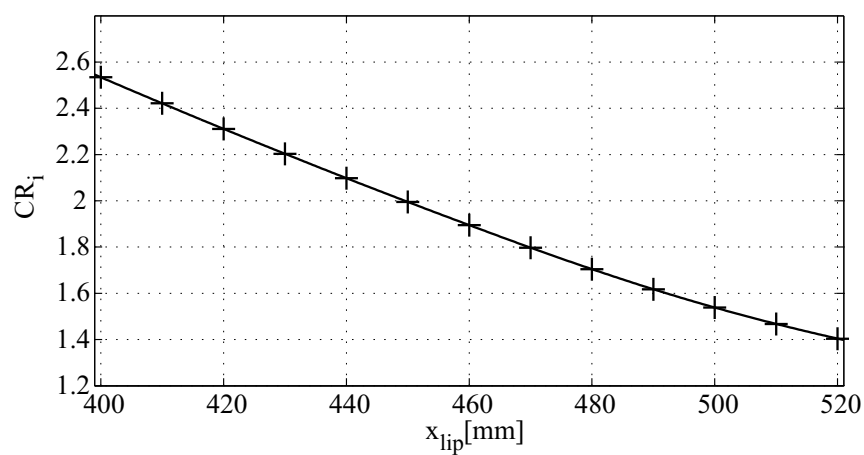
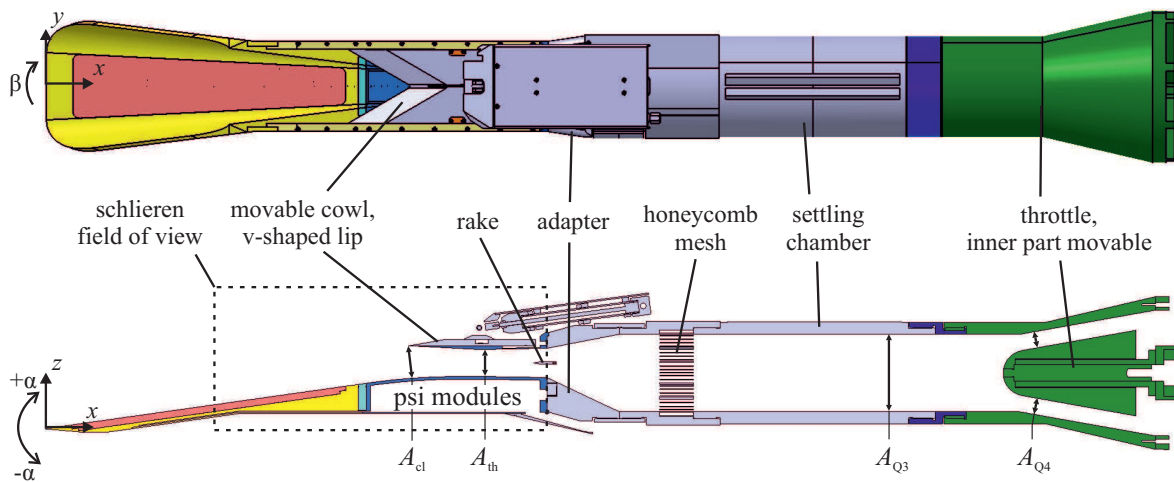


Figure 6.2: Internal contraction ratio, plotted against the distance from the intake leading edge to the cowl closure location; image from [36].



**Figure 6.3: Top and cross sectional view of intake configuration along with throttle and wind tunnel mount; image from [36].**

### 6.1.2 Streamline Traced Intake 1 – ST1

A three-dimensional intake was designed with the method of streamline tracing with Busemann flow as the underlying compression flow field. In the further context the intake is referred to as ST1. The design point was equal to the 3D-GRK design, namely a Mach 8 flight at an altitude of 30 km, and the design pressure ratio was 43. The cross sectional shape at the interface to the combustor was set equal to the 3D-GRK model and a rectangular shape ( $40 \times 60$  mm) with rounded corners was placed in the axisymmetric compression flow field according to figure 4.3. A viscous correction was applied to each individual inviscid wall streamline by widening the classical contour with the boundary layer displacement thickness. The boundary layer state and wall temperature were set to turbulent and 900 K, respectively.

In figure 6.4 the flow path of the ST1 intake is illustrated along with important dimensions given in millimeter. With its swept side walls and the v-shaped cowl geometry the intake looks similar to the 3D-GRK model. However, the main ramp of the streamline traced geometry had a swept back leading edge (see position  $0 < x < 68$  mm,  $z = -124$  mm). Furthermore, the wall contours were gradually curved and no planar portions were present. By truncating the intake at the leading edge, the length to the throat position of the ST1 intake was adjusted to the corresponding length of the 3D-GRK intake. A truncation angle of 6.8 deg resulted in a throat position of  $x = 0.652$  m. No rear side truncation was applied and the length to cowl closure was 0.428 m. The overall and internal contraction ratio were 9.55 and 3.06, respectively.

The rear portion, starting at 0.652 m was designed equal to the diverging portion of the 3D-GRK intake with a constant width and diverging height (opening angle = 2 deg). The overall length was 0.8 m and therefore 50 mm greater than the 3D-GRK length. Nevertheless intake performance parameters were extracted at the rake position of the 3D-GRK intake at 0.722 m, and were therefore comparable to parameters from the 3D-GRK intake. Finally, it is noted that due to the similarities to the 3D-GRK layout, a wind tunnel model could be designed analogously to the 3D-GRK model.

### 6.1.3 Streamline Traced Intake 2 – ST2

The ST2 intake was designed for  $\Pi_{st} = 43$  and  $M_\infty = 8$  and was truncated at the rear side to enhance intake starting. Following the semi-empirical modification of the Kantrowitz theory and experience from starting experiments, intake starting at  $M_\infty = 8$  should occur at internal contraction ratios as high as 2.1. To add some safety the desired  $CR_i$  was set to 2.0 during the design of the inviscid axisymmetric flow

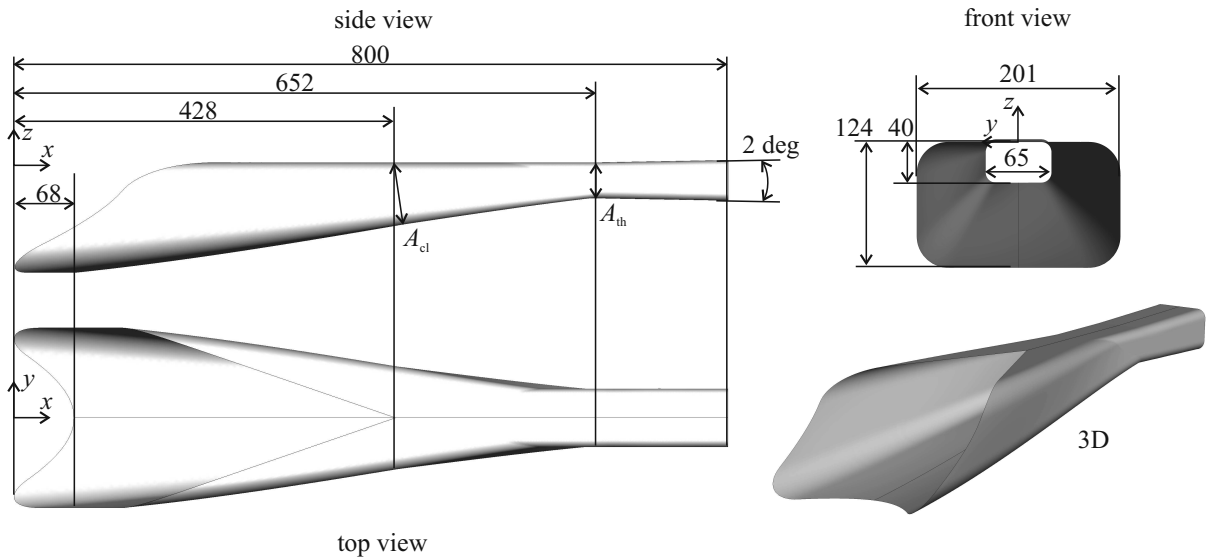


**Figure 6.4:** Different perspectives of the streamline traced intake ST1; dimensions are in millimeter.

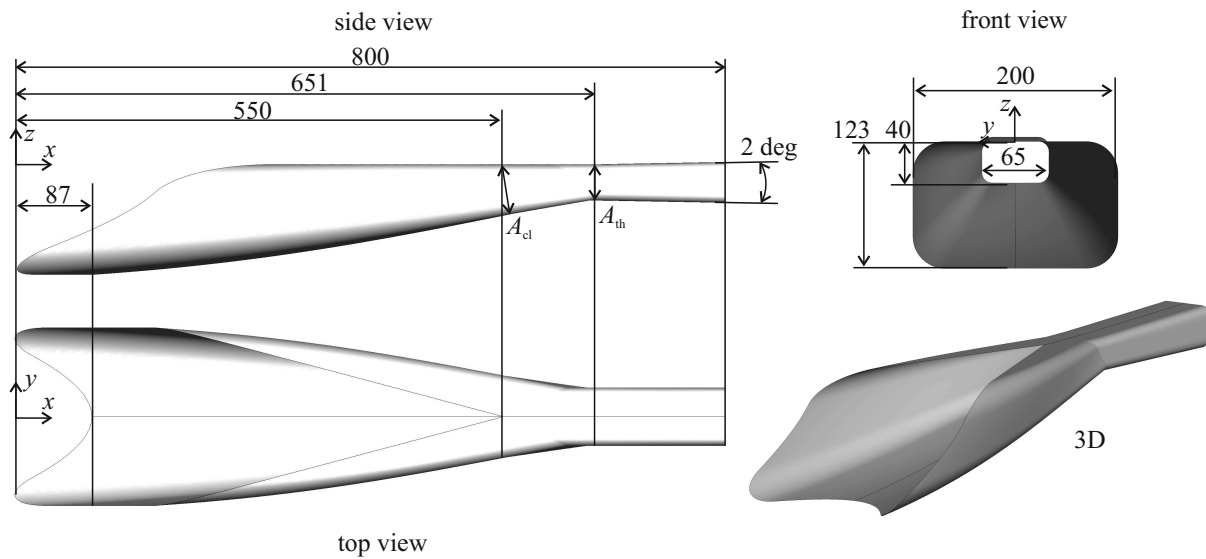


**Figure 6.5:** Different perspectives of the streamline traced intake ST2; dimensions are in millimeter.

field. To maintain a length of 0.65 m from the leading edge to the intake throat,  $\delta$  dropped to 4.7 deg. The viscous correction was performed for the same condition as in the ST1 design ( $p_\infty = 1170$  Pa,  $T_\infty = 226$  K,  $T_{\text{wall}} = 900$  K, turb. wall). The rear part ( $x > 0.65$  m) was designed correspondingly to the 3D-GRK flow path.

In figure 6.5 the flow path of the streamline traced ST2 configuration is displayed along with the major dimensions in millimeter. Compared to the ST1 design, the overall length was constant at 0.8 m while the overall contraction ratio slightly decreased to 9.44. The cowl closure location moved further downstream to  $x = 0.55$  m and  $CR_i$  decreased to 1.96. Note that after the viscous correction the internal contraction ratio slightly decreased. Nevertheless, the streamline traced shape and the ST1 heritage appearance is clear.

### 6.1.4 Streamline Traced Intake 3 – ST3

The ST3 intake contained the same cross sectional shape and streamlines as the ST1 configuration, however with different translation in streamwise direction. The underlying axisymmetric geometry was the same as for the ST1 geometry ( $M_\infty = 8$ ,  $\Pi_{\text{st}} = 43$ ,  $\delta = 6.8$  deg), and the Mach number contour of an axisymmetric CFD calculation for an intake exit height of 0.0475 m is shown in figure 6.6. The intake exit height corresponded to the streamline of the intake with the largest distance from the center line of the compression flow field, similar to point 2 in figure 4.3. Normally, during a streamline tracing procedure streamlines were translated in  $x$ -direction via  $h_{\text{cc}}/\tan(\theta_3)$ , which determined the position of the cowl closure. Note that the angle  $\theta_3$  is the angle of the conical shock and is known from the Busemann flow field. However, the contour plot (figure 6.6) and also subsequent ST1 results showed that in this case the ramp shock hit underneath the cowl. This induced unnecessary drag and created a separation region underneath the cowl. To avoid this and to create what is sometimes referred to as shock-on-lip condition, the intake cowl was re-located in  $x$ -direction at  $3 \times h_{\text{cc}}$ . For the ST3 geometry a 95% margin was included and the streamlines were moved to  $2.85 \times h_{\text{cc}}$ . Note that it was not possible to determine the streamwise translation analytically due to the curved shape of the ramp shock.

The resulting ST3 geometry is shown in figure 6.7. While the overall contraction ratio as well as the length to the throat and to the intake exit were identical to the ST1 configuration, the different  $x$ -translation induced the following changes: The internal contraction ratio decreased to 1.95 and consequently the length to the cowl closure location increased to 0.527 m. Interestingly, the internal contraction ratio was approximately equal to what could be predicted with the semi-empirical starting limit and to the internal contraction ratio that was used for the ST2 configuration. The ST3 intake was expected to have similar performance characteristics to the ST1 intake, with a small amount of spillage mass flow across the intake cowl.

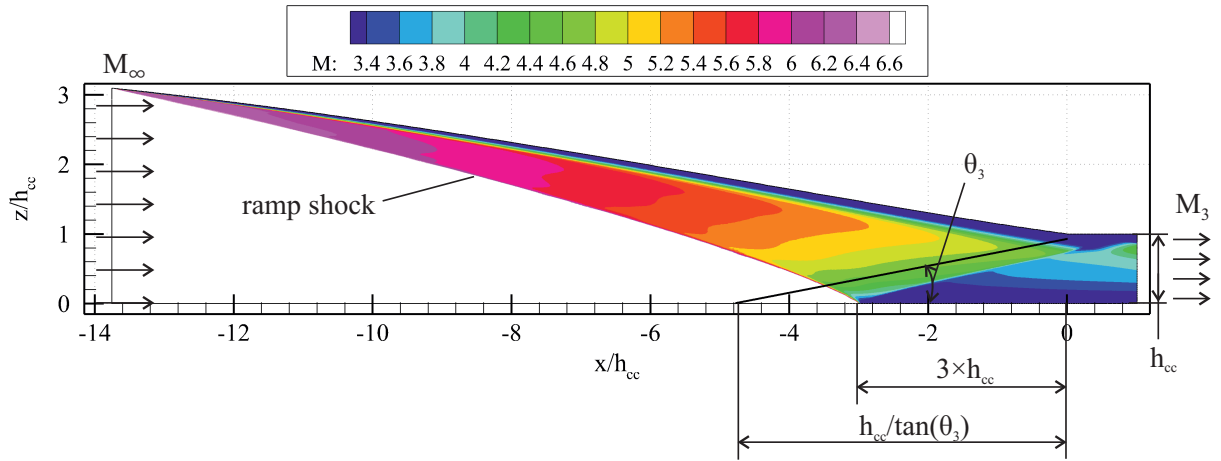


Figure 6.6: Mach number contour plot extracted from axisymmetric CFD simulation for ST3 configuration.

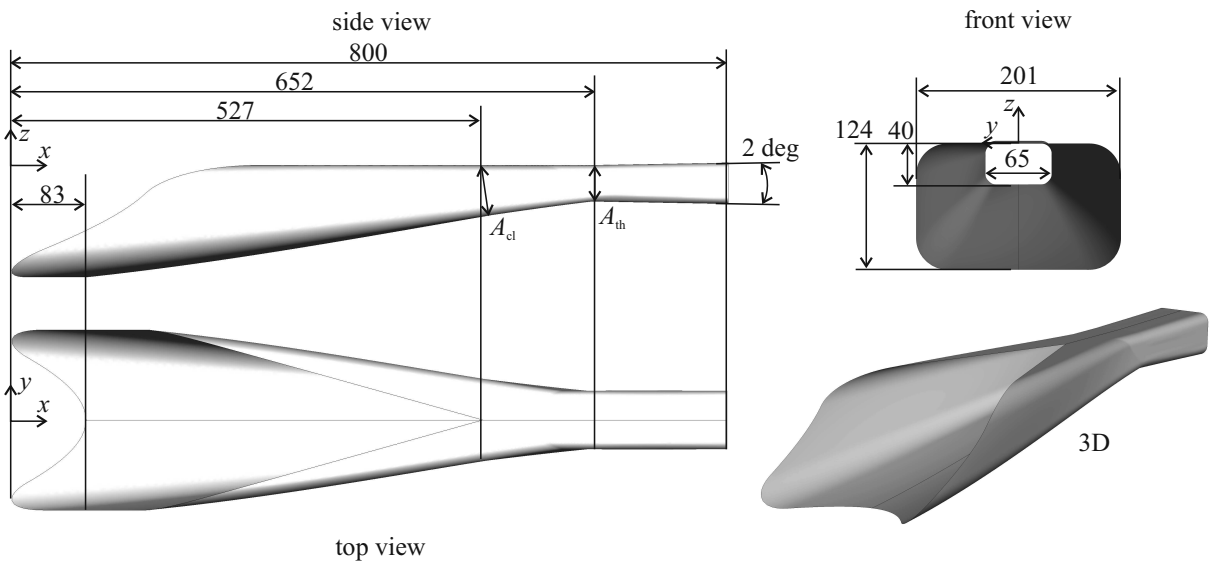


Figure 6.7: Different perspectives of the streamline traced intake ST3; dimensions are in millimeter.

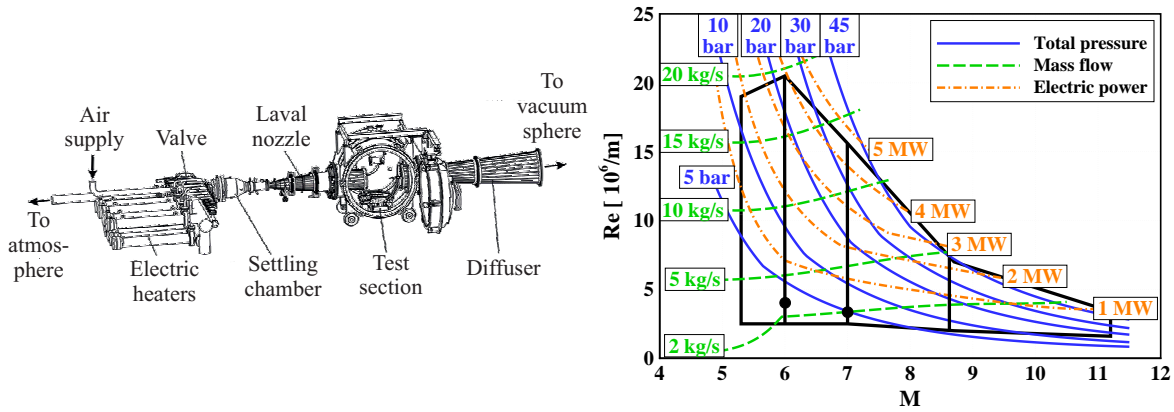


Figure 6.8: Schematic set-up of the H2K wind tunnel (left) along with characteristic diagram (right); image adapted from [70].

## 6.2 Blow Down Wind Tunnel H2K

The H2K blow down wind tunnel was used for the experiments with the 3D-GRK intake model. It could maintain testing times of up to 35 s. A schematic of the wind tunnel set-up along with a diagram of the achievable ranges of operation is displayed in figure 6.8. Wind tunnel conditions used during this study are marked by black circles (●). High pressurized, dried air was heated in the electric heaters and once the desired temperatures were reached, the valve was triggered to release the air stream through a settling chamber and Laval nozzle into the test section. The model section was overflowed by a circular free jet. Mach number was fixed by using one of the five different nozzles (Mach 5.3, 6, 7, 8.7 and 11.2), all with an exit diameter of 600 mm. Finally, the air stream exited through a diffuser into the vacuum sphere.

Generally, the desired Reynolds number could be adjusted by either varying the pressure or the temperature on the high pressure portion. However, if a certain  $T_{t,\infty}/T_{\text{wall}}$  was desired, the Reynolds number had to be adjusted via the pressure. With a given vessel temperature and pressure, and assuming isentropic flow, the static conditions in the free stream could be directly calculated via equations (3.4) and (3.5) for each Laval nozzle. For further information on the H2K wind tunnel, please refer to [70].

## 6.3 Complementary Measurement Equipment

### 6.3.1 Pressure Data Recording

Pressure data was recorded with Pressure Systems, Inc. (PSI) modules, that were located in the structure of the intake model. Therefore, the pressure ducts could be cut shorter than in previous studies [44], which accelerated the time response. The data acquisition rate was 3 Hz. Throughout this work pressures were usually normalized with the free stream pressure via:

$$\Pi_{\text{st}} = \frac{p}{p_{\infty}}. \quad (6.1)$$

The pressure modules were calibrated with a baratron pressure device and the uncertainties were 100 Pa (0.1% of the full range of the PSI module).

A rake was located at the intake exit plane at  $x = 0.722$  m. The rake (figure 6.9) contained static and pitot pressure ports which were alternately distributed.

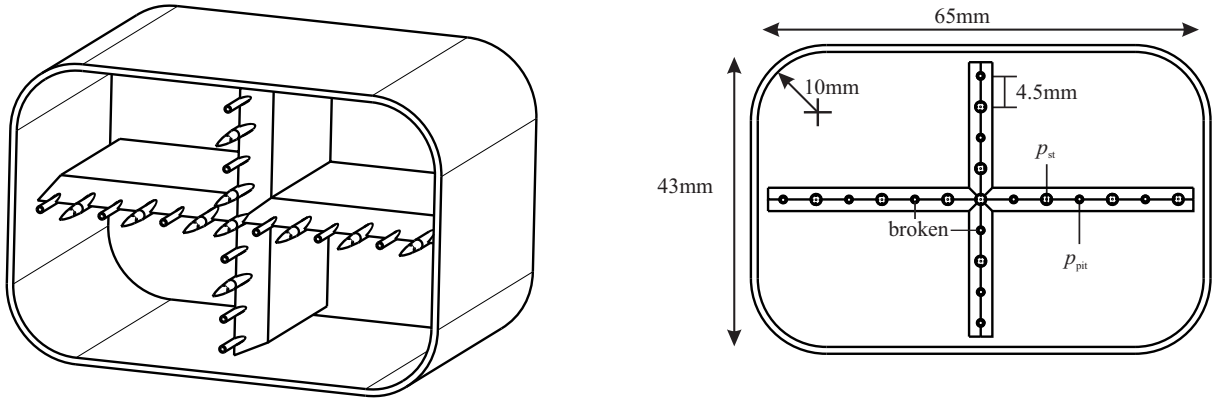


Figure 6.9: Rake with pitot and static pressure tubes; image from [36]

### Static Pressure at Rake

The static pressure tubes were designed according to Pinckney [80], who developed a shorter probe, which was less disturbing to neighboring probes compared to a conventional one. In a previous study [50] the rake was calibrated in the trisonic wind tunnel (TMK) and a second order polynomial was developed to calibrate the probes. For the present study the probe was additionally analyzed numerically and the calibration was slightly modified to a fourth order polynomial valid for  $M > 1.5$ :

$$\frac{p_{\text{measured}}}{p_{\text{corrected}}} = c_0 + c_1M + c_2M^2 + c_3M^3 + c_4M^4. \quad (6.2)$$

The constants  $c_i$  are listed in the appendix (section A.3). The CFD investigation implied that Reynolds number influence on the calibration was negligible. Pinckney reported an uncertainty of up to 10%. Although calibrations were performed, this relatively large uncertainty was used for the static pressure measurements.

### Pitot Pressure at Rake

Pitot pressure ports were located at the same  $x$ -location (0.722 m) as the holes of the static pressure ports. It was assumed that the measured pressure was equal to the pitot pressure of the free stream, and that the pitot and static pressure ports did not interfere with one another.

## 6.3.2 Mach Number Determination

To calculate the Mach number from a pitot pressure measurement, the following approach was applied. First, information on the static pressure on the same location was needed. This information was interpolated from neighboring values. Next, the ratio between pitot and static pressure determined whether the flow was sub- or supersonic. If  $p_{\text{pit}}/p > 1.893$ , the flow was supersonic and the Mach number was calculated with Newton's method [6, p. 292] via:

$$\frac{p_{\text{pit}}}{p} = \left[ \frac{(\gamma + 1)^2 M^2}{4\gamma M^2 - 2(\gamma - 1)} \right]^{\gamma/(\gamma-1)} \frac{1 - \gamma + 2\gamma M^2}{\gamma + 1}. \quad (6.3)$$

If  $p_{\text{pit}}/p < 1.893$ , the flow was subsonic and the following equation was directly applied to calculate Mach number:

$$M^2 = \frac{2}{\gamma - 1} \left[ \left( \frac{p_{\text{pit}}}{p} \right)^{(\gamma-1)/\gamma} - 1 \right]. \quad (6.4)$$

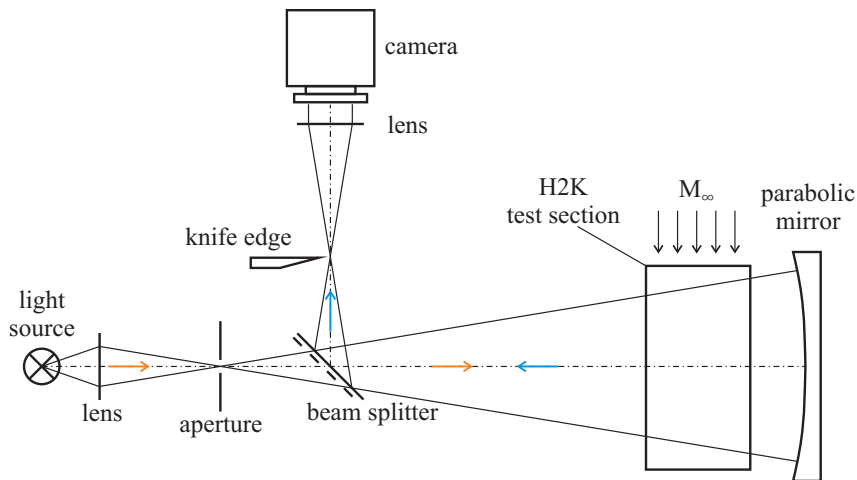


**Figure 6.10: Schematic of double-pass schlieren apparatus [66] used during H2K wind tunnel experiments.**

For further information on calculating the Mach number from a pitot pressure, please refer to Anderson [4, chapter 8].

### 6.3.3 Schlieren Imaging

The schlieren technique takes advantage of the varying refraction index in flows with strong density gradients. An optical apparatus is used to focus the light that traversed perpendicular to the free stream through the test section in one location and with a knife edge deviating rays are blocked off and density gradients become visible.

In the H2K wind tunnel a double pass schlieren system, suited for the low density environment in the test section, was used. A schematic is shown in figure 6.10. Light from a LOT arc lamp (LSB 551) passed through a lens, aperture and beam splitter onto a parabolic mirror. There the diverging beam was refracted into a converging beam and reflected back onto the beam splitter. Thereby the beam passed the test section twice. It was then focused near the knife edge which cut off the deviating rays, and was captured by the camera (Nikon D200). Data acquisition rate was approximately 1 Hz and images of the field of view (figure 6.3) contained  $3872 \times 2592$  pixels. Further information on schlieren flow visualization can be found in [66, 109].

### 6.3.4 Throttle System

A close-up image of the throttle system, which was attached to the wind tunnel model and sword apparatus, is shown in figure 6.11. The throttle was designed for supersonic intakes [108], and was used for SCRamjet intake research in previous studies [44, 50]. The intake exit flow was guided through a diverging section and honeycomb mesh into a settling chamber. Towards the rear end, the flow path became conical and a conical center body was installed in the axis of symmetry. The center body was movable in streamwise direction and created a throttle throat at  $Q4$ .

The throttle had two main objectives. First, the maximum sustainable back pressure of an intake was determined. During a combustion process, pressure peaks that stem from combustion instabilities or heterogeneous fuel injection can reach the intake exit and can cause intake unstart. This process was simulated by moving the inner conical piece of the throttle upstream. The degree of throttling was described by the Throttle Ratio ( $TR$ ), which was 0 and 1 for a fully opened and closed throttle, respectively:



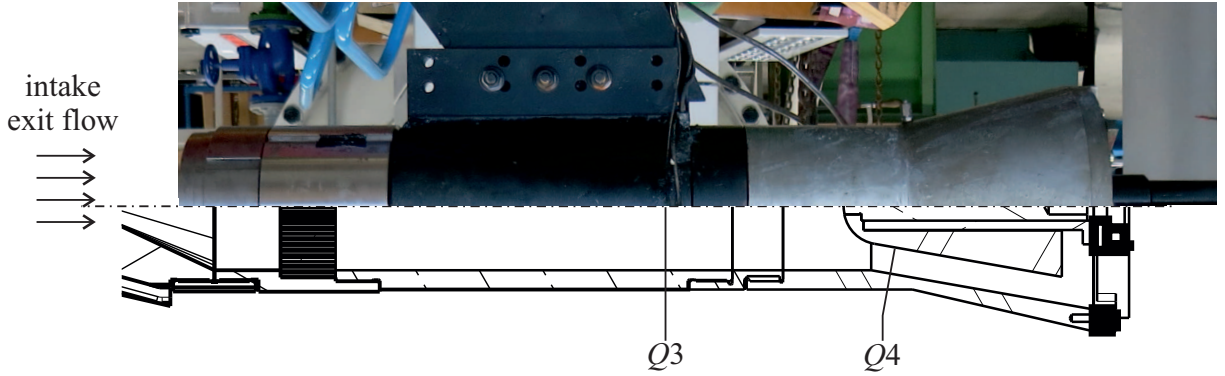


**Figure 6.11: Settling chamber and throttle as attached to the 3D-GRK intake model to measure mass flow and simulate back pressure.**

$$TR = \frac{A_{Q4,\max} - A_{Q4}}{A_{Q4,\max}}. \quad (6.5)$$

The pressure at the intake exit rose with higher throttle ratio and therefore the maximum sustainable back pressure  $\Pi_{\text{st,max}}$ , before the intake choked, could be measured.

Second, the mass flow through the intake was calculated via:

$$\dot{m}_{\text{intake}} = \rho_{Q3} V_{Q3} A_{Q3}. \quad (6.6)$$

At position  $Q3$ , static pressure was measured and to consider heat losses into the intake structure a thermo couple was installed that measured total temperature. If the contraction imposed by the throttle was high enough and if the flow in the settling chamber was subsonic, the flow was choked at position  $Q4$ , and an expression for  $M_{Q3}$  could be derived via equation (3.3). Further transformation with the equation of state, the Mach number definition (3.2) and equation (3.4) led to:

$$\dot{m}_{\text{intake}} = p_{Q3} M_{Q3} A_{Q3} \sqrt{\frac{\gamma}{RT_{t,Q3}} \left( 1 + \frac{\gamma - 1}{2} M_{Q3}^2 \right)}. \quad (6.7)$$

The throttle was additionally calibrated in a separate test campaign with an orifice apparatus, following DIN EN ISO 5167. A polynomial expression was developed, with which the mass flow was modified to yield the corrected mass flow:

$$\dot{m}_{\text{corr}} = \dot{m} (k_0 + k_1 A_{Q4} + k_2 A_{Q4}^2 + k_3 A_{Q4}^3 + k_4 A_{Q4}^4 + k_5 A_{Q4}^5 + k_6 A_{Q4}^6) \quad (6.8)$$

The polynomial constants from equation (6.8) are summarized in the appendix (section A.3).

### 6.3.5 Temperature Data Recording

Type K thermocouples (class 1) were used during the experiments. Thermocouples were used to measure total temperature of the free stream and in the settling chamber of the attached nozzle. Therefore, heat losses into the intake structure could be estimated. Since the thermocouples were placed in the air stream and not near the wall, they were mounted in a robust housing to withstand aerodynamic loads. Because of this housing and the relatively low-density air stream, the measured total temperature only slowly approached steady state. Therefore, total temperature was extracted at the end of each wind tunnel run and assumed to be constant throughout the experiment.

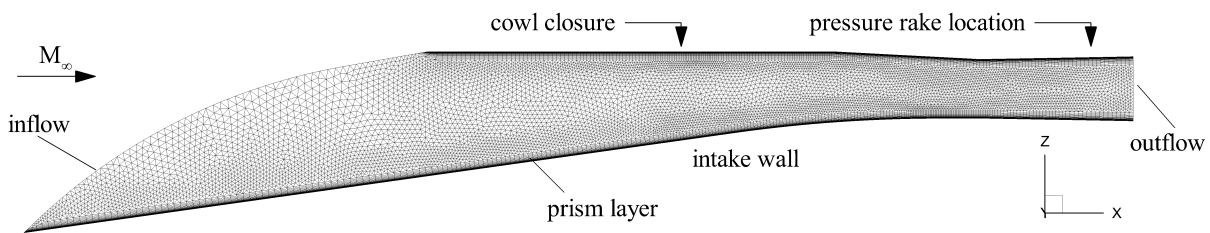


Figure 6.12: Starting mesh for 3D-GRK intake configuration.

## 6.4 Numerical Simulation

### 6.4.1 DLR-TAU Software System

The DLR-TAU software system was used to solve the Reynolds-Averaged Navier-Stokes (RANS) and Euler equations. DLR-TAU is a finite volume solver and implicit time stepping was used in this work. Furthermore, it was capable of parallelization to simultaneously run one simulation on multiple cores, thus absolute run times were reduced. For supersonic flow, inviscid terms were discretized with a second order upwind scheme, while second order central discretization was used for viscous terms. To faster damp out low frequency oscillations during time integration, the solver could be set to multigrid mode. Turbulence could be modeled with various models, such as one- or two-equation approaches. The  $k - \omega$  Shear-Stress Transport (SST) model [64] was used throughout this work, because it proved to accurately model hypersonic intake flow fields [84, 35]. To refine the mesh the integrated TAU-adaptation tool was used. It detected regions with large changes in flow variables and locally refined the mesh. Mach number, pressure, and density were used as the sensing variables. Note that mesh generation could not be performed within DLR-TAU, but another tool was used and is explained in the following section. Extensive information on the software system, its current status, and related literature can be found on the DLR-TAU website (<http://tau.dlr.de/>).

### 6.4.2 Mesh Generation

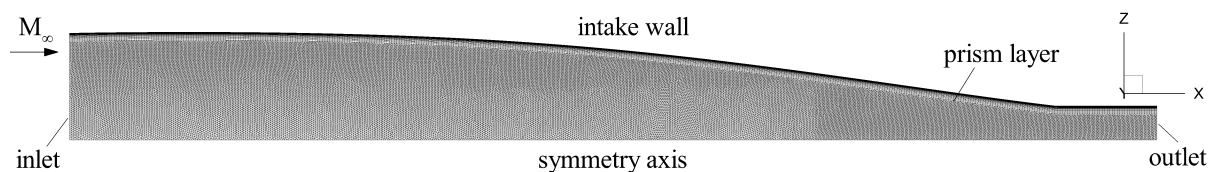
For the numerical simulations, meshes were generated with the Centaur software package, which was able to read the common CAD formats *\*.iges* and *\*.stp*. Furthermore, there was an internal *\*.dat* format affiliated with the software, which was used for two-dimensional and axisymmetric cases to automate mesh generation. For most of the grids, version v10.0.2 was used, but also a later version (v10.6) was tested in some cases. No noticeable difference in grid quality was detected between the two versions. For RANS simulations, hybrid grids were generated with a prismatic layer in the vicinity of viscous wall boundaries. Usually 30 – 40 prismatic layers were used, and perpendicular to the wall a non-dimensional wall spacing lower one was ensured ( $y^+ < 1$ ). The remaining volume was filled with tetrahedral elements. For Euler simulations two options were available. First, the same grid as for the RANS simulations could be used, but the wall boundary conditions were set to be inviscid. Second, an unstructured grid was generated, in which all elements were tetrahedral. The downside of the first option was that meshes were usually unnecessarily large due to the highly resolved region in the vicinity of the wall. Other than that no noticeable differences between the two options were detected.

### 6.4.3 Mesh Analysis

In the present section the grid sizes for the conducted three-dimensional and axisymmetric CFD simulations are presented. The starting mesh for the three-dimensional (figure 6.12) and axisymmetric simulation (figure 6.13) were further refined with the DLR-TAU adaptation tool. For each adaption the number of grid points was nearly doubled and the approximate mesh sizes are summarized in table 6.1.

**Table 6.1: Approximate mesh sizes for three-dimensional and axisymmetric cases.**

	3D case		axisymmetric case	
	Elements	Grid Points	Elements	Grid points
starting grid	$1 \times 10^6$	$0.1 \times 10^6$	64,000	64,000
grid 1	$12 \times 10^6$	$2 \times 10^6$	130,000	130,000
grid 2	$29 \times 10^6$	$5 \times 10^6$	290,000	290,000
grid 3	$67 \times 10^6$	$12 \times 10^6$	630,000	630,000

**Figure 6.13: Starting mesh for axisymmetric Busemann intake configuration.**

### Three-Dimensional Mesh

Three-dimensional RANS simulations were performed for the 3D-GRK intake as well as for streamline traced geometries. The different intake geometries and flow fields were similar and therefore the 3D-GRK Mach 7 case with the v-shaped cowl, simulated at wind tunnel conditions, was used as reference configuration in the following context. When refining from grid 1 to grid 2, small variations occurred in pressure and temperature across the height and width at the rake location (figure 6.14). The variations were negligible when further refining to grid 3. Wall pressure, mass- and stream-thrust-averaged pressures, and temperatures were practically independent of the grid size (see figure A.1 and A.2 in the appendix). Therefore, mesh properties as those of the medium sized grid 2 were taken for further analysis.

### Axisymmetric Mesh

A classical Busemann intake with viscous correction and without truncation was used as reference condition for the grid analysis ( $M_\infty = 8$ ,  $\Pi_{st} = 43$ ,  $h = 30$  km). The number of grid points and elements are shown in table 6.1. Due to the axisymmetric grid the number of elements and grid points was approximately equal. After refining grid 1 to grid 2, there were small variations in wall pressure near the beginning of the isolator ( $x = 0$ , figure 6.15). Variations became negligible, after refining to grid 3. Averaged properties were practically grid independent. Thus, mesh properties as those of the medium sized grid 2 were taken for the analysis of axisymmetric cases.

## 6.5 One-Dimensional Post-Analysis

To calculate overall engine parameters from intake performance data, a one-dimensional post-analysis [35, 39] was used and is explained in the present section. The intake performance parameters were extracted from CFD at the intake exit plane and served as entrance conditions of the combustor. The combustion chamber and nozzle were modeled with a one-dimensional analysis. In the analysis fuel-air mixing or ignition delay times were not considered. No high temperature effects, such as vibrational excitation or dissociation were considered, and the gas was treated as calorically perfect. Note that the

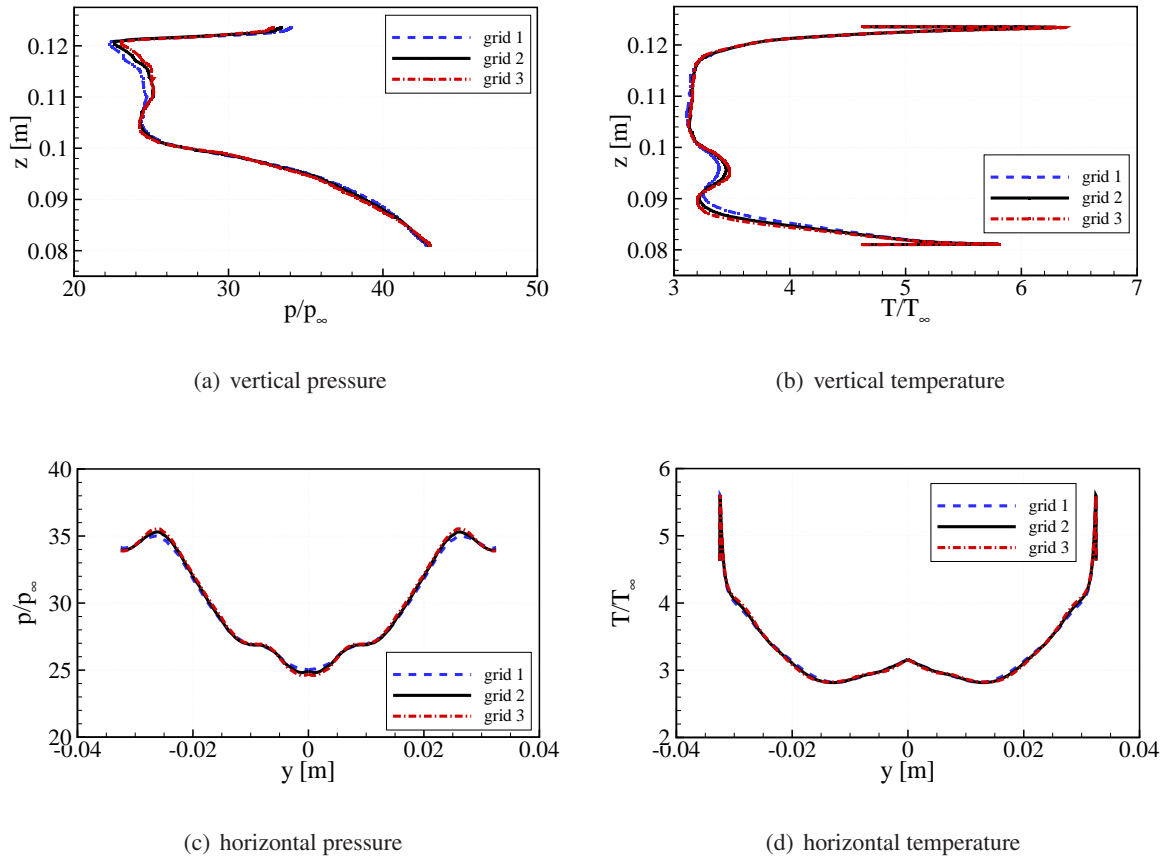


**Figure 6.14: Influence of mesh size on pressure and temperature in intake exit plane at  $x = 0.722$  m.**

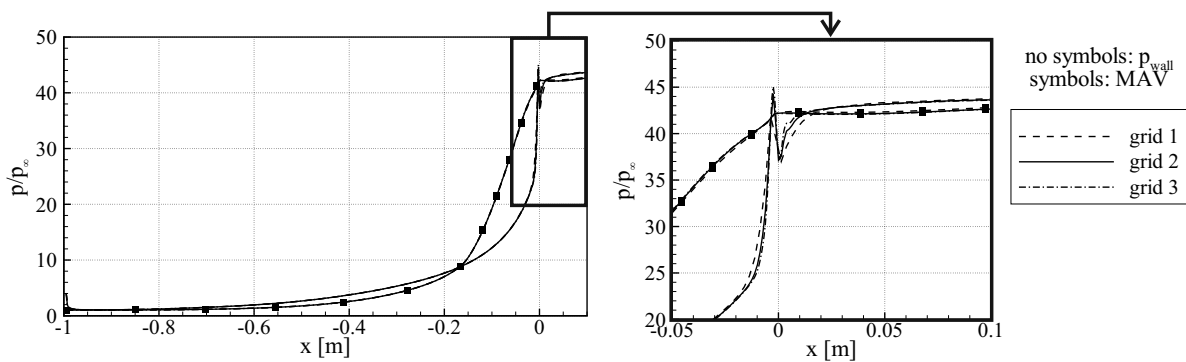


**Figure 6.15: Influence of mesh size on pressure in axisymmetric SCRamjet configuration.**

calculated performance parameters are valid for the engine flow path only, and do not include the outer aircraft structure. Those performance parameters are also referred to as uninstalled properties.

### 6.5.1 Combustion Chamber Model

The combustion chamber was modeled by a sudden heat release to simulate the combustion, and a subsequent duct with area change and frictional flow to represent viscous forces within the combustor. Hydrogen was used as fuel and its Lower Heating Value ( $LHV$ ) was  $119 \times 10^6$  J/kg. The changes in properties due to heat release were calculated with the Rayleigh-flow equations, which are valid for inviscid and steady flow and can be found in [119]. Position 3 and 4 denote the beginning and end of heat release, respectively and the following steps describe the process in more detail.

1. Calculate the change in total temperature or specific enthalpy due to the heat release of the fuel, with the respective equivalence ratio  $\varphi$ , stoichiometric mass ratio  $\hat{m}_{\text{stoi}} = 34.06$ , and combustion efficiency that was set to  $\eta_{\text{cc}} = 0.8$ :

$$h_{t,4} = h_{t,3} + \eta_{\text{cc}} LHV \frac{\varphi}{\hat{m}_{\text{stoi}}}. \quad (6.9)$$

Equivalence ratio was set to the maximum value at which Mach numbers were supersonic.

2. With the conservation of mass and momentum equations, an expression that relates total temperature and Mach number of the two states 3 and 4 could be derived:

$$\frac{T_{t,4}}{T_{t,3}} = \frac{\left(1 + \frac{\gamma-1}{2} M_4^2\right) M_4^2}{\left(1 + \frac{\gamma-1}{2} M_3^2\right) M_3^2} \left(\frac{1 + \gamma M_3^2}{1 + \gamma M_4^2}\right)^2. \quad (6.10)$$

With the total temperature known, Mach number was then calculated by iteratively solving equation (6.10) for  $M_4$ .

3. Finally, temperature and pressure were calculated via:

$$T_4 = T_{t,4} \left(1 + \frac{\gamma-1}{2} M_4^2\right)^{-1}, \text{ and} \quad (6.11)$$

$$\frac{p_4}{p_3} = \frac{1 + \gamma M_3^2}{1 + \gamma M_4^2}. \quad (6.12)$$

Note that after the heat release, the ratio of specific heats and heat capacity of the combustion products changed to 1.31 and 1255 J/kg/K, respectively. The changes in properties in the subsequent duct were calculated for steady, frictional and adiabatic flow. To calculate the Mach number in  $x$ -direction, the following differential equation, taken from [76, p. 252], was integrated numerically:

$$\frac{dM}{M} = \underbrace{-\left(\frac{1 + \frac{\gamma-1}{2} M^2}{1 - M^2}\right) \frac{dA}{A}}_{\text{influence of area change}} + \underbrace{\left(\frac{1 + \frac{\gamma-1}{2} M^2}{1 - M^2}\right) \frac{\gamma M^2}{2} \frac{4c_f dx}{D_H}}_{\text{influence of friction}}. \quad (6.13)$$

The friction-coefficient  $c_f$  was set to 0.02, which was at the upper limit of what can be expected for turbulent, high Reynolds number ( $> 10^6$ ) flow over a flat plate [30]. The length and opening angle of the combustion chamber were 0.4 m and 1 deg, respectively, and were chosen corresponding to the com-

bustion chamber investigated in previous work [84]. The hydraulic diameter  $D_H$  varied with combustor length.

With the Mach number distribution known, the temperature could be calculated from the energy equation and the definition of Mach number:

$$\frac{dT}{T} = -\frac{(\gamma - 1)M^2}{1 + \frac{(\gamma-1)}{2}M^2} \frac{dM}{M}. \quad (6.14)$$

Pressure could be calculated from the continuity equation and the definition of Mach number:

$$\frac{dp}{p} = -\frac{dA}{A} + 0.5\frac{dT}{T} - \frac{dM}{M}. \quad (6.15)$$

Further information on flow with friction and area change can be found in [76, chap. 9].

### 6.5.2 Nozzle Model

To model the flow through the nozzle the isentropic flow relations for a given area ratio were used. Position 4 and 10 denote the nozzle entrance and exit, respectively. Transformation of equation (3.3) led to:

$$\left(\frac{A_{10}}{A_4}\right)^2 = \left(\frac{M_4}{M_{10}}\right)^2 \left(\frac{1 + \frac{\gamma-1}{2}M_{10}^2}{1 + \frac{\gamma-1}{2}M_4^2}\right)^{\frac{\gamma+1}{\gamma-1}}, \quad (6.16)$$

with which the change in Mach number for the given area ratio was calculated iteratively. Assuming inviscid and adiabatic flow:

$$p_4^{1-\gamma} T_4^\gamma = p_{10}^{1-\gamma} T_{10}^\gamma = \text{const.}, \quad (6.17)$$

$$T_4 \left(1 + \frac{\gamma-1}{2}M_4^2\right) = T_{10} \left(1 + \frac{\gamma-1}{2}M_{10}^2\right), \quad (6.18)$$

the pressure and temperature could be calculated. The contraction ratio of the nozzle was set equal to the intake overall contraction ratio. Thus, the nozzle contraction ratio was 8.12 and  $\approx 9.5$  for the 3D-GRK and streamline traced configurations, respectively. Further information on isentropic flow through nozzles can be found in [4, chap. 10].

The data from the one-dimensional post-analysis should be regarded as a qualitative result and direct comparison to results from more sophisticated cycle analysis should be done carefully. Nevertheless, the idea was to have engine parameters calculated with simple models, rather than to have no engine parameters at all.

## 6.6 Averaging

Figure 6.16 shows a typical CFD Mach number distribution within the intake exit plane of the 3D-GRK intake, along with a hybrid mesh which has a structured grid near the viscous wall and an unstructured grid in the core region. Averaged variables of the flow field could be of greater interest, for instance when comparing different intake configurations, or when one-dimensional values are needed for further analysis of the combustor and nozzle. Therefore, in the following context conventional averaging techniques, such as the mass-weighted or mass-flow-weighted average are discussed. Furthermore, the method of stream-thrust averaging is explained in which the conservation of mass, continuity and momentum were

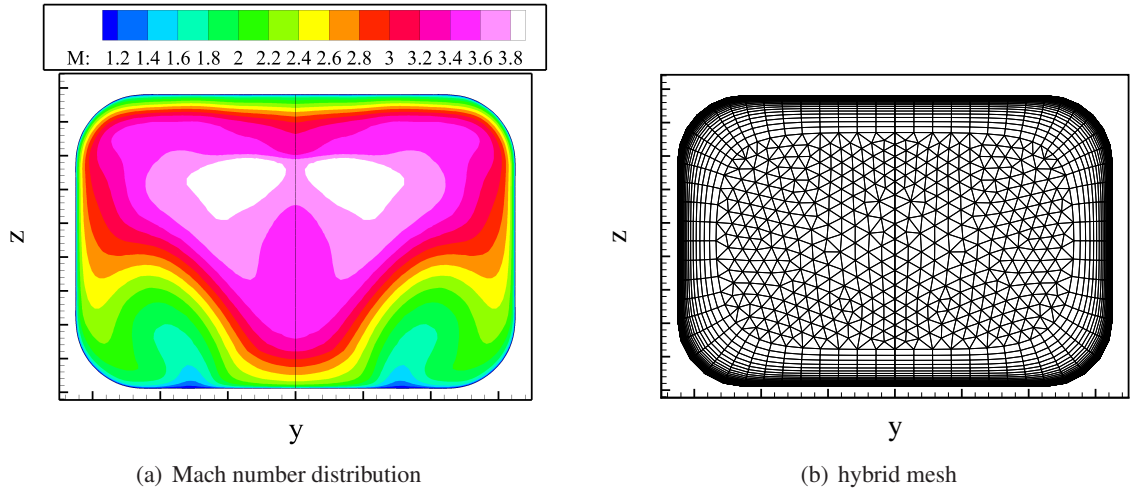


Figure 6.16: Sample intake exit plane.

considered.

### 6.6.1 Conventional Averaging

The average value of the sample variable  $\Omega$  was calculated via:

$$\bar{\Omega} = \frac{\sum_{i=1}^n \Omega x_i}{\sum_{i=1}^n x_i}, \quad (6.19)$$

while the total number of elements in figure 6.16 (right) was labeled  $n$ . The most general approach was to set  $x_i = 1$ , which led to the arithmetic mean. With different choices of the weighting variable  $x_i$  emphasis could be put on different demands [8]. In figure 6.16 for example, the area of the elements should be considered during averaging, and therefore the area average can be calculated via:

$$\bar{\Omega} = \frac{\sum_{i=1}^n \Omega A_i}{\sum_{i=1}^n A_i}. \quad (6.20)$$

Mass-weighted and mass-flow-weighted averages could be calculated by setting  $x_i$  equal to  $A_i \rho_i$  and  $A_i \rho_i (\vec{v}_i \cdot \vec{n}_i)$ , respectively.

### 6.6.2 Stream-Thrust Averaging

Stream-thrust-averaged parameters were extracted from a flow field by considering the conservation of mass, momentum and energy equations [47, 8]. Therefore, they provide more physical one-dimensional values of the flow, and are also referred to as flux based averages.

For the cross sectional surface in figure 6.16 the conservation of mass, momentum and energy equations could be written as:

$$\dot{m} = \sum_{i=1}^n (\rho_i A_i (\vec{v}_i \cdot \vec{n}_i)), \quad (6.21a)$$

$$\vec{F} = \sum_{i=1}^n (\dot{m}_i \vec{v}_i + p_i A_i \vec{n}_i), \text{ and} \quad (6.21b)$$

$$h_t = \frac{1}{\dot{m}} \sum_{i=1}^n \left( \dot{m}_i \left( c_p T_i + \frac{1}{2} V_i^2 \right) \right). \quad (6.21c)$$

Assuming that equation (6.21) could be reproduced by one-dimensional parameters, the conservation of mass, momentum and energy equation could be rewritten as:

$$\dot{m} = \rho_{sta} A (\vec{v}_{sta} \cdot \vec{n}), \quad (6.22a)$$

$$\vec{F} = \dot{m} \vec{v}_{sta} + p_{sta} A \vec{n}, \text{ and} \quad (6.22b)$$

$$h_t = c_p T_{sta} + \frac{V_{sta}^2}{2}, \quad (6.22c)$$

where the index *sta* denoted stream-thrust-averaged variables. Equation (6.22), along with the equation of state  $p = \rho RT$  provided six equations for the six unknowns:  $\vec{v}_{sta}$ ,  $p_{sta}$ ,  $T_{sta}$  and  $\rho_{sta}$ .

Generally, there were two possible solutions, which are referred to as a subsonic and supersonic solution [27]. The choice of the applicable solution was made based on an observation of the flow field, or of conventionally averaged variables. Baurle et al. [8] observed that conventionally averaged variables generally reproduce a flow field qualitatively, while flux based averaging techniques have problems in regions with large non-uniformity. However, as soon as extracted values are used for one-dimensional engineering tools, flux based approaches are favorable. Furthermore, they noted that when flux based averaging techniques are applied to symmetrical regions of interest, the calculated values can be different depending on whether the full geometry is shown or only parts of it. This is due to the usage of the vector quantities that partly cancel out when considering the full geometry.

The averaging algorithms were implemented in a FORTRAN (f95) subroutine that could be compiled on Windows (Intel FORTRAN Composer XE2011) or UNIX (GNU FORTRAN compiler) operating systems. Analogously to the intake design tool, the averaging routine could be automated and run in manual or stack mode. Please refer to [9] for a more detailed description of the method and of other flux based averaging methods. With the programmed routine, extraction of the stream-thrust-averaged values from a CFD plane was straight forward. However, for experimental results where only parts of a flow field plane are known, the averaging method is not suitable.



## 7 Results

First, the analytical approaches to truncation and viscous effects are validated. To do this, the axisymmetric Busemann and reversed nozzle flow fields are investigated separately and then compared to each other. Hereafter, results obtained numerically for different streamline traced geometries are presented. Then experimental results, such as intake starting data or throttle measurements obtained for the 3D-GRK intake are shown. Beyond that, numerical results for the 3D-GRK intake are validated to experimental data. Finally, intake geometries, performance, and the design methodology of the streamline tracing approach are directly compared to the 3D-GRK intake.

### 7.1 Validation of Approach to Truncation Effects

As reference condition a Mach 8 flight and a design pressure ratio of 43 were used. Due to this fixed design point and the additional calculations applied to the truncated configuration (section 4.3), the truncated geometries differed in shape from the classical geometries, as can be seen from figures 7.2, 7.5, 7.9, and 7.12. Busemann and reversed nozzle flow fields are discussed separately, while a direct comparison is given in section 7.3.

#### 7.1.1 Leading Edge Truncation

In the current section the approach to leading edge truncation, which was described in section 4.3.1, is validated by comparing analytical predictions to axisymmetric Euler simulations. No viscous correction was applied and intakes were truncated at the leading edge only. In some cases, to increase clarity, only every other truncation case is displayed. However, the conclusions are based on the full range of leading edge truncation angles described in section 4.3.1.

##### *Busemann Flow*

Results on leading edge truncation applied to Busemann flow fields were also published in [38] and the analytical performance parameters are summarized in table 7.1. The Mach number contour is plotted in figure 7.1 (top) representatively for the 4 deg truncation case. As described in section 2.1.2 an oblique shock formed at the leading edge and interfered with the iso-lines of the isentropic compression. Furthermore, the outflow was no longer uniform. The intake contours along with the normalized wall pressure distributions extracted from CFD are plotted for increasing leading edge truncation in figure 7.2. With increasing leading edge truncation, intake length decreased and wall pressures fluctuated more near the design value of 43. This is a sign of flow non-uniformity, which increased with increasing leading edge truncation angle. In figure 7.3, cross-stream pressures and Mach numbers at the intake exit are plotted to further demonstrate the increase in non-uniformity with truncation angle.

To better understand the average flow field, Mass-AVeraged (MAV) and Stream-Thrust-Averaged (STA) values of different variables, extracted from the numerical solutions are plotted in figure 7.4. From these plots it can be seen that the stream-thrust-average static pressure was within 1% of the design pressure ratio of 43; the slight overshoot at  $x \approx 0$  (figure 7.4(a)) resulted from differences in the averaging techniques. Since leading edge shock strength increased with truncation angle, total pressure decreased as can be seen in figure 7.4(b). There are minimums in stream-thrust-averaged total pressure, which may seem non-physical and are explained in the following.

**Table 7.1: Design parameters for leading edge truncated Busemann intakes with  $p_3$ -adjustment; all intakes designed for  $M_\infty = 8$  and  $\Pi_{st} = 43$ .**

$\delta$ [deg]	$\Pi_{tot}$	$\Theta_{st}$	$L/h_{cc}$	$CR_o$	$CR_i$
0	0.981	2.95	34.2	13.5	2.90
2	0.909	3.01	24.6	13.1	2.95
4	0.784	3.14	19.6	12.5	3.06
6	0.634	3.34	16.1	11.7	3.19

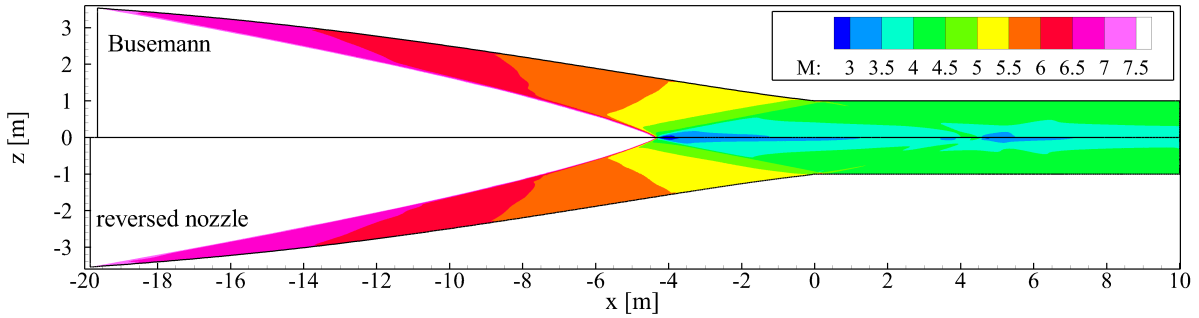


**Figure 7.1: Mach number contour plot extracted from CFD for 4 deg leading edge truncation.**

The radial stream-thrust components ( $\pm y$ -axis and  $\pm z$ -axis) canceled each other out in equation 4.11. Nevertheless, these components of flow velocity contained kinetic energy which was taken into account in the energy equation (see (6.21c)). Therefore, an incorrect higher temperature and thus lower Mach number was calculated during the one-dimensionalization. This generally occurred when the flow varied in more than one dimension and energy was incorrectly associated with internal energy, not kinetic energy. This phenomenon was described in detail by Baurle and Gaffney [9]. Towards the end of the intake the mass-averaged total pressures approached the constant level of the stream-thrust-averaged values. Finally, the average temperature and the maximum temperature in a cross-stream plane extracted from CFD solutions for increasing leading edge truncation angle are shown in figure 7.4(c) and 7.4(d). Note that average temperature from the numerical simulations was within 1% of the analytical values from table 7.1.

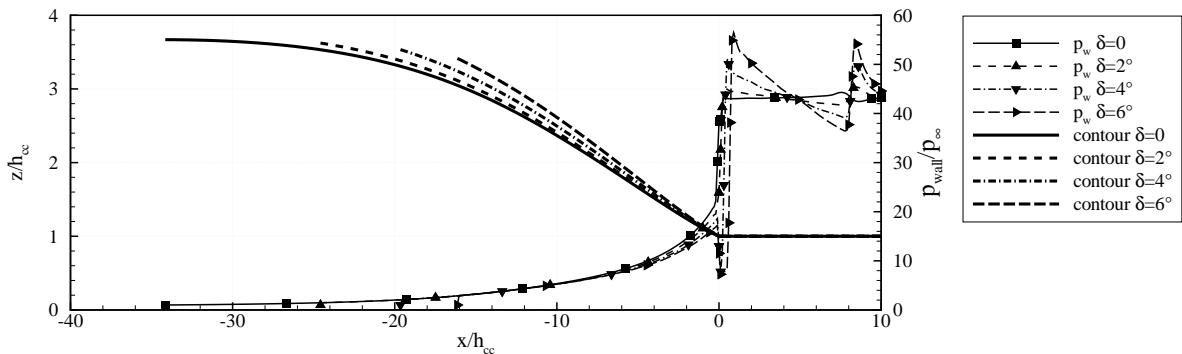


**Figure 7.2: Busemann intake contours along with wall pressure plots for increasing leading edge truncation; all intakes designed for  $M_\infty = 8$  and  $\Pi_{st} = 43$ ; image from [38].**

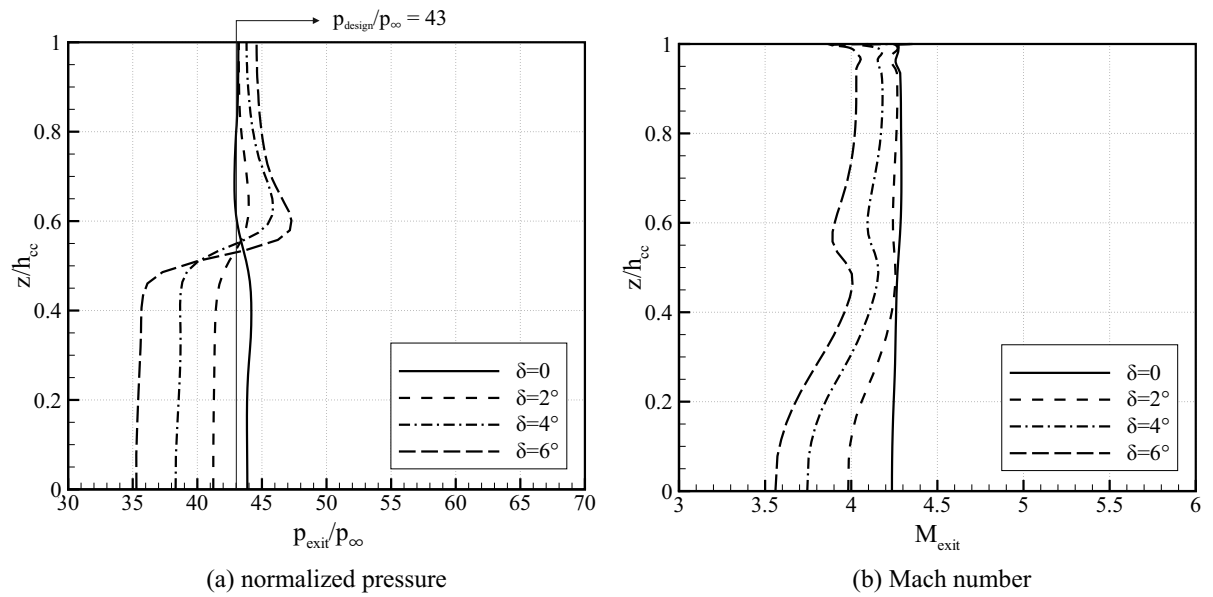


Figure 7.3: Cross-stream pressure and Mach number of leading edge truncated Busemann intakes at outlet plane; all intakes designed for  $M_\infty = 8$  and  $\Pi_{st} = 43$ ; image from [38].

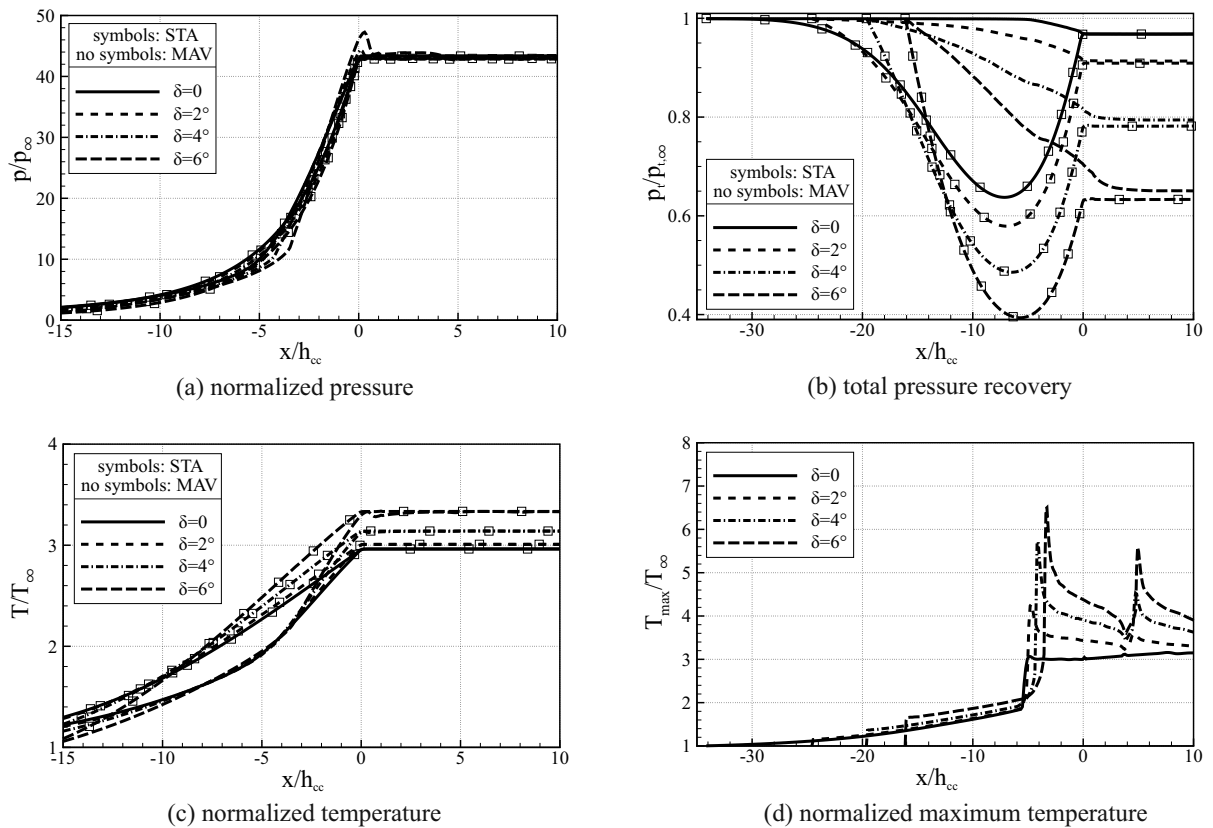


Figure 7.4: Mass- and stream-thrust-averaged parameters and maximum temperature of leading edge truncated Busemann intakes; all intakes designed for  $M_\infty = 8$  and  $\Pi_{st} = 43$ ; image from [38].

**Table 7.2: Design parameters for leading edge truncated reversed nozzle intakes with  $p_3$ -adjustment; all intakes designed for  $M_\infty = 8$  and  $\Pi_{st} = 43$ .**

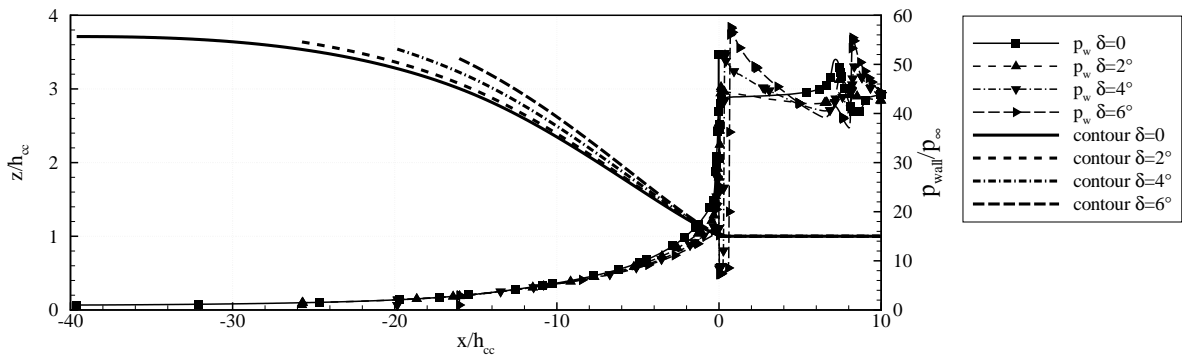
$\delta$ [deg]	$\Pi_{tot}$	$\Theta_{st}$	$L/h_{cc}$	$CR_o$	$CR_i$
0	1.0	2.93	39.6	13.8	2.29
2	0.935	2.98	25.7	13.2	2.32
4	0.790	3.13	19.8	12.5	2.37
6	0.633	3.34	16.0	11.6	2.43

### Reversed Nozzle Flow

The leading edge truncation in reversed nozzle intakes was investigated analogously to the Busemann configurations from the previous section and results were very similar. Analytical performance parameters are summarized in table 7.2. The  $p_3$ -adjustment was used in the same manner and intakes were truncated up to truncation angles of 7 deg.

The Mach number contour is plotted in figure 7.1 (bottom) representatively for the 4 deg truncation case. Qualitatively the reversed nozzle and Busemann flow fields were equal. In figure 7.5, geometries and wall pressure plots are shown for different truncation angles. Intake length decreased with higher leading edge truncation. E.g. for truncation angles around 4 deg intakes were half as long as compared to the classical case. Wall pressure fluctuations around  $\Pi_{st} = 43$  were found to increase with higher leading edge truncation. Further, internal contraction ratio rose from 2.29 for the classical case to 2.43 for  $\delta = 6$  deg; overall contraction ratio fell from 13.8 for the classical case to 11.6 for  $\delta = 6$  deg. In figure 7.6 cross-stream pressure and Mach number are plotted against intake exit height. Mach number non-uniformity increased with higher leading edge truncation. The increase in pressure non-uniformity was not as distinct as for Busemann flows, since generally pressure seemed to be less uniform for reversed nozzle flows.

Figure 7.7 shows mass- and stream-thrust-averaged values of  $p$ ,  $p_t$ ,  $T$ , and maximum temperature for different truncation angles. Static pressure was found to hold constant for all configurations, while larger truncation and therefore higher shock losses caused a decrease in total pressure recovery (figure 7.7(a),(b)). Average static temperature rose with higher  $\delta$  (figure 7.7(c)), and resembled the trend predicted analytically. Maximum temperature also increased, which enhances ignition with increasing leading edge truncation (figure 7.7(d)).

**Figure 7.5: Reversed nozzle intake contours along with wall pressure plots for increasing leading edge truncation; all intakes designed for  $M_\infty = 8$  and  $\Pi_{st} = 43$ .**

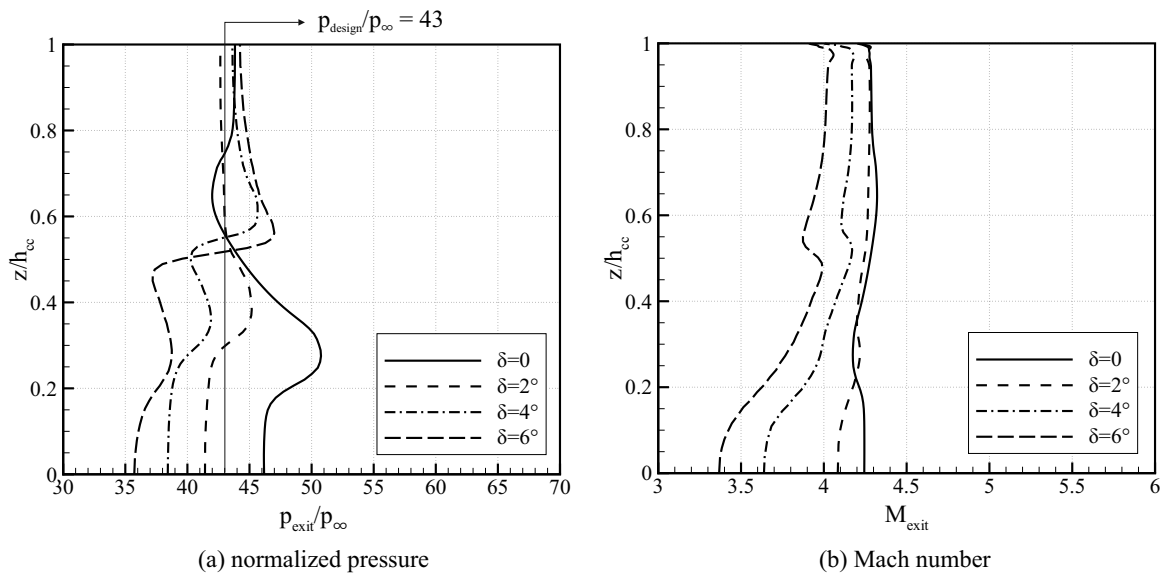


Figure 7.6: Cross-stream pressure and Mach number of leading edge truncated reversed nozzle intakes at outlet plane; all intakes designed for  $M_{\infty} = 8$  and  $\Pi_{st} = 43$ .

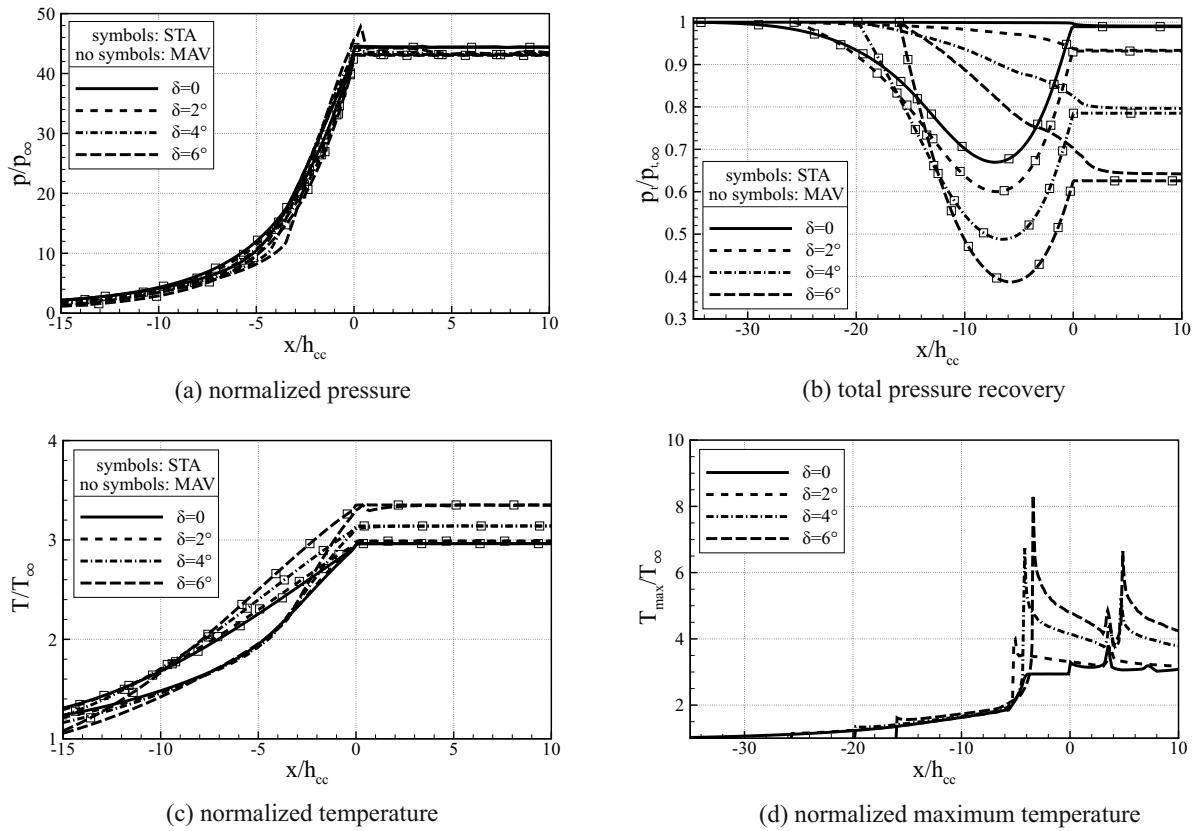


Figure 7.7: Mass- and stream-thrust-averaged parameters and maximum temperature of leading edge truncated reversed nozzle intakes; all intakes designed for  $M_{\infty} = 8$  and  $\Pi_{st} = 43$ .

It was concluded that modeling the property change at the leading edge with an oblique shock and then adjusting the pressure level at the intake exit, based on the continuity equation, yielded good agreement between analytical and numerical values. In summary, increasing leading edge truncation for constant pressure ratio reduced total pressure recovery, increased average and maximum temperature, and reduced intake length.

### 7.1.2 Rear Side Truncation

The approach to rear side truncation, described in section 4.3.2, was validated by comparing analytical predictions to axisymmetric Euler simulations. No viscous correction was applied and intakes were truncated at the rear side only. In some cases, to increase clarity, only every other truncation case is displayed, but once again the conclusions are based on the full range of internal contraction ratio described in section 4.3.2.

**Table 7.3: Design parameters for Busemann intakes truncated at their rear-side; all intakes designed for  $M_\infty = 8$ ,  $\delta = 0$ , and  $\Pi_{st} = 43$ .**

$CR_i$	$\Pi_{tot}$	$\Theta_{st}$	$L/h_{cc}$	$CR_o$
2.9 <sup>†</sup>	0.981	2.95	34.2	13.5
2.4	0.861	3.06	31.8	12.9
2.0	0.757	3.18	30.1	12.4
1.6	0.649	3.32	28.4	11.8

<sup>†</sup> no rear side truncation

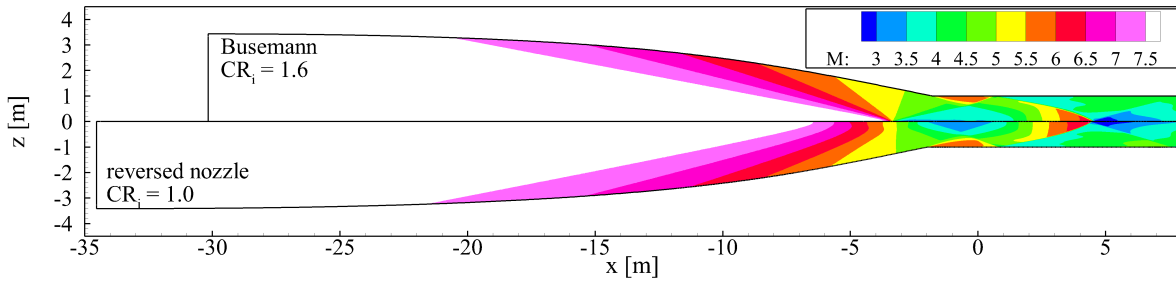


**Figure 7.8: Mach number contour plot extracted from CFD for largest rear side truncation.**

#### *Busemann Flow*

Results on rear side truncation applied to Busemann flow fields were also published in [37, 38] and the analytical performance parameters are summarized in table 7.3.

The Mach number contour is plotted in figure 7.8 (top) representatively for maximum rear side truncation. As described in section 2.1.2 the isentropic compression was terminated earlier and an expansion disturbed the flow field. Thus, the outflow was no longer uniform. In figure 7.9 Busemann intake contours along with normalized wall pressure distributions are plotted for increasing rear-side truncation. The intake length decreased for rear-side truncation, although the amount of reduction was smaller than for leading edge truncation. Furthermore, with higher rear-side truncation the expansion and therefore Mach number at the intake exit ( $x \approx 0$ ) increased. Thus, the pressure jump and the fluctuations around the design pressure level rose, which was a sign of greater non-uniformity. To further illustrate this effect in figure 7.10 the cross-stream pressure and Mach number are plotted against the intake height at the exit

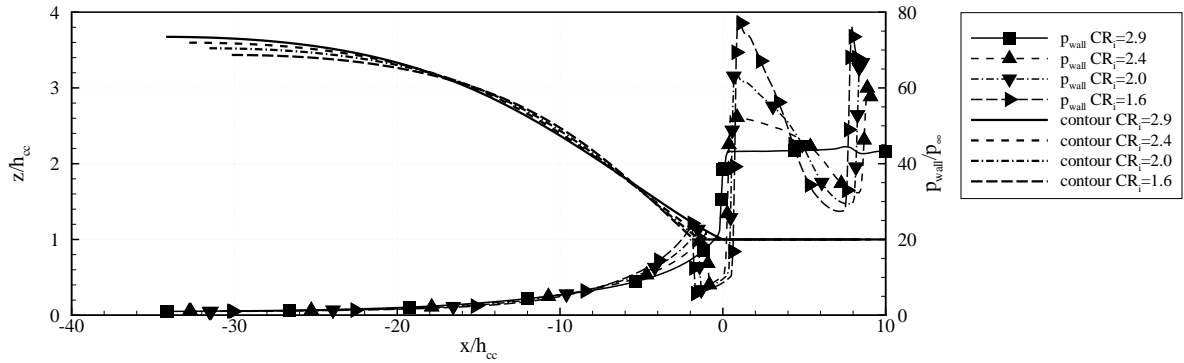


**Figure 7.9:** Busemann intake contours along with wall pressure plots for increasing rear side truncation; all intakes designed for  $M_\infty = 8$ ,  $\delta = 0$ , and  $\Pi_{st} = 43$ ; image from [38].

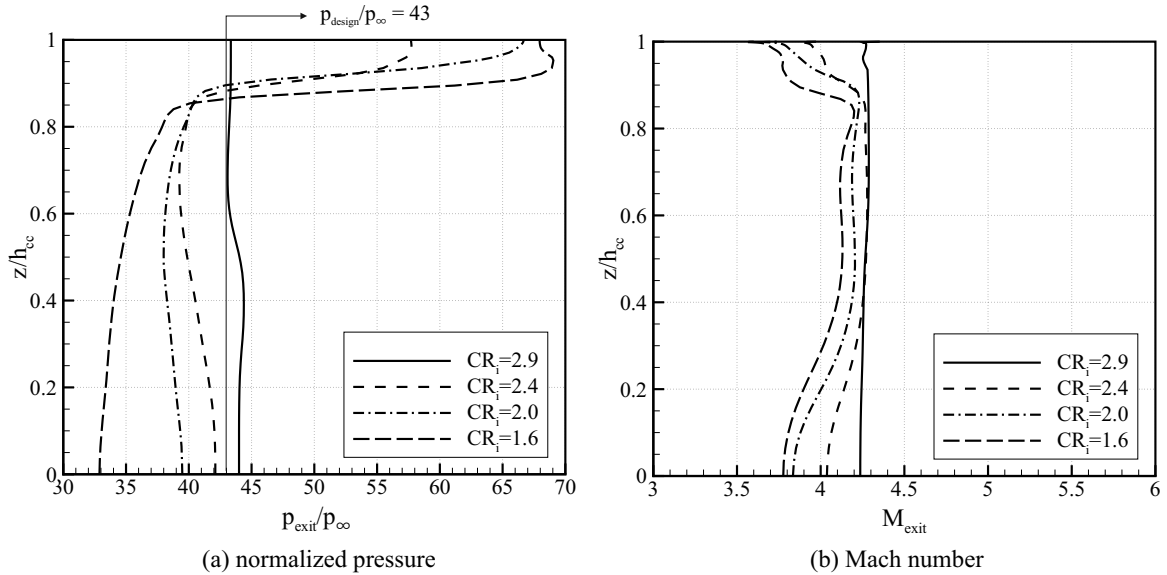


**Figure 7.10:** Cross-stream pressure and Mach number of rear side truncated Busemann intakes at outlet plane; all intakes designed for  $M_\infty = 8$ ,  $\delta = 0$ , and  $\Pi_{st} = 43$ ; image from [38].

plane. The deviations from the design pressure level, and therefore flow non-uniformity, increased with higher rear side truncation.

Since pressures at discrete locations do not represent the mean flow characteristics, mass-averaged and stream-thrust-averaged flow properties are plotted in figure 7.11. The stream-thrust-averaged static pressure ratios (figure 7.11(a)) matched the design pressure ratio of  $\Pi_{st} = 43$  very accurately at the intake throat. Stream-thrust-averaged pressures were within 1% of the analytically predicted data. With higher rear-side truncation there was an increase in overshoot in mass-averaged static pressure, which damped out further down the isolator. Total pressure recoveries generally dropped with higher rear-side truncation (figure 7.11(b)), while again the mass-averaged values approached the constant plateau of the stream-thrust-averaged levels. The non-physical drop of total pressure is again caused by the canceling of the radial velocity components during the stream-thrust analysis.

For increasing rear-side truncation the average static temperature levels rose (figure 7.11(c)), and matched the analytical values from table 7.3. Similarly to wall pressure, the mass-averaged profiles fluctuated stronger with increasing rear-side truncation and damped out further downstream. Interestingly,

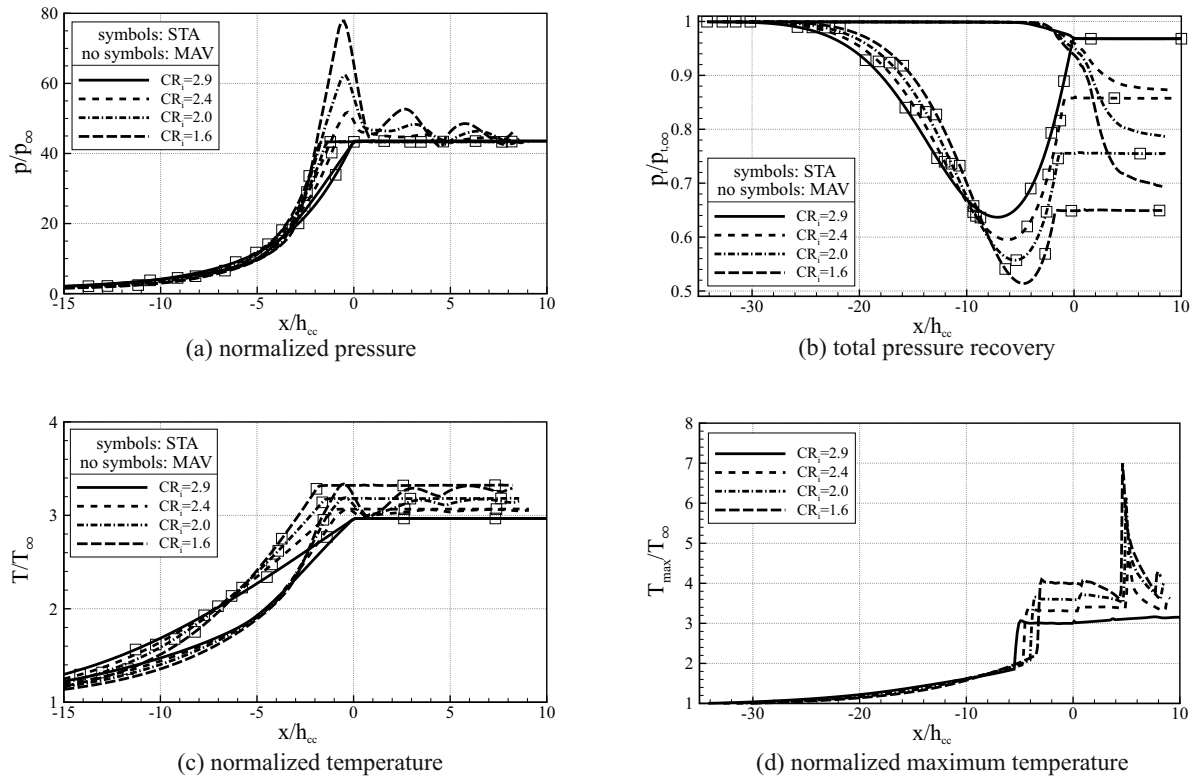


**Figure 7.11: Mass- and stream-thrust-averaged parameters and maximum temperature of rear side truncated Busemann intakes; all intakes designed for  $M_\infty = 8$ ,  $\delta = 0$ , and  $\Pi_{st} = 43$ ; image from [38].**

the mass-averaged temperature matched the stream-thrust-averaged temperature at locations where the mass-averaged pressure had a local maximum in overshoot and vice versa. Finally, maximum static temperature increased with higher rear-side truncation (figure 7.11(d)).

### Reversed Nozzle Flow

The rear side truncation in reversed nozzle intakes was investigated analogously to the Busemann configurations from the previous section and results were very similar. The stream-thrust analysis was applied in the same manner to the rear portion of the intake. Internal contraction ranged from 2.3 for a non-truncated geometry to 1.0 for the highest amount of rear side truncation. The maximum rear side truncation in the reversed nozzle and Busemann configurations both caused the same length reduction of  $\approx 6 \times h_{cc}$ .

In table 7.4, analytical performance parameters are summarized. The Mach number contour is plotted in figure 7.8 (bottom) representatively for maximum rear side truncation. Except for the longer intake geometry, the reversed nozzle flow was qualitatively equal to the Busemann flow. Figure 7.12 shows intake contours and wall pressure for different internal contraction ratios. For a constant design pressure of 43, length and overall contraction ratio decreased with more rear side truncation. Furthermore, wall pressures showed stronger fluctuations around  $\Pi_{st} = 43$ , thus non-uniformity increased. In figure 7.13, cross-stream pressure and Mach number are plotted against exit height and stronger non-uniformity with lower  $CR_i$  was clearly visible.

Finally, mass- and stream-thrust-averaged static pressure and temperature, total pressure recovery, and maximum temperature are plotted in figure 7.14. Towards the rear, average pressure was constant while the large differences between mass- and stream-thrust-averaged values indicated large non-uniformity. Stream-thrust-averaged pressure and temperature were within 3% of the analytically predicted data. Total



**Table 7.4: Design parameters for reversed nozzle intakes truncated at their rear-side; all intakes designed for  $M_\infty = 8$ ,  $\delta = 0$ , and  $\Pi_{st} = 43$ .**

$CR_i$	$\Pi_{tot}$	$\Theta_{st}$	$L/h_{cc}$	$CR_o$
2.3 <sup>†</sup>	1.0	2.93	39.6	13.8
1.8	0.880	3.03	36.7	12.9
1.4	0.761	3.16	34.8	12.3
1.0	0.637	3.33	32.6	11.7

<sup>†</sup> no rear side truncation

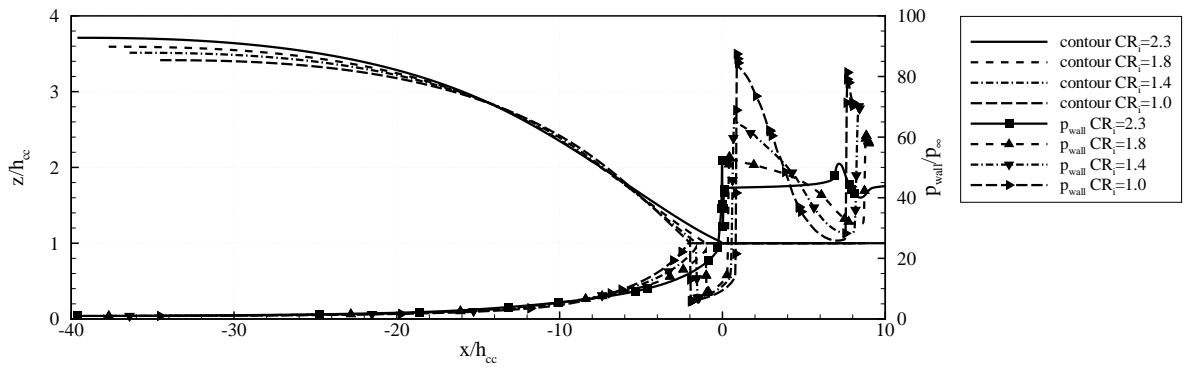


**Figure 7.12: Reversed nozzle intake contours along with wall pressure plots for increasing rear side truncation; all intakes designed for  $M_\infty = 8$ ,  $\delta = 0$ , and  $\Pi_{st} = 43$ .**

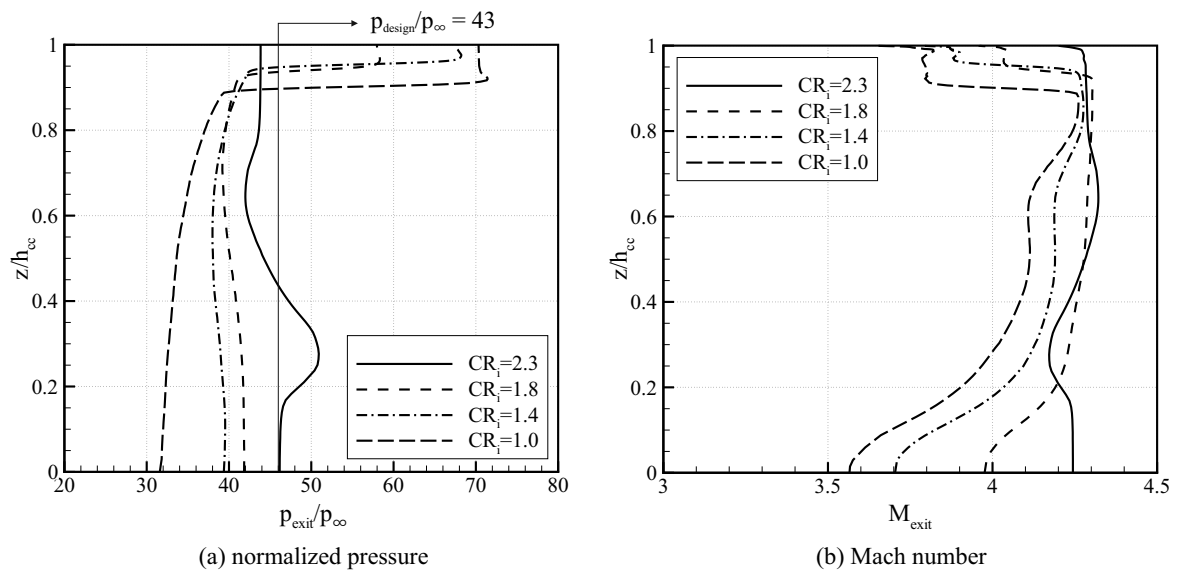


**Figure 7.13: Cross-stream pressure and Mach number of rear side truncated reversed nozzle intakes at outlet plane; all intakes designed for  $M_\infty = 8$ ,  $\delta = 0$ , and  $\Pi_{st} = 43$ .**

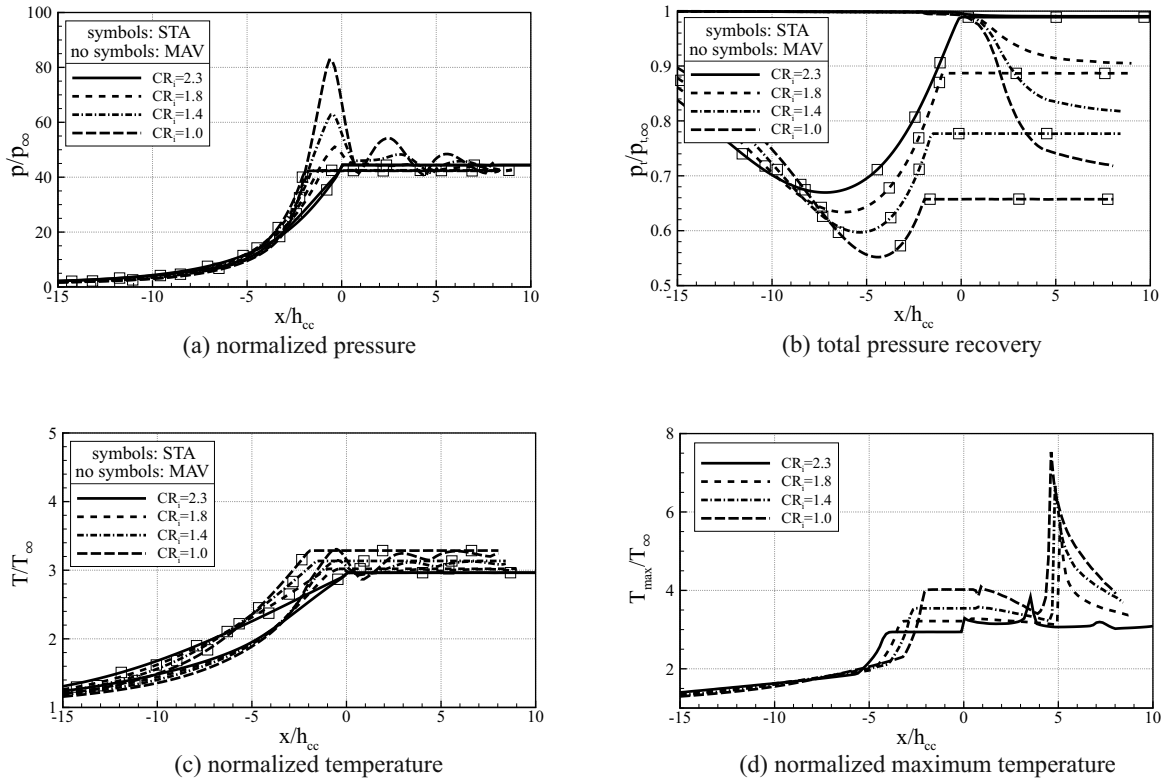


**Figure 7.14: Mass- and stream-thrust-averaged parameters and maximum temperature of rear side truncated reversed nozzle intakes; all intakes designed for  $M_{\infty} = 8$ ,  $\delta = 0$ , and  $\Pi_{st} = 43$ .**

pressure recovery decreased with lower  $CR_i$  due to the disturbed isentropic compression at the rear (figure 7.14(b)). Static temperature increased with lower  $CR_i$  and matched the analytical values (figure 7.14(c)). Interestingly, mass- and stream-thrust-averaged temperatures once again matched at locations where mass-averaged pressure had a local maximum and vice versa. Maximum temperature increased with more rear side truncation, which enhances ignition (figure 7.14(d)).

In conclusion, the stream-thrust analysis was a valid tool to predict the change in flow properties caused by the rear-side truncation. Non-uniformity increased with increasing rear-side truncation, which also decreased total pressure recovery. Temperature levels increased, which is beneficial for fuel-air ignition in a downstream combustor.

## 7.2 Validation of Approach to Viscous Effects

The approach to viscous effects, which was described in section 4.5, was validated by comparing analytical predictions to axisymmetric RANS simulations. First, Busemann flow fields and then reversed nozzle flow fields are discussed. Mach number was varied from 6 to 12 in steps of 2. The design intake pressure ratio was held constant at 43. The intake exit radius of the inviscid contour was fixed at 0.0294 m, thus the intake exit area was equal to the 3D-GRK intake. Input to the viscous correction and CFD was a constant wall temperature of 900 K and a turbulent wall boundary condition. Note that the resulting intake exit radii varied due to the viscous correction. Dynamic pressure was constant and therefore altitude, free stream pressure and temperature varied along the trajectory according to table A.1 in the appendix.

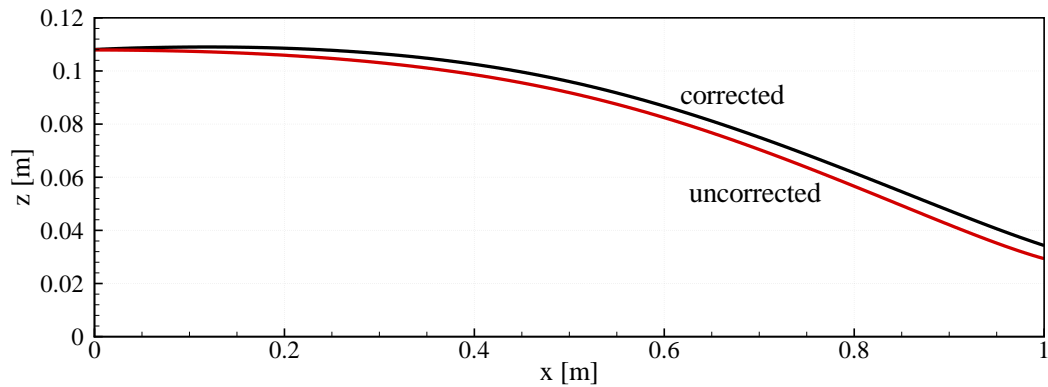


Figure 7.15: Busemann intake contours for Mach 8 case with and without viscous correction.

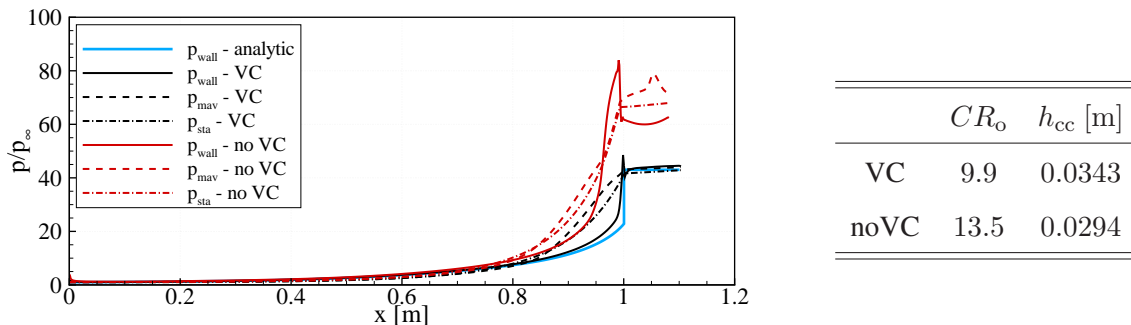


Figure 7.16: Normalized pressures for Mach 8 Busemann configurations with and without viscous correction plotted against  $x$ -coordinate.

### 7.2.1 Busemann Flow

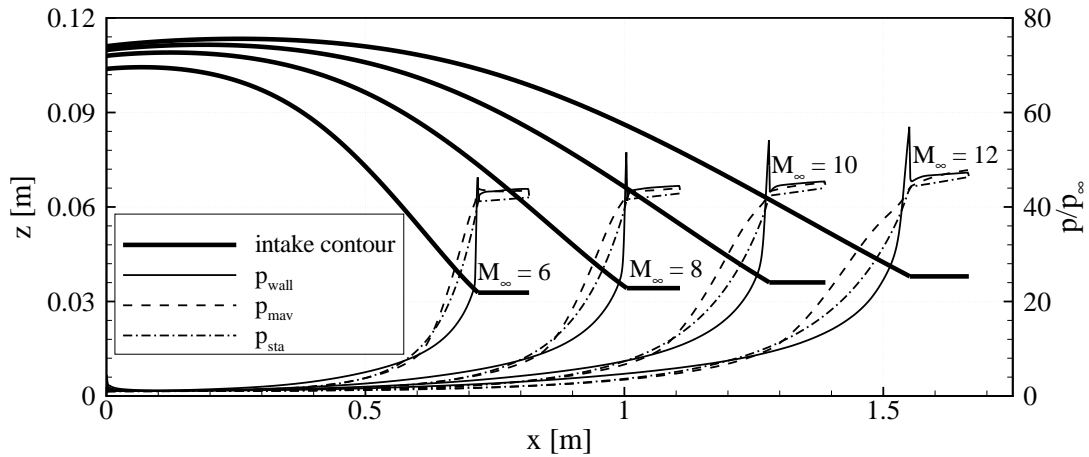
Results on viscous correction applied to Busemann flow fields were also published in [37, 38]. For the Mach 8 reference configuration two geometries are shown in figure 7.15; an uncorrected geometry and a corrected geometry. Shortly downstream of the leading edge the intake wall opened up in radial direction due the viscous correction. This caused a small expansion region, which usually disappeared when applying leading edge truncation. The intake contraction ratio was larger for the uncorrected contour, and the average intake exit pressure was  $\approx 60\%$  higher than the design pressure (figure 7.16). After applying the viscous correction, the intake contraction ratio decreased, which shifted intake exit pressures close to the design pressure. The deviation between numerically and analytically calculated pressure was lower than 5%. For a qualitative impression of the flow field a Mach number contour is given in the appendix (figure A.3).

As mentioned before, Mach number was varied from 6 to 12 in steps of 2 to extend the study to a broader velocity range. In table 7.5 analytical performance parameters are summarized and the following was observed. Contraction ratio decreased with Mach number; length increased with Mach number, which also caused a thicker boundary layer as can be seen from the increase in intake exit radius.

Figure 7.17 shows mass-averaged, stream-thrust-averaged and wall pressures extracted from CFD of the different intake configurations. Since no viscous correction was applied in the isolator pressures increased slightly in streamwise direction for all Mach numbers. In the isolator section stream-thrust-averaged pressures were lowest and could be regarded as a conservative pressure level. Nevertheless, all pressures were close to one another, which indicated little non-uniformity. The average pressure levels extracted from CFD were generally very close to the design pressure level, while only a slight increasing trend with Mach number was observed. At Mach 6 for example the deviation in mass-averaged static

**Table 7.5: Design parameters for Busemann intakes with viscous correction; all intakes designed for  $\Pi_{st} = 43$  and flight along constant dynamic pressure trajectory.**

$M_\infty$	$\Pi_{tot}$	$\Theta_{st}$	$h_{cc}$ [m]	$L/h_{cc}$	$CR_o$
6	0.567	3.41	0.0328	21.9	10.0
8	0.404	3.73	0.0342	29.4	9.9
10	0.280	4.11	0.0361	35.5	9.3
12	0.198	4.54	0.0380	40.8	8.5

**Figure 7.17: Normalized pressures extracted from Busemann intakes for various Mach numbers plotted against  $x$ -coordinate.**

pressure from design pressure was around 1%, and increased to 6% for Mach 12.

The influences of wall temperature and of intake size, thus Reynolds number, were investigated during another analysis by the author [37]. However, in the investigated ranges wall temperature and Reynolds number had minor influence on the results and therefore are excluded from this work.

### 7.2.2 Reversed Nozzle Flow

To verify the viscous correction for reversed nozzle flow fields, RANS simulations were performed on axisymmetric flow fields and results were compared to analytical predictions. For the Mach 8 reference condition two geometries are shown in figure 7.18; an uncorrected geometry and a corrected geometry. For the uncorrected contour the intake contraction ratio was larger and the average intake exit pressure was  $\approx 65\%$  higher than the design pressure (figure 7.19). After applying the viscous correction, the intake contraction ratio decreased, which also shifted intake exit pressures close to the design pressure. The deviation between numerically and analytically calculated pressure was lower than 5%. For a qualitative impression of the flow field, Mach number contour plots are given in the appendix (figure A.4).

During Mach number variation intake pressure ratio and free stream conditions were equal to the Busemann case. Findings were similar to the Busemann flow results. With Mach number contraction ratio decreased, while intake length and therefore boundary layer displacement thickness increased.

Figure 7.20 shows mass-averaged, stream-thrust-averaged and wall pressures extracted from CFD of the different intake configurations. The same trends as for the Busemann intakes were observed, meaning increasing pressure within the isolator, little non-uniformity and an accurate fit between pressures ex-

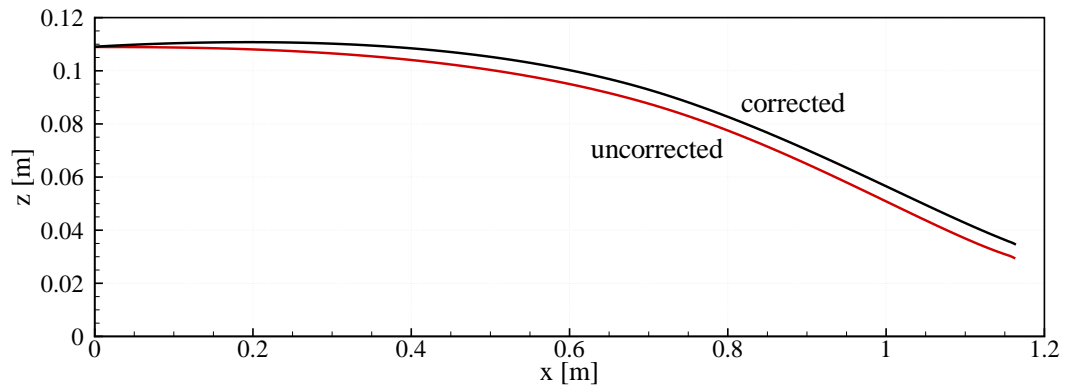
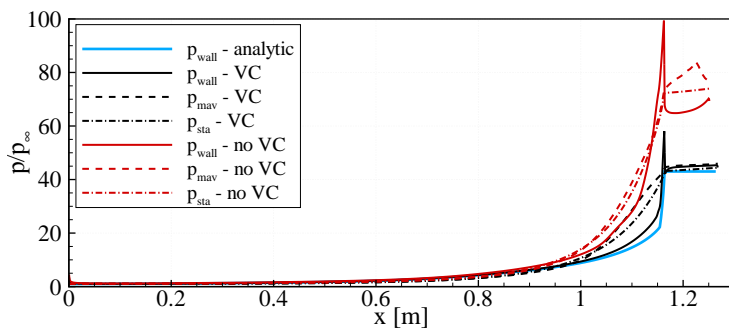


**Figure 7.18: Reversed nozzle contours for Mach 8 reference case with and without viscous correction.**

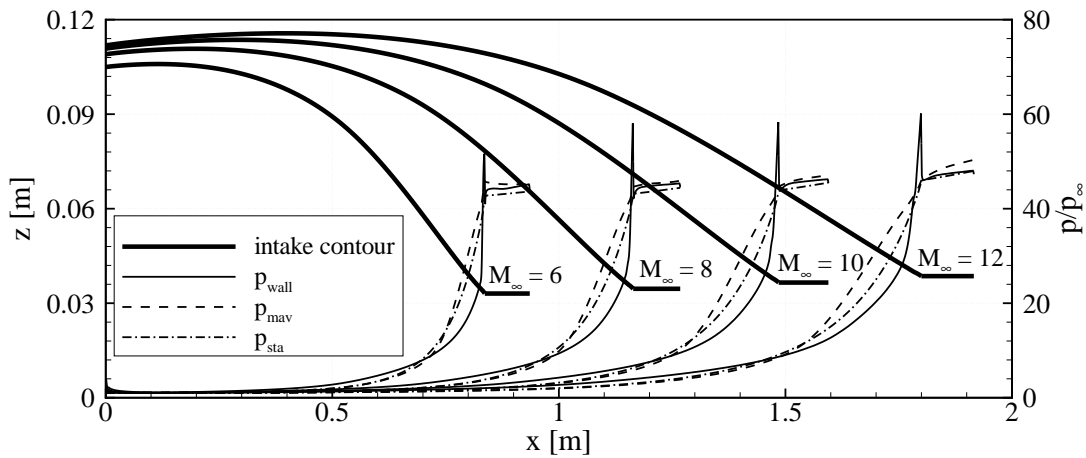


	$CR_o$	$h_{cc}$ [m]
VC	9.9	0.0346
noVC	13.8	0.0294

**Figure 7.19: Normalized pressures for Mach 8 reversed nozzle configurations with and without viscous correction plotted against  $x$ -coordinate.**

**Table 7.6: Design parameters for reversed nozzle intakes with viscous correction; all intakes designed for  $\Pi_{st} = 43$  and flight along constant dynamic pressure trajectory.**

$M_\infty$	$\Pi_{tot}$	$\Theta_{st}$	$h_{cc}$ [m]	$L/h_{cc}$	$CR_o$
6	0.555	3.44	0.0331	25.3	10.1
8	0.384	3.79	0.0346	33.6	9.9
10	0.259	4.21	0.0366	40.6	9.2
12	0.179	4.67	0.0386	46.6	8.4

**Figure 7.20: Normalized pressures extracted from reversed nozzle flows for various Mach numbers plotted against  $x$ -coordinate.**

tracted from numerical simulations and design pressure. The deviations between mass-averaged and design pressure ratio at the intake exit, for instance, increased from 5% for Mach 6 to 8% for Mach 12, and were therefore slightly larger than in the investigated Busemann cases.

In conclusion, calculating the displacement thickness with an integral method and widening the classical compression flow field was a valid approach to quantify viscous effects. Independent of the compression flow field in use, contraction ratio decreased with Mach number, while intake length and boundary layer thickness increased.

### 7.3 Comparison of Busemann Flow and Reversed Nozzle Flow

While in the previous section the intake generation tool was investigated with regard to the deviations between analytical and numerical values, the present section directly compares Busemann flows to reversed nozzle flows. Furthermore, intake performance parameters of the two flow fields are directly compared to gain further insight into their differences.

#### 7.3.1 Geometry

Figure 7.21 shows geometries of Busemann and reversed nozzle intakes with and without viscous correction, as well as the corresponding deflection angle of the uncorrected intake contours. The intakes were designed for a Mach 8 flight and a static pressure ratio of 43.

Generally, the two compression flow fields provided very similar results due to their large amounts of isentropic compression. The increase in contraction ratio due to viscous correction was approximately

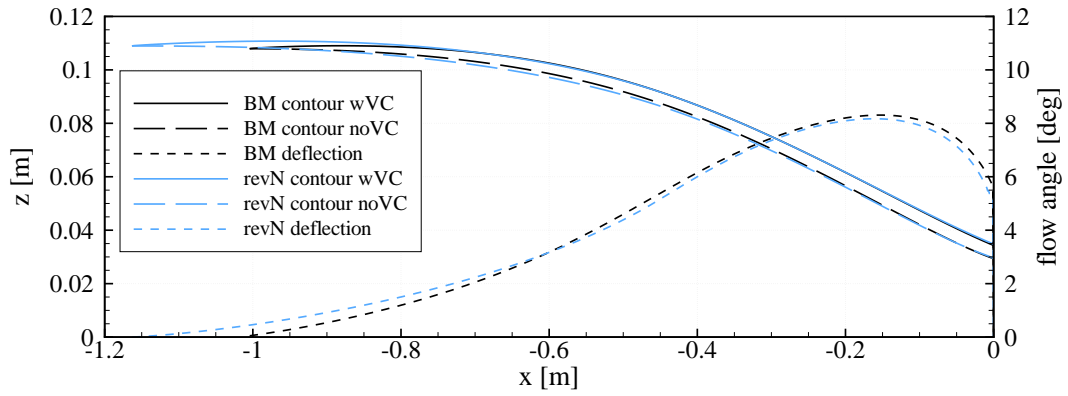


Figure 7.21: Geometry overview of Busemann and reversed nozzle geometry for Mach 8 condition.

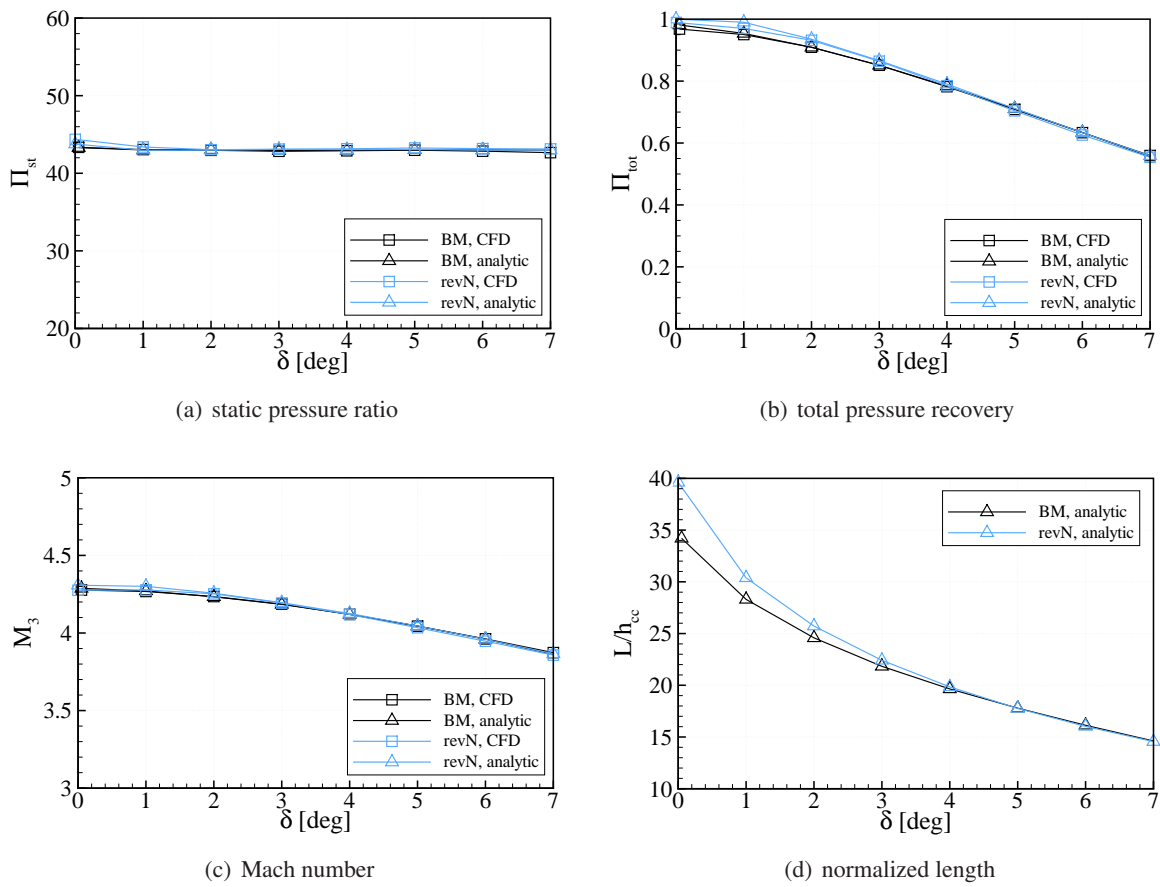


Figure 7.22: Intake performance parameters for leading edge truncation.

equal and the displacement thickness at the rear end was in both cases  $\approx 5$  mm, though slightly larger for the reversed nozzle case. The deflection angle increased gradually from a zero degree inflow, and the maximum deflection was independent of the flow field and constant at 8 deg. Intake lengths, however, were different, as the reversed nozzle contours always exceeded the Busemann geometries. In viscous simulations the longer geometries and therefore higher friction drag of reversed nozzle intakes counteracted the benefit of the fully isentropic compression.

### 7.3.2 Leading Edge Truncation

To compare the Busemann and reversed nozzle intakes under the influence of leading edge truncation, stream-thrust-averaged values were extracted from the outlet plane of the numerical domain, along with analytical results for increasing truncation angles. These values are plotted in figure 7.22. Simulations and analytical values were for inviscid flow.

Overall, numerical and analytical values fit accurately for all parameters shown. For  $\delta < 4$  deg total pressure was slightly higher for the reversed nozzle case but equal for larger truncation angles (figure 7.22(b)). Exit Mach numbers for both flow fields were equal (figure 7.22(c)) and directly corresponded to a match in static temperature. For  $\delta < 4$  deg reversed nozzle intakes were longer, and for the non-truncated case the reversed nozzle intake exceeded the Busemann intake by  $\approx 5 \times h_{cc}$  (figure 7.22(d)). Intake length was equal for both compression flow fields for  $\delta > 4$  deg.

### 7.3.3 Rear Side Truncation

To compare the Busemann and reversed nozzle intakes under the influence of rear side truncation, in figure 7.23 stream-thrust-averaged values extracted from the outlet plane of the numerical domain are plotted along with analytical results. Simulations and analytical results were performed for inviscid flow. Maximum rear side truncation resulted in a constant length reduction of  $6 \times h_{cc}$  (figure 7.23(d)). For constant length reduction the total pressure recovery dropped to a constant value, independent of the flow field. E.g. the maximum length reduction caused a  $\Pi_{tot}$  of 0.65 for both compression flow fields (figure 7.23(b)). The trend was similar on Mach number (figure 7.23(c)). Finally, the length reduction for the rear side was not as effective as for the leading edge case, and the reversed nozzle geometries always exceeded the Busemann geometries in length.

### 7.3.4 Viscous Effects

The two flow fields were compared for different Mach numbers in viscous flow. Stream-thrust-averaged results were extracted from the outlet of the numerical domain and plotted against Mach number along with the analytically predicted values for inviscid and viscous flow (figure 7.24). The intakes were designed for a constant pressure ratio of 43 along a constant dynamic pressure trajectory. A viscous correction was applied for a turbulent wall at a constant temperature,  $T_{wall} = 900$  K.

Static pressure in CFD simulations increased slightly with Mach number, while the reversed nozzle cases were always larger than the Busemann flow fields by  $\approx 2$  (figure 7.24(a)). These increased pressure levels also caused higher temperatures (figure 7.24(d)). Presumably the integral method became less valid with increasing Mach number. Normalized static temperatures for inviscid cases were independent of the flow field and at a constant level of  $\approx 2.9$ . When considering viscosity, temperatures increased, while the reversed nozzle intakes had slightly higher values. Temperatures were slightly under-predicted in the analytical tool. Finally, the deviation between numerical and analytical total pressure was small, while total pressure for the Busemann intakes was slightly larger due to the shorter geometries and therefore lower skin friction (figure 7.24(b)). This also led to slightly higher Mach numbers at the intake exit for the Busemann intakes (figure 7.24(c)).



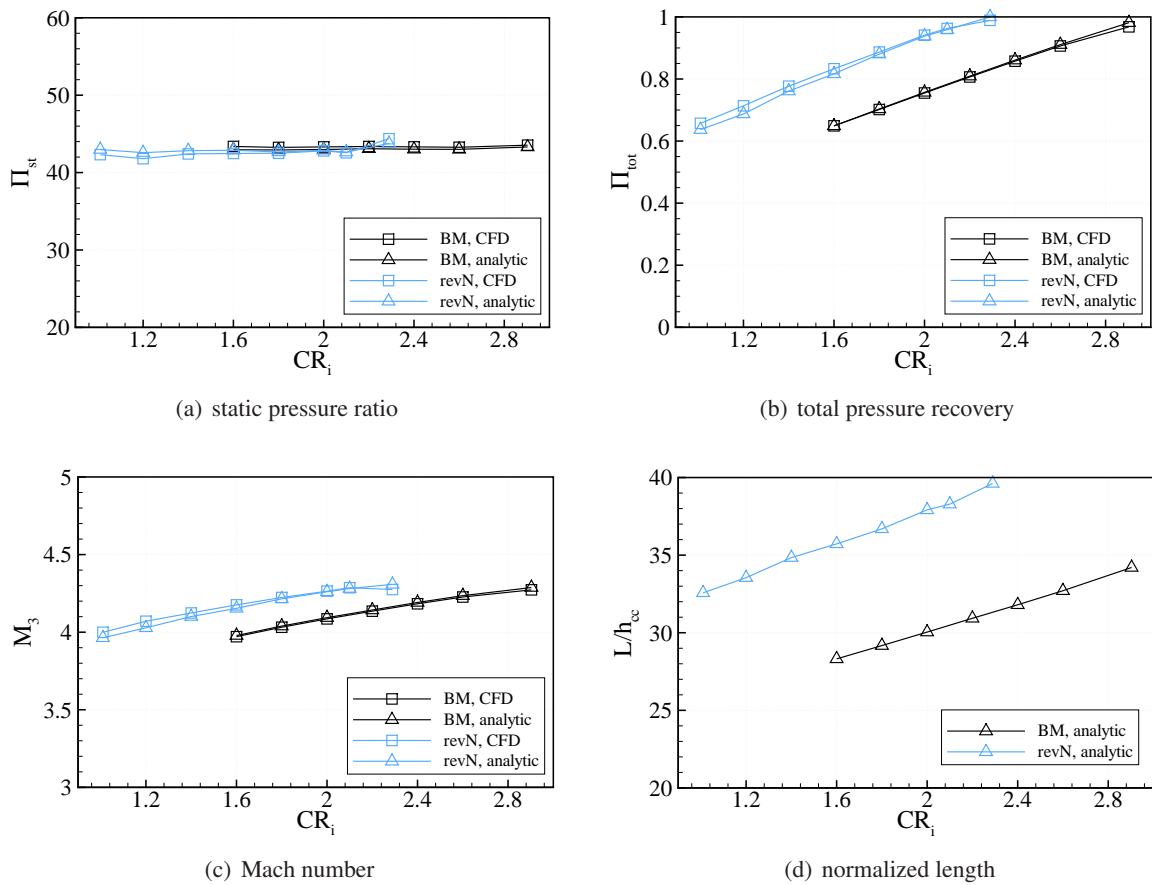


Figure 7.23: Intake performance parameters for rear side truncation.

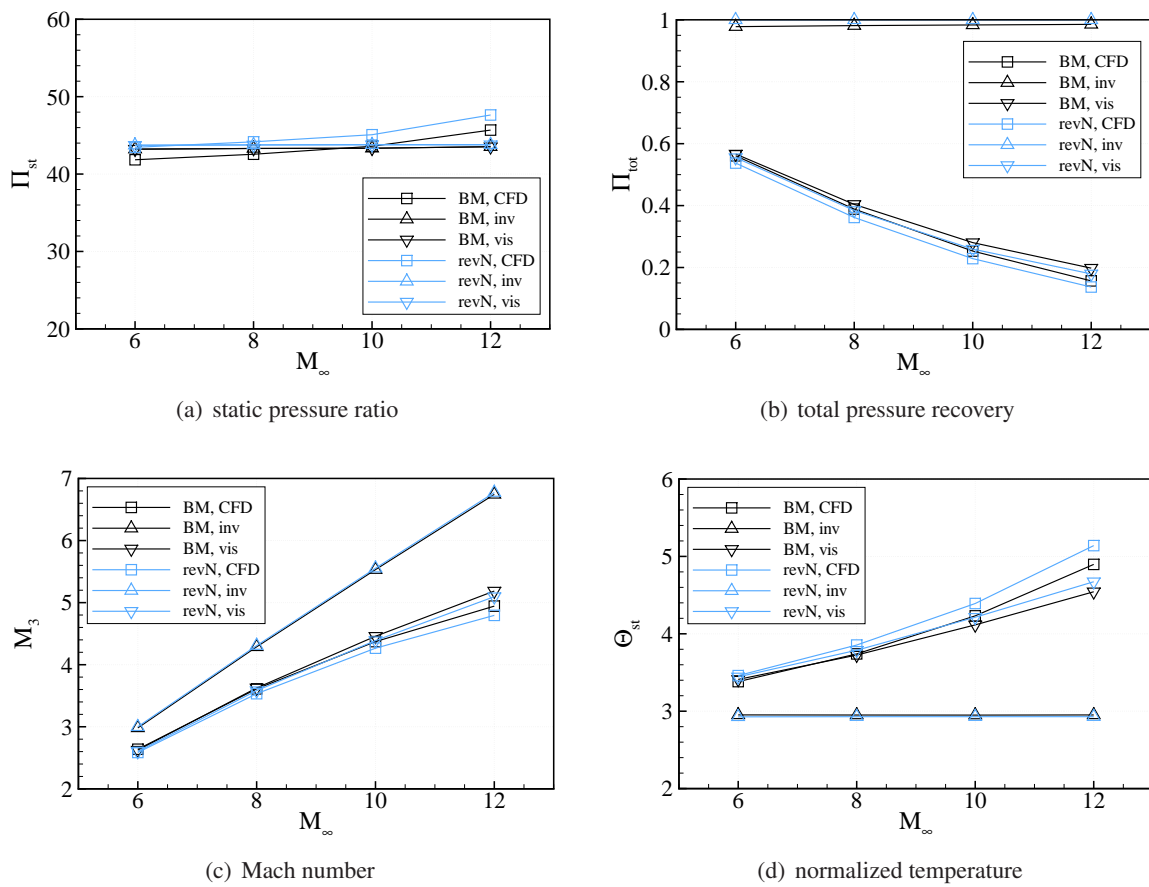


Figure 7.24: Intake performance parameters for Mach number variation.

### 7.3.5 Superimposed: Leading Edge Truncation and Viscous Effects

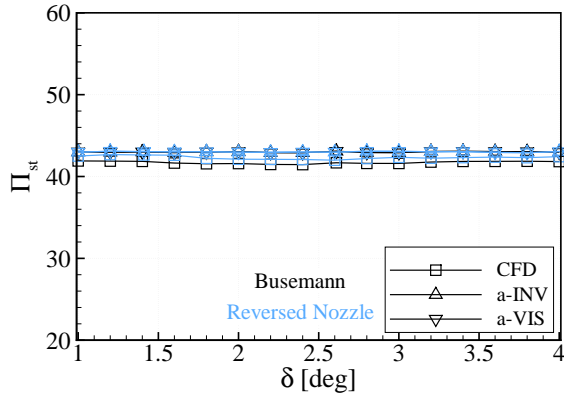
After analyzing truncation and viscous effects separately, both effects were superimposed by varying leading edge truncation and applying viscous correction simultaneously. As a result CFD simulations were compared with the analytical predictions in order to study intake performance and to more thoroughly validate the intake design tool. For this purpose intakes were designed for Mach 8 flight at an altitude of 30 km and for  $\Pi_{st} = 43$ . Ogawa [75] reported a weak maximum in total pressure around 2 deg, and therefore  $\delta$  was varied between 1 deg and 4 deg in steps of 0.2 deg. The inviscid configurations were scaled to an intake exit radius of 0.0294 m and the viscous correction was applied for a turbulent wall at 900 K. Performance parameters were calculated according to section 4.6 and heat losses into the intake wall were considered.

Figure 7.25 shows exit properties of static and total pressure and temperature, as well as overall contraction ratios and normalized drag forces in  $x$ -direction ( $F_{x,\text{norm}} = F_x / (\dot{m}a)_\infty$ ). The Busemann and reversed nozzle intakes are indicated by black and blue coloring, respectively, while inviscid and viscous analytical results are abbreviated by a-INV and a-VIS, respectively. Altogether the match between CFD and analytic results was good and the two flow fields revealed very little differences.

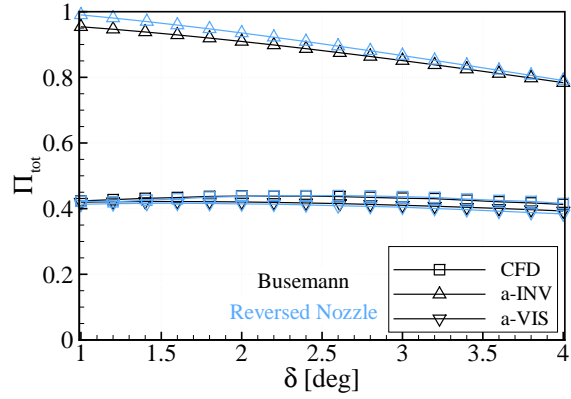
As shown, static pressure ratio was constant at 43, while the CFD Busemann and CFD reversed nozzle configurations were consistently lower by 3.5% and 2.3%, respectively (figure 7.25(a)). Total pressure recoveries dropped drastically from values  $> 0.8$  for inviscid configurations to values slightly larger 0.4 for viscous configurations. Similar to Ogawa, only a weak maximum in total pressure recovery was detected (figure 7.25(b)). The corresponding truncation angle varied slightly between 2.5 deg and 2 deg for CFD and analytical values, respectively. Nevertheless, it is stressed that the difference between maximum and minimum total pressure recovery was only 0.02 – 0.03 for the  $\delta$ -range investigated, and that the maximum was very weak. Wall heat losses were modeled correctly by the Reynolds analogy and a constant drop in total enthalpy by  $\approx 2\%$  was detected in CFD as well as analytically (figure 7.25(d)). If viscosity was considered, static temperature ratio increased (figure 7.25(c)) to around 3.7, which corresponded to an average intake exit temperature of  $\approx 840$  K. CFD simulations resulted in temperatures slightly lower ( $\Theta_{st} = 3.6$ ). While the leading edge truncation without viscous correction lead to a decrease in overall contraction ratio with truncation angle, the geometry modification by the viscous contraction counteracted this effect and reduced overall contraction ratio to a constant value of  $\approx 10.2$  (figure 7.25(e)). Finally, normalized drag forces in  $x$ -direction are shown (figure 7.25(f)). A subdivision into pressure and viscous portions revealed, that skin friction and pressure drag were responsible for 1/3 and 2/3 of the total drag, respectively.

### 7.3.6 Evaluation and Summary

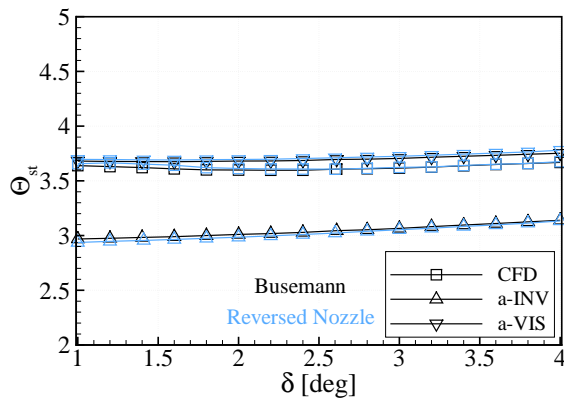
The analytical design tool developed in the frame of this work was used to design Busemann and reversed nozzle intakes. The two axisymmetric flow fields were extensively validated with CFD simulations for various Mach numbers and degrees of leading edge and rear side truncation. Overall the agreement between CFD and analytical prediction was good, while maximum deviations of 3% and 8% were observed for inviscid (truncation effects) and viscous cases, respectively. Only a weak maximum in total pressure recovery was detected for  $2.0 < \delta < 2.5$ . The performance of the reversed nozzle and Busemann flow fields differed only marginally from one another. The generally larger amount of isentropic compression of the reversed nozzle flow was compensated for by the shorter length, and therefore lower skin friction, of the Busemann flow. Total pressure recovery for a certain configuration was therefore approximately independent of the flow field in use. Therefore, it was decided to use only one flow field for subsequent analysis of fully three-dimensional, streamline traced intakes. Since the design tool generally ran more robust while solving the Taylor McColl equations, the Busemann flow was used as the underlying flow field for the remainder of this work.



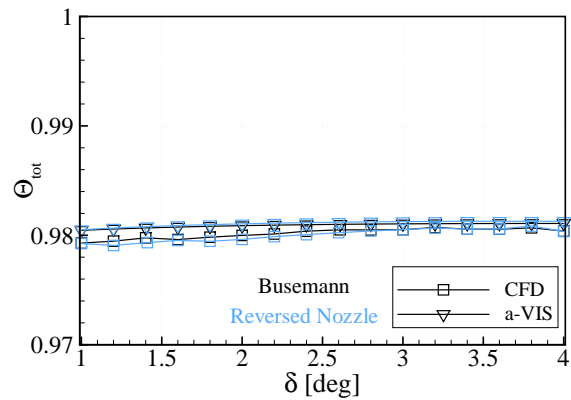
(a) static pressure ratio



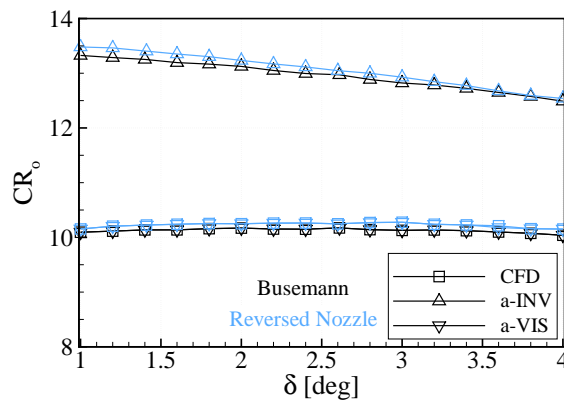
(b) total pressure recovery



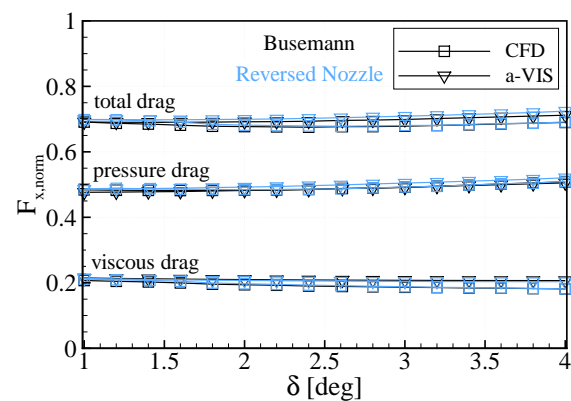
(c) static temperature ratio



(d) total temperature ratio



(e) overall contraction ratio



(f) drag forces

**Figure 7.25: Intake performance parameters for leading edge truncation with viscous correction.**

## 7.4 Streamline Traced Intakes

In the present section, numerical results of the three streamline traced intake configurations ST1, ST2 and ST3 are presented. All configurations were designed for Mach 8 flight at an altitude of 30 km and for a static pressure ratio of 43. Please refer to section 6.1 for detailed information.

### 7.4.1 ST1 Intake

Numerical results of the streamline traced ST1 configuration, which was truncated at the leading edge only and is described in 6.1.2, are summarized in the present section. Figure 7.26 was extracted from a numerical simulation for Mach 8 flight at a free stream pressure and temperature of 1170 Pa and 226 K, respectively and shows three pieces of information.

First, the Mach number contour of the symmetry plane is plotted to give an impression of the general flow field. The main ramp shock and portions of the isentropic compression were clearly visible. The main ramp shock hit underneath the cowl and caused a separation zone. Second, for the symmetry plane wall pressures along the ramp and cowl side are plotted. Wall pressure on the ramp side gradually rose until  $x = 0.625$  m where a sharp pressure decline, caused by the expansion corner, followed. Furthermore, the analytical wall pressure distribution is plotted along the ramp side and is slightly larger than the pressure level extracted from CFD. On the cowl side, wall pressure increased sharply due to the incoming main ramp shock, and small pressure fluctuations were present in the wake of the separation region. Due to the reflected ramp shock within the isolator wall pressures on each side were different, which indicated a non-uniform flow field. Third, mass- and stream-thrust-averaged pressures are plotted for the internal portions ( $x > 0.428$  m). After a smooth increase average pressure reached a maximum while mass-averaged pressure always exceeded stream-thrust-averaged pressure. Maximum stream-thrust-averaged pressure was reached at the intake throat ( $x = 0.65$  m,  $\Pi_{st} = 45.8$ ). Maximum mass-averaged pressure was reached further upstream ( $x = 0.641$  m,  $\Pi_{st} = 49.2$ ). Thus, stream-thrust- and mass-averaged pressure were within 6.5% and 14.4% of the design value, respectively.

In addition to the averaged pressures, in figure 7.27 other averaged properties are shown for the internal portion of the intake along with a density gradient contour plot. Within the isolator, Mach number and normalized temperature were approximately constant at their minimum and maximum values of 3.4 and 4.1, respectively. Total pressure decreased gradually while the mass-averaged value exceeded the stream-thrust-averaged one. At the intake throat mass-averaged and stream-thrust-averaged total pressure were 0.447 and 0.299, respectively. Table 7.7 compares stream-thrust-averaged variables, extracted at the throat plane with variables from the design tool. The largest difference was in static pressure ratio ( $\Delta = 6.5\%$ ), followed by total pressure ratio ( $\Delta = 3.6\%$ ). Temperature and Mach number were predicted within 0.5% and 2.0% of their design values, respectively.

The density gradient (figure 7.27) illustrated the location of shocks within the symmetry plane. The final "conical" shock of the Busemann flow field impinged on the expansion corner on the ramp side wall and reflected only weakly. Note that the term "conical" was only used as an artifact from the axisymmetric flow field, because it was assumed that the shock structure was fully three-dimensional. Furthermore, the main ramp shock hit the ramp side at  $x = 0.5$  m and was reflected down the isolator as a shock train.

Finally, figure 7.28(a) shows normalized pressure, extracted from CFD at the cross-stream plane  $x = 0.722$  m, which was comparable to the rake location of the 3D-GRK intake. The difference between highest and lowest pressure ratio occurred near the center, and was approximately 30. The temperature profile, which is given in the appendix (section A.6), appeared more uniform, and a local hot spot occurred near the ramp side and was around 1400 K.

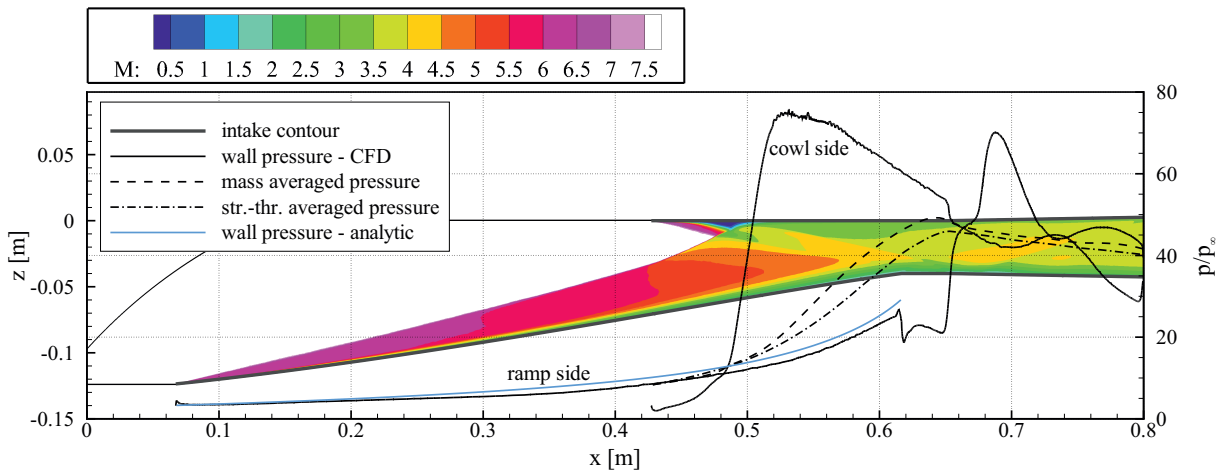


Figure 7.26: Wall pressure, averaged pressure, and Mach number contour plot extracted from CFD for ST1 intake configuration for on-design condition.

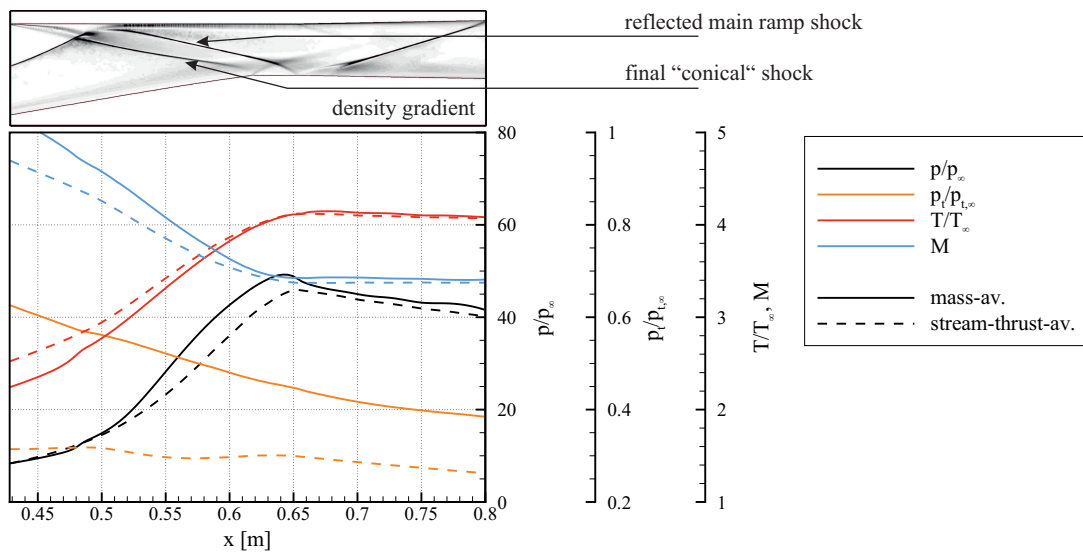
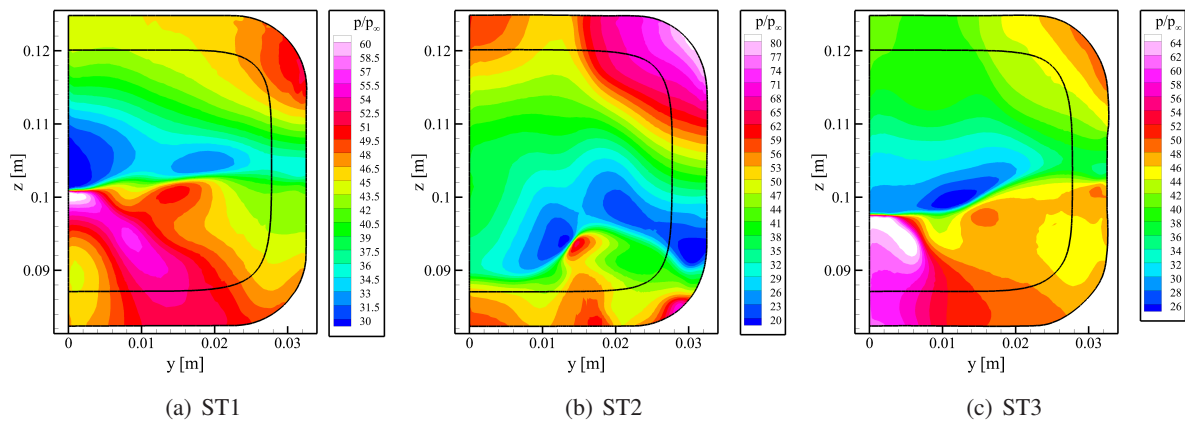


Figure 7.27: CFD-schlieren plot and averaged variables extracted from internal portion of ST1 intake configuration for on-design condition.

Table 7.7: Stream-thrust-averaged data extracted from CFD at intake throat ( $x = 0.65$  m) compared to tool predictions for ST1, ST2, and ST3 on-design conditions.

	$\Pi_{st}$			$\Pi_{tot}$			$\Theta_{st}$			$M_{th}$		
	tool	CFD	$\Delta, \%$	tool	CFD	$\Delta, \%$	tool	CFD	$\Delta, \%$	tool	CFD	$\Delta, \%$
ST1	43.0	45.8	6.51	0.311	0.299	3.56	4.10	4.12	0.49	3.44	3.37	2.03
ST2	43.0	45.2	5.12	0.295	0.300	1.69	4.15	4.11	0.96	3.41	3.39	0.59
ST3	43.0	44.4	3.26	0.311	0.311	0.28	4.10	4.04	1.46	3.44	3.42	0.58



**Figure 7.28: Normalized pressure on cross sectional planes of ST1, ST2, and ST3 configuration for Mach 8, extracted from CFD at  $x = 0.722$  m.**

### 7.4.2 ST2 Intake

#### *ST2 Intake – On-Design*

Numerical results of the streamline traced ST2 configuration, which was truncated at the leading edge and the rear and which was described in 6.1.3, are summarized in the present section. Illustration and discussion of the results, as well as numerical reference conditions are analogous to the previous section. Figure 7.29 shows a Mach number contour plot of the symmetry plane along with the corresponding wall pressures. Furthermore, averaged pressures within the internal portion of the intake are displayed. The shock hit slightly underneath the cowl at  $x = 0.55$  m. The size of the separation zone was smaller compared to the separation region of the ST1 configuration, because of the lower leading edge truncation and therefore weaker ramp shock. Wall pressures were similar to the ST1 wall pressures, but on the cowl side pressures reached values as high as  $\Pi_{st} = 100$ . Analytical and numerical wall pressure on the ramp side agreed well, while the analytical value slightly exceeded the numerical one. Again, wall pressures on each side wall were different, which indicated non-uniformity. The stream-thrust-averaged pressure was maximum at the intake throat ( $x = 0.65$  m), while the mass-averaged pressure had a maximum further downstream ( $x = 0.665$  m). Near the throat location, mass-averaged pressure ratio exceeded stream-thrust-averaged pressure ratio by  $\approx 15$ , which is a sign of large non-uniformity. Maximum stream-thrust- and mass-averaged pressure were 45.2 and 62.3, respectively. Thus, stream-thrust- and mass-averaged pressure were within 5.1% and 44.9% of the design value, respectively.

Additional averaged parameters are plotted in figure 7.30, along with a density gradient contour plot of the internal part of the intake. In the isolator, Mach number and normalized temperature reached a constant level of about 3.5 and 4.1, respectively. Total pressure gradually decreased and at the intake throat mass- and stream-thrust-averaged total pressure were 0.532 and 0.300, respectively. Table 7.7 compares stream-thrust-averaged variables, extracted at the throat plane to variables from the design tool. The largest difference was in static pressure ratio ( $\Delta = 5.1\%$ ), followed by total pressure ratio ( $\Delta = 1.7\%$ ). Temperature and Mach number were predicted within 1.0% and 0.6% of their design values, respectively.

In the density gradient (figure 7.30) the final "conical" shock could be identified, and did not hit the expansion corner due to the geometry changes introduced by the rear side truncation. The main ramp shock was reflected from the cowl side and marched down the isolator. A large expansion region ( $0.64 \text{ m} < x < 0.69 \text{ m}$ ), caused by the rear side truncation, existed on the ramp side and introduced strong non-uniformity.

Finally, figure 7.28(b) shows normalized pressure, extracted from CFD at the cross-stream plane  $x =$

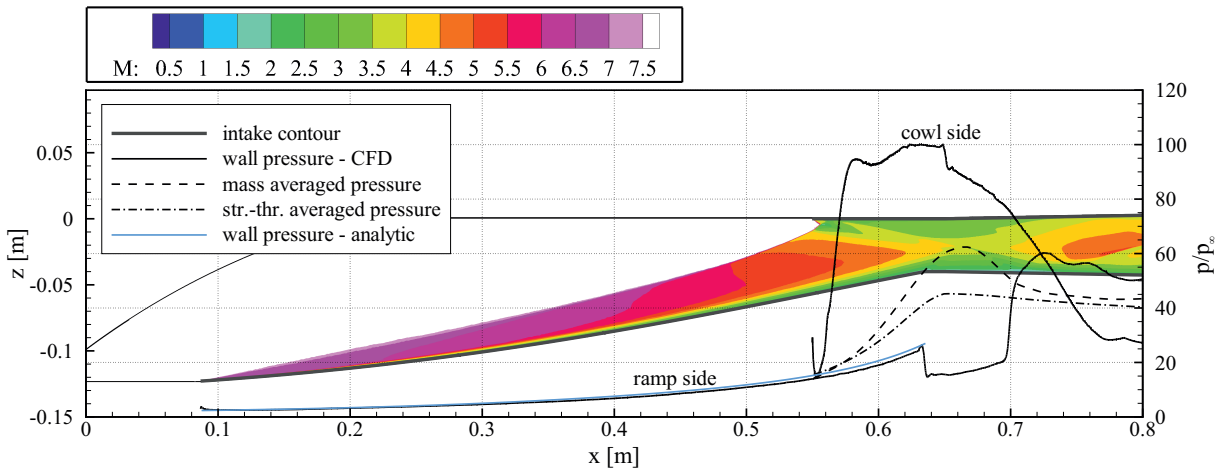


Figure 7.29: Wall pressure, averaged pressure, and Mach number contour plot extracted from CFD for ST2 intake configuration for on-design condition.

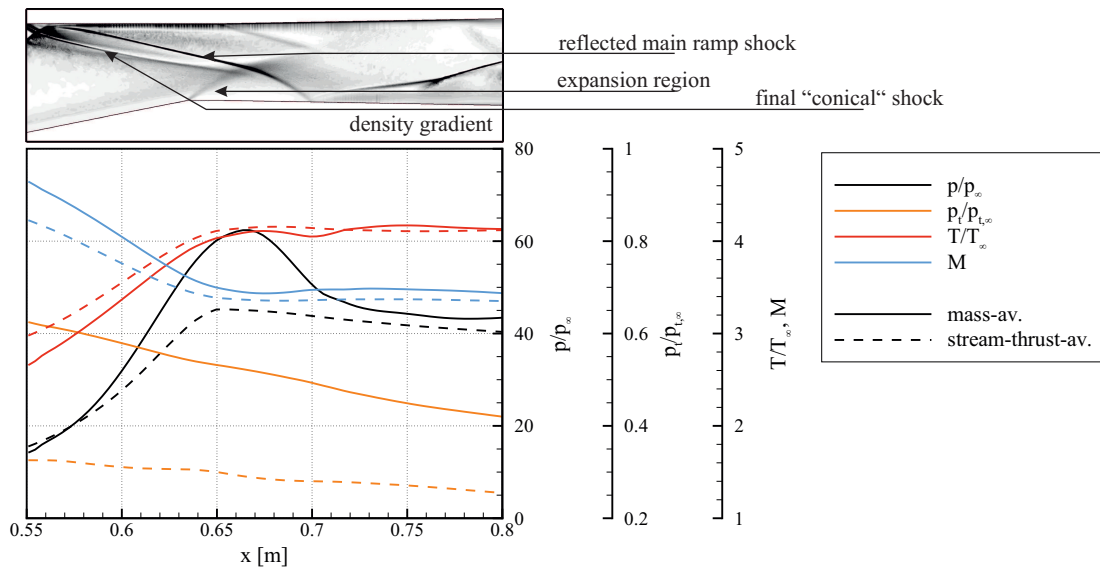


Figure 7.30: CFD-schlieren plot and averaged variables extracted from internal portion of ST2 intake configuration for on-design condition.



0.722 m, which was comparable to the rake location of the 3D-GRK intake. The difference between highest and lowest pressure ratio was approximately 60 and resembled the configuration with the largest non-uniformity. The temperature profile, which is given in the appendix, appeared more uniform, and a local hot spot occurred near the ramp side and was around 1800 K.

### *ST2 Intake – Off-Design*

The streamline traced ST2 fixed geometry intake was investigated for the off-design Mach numbers 7 and 6. Flight conditions were adjusted to a constant dynamic pressure trajectory  $q_\infty = 0.5$  bar. An analytical estimate could not simply be developed for a fixed geometry at off-design condition. Therefore, one had to rely upon CFD to determine intake performance.

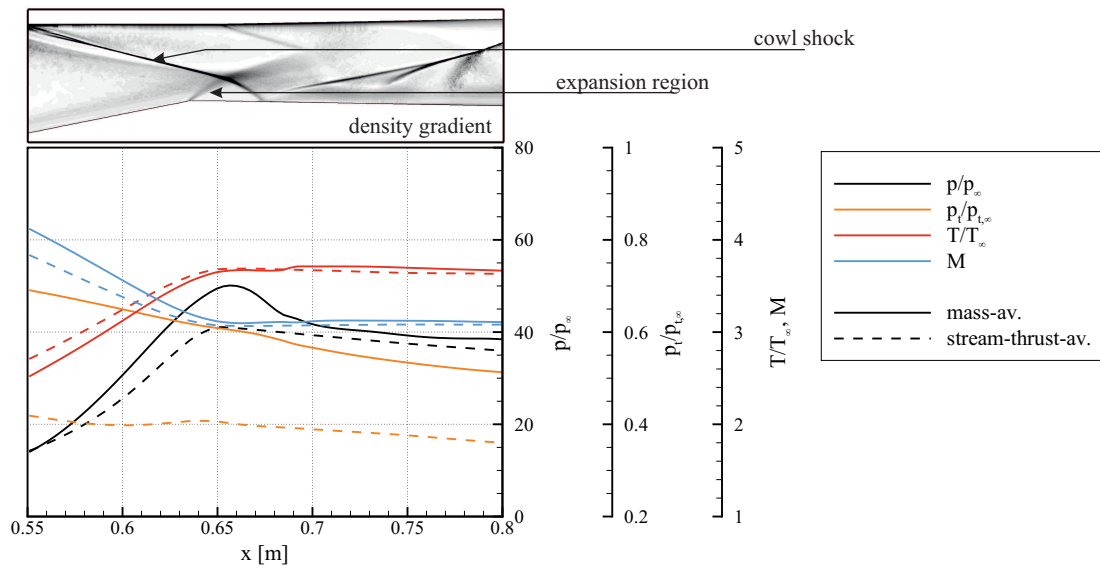
In figure 7.31 and 7.32 CFD schlieren images and averaged variables, extracted from numerical simulations, are plotted for the internal portion of the intake. The shock structure was different due to lower shock losses for decreasing Mach number. The main ramp shock did not hit underneath the intake cowl, which indicated spillage mass flow. Furthermore, the main ramp shock was not reflected, but rather a cowl shock formed and traveled down the isolator. The expansion region that was relatively large in the ST2 on-design case decreased with Mach number, which indicated more uniform flow. No conical shock was visible, presumably due to the off-design nature of the lower speed flow field. Mass- and stream-thrust-averaged Mach number, pressure and temperature ratio generally decreased, while the total pressure level increased with free stream Mach number. The variables followed a similar trend, namely approximately constant Mach number and temperature in the isolator, a maximum in static pressure near the intake throat, and a monotonic decline in total pressure for  $x > 0.65$  m. The difference between mass- and stream-thrust-averaged pressure, thus the level of non-uniformity, dropped with Mach number. Figure 7.33 shows cross-stream planes of normalized pressure, extracted from CFD at  $x = 0.722$  m, which corresponded to the rake location of the 3D-GRK intake. Due to the different shock positions in streamwise direction, the general pattern of the cross-stream planes varied with Mach number. Strong non-uniformity was present, which reduced with Mach number. For instance the maximum differences between highest and lowest static pressure ratio were 60, 32, and 23 for free stream Mach numbers of 8, 7, and 6, respectively. Temperature contour plots of the configurations can be found in the appendix and were generally more uniform. Maximum static temperature was always  $> 1000$  K, and decreased with Mach number from 1900 K to 1470 K and 1150 K for free stream Mach numbers of 8, 7, and 6, respectively.

### **7.4.3 ST3 Intake**

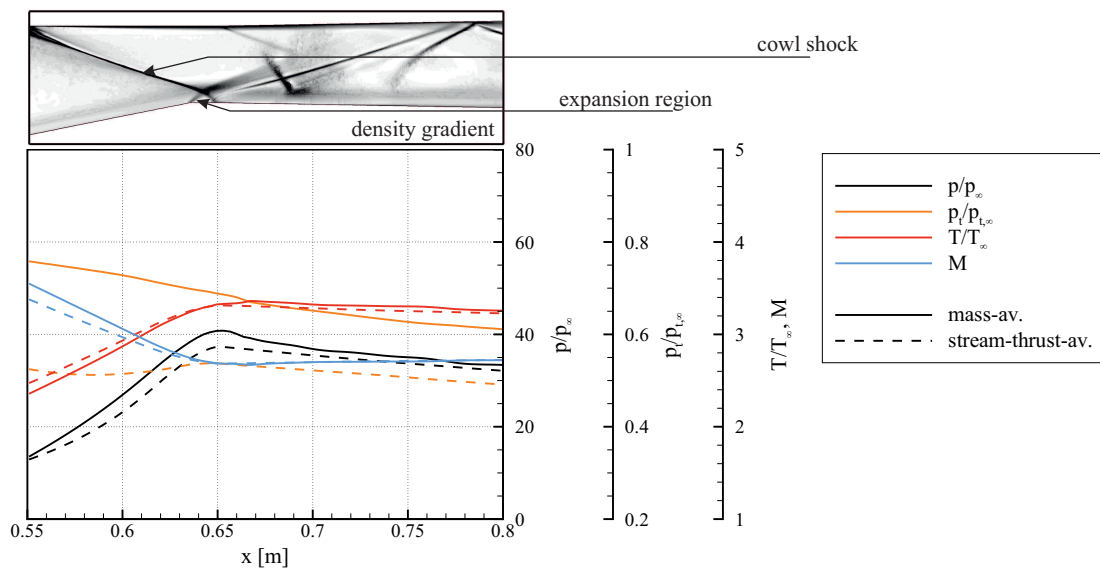
Numerical results of the streamline traced ST3 configuration, which was translated in streamwise direction and described in section 6.1.4, are summarized in the present section. Illustrations and discussion of the results, as well as numerical reference conditions, are analogous to the previous sections.

Figure 7.34 was extracted from a numerical simulation for Mach 8 flight and shows three pieces of information. First, a Mach number contour plot of the symmetry plane gives a general impression of the flow field. As intended by the translation in streamwise direction, the ramp shock did not hit under the intake cowl, and therefore a spillage flow was present. Furthermore, no separation region was detected underneath the intake cowl. Second, wall pressures along the cowl and ramp side are plotted. On the ramp side, pressure gradually increased while the analytical values exceeded the numerical ones. On the cowl side, a pressure peak was followed by a sharp decrease in pressure. This favorable pressure gradient hindered the development of separation. Third, mass- and stream-thrust-averaged pressures are shown for the internal portion of the intake. A maximum in pressure occurred near the throat and was followed by a gradual pressure decrease. Stream-thrust-averaged pressure was always lower than mass-averaged pressure.

A close-up of the internal portion and of other averaged variables is given in figure 7.35. The maximum stream-thrust- and mass-averaged pressures were 44.4 and 50.6, respectively, which corresponded to a



**Figure 7.31: CFD-schlieren plot and averaged variables extracted from internal portion of ST2 intake configuration for Mach 7 off-design condition.**



**Figure 7.32: CFD-schlieren plot and averaged variables extracted from internal portion of ST2 intake configuration for Mach 6 off-design condition.**

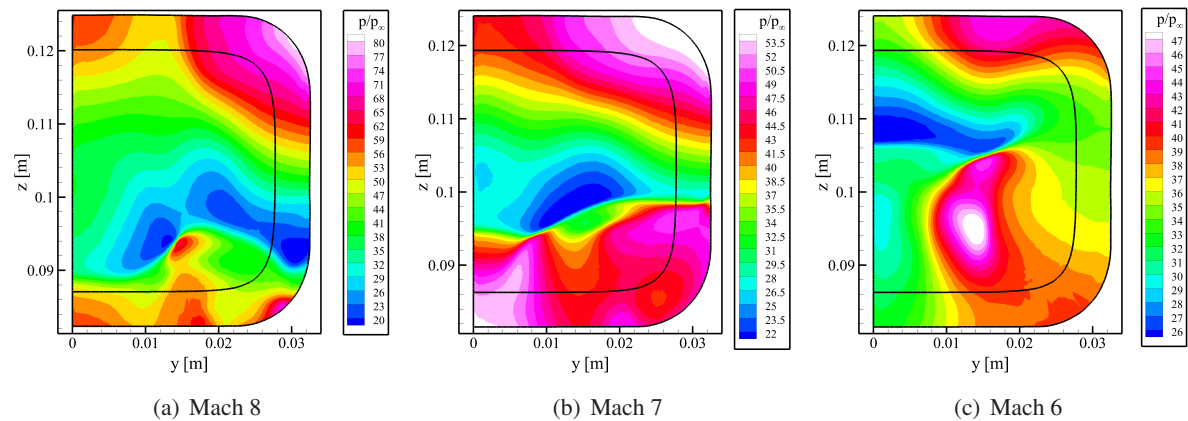


**Figure 7.33: Normalized pressure on cross sectional planes of ST2 configuration for different Mach numbers, extracted from CFD at  $x = 0.722$  m.**

deviation from the design value of 3.3% and 17.7%, respectively. The maximums were very close to the intake throat, while the stream-thrust-averaged maximum was slightly downstream ( $x = 0.652$  m) of the mass-averaged peak ( $x = 0.648$  m). In the isolator, Mach number and normalized temperature were approximately constant at 4.0 and 3.5, respectively. Downstream of the intake throat, total pressure recovery linearly decreased, while mass-averaged total pressure always exceeded stream-thrust-averaged values. Table 7.7 compares stream-thrust-averaged variables, extracted at the throat plane with variables from the design tool. As before the largest difference was in static pressure ratio ( $\Delta = 3.3\%$ ). Total pressure, static temperature, and Mach number were predicted within 0.3%, 0.5%, and 2.0% of their design values, respectively.

In figure 7.35 the density gradient, extracted from the symmetry plane, is shown for the internal portion of the intake. Since the ramp shock passed the intake cowl, no reflected ramp shock was visible. Instead, a cowl shock formed, impinged on the ramp side and traveled down the isolator. A small expansion region was visible, which was smaller in size than in the ST2 case. This indicated more uniform flow than in the rear side truncated ST2 intake configuration.

Finally, figure 7.28(c) shows normalized pressure in the cross-stream plane, extracted from CFD at  $x = 0.722$  m, which was comparable to the rake location of the 3D-GRK intake. The difference between highest and lowest pressure ratio occurred near the center, and was approximately 38. The temperature profile, which is given in the appendix, appeared more uniform, and a local hot spot occurred near the ramp side and was around 1500 K.

#### 7.4.4 Summary

The streamline traced intakes were investigated numerically at their Mach 8 design condition. In addition, the ST2 configuration was examined at the off-design Mach numbers 7 and 6. For all intakes at design Mach number the performance parameters extracted from CFD were within 7% of the analytical predictions. The overall intake performance was similar due to the identical design condition. Therefore, the specific modifications to the ST1 – ST3 geometries had only little influence on overall performance. On a more detailed level, however, the following differences were observed. For the ST1 configuration, the ramp shock hit underneath the intake cowl which should be avoided due to larger aerodynamic and heat loads. Furthermore, internal contraction was with 3.06 too high for self-starting. The ST2 configuration had internal contraction in the range where self-starting for Mach 8 was expected. However, intake exit flow was highly non-uniform. The ST3 configuration also had low internal contraction and also more uniform exit flow. In turn, due to the different translation in streamwise direction an additional axisymmetric CFD simulation was necessary during the intake design.

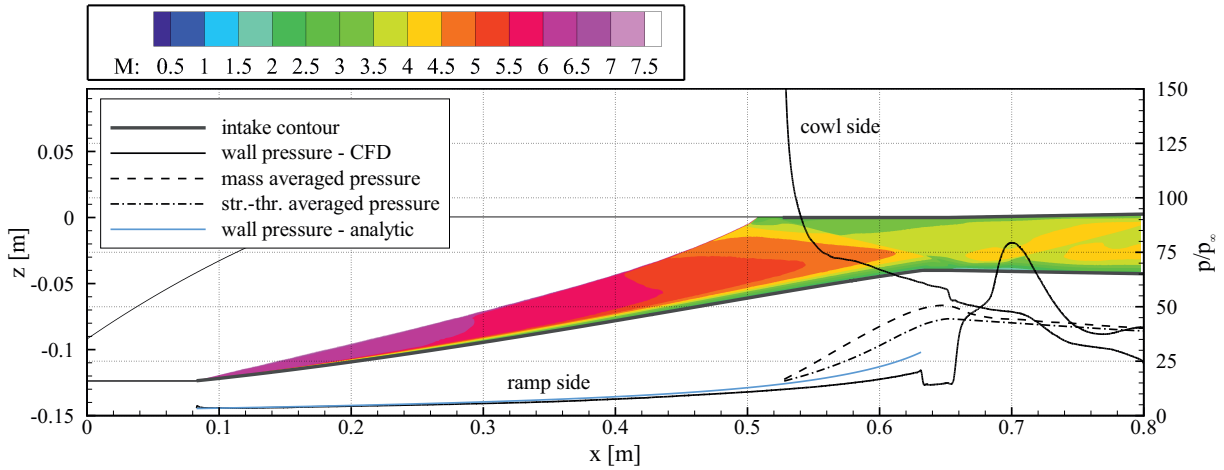


Figure 7.34: Wall pressure, averaged pressure, and Mach number contour plot extracted from CFD for ST3 intake configuration for on-design condition.

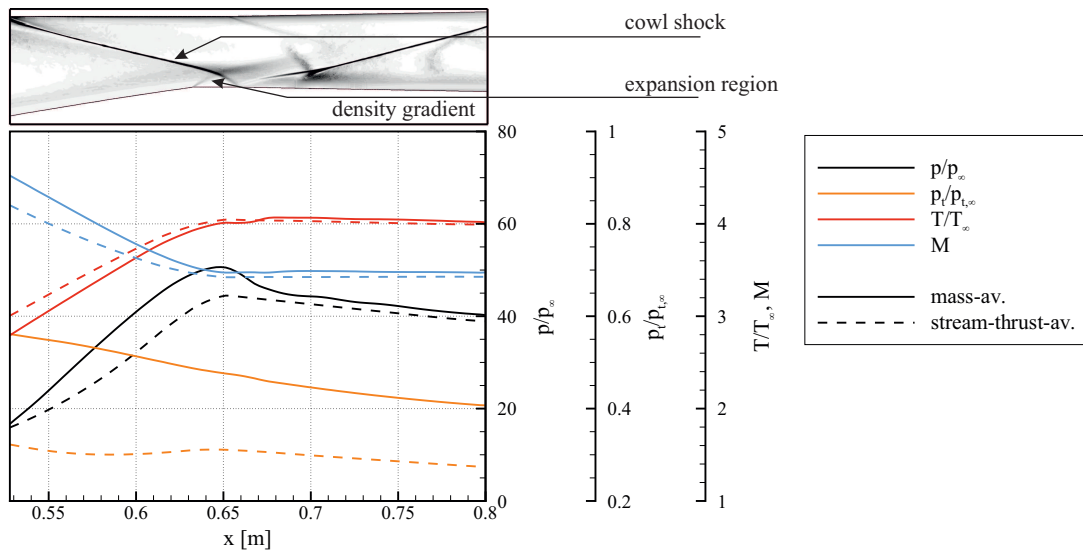
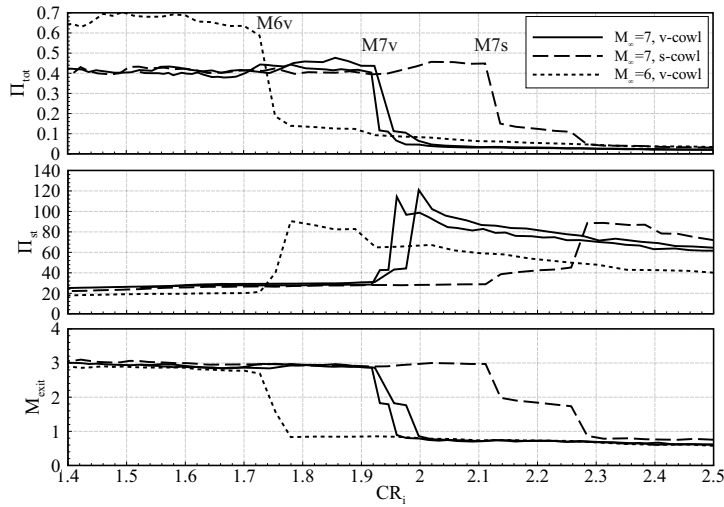


Figure 7.35: CFD-schlieren plot and averaged variables extracted from internal portion of ST3 intake configuration for on-design condition.



	$CR_i$	$M_{cl}$	$\dot{m}/\dot{m}_0$
M6v	1.72	3.60	0.686
M7v	1.91	4.14	0.877
M7s	2.11	4.35	0.867

**Figure 7.36: Starting behavior for different free stream Mach numbers and different cowl geometries; image from [36].**

## 7.5 Starting Experiments

The starting experiments were performed in the H2K wind tunnel and results were also published in [34, 36]. During a starting experiment the cowl of the initially unstarted intake was moved downstream, thus decreasing the internal contraction ratio. Intake start was detected either by schlieren images, or a sudden increase in total pressure measured at the rake. The corresponding internal contraction ratio is then equal to the self-starting limit for the specific configuration. For all experiments the free stream total temperature was 700 K, while the Reynolds number was adjusted to a flight along a trajectory with constant dynamic pressure (0.53 bar). In the following, the influence of Mach number, cowl geometry, and angle of attack on intake starting is discussed. Once a configuration was started, it could not be unstarted by moving the cowl back upstream. This indicates that hysteresis effects are present during the starting and unstarting process of intakes.

### 7.5.1 Mach Number Influence

In the present section results of wind tunnel experiments at different free stream Mach numbers and their influence on the starting behavior of the 3D-GRK intake are presented. Experiments were performed for the v-shaped cowl geometry and with the Mach 7 and Mach 6 nozzle, and unit Reynolds numbers were  $3.4 \times 10^6 \text{m}^{-1}$  and  $4.0 \times 10^6 \text{m}^{-1}$ , respectively. The Mach 7 experiment with the v-cowl was considered as a reference case and is plotted twice to illustrate run-to-run variations during two experiments.

Figure 7.36 shows static pressure ratio, total pressure ratio, and Mach number at the rake ( $x = 0.722 \text{ m}$ ) plotted against internal contraction ratio. Note that during the experiments the internal contraction ratio was decreased and therefore the plots have to be read from right to left. In the table the internal contraction ratios, which correspond to the critical condition where the intake just started, are given. Furthermore, the corresponding captured mass flow, measured with the attached throttle, is divided by the unit mass flow  $\dot{m}_0$  through the capture area and is shown as the mass capture ratio. The Mach number at the cowl closure position was estimated from CFD data and given as the mass-averaged value.

The unstarted mode is clearly visible and is characterized by a high static pressure ratio, low total pressure recovery and subsonic Mach number, mainly caused by a strong shock located in front of the cowl closure. Once the intake started static pressure dropped to, and total pressure and Mach number increased to the level of operation. Increasing Mach number from 6 to 7 increased operating static pressure and mass capture ratio from around 22 to 30 and 0.686 to 0.877, respectively, and lowered total pressure

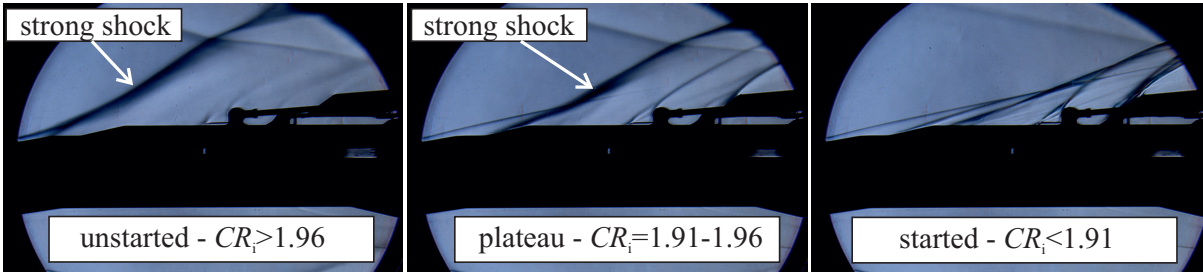


**Figure 7.37: Schlieren images of unstarted, started, and plateau case for  $M_\infty = 7$  and the v-shaped cowl configuration; image from [36].**

recovery from around 0.6 to 0.4. Intake exit Mach number was constant at  $\approx 3$ . For Mach 7, between the fully started mode and the unstarted mode, a plateau region was detected, in which the performance parameters ( $\Pi_{st}$ ,  $\Pi_{tot}$ ,  $M_{exit}$ ) were in between the two modes. In figure 7.37 schlieren images are shown to give a better impression of the flow field during the starting process. For unstarted flow a strong shock was located in front of the intake, while further downstream the flow was mainly subsonic and mass was spilled over the intake cowl. In the plateau mode there was also a strong shock located in front of the intake, while further downstream the flow was partially supersonic and therefore less mass was spilled over the intake cowl. For started intake flow the strong shock diminished and the flow further downstream became fully supersonic, while the spillage mass flow further decreased.

### 7.5.2 Cowl Geometry Influence

In the present section two different cowl geometries are compared concerning their influence on intake starting. A v-shaped and a straight cowl geometry, as explained in section 6.1.1, were tested at a constant Mach and Reynolds number of 7 and  $3.4 \times 10^6 \text{m}^{-1}$ , respectively. Results are plotted along with the results for different Mach numbers in figure 7.36.

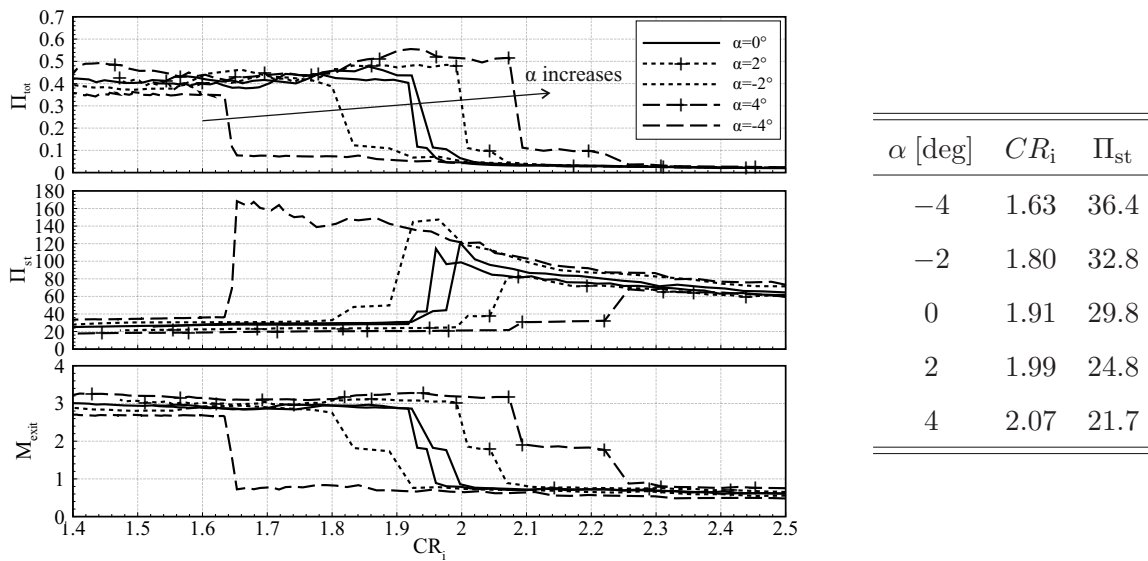
During started and unstarted mode static pressure, total pressure recovery and Mach number, all measured at the intake exit, were practically unaffected of cowl geometry. The internal contraction ratio was measured at the cowl closure position and therefore for a constant  $CR_i$  the straight cowl spilled more air. According to [69] this improves the starting characteristics. This was confirmed as for the straight lip the critical internal contraction ratio, where the intake started, increased to 2.11. However, the captured mass flow decreased slightly from 0.88 to 0.87. For the straight cowl the critical cowl closure position moved upstream, and therefore the mass-averaged  $M_{cl}$ , extracted from CFD, increased to 4.35. Moreover, the plateau region extended to a broader range of internal contraction ratios.

### 7.5.3 Angle of Attack Influence

In the present section the starting behavior for various angles of attack was investigated for the v-shaped cowl and a constant Mach and Reynolds number of 7 and  $3.4 \times 10^6 \text{m}^{-1}$ , respectively. Table 7.8 summarizes the investigated angles of attack. A positive  $\alpha$  corresponded to lifting the intake nose, thus lowering the strength of the main ramp shock (see figure 6.3 for notation of  $\alpha$ ). Due to symmetry reasons, no negative  $\beta$  component was investigated. Results are displayed analogously to the previous subsections. Increasing pitch angle moved total pressure recovery and the critical internal contraction ratio to higher levels, while the change in  $CR_i$  could reach as high as 0.4 for  $\alpha = \pm 4$ . At the same time, however, the static pressure ratios dropped due to the lower deflection and therefore weaker shock. It can also be assumed that more mass flow was spilled overboard the intake because the capture area decreased with pitch angle. Mach number and total pressure recovery both increased with increasing pitch angle. Except for the  $\alpha = -4$  deg case, the plateau region with supersonic flow in the intake was present for all configurations. To explain the influence of  $\alpha$ , one can imagine what happens to the flow when the intake

**Table 7.8: Overview of investigated angle of attack configurations.**

$\beta$ , deg	$\alpha$ , deg	-4	-2	0	2	4
0		×	×	×	×	×
2			×	×	×	
4				×		

**Figure 7.38: Influence of pitch angle ( $\alpha$ ) variation on starting behavior of intake; yaw angle was kept zero; image from [36].**

is pitched. As stated earlier, by lifting the intake nose, the deflection caused by the main ramp decreased, and therefore, the leading-edge shock became weaker. This then led to a higher Mach number behind the leading-edge shock and, in the first approximation, to a higher Mach number at the cowl closure position. Analogous to the previous section, intake starting was enhanced by this higher Mach number.

With increasing yaw angle the deflection at one side wall increased while it decreased on the opposite side. Therefore, the oblique shocks emanating at the swept side walls increased and decreased in strength correspondingly and the capture area, thus captured mass flow, decreased. Furthermore, the critical contraction ratio at which the intake started and the corresponding operating static pressure ratio both decreased for increasing yaw angle (figure 7.39). Total pressure recovery was barely affected by angle of yaw. The influence of yaw angle on intake starting was generally weaker than the influence of pitch and for  $\beta = 4$  deg the maximum change in  $CR_i$  was about 0.1.

Superimposing pitch and yaw should have the following effect: For  $\alpha > 0$  and  $\beta > 0$  static pressure ratio should drop drastically, while the stronger influence of pitch should slightly increase the internal contraction ratio for starting. For  $\alpha < 0$  and  $\beta > 0$  internal contraction ratio should decrease, while the stronger influence of pitch should slightly increase the static pressure ratio. These two trends were reproduced experimentally for  $\alpha, \beta = 2, 2$  deg and  $\alpha, \beta = -2, 2$  deg. In figure 7.39 it can be seen that for  $\alpha, \beta = 2, 2$  deg the static pressure ratio decreased and the intake started for  $CR_i = 1.97$ . Setting  $\alpha, \beta$  to  $-2, 2$  deg increased static pressure ratio slightly and hindered intake starting.

In conclusion angle of attack could improve the starting characteristics for  $\alpha > 0$ . However, this improvement was always accompanied by a decrease in static pressure ratio and captured mass flow. Angle

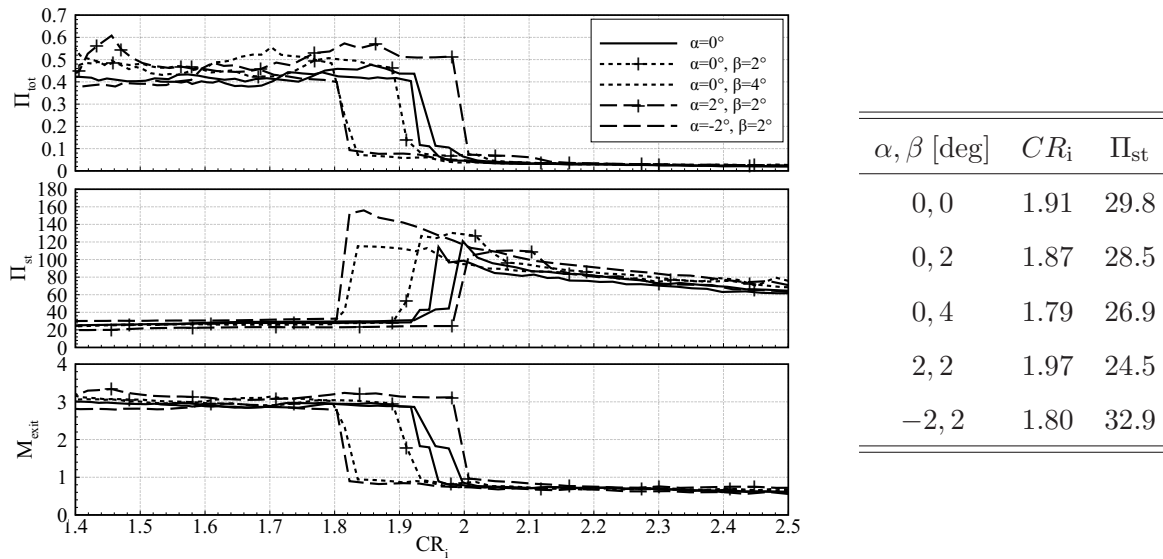


**Figure 7.39: Influence of yaw angle ( $\beta$ ) and of simultaneous pitch and yaw angle on intake starting for v-shaped lip at Mach 7; image from [36].**

of yaw always delayed intake starting to lower  $CR_i$  and  $\Pi_{st}$ . Thus, during a possible flight experiment or maneuver, in which angle of attack is inevitable, there are going to be regions where intake starting is enhanced (large  $\alpha$  and  $\beta$  near zero) and regions with delayed intake starting, when compared to the zero angle of attack condition.

#### 7.5.4 In the Context of Kantrowitz Theory

Self-starting configurations that were investigated experimentally in the H2K wind tunnel are plotted in the Kantrowitz diagram in figure 7.40. Mach numbers at the cowl closure position were extracted from numerical simulations, while for  $\alpha = \pm 4$  deg the corresponding zero degree value was used. All data points were within the critical region. The zero degree angle of attack cases agreed especially well with the empirical relations from the literature.

Figure 7.40 is replotted in figure 7.41 along with the collected self-starting data from the literature (section 2.3.2). Unstarted configurations are shown as unfilled symbols. All contraction ratios fell into the critical region and emphasize the conservative nature of the Kantrowitz theory. Furthermore, the self-developed semi-empirical relation (equation (5.1)) is plotted and gave a better estimate for starting. Compared to the experimental data points the semi-empirical limit was located at the critical end at which intakes were self-starting and therefore could be regarded as an optimistic limit.

Compared to Smart's limit [99], the semi-empirical relation was similar for  $M < 3.5$  and became more conservative for higher Mach numbers. Compared to Sun's limit [105], the semi-empirical relation was slightly more optimistic. Furthermore, the semi-empirical relation was valid for the entire Mach number range and correctly predicted the high Mach number results by Goldberg [41]. If desired, the semi-empirical limit could be approximated by setting  $C_1 = 1.5$  in the self-developed empirical relation (equation (5.1)).



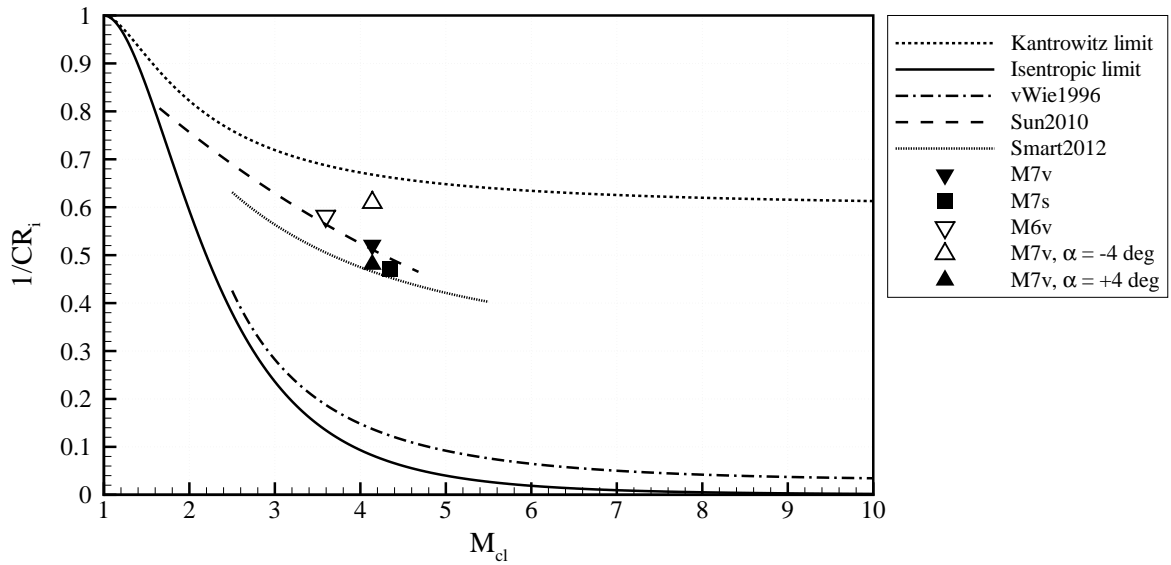


Figure 7.40: Self-starting limits of the 3D-GRK intake configurations plotted in the Kantrowitz diagram.

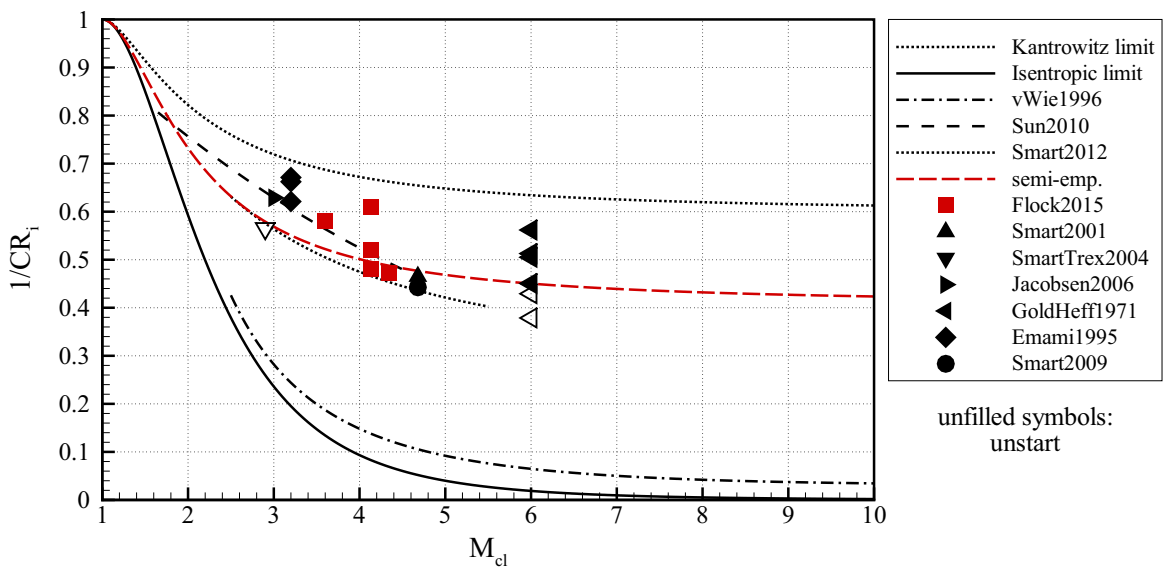
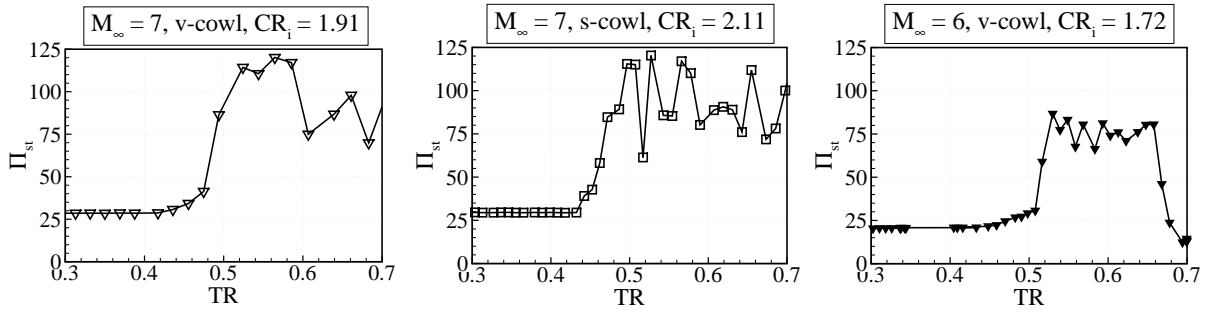


Figure 7.41: Self-developed semi-empirical relation in comparison with self-starting intake configurations plotted in the Kantrowitz diagram.



**Figure 7.42: Intake exit pressure, averaged at rake, plotted against throttle ratio (throttle closed for increasing throttle ratio) for the three different self-starting configurations; image from [35].**

## 7.6 3D-GRK Intake

### 7.6.1 Back Pressure Influence

To simulate pressure peaks, which can occur during the combustion process, the throttle described in section 6.3.4 was attached to the intake exit. During a wind tunnel run the throttle was closed and the pressure at the intake exit was measured with the rake located at  $x = 0.722$  m. The self-starting configurations, as reported in the previous section, were investigated. Normalized pressures are displayed in figure 7.42 and an increasing throttle ratio corresponded to closing the throttle and therefore higher blockage. Pressures were calculated by averaging data of the 10 static pressure probes at the intake rake and of the two wall probes at the same streamwise location.

For the Mach 7 cases the static pressure ratio in the non-throttled case was at around 30. When the intake was throttled, the pressure levels increased until  $\Pi_{st,max} \approx 120$  and then decreased. Therefore, the maximum static pressure ratio was approximately 4 times the operating static pressure ratio. Thus, during throttling the influence of cowl geometry was negligible. When the Mach number was decreased to 6, the operating static pressure ratio dropped to  $\approx 20$ . During throttling, the maximum back pressure was  $\Pi_{st,max} \approx 80$ , and therefore lower than in the Mach 7 cases. However, the ratio of maximum to operating static pressure was approximately constant at 4:1.

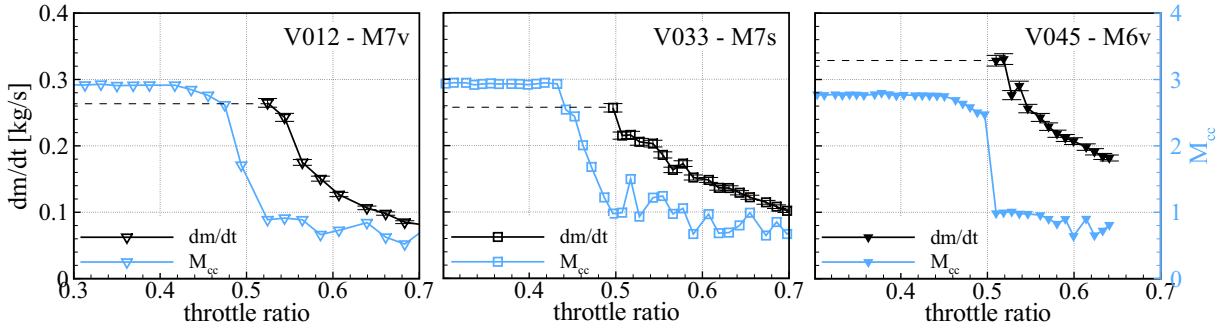
### 7.6.2 Mass Flow Measurement

The captured mass flow through the intake was measured experimentally with the throttle, as described in section 6.3.4. The applied procedure was only applicable if the flow in the settling chamber, upstream of the throttle was subsonic. Therefore, along with the calculated mass flow, the Mach number measured at the intake rake is displayed in figure 7.43. The only time when subsonic flow in the settling chamber could be assured was for large throttle ratios. Then the Mach number at the rake was subsonic and the flow could not further accelerate due to the high back pressure. This corresponded to throttle ratios  $\gtrsim 0.5$ . For lower throttle ratios the Mach number at the rake was supersonic and further accelerated in the diverging entrance of the settling chamber. Therefore, the underlying calculation was no longer valid, and no mass flow data points were displayed for low throttle ratios in figure 7.43. For  $TR \lesssim 0.5$  the intake flow was started, and thus unaffected by downstream changes to the flow. Therefore, the mass flow through the intake was constant, which is indicated by the dashed lines in figure 7.43.

The Mach 7 cases had similar mass captures, while the v-shaped lip captured 1% more mass than the straight lip. When Mach number dropped to 6 mass capture decreased, caused by the lower leading edge shock and internal contraction ratio, which both favored overboard spillage. Measured mass capture ratio for the Mach 6 case was lower than what was calculated from numerical simulations ( $\approx 0.778$  from table 7.10). This anomaly is further analyzed with figure 7.44. The throttle experiment for Mach 6 was

**Table 7.9: Captured mass flow for different configurations measured with attached throttle.**

	$M_\infty = 7$ , v-cowl	$M_\infty = 7$ , s-cowl	$M_\infty = 6$ , v-cowl	
	V012	V033	V045	V044
$\dot{m}_\infty$ [kg/s]	0.3065	0.3032	0.4907	0.4882
$\dot{m}_{\text{intake}}$ [kg/s]	$0.264 \pm 0.007$	$0.258 \pm 0.007$	$0.328 \pm 0.008$	$0.355 \pm 0.008$
$\dot{m}_{\text{intake}}/\dot{m}_\infty$	0.861	0.851	0.668	0.727

**Figure 7.43: Measured captured mass flow and intake exit velocity for different intake configurations.**

performed twice, because wind tunnel run #44 showed throttle malfunctions, which originated within the hydraulic actuators, at low throttle ratios ( $TR < 0.45$ ). Nevertheless, because the important data points were located at higher throttle ratios, run #44 could still be used as support. As can be seen in figure 7.44 mass capture ratio for run #44 jumped to a higher level (0.355 kg/s,  $MCR = 0.727$ ), which was closer to what was predicted numerically. It was therefore concluded that the Mach 6 configuration was more sensitive to the throttling process, and that the correct  $\dot{m}$  was not always sampled with the relatively low data acquisition rate.

### 7.6.3 CFD Analysis

The DLR-TAU code was validated for multiple test cases and examples can be found in [61, 85]. Nevertheless, in the present section, three example cases are presented, and numerical and experimental results were compared to demonstrate a proper usage of the simulation tools. As reference configuration the three test cases, which were also used for the starting and throttle investigations, were taken and numerical results were performed for the corresponding wind tunnel conditions.

Figures 7.45 - 7.47 compare the numerical results to the wall pressure measurements along the symmetry plane of the intake model. The rendering in all graphs is equal and each figure contains three pieces of information: First, the Mach number contour plot is shown, to give a first impression of the flow field. The ramp shock could be seen clearly, and also a shock train running down the isolator was visible. Furthermore, in all cases a spillage mass flow above the intake cowl was detected, and at  $x \approx 0.59$  m, where the cowl shock impinged on the ramp side of the intake, a separation region was present. Second, the wall pressure measurements and their uncertainties are plotted in comparison to the CFD wall pressure results. The measured and CFD pressures very accurately matched each other until  $x \approx 0.59$  m, which is approximately the same location at which the separation region was located. Further downstream, the pressures were slightly different, which was presumably caused by not modeling the separation accurately enough. However, the shift was only small and the pressure level was unaffected. The straight cowl geometry decreased wall pressure directly underneath the cowl. Third, mass- and

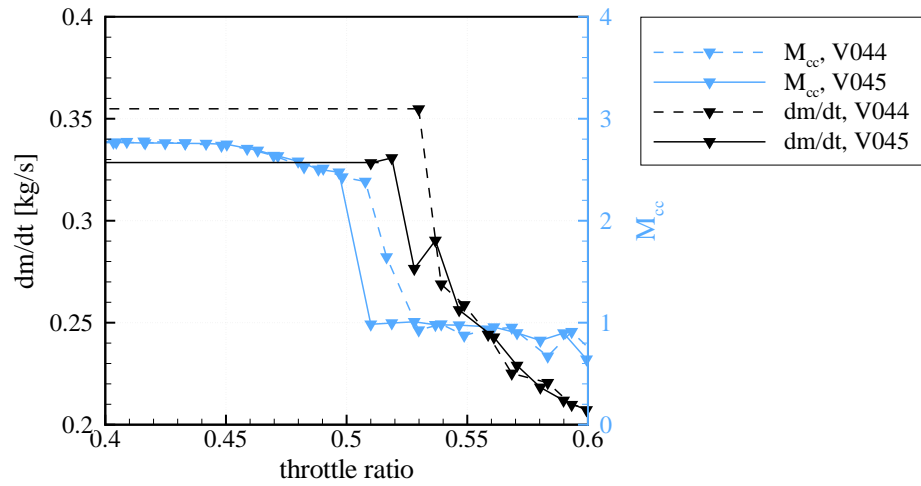


Figure 7.44: Close-up of captured mass flow and intake exit velocity for Mach 6 configuration.

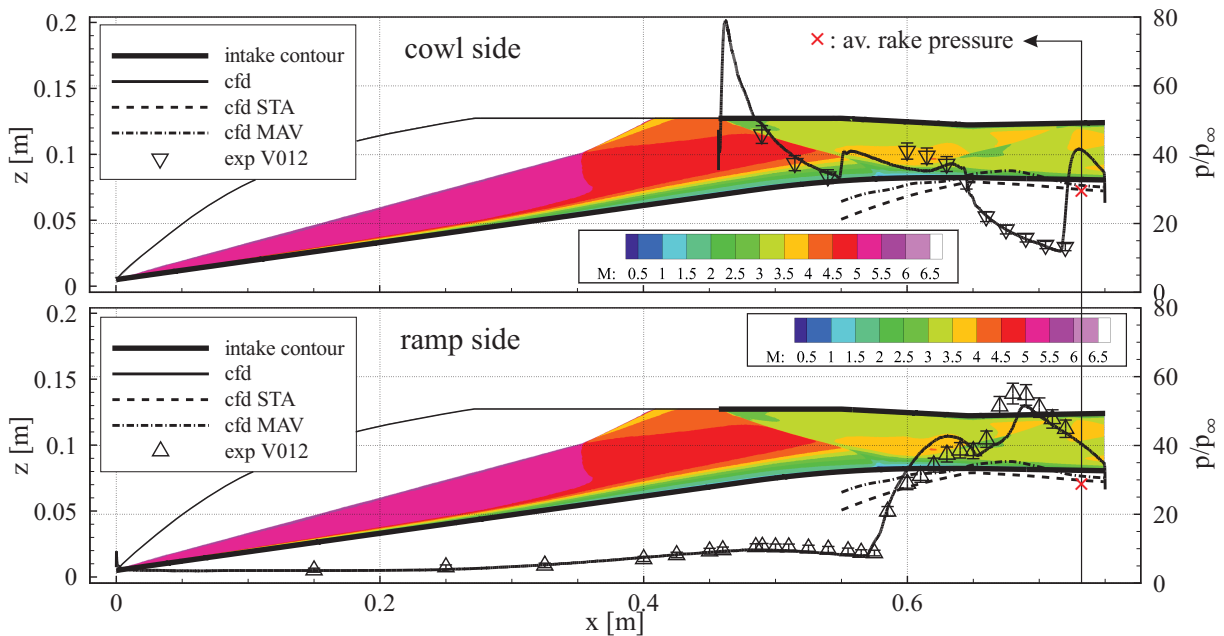


Figure 7.45: Numerical and experimental results of Mach 7, v-cowl configuration; image adapted from [35].

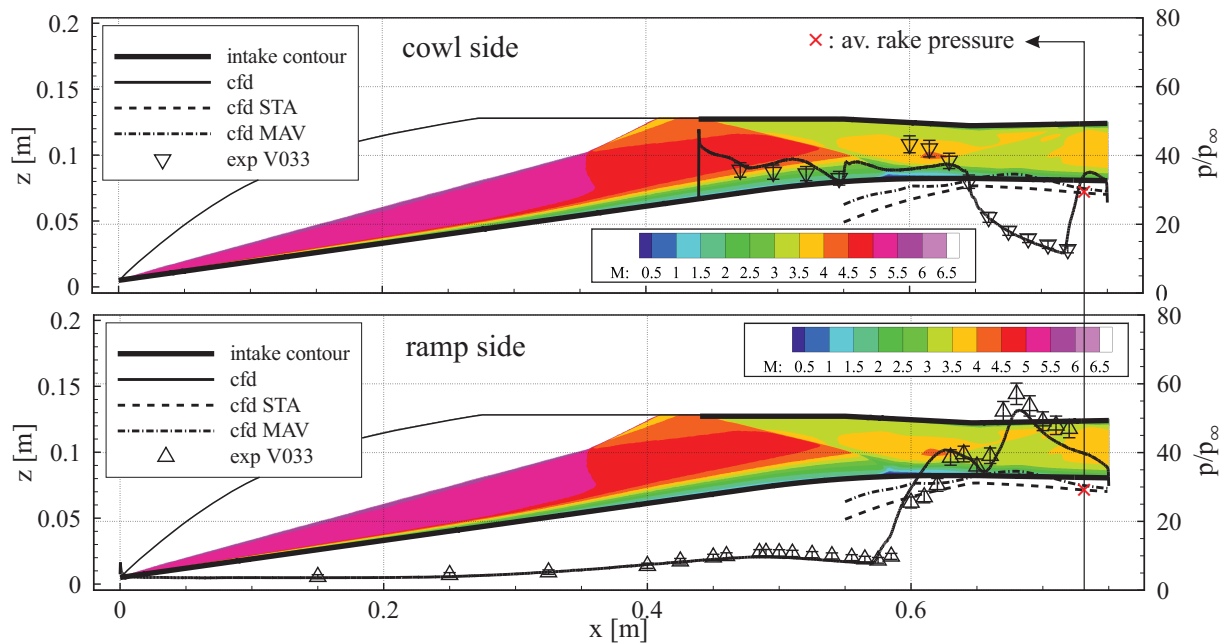


Figure 7.46: Numerical and experimental results of Mach 7, s-cowl configuration; image adapted from [35].

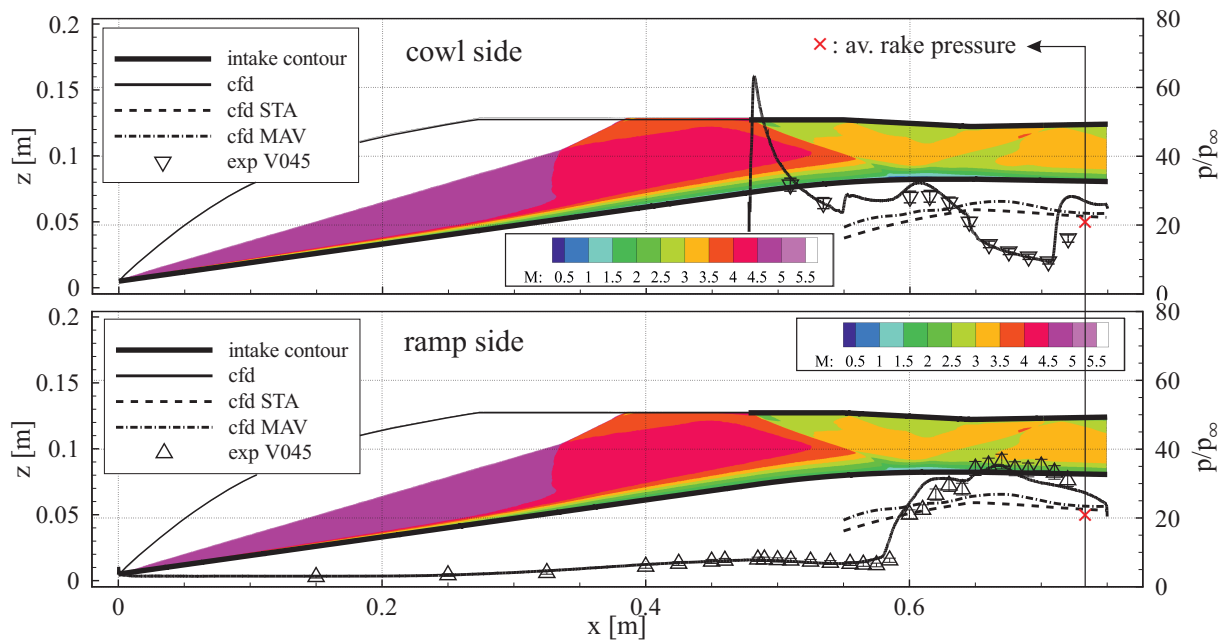
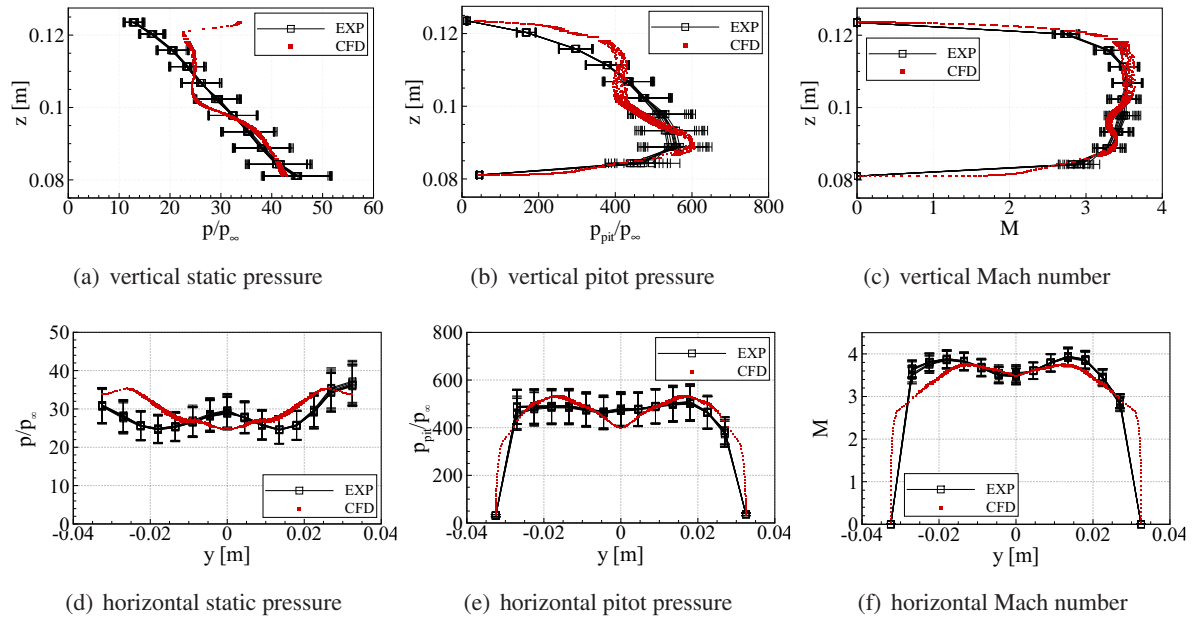


Figure 7.47: Numerical and experimental results of Mach 6, v-cowl configuration; image adapted from [35].



**Figure 7.48: Static and pitot pressure, as well as Mach number for the Mach 7, v-cowl configuration, at  $x = 0.722$  m; image from [35].**

stream-thrust-averaged values, calculated from the CFD flow field are shown for  $x > 0.55$  m. The stream-thrust-averaged pressures were slightly lower and the pressure maximums were at around  $x \approx 0.65$  m and  $x \approx 0.675$  m for stream-thrust- and mass-averaged cases, respectively. At the rake location the ensemble average of all static rake pressure ports is plotted. The results were in between or lower than the numerical averages for the Mach 7 and 6 case, respectively.

In figures 7.48, 7.49, and 7.50 measurements along the horizontal and vertical part of the rake are plotted along with measurement uncertainties as error bars. Multiple measurements are plotted, to show fluctuations during a wind tunnel run. The diameter of a pressure tube was 0.7 mm. Therefore, CFD data is plotted for  $z = 103 \pm 0.35$  mm (horizontal ports) and  $y = 0 \pm 0.35$  mm (vertical ports) to illustrate the uncertainty in location. First, the static and pitot pressures are given, which were measured directly. From the static and pitot pressure, the Mach number was calculated, and is additionally plotted as third variable.

Overall the data uncertainty of the in stream measurements is larger compared to the wall pressure measurements. This is caused by the generally larger uncertainty of the static and pitot tubes, but also by the fact, that pressures were partially interpolated from their neighboring values.

In the Mach 7 case the static pressure ratio decreased from 40 – 45 at the bottom, to  $\approx 15$  at the top. In the numerical results a small high pressure region at the top was observed, which indicated an incoming shock wave. In horizontal direction, the static pressure measurements of the simulations behaved anticyclic to the experiments: While during the experiments the pressure in the middle and at the sides was higher and lower, respectively, during the simulations the opposite behavior was observed. The pitot pressure at the top was generally lower than at the bottom, while in the numerical simulations a plateau was detected at  $z \approx 0.105$  m, which was not present in the measurements. In horizontal direction, the measured and numerically calculated pitot pressures matched, with the only exception in the very center. There, a static pressure port was located and the respective pitot pressure was interpolated from the neighboring values. The Mach numbers, which were calculated from the pitot and static pressure values were met in the vertical direction and only slightly differed at the sides in horizontal direction.

Replacing the v-shaped cowl with the straight cowl had little influence on the numerical results. However, the experimental rake data was more affected by the change in cowl geometry. The pressure distributions

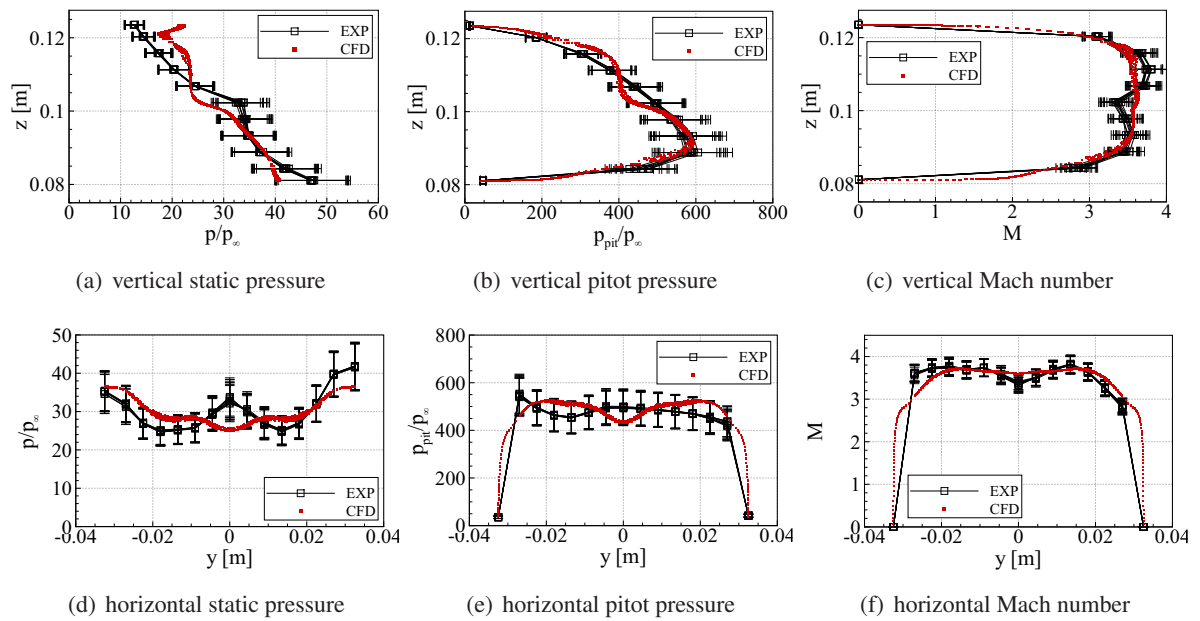


**Figure 7.49:** Static and pitot pressure, as well as Mach number for the Mach 7, s-cowl configuration, at  $x = 0.722$  m; image from [35].

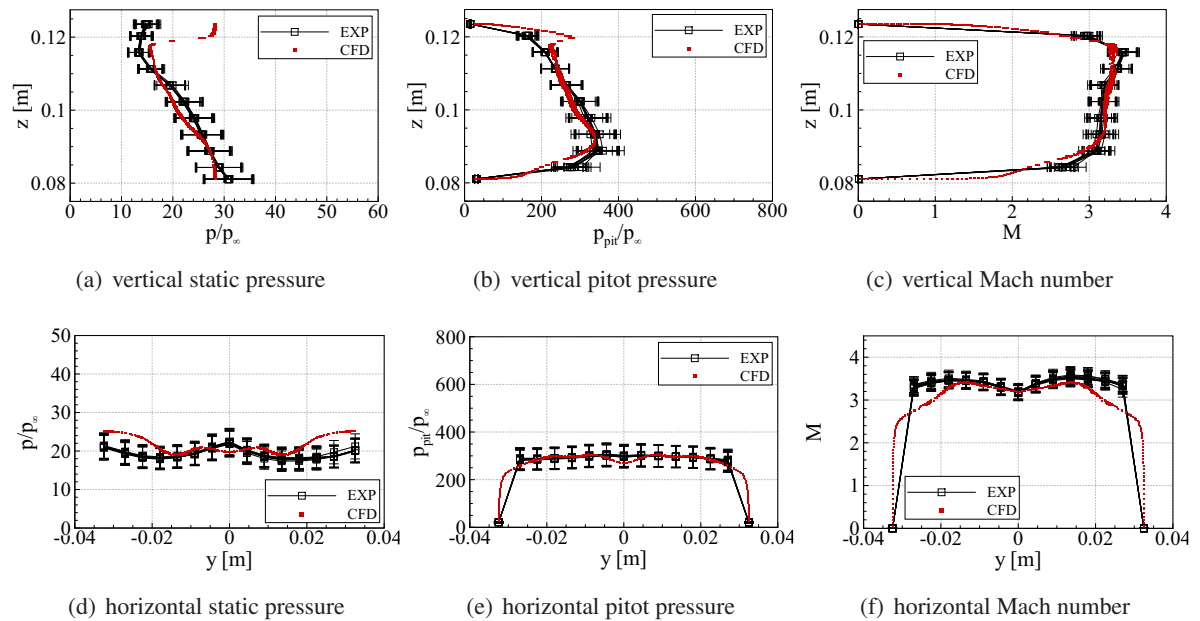


**Figure 7.50:** Static and pitot pressure, as well as Mach number for the Mach 6, v-cowl configuration, at  $x = 0.722$  m; image from [35].

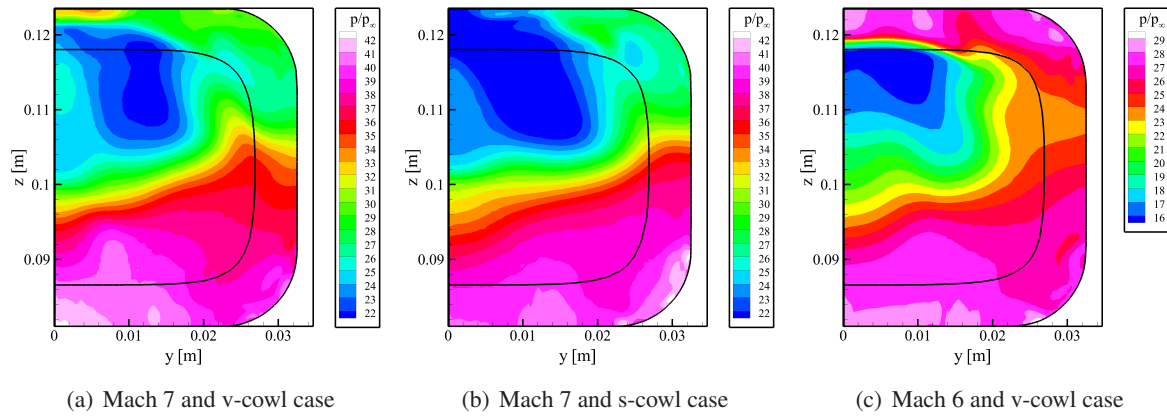


**Figure 7.51: Normalized pressure on cross sectional planes, extracted from CFD at  $x = 0.722$  m; image from [35].**

of the straight cowl configurations were less continuous, which indicated a more heterogeneous flow field.

In the Mach 6 case pressures were generally lower and numerical results matched the experiments better. In numerical simulations the region near the top with high static pressure was detected to be larger. Furthermore, in experimental results a tendency towards an increase in static pressure was visible.

To further illustrate the difference between the ensemble average pressure, calculated from the rake data and the average pressure extracted from CFD, pressure contour plots are shown in figure 7.51. Due to the shape of the rake, pressures were only measured across the height and width and therefore the information from the corner regions were not considered in the rake average. Furthermore, normalized temperature and Mach number contour plots in the appendix (section A.7) confirm the three-dimensional behavior of the flow field. Thus, due to the good fit between experimental and numerical results, and due to the highly non-uniform flow, the numerical averages were a more reasonable representation of the flow field.

#### 7.6.4 Extrapolation to Flight Condition

The good agreement between experimental wind tunnel data and the corresponding numerical simulations allowed for an extrapolation to real flight velocities, pressures and temperatures. Therefore, the numerical simulations were repeated at flight conditions and compared to simulations at wind tunnel conditions. Since the similarity parameters ( $Re$ ,  $M$ ,  $T_t/T_w$ ) were held constant, only minor changes were expected. Flight and wind tunnel conditions are summarized in the appendix (section A.1). This was confirmed by negligible differences in normalized wall and average pressure when comparing CFD of flight data to wind tunnel data (figure A.9 in appendix). Normalized stream-thrust-averaged variables at flight condition, for instance, extracted at the intake exit plane ( $x = 0.722$  m), were within 2% of the corresponding wind tunnel variables. Therefore, normalized intake performance was assumed to be practically equal to what was measured and calculated at wind tunnel conditions.

### 7.7 Comparison: 3D-GRK and Streamline Traced Intakes

#### 7.7.1 Design Approach

The developed design methodology had two advantages over the iterative concept, which was used for the design of the 3D-GRK intake.



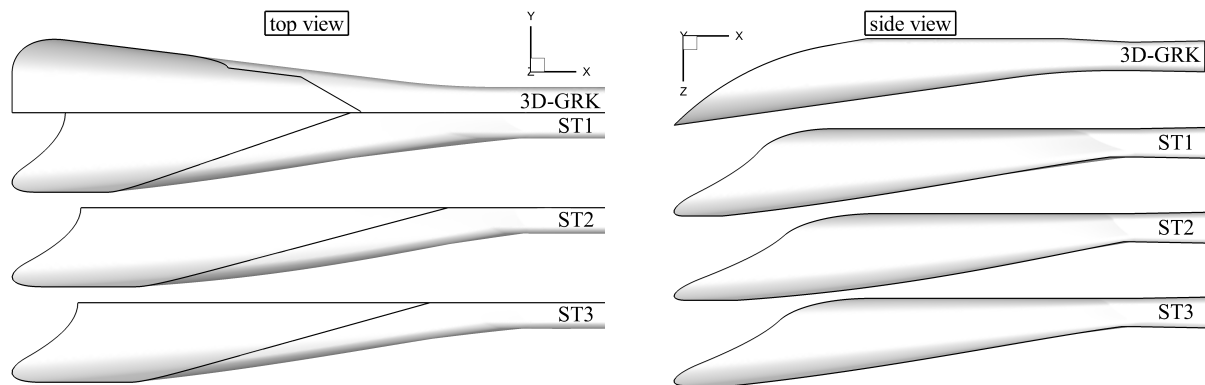


**Figure 7.52: Geometrical overview of streamline traced intakes and v-cowl 3D-GRK intake.**

- First, the run-time of the analytical tool was on the order of 10 minutes, and therefore relatively quick. The design of the 3D-GRK intake relied upon CFD simulations for a performance estimate and therefore was on the order of 100 – 1000 minutes. Furthermore, the cross sectional shape of a streamline traced intake could be chosen arbitrary. Thus, overall the analytical design approach showed superior flexibility.
- Second, throughout this work it was shown that the analytical performance estimate accurately agreed with results obtained from CFD. It was shown that stream-thrust-averaged intake parameters were properly calculated by the tool, which was beneficial for further analysis of SCRamjet cycle systems. The design methodology of the 3D-GRK intake on the other hand did not allow for a reliable performance estimate a priori.

Structural restrictions, such as length-dimensions or leading edge angles could be considered by both design approaches. Finally, even though in the context of this work, no streamline traced intake was built and experimentally tested, experimental research of other groups on similar configurations (section 2.3.2) underlined the advantages of the analytical design approach.

### 7.7.2 Geometry

The 3D-GRK intake and the streamline traced intakes are plotted for direct comparison in figure 7.52 and here various similarities exist. As it was required a priori for the streamline traced intakes, their length to the throat section, the cross sectional shape there, and the downstream portion ( $x > 0.65$  m) were equal to the 3D-GRK geometry. Furthermore, the intake configurations were highly swept with a partially enclosed, internal portion, while the cowl pattern was geometrically similar to the v-shaped cowl of the 3D-GRK intake. Otherwise, there were certain differences between the streamline traced and 3D-GRK geometries, which eventually caused a difference in performance, as is shown in the upcoming section. First, the streamline traced intakes all had continuously curved surfaces, which stood in contrast to the planar ramp and side walls of the 3D-GRK configuration. Furthermore, the overall contraction ratio was  $\approx 16\%$  larger for the streamline traced configurations and the leading edge on the main ramp was swept, while being straight for the 3D-GRK intake. Finally, no movable cowl was implemented in the streamline traced geometries, but could be added to the configuration in a possible manufacturing of an intake model. Therefore, internal contraction was variable for the 3D-GRK intake, while being fixed at the predefined value for the streamline traced geometries.

### 7.7.3 Intake Performance

Performance, which was calculated based on numerical simulations at flight conditions, is discussed in three steps. First, mass capture ratio for the different configurations was compared. Second, stream-

**Table 7.10: Mass capture ratios for various intake configurations; data extracted from CFD for flight conditions.**

$M_\infty$	6	7	8
3D-GRK*	0.778	0.889	0.979
3D-GRK†	0.871	0.935	0.979
ST1	–	–	1.0
ST2	0.971	0.996	0.999
ST3	–	–	0.992

\* self-starting, v-cowl configurations

† fixed Mach 8 geometry, v-cowl configuration

thrust-averaged variables at Mach 8 were compared, namely: static pressure, total pressure, static temperature and Mach number. Third, the uninstalled specific impulse was calculated, as described in section 6.5, and discussed for the various configurations.

Table 7.10 shows the mass capture ratios, extracted from CFD for flight conditions, of the different self-starting 3D-GRK intakes. Furthermore, the Mach 8 configuration was used as a fixed geometry and investigated at the lower Mach 6 and Mach 7 condition. Additionally, data for the streamline traced configurations, which were discussed in detail in section 7.4, are given. At Mach 8 the mass capture ratios were always near 1, which indicated little spillage. Mass capture was largest for the ST1 configuration, followed by the ST2, ST3, and 3D-GRK configurations. With lower Mach number  $MCR$  decreased. The difference in mass capture between Mach 6 and Mach 8 was  $\approx 3\%$  and  $\approx 10\%$ , for the ST2 and fixed geometry 3D-GRK configuration, respectively. The self-starting configurations had adjusted internal contraction ratios, therefore cowl closure positions located further downstream. Thus, the maximum difference between mass capture at Mach 6 and Mach 8 increased to  $\approx 20\%$ . In general the streamline traced intakes had better mass capture characteristics.

In figure 7.53 stream-thrust-averaged variables are plotted for the internal portion of the intakes. Averaged static pressure always had a maximum near  $x = 0.65$  m. The maximum pressure of the 3D-GRK intake was 40, thus approximately 7% lower than the design value. The maximum pressure of the streamline traced intakes were all larger than the design value, by 6.5%, 5.1% and 3.3% for the ST1, ST2, and ST3 configuration, respectively. Average total pressure of the streamline traced configurations was always larger than for the 3D-GRK configuration. For instance at the intake exit plane ( $x = 0.722$  m), total pressure recovery was approximately 0.22 for the 3D-GRK whereas it was 0.28 – 0.30 for streamline traced configurations. Average temperature behaved similar for all configurations and was approximately constant ( $\approx 4.1$ ) downstream of the intake throat. The 3D-GRK configuration had slightly larger average static temperature, compared to streamline traced geometries. Average Mach number behaved similar for all configurations and was approximately constant ( $\approx 3.4$ ) downstream of the intake throat. The 3D-GRK configuration had slightly lower average Mach number, compared to streamline traced geometries. The intake performance parameters extracted at  $x = 0.722$  m were post-processed as described in section 6.5. When increasing Mach number from 6 to 8, specific impulse of the streamline traced configurations decreased nearly linear from 3200 s to 2300 s (figure 7.54). The specific impulse of the 3D-GRK configurations was lower by  $\approx 300$  s, compared to the streamline traced cases. Note that even though the 3D-GRK fixed geometry configuration had higher mass capture, its specific impulse did not differ significantly from the results for the self-starting configurations. The reason for this is that during the  $I_{sp}$  calculation (equation (1.1)) the larger thrust is normalized with the fuel flow rate, which itself is directly related to captured mass flow. Specific impulse among streamline traced intakes was within 15 s, thus

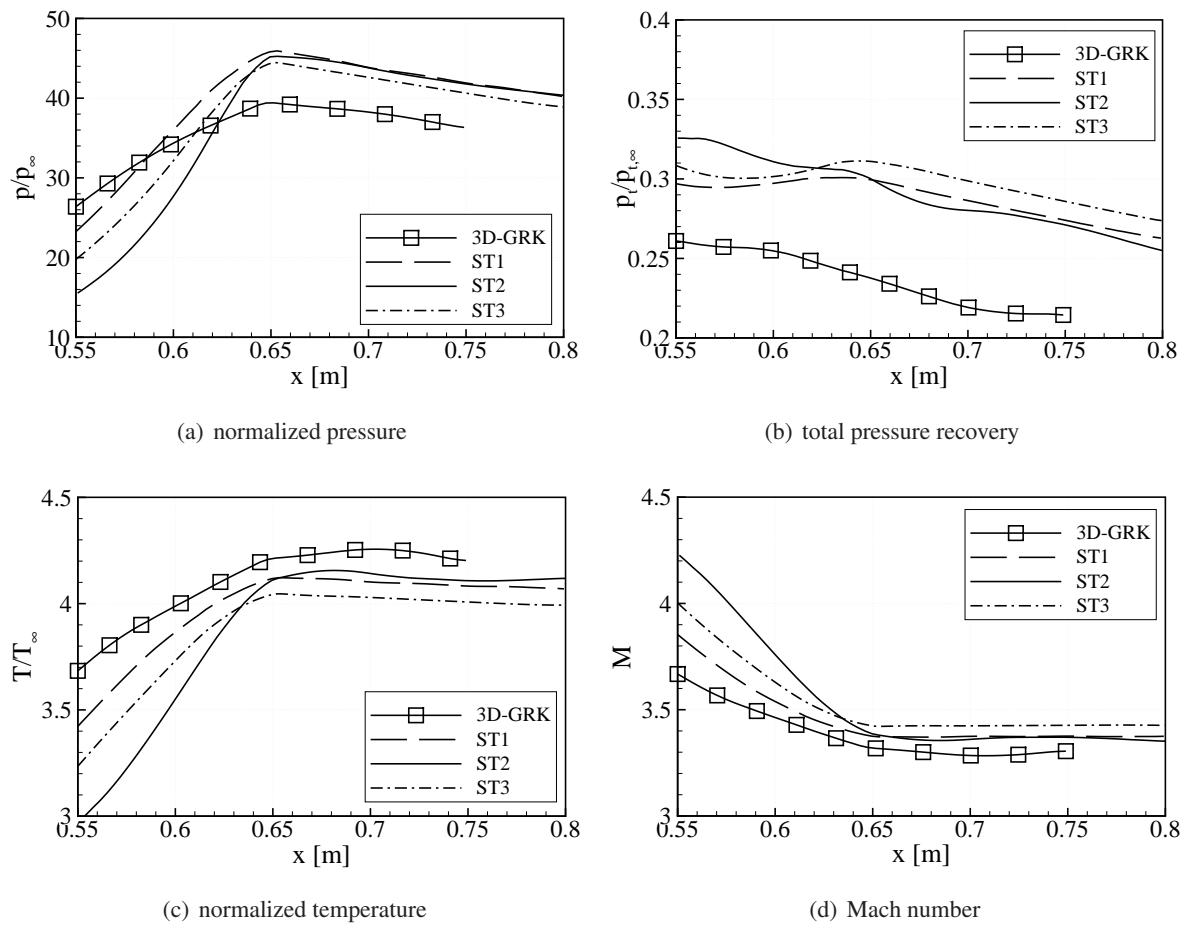
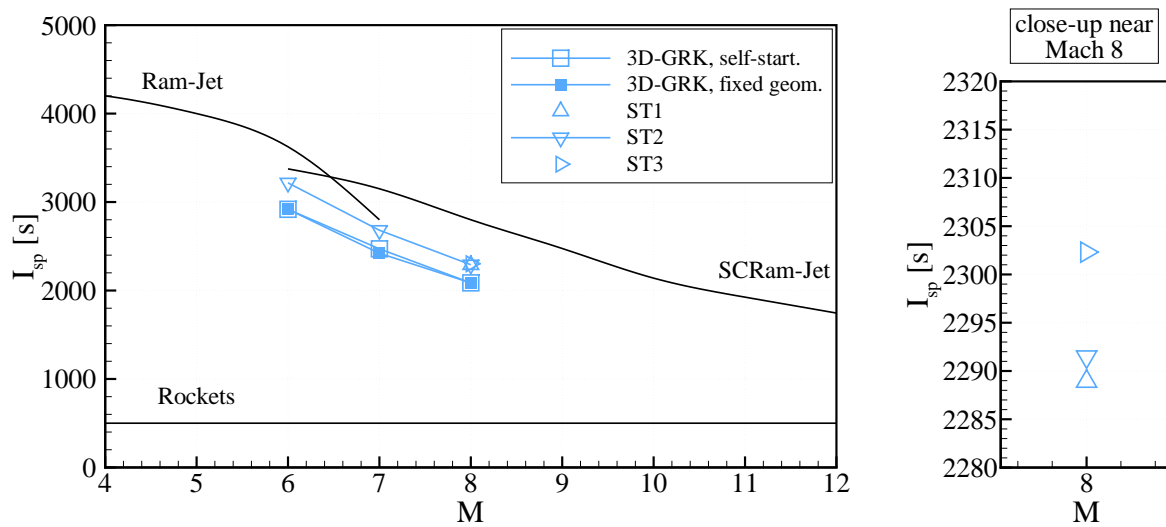


Figure 7.53: Stream-thrust-averaged variables for 3D-GRK and streamline traced intakes, extracted for Mach 8; data for internal portion of intakes.



**Figure 7.54: Specific impulse from figure 1.2 replotted along with various intake configurations and close-up near Mach 8 region of streamline traced intake configurations.**

their performance was practically equal. Therefore, it was expected that the off-design performance of the ST1 and ST3 configurations would be similar to the ST2 cases investigated.

#### 7.7.4 Summary

The analytical design approach allowed for flexible intake design with reliable performance estimate. The greatest geometrical difference was the continuously curved surface of streamline traced intakes in comparison to planar surfaces of the 3D-GRK intake. Furthermore, specific impulse between Mach 6 and 8 of the streamline traced configurations was approximately 300 s larger than the corresponding 3D-GRK values. Finally, in this study the streamline traced configurations were not experimentally tested. The close agreement between experiments and numerical simulations, however, emphasized the reliability of the performance estimate for streamline traced configurations.

## 8 Conclusion

### 8.1 Summary

The Supersonic Combustion Ramjet (SCRamjet) engine is a key propulsion technology for hypersonic air breathing flight. The present work focused on the analytical design of three-dimensional, streamline traced SCRamjet intakes. Furthermore, a semi-empirical relation to predict intake starting was developed. Various performance parameters were measured for a three-dimensional intake (3D-GRK) with planar surfaces. The performance of the streamline traced intakes was validated with numerical data, and compared to experimental and numerical results obtained for the 3D-GRK intake model. More specifically the work could be summarized by the following core topics.

The first core topic was the development and evaluation of an analytical intake design tool. The developed tool could use an axisymmetric Busemann flow field or reversed nozzle flow field, the latter designed with the method of characteristics, as the underlying compression flow field. Truncation and viscous effects were identified, which influenced intake performance and needed to be captured analytically. For this purpose, leading edge truncation effects were modeled with an oblique shock at the leading edge and a pressure adjustment at the rear. Rear side truncation effects were modeled with a stream-thrust analysis. Viscous effects were considered by widening a classical contour with the boundary layer displacement thickness. The displacement thickness was calculated with an integral method and also allowed for a calculation of friction drag of the intake. Axisymmetric flow fields were extensively validated with Computational Fluid Dynamics (CFD) for various Mach numbers and degrees of leading edge and rear side truncation. Overall the agreement between CFD and analytical prediction was good, while maximum deviations of 3% and 8% were observed for inviscid (truncation effects) and viscous cases, respectively. A weak maximum in total pressure recovery was detected for axisymmetric contours near  $2.0 \text{ deg} < \delta < 2.5 \text{ deg}$ . The performance of the reversed nozzle and Busemann flow fields differed only marginally from one another. The generally larger amount of isentropic compression of the reversed nozzle flow was compensated by the shorter length, and therefore lower skin friction, of the Busemann flow. Thus, total pressure recovery for a certain configuration was considered independent of the flow field in use. Therefore, it was decided to use a Busemann flow as the underlying flow field for further analysis of streamline traced intakes.

A streamline tracing algorithm was implemented to the design tool to generate the outer shape of three-dimensional intake geometries. Note that the viscous correction had to be applied to each streamline individually. Three streamline traced intakes were designed and labeled ST1 – ST3. All intakes had length dimensions comparable to the 3D-GRK intake and were designed for Mach 8 flight and a static pressure ratio of 43. In particular, the ST1 configuration was not truncated at the rear, whereas the ST2 configuration was truncated to an internal contraction ratio of 1.96. The ST3 configuration was differently translated in streamwise direction, but otherwise identical to the ST1 configuration. The streamline traced intakes were investigated numerically at their Mach 8 design condition. In addition the ST2 configuration was examined at the off-design Mach numbers 7 and 6. For all intakes at design Mach number the performance parameters extracted from CFD were within 7% of the analytical predictions. The overall intake performance was similar due to the identical design condition. Therefore, the specific modifications to the ST1 – ST3 geometries had only little influence on overall performance. On a more detailed level, however, the following differences were observed. For the ST1 configuration, the ramp shock impacted underneath the intake cowl which should be avoided due to larger aerodynamic and heat loads. Furthermore, internal contraction was too high for self-starting. The ST2 configuration had internal contraction in the range where self-starting for Mach 8 was expected. However, intake exit flow

was highly non-uniform. The ST3 configuration had low internal contraction, as well as more uniform exit flow. In turn, an additional axisymmetric CFD simulation was necessary during the ST3 design due to the translation in streamwise direction.

The second core topic was intake starting behavior. Wind tunnel experiments with the 3D-GRK intake were performed at Mach numbers of 6 and 7. The experimental starting results along with collected data from the literature, were used to develop an empirical as well as semi-empirical starting relation. The empirical starting limit was adjustable with an arbitrary constant factor and could be calibrated to a certain set of data. The semi-empirical relation used a varying total pressure loss, which depended on Mach number, to modify the isentropic limit. The resulting self-starting limit presented maximum internal contraction at which intake configurations were self-starting. The semi-empirical relation was used during the design of the streamline traced intakes for an a priori estimate of the needed internal contraction ratio. The particular findings of the experiments were:

- For all configurations the internal contraction ratio for intake starting was higher than the values predicted by Kantrowitz theory.
- Once intakes were started, increasing the internal contraction to values as high as 2.56 did not cause intake unstart for either Mach number.
- The straight intake cowl shifted the self-starting internal contraction ratio from 1.91 for the v-cowl to 2.11. This phenomenon was mainly caused by the increase in overboard spillage for the straight cowl. However, the mass capture ratio for the v-shaped cowl configuration was 1% larger than for the straight cowl.
- With decreasing free stream Mach number, intake starting was reduced to lower internal contraction ratios.
- Angle of attack effects were twofold: For positive pitch angles, intake starting was enhanced, whereas for negative pitch angles and increased yaw angles, intake starting was delayed. Overall, pitch angle influence was stronger compared to yaw angle.

The third core topic was the performance characterization of the 3D-GRK intake model. Starting experiments were excluded in this context since they were subject of the general analysis of intake starting discussed previously. The self-starting configurations were investigated at Mach 7 for the v-shaped and straight cowl, and at Mach 6 for the v-shaped cowl only. With the attached throttle, the maximum sustainable back pressure of each configuration was measured. Independent of cowl geometry, the average operating pressure ratio and maximum sustainable pressure ratio of the Mach 7 configurations were around 30 and 120, respectively. For the Mach 6 case static pressure ratio and maximum sustainable pressure ratio dropped to 20 and 80, respectively. Therefore, the maximum sustainable pressure to operating pressure ratio was constant at  $\approx 4:1$ , in other words independent of Mach number. As mentioned before, mass capture ratio of the self-starting Mach 7 configurations was approximately constant ( $\approx 0.85$ ) and dropped to 0.73 for the Mach 6 case. Mass capture ratios, calculated with CFD, were around 3% and 7% larger for the Mach 7 and Mach 6 configurations, respectively. CFD data were further validated with experimentally measured wall and rake pressures. The match in pressure was within the experimental uncertainty, except for minor displacements near regions with separated flow. Since CFD was validated with experiments, performance parameters were extrapolated to flight conditions. Average properties were then extracted from CFD via a stream-thrust approach and further processed with one-dimensional tools.

The last core topic was to compare the 3D-GRK intake to the streamline traced intakes. The analytical design approach allowed for flexible intake design with reliable performance estimate, whereas the 3D-GRK design relied upon CFD. Overall, performance of the streamline traced intakes was superior to performance of the 3D-GRK intake. This was mainly due to continuously curved surfaces within the

streamline traced intakes in contrast to planar surfaces within the 3D-GRK intake. Comparing stream-thrust-averaged parameters at the intake exit resulted in the following: Normalized static pressure of streamline traced intakes was  $> 43$  and therefore larger than for the 3D-GRK intake. The same was true for total pressure recovery, which was 0.29 and 0.22 for the streamline traced and the 3D-GRK intake, respectively. The 3D-GRK intake had average Mach numbers lower by  $\approx 5\%$ , and average temperatures larger by  $\approx 6\%$ . Furthermore, overall engine performance was estimated with one-dimensional analytical tools. For the streamline traced geometries, specific impulse increased nearly linearly from 2300 s to 3200 s, when Mach number was lowered from 8 to 6, respectively. For the 3D-GRK configurations, specific impulse was approximately 300 s lower. Finally, in this study the streamline traced configurations were not experimentally tested. The close agreement between experiments and numerical simulations, however, emphasized the reliability of the performance estimate for streamline traced configurations.

## 8.2 Outlook

Throughout the current work a variety of ideas and questions emerged, which could not be further analyzed. In the hope to trigger further research, these topics are outlined below in subjective order of importance.

### *Numerical Topics*

Related to numerical investigations, an extensive analysis of the influence of turbulence models on intake performance is recommended. As it was shown, turbulence models currently have problems in regions with separated flow. A thorough sensitivity analysis of existing turbulence models can be used to develop numerical uncertainty. Furthermore, the investigated conditions could be extended to include a broader Mach number range, different angles of attack, various constant dynamic pressure trajectories, or the like. Finally, if the flow solver can model reacting flows, it could be examined if conditions at the intake exit are sufficient for ignition.

### *Specialized Topics*

Specialized topics focus on a more detailed component or phenomenon of the intake. For instance, it could be investigated how fuel injection within the intake influences the flow field. The additional residence time of the fuel-air mixture would likely improve mixing and combustion. Furthermore, a generic model could be developed to investigate intake starting at a broad variety of Mach numbers and internal contraction ratios. This data can subsequently be used to validate analytical predictions. Finally, laminar-turbulent transition on the intake ramp or SCRamjet forebody should be investigated. If transition can be delayed, without risking earlier separation, drag forces and aerothermal loads can be drastically reduced.

### *Intake Design Tool Related Topics*

Even though the design tool was extensively discussed in the present work, there is potential to improve the approach. First, the code could be run-time optimized, since the present study rather focused on the physical context. Second, and also software related, a direct readout of streamline traced contours into any common computer aided design format would increase user friendliness. Third, it should be investigated whether analytical predictions for off-design conditions are possible. This would further accelerate the design process of the intake. Finally, the intake tool should be coupled with other tools, which for instance model structural or thermal loads. Then, as part of a multidisciplinary design optimization, configurations optimized for different boundary conditions can be compared.

### *Wind Tunnel Testing*

To further qualify the analytical design tool, manufacturing and wind tunnel testing of a streamline traced configuration is inevitable. Certain effects, such as the intake behavior during unstart or back pressure, are hard to capture numerically. Therefore, wind tunnel experiments of a streamline traced model would add to the reliability of the analytical predictions. Besides, experience in manufacturing and handling of streamline traced geometries can be gained, which is essential during the preparation of a flight test.

### *Flight Testing*

The final step to prove the concept of hypersonic air breathing flight is flight testing. Current experimental facilities and numerical solvers are limited and cannot fully duplicate the exact conditions during flight. Therefore, flight testing would verify what was examined elsewhere and possibly reveal any inconsistencies. Furthermore, it has to be proven that the vehicle can operate as a system with all components connected properly. Only then is the concept of hypersonic air breathing flight proven. The author hopes that the present work contributes to this goal.



## A Appendix

### A.1 Overview of Flow Conditions

Flight and wind tunnel conditions used throughout this work are summarized below.

#### *Flight Conditions*

Based on the Mach 8 reference condition of the research training group flight conditions were generated for higher and lower Mach numbers along a trajectory with constant dynamic pressure.

**Table A.1: Overview of different flight conditions along a trajectory with constant dynamic pressure ( $q_\infty = 0.53$  bar).**

$M_\infty$	$Re$ [ $10^6 \text{ m}^{-1}$ ]	altitude [km]	$T_{t,\infty}/T_w$	$p_\infty$ [Pa]	$T_\infty$ [K]
6	4.01	26.2	2.03	2080.0	222.9
7	3.39	28.2	2.43	1528.2	224.9
8	2.94	30.0	3.47	1170.0	226.7
10	2.29	33.0	5.40	748.8	231.4
12	1.83	35.5	7.90	520.0	238.5

#### *Wind Tunnel Conditions*

The wind tunnel conditions were generated by matching Reynolds and Mach number during wind tunnel experiments to Reynolds and Mach number during flight.

**Table A.2: Overview of different wind tunnel test conditions.**

$M_\infty$	$Re$ [ $10^6 \text{ m}^{-1}$ ]	respective altitude [km]	$T_{t,\infty}/T_w$ *	$p_\infty$ [Pa]	$T_\infty$ [K]
$6 \pm 0.05$	4.01	26.2	$2.33 \pm 0.05$	523.3	85.4
$7 \pm 0.05$	3.39	28.2	$2.33 \pm 0.05$	251.3	64.8

\* assumed constant wall temperature,  $T_w = 300$  K

## A.2 Integral Method – Rechenverfahren II

The additional variables used for the integral method by Walz [111, pp. 230] are summarized below. First, the additional variables  $F_i$  are given as:

$$F_1(H, M_e, \Theta) = 2 + n + (1 + n) \frac{\delta_1}{\delta_2}(H, M_e, \Theta) - M_e^2, \quad (\text{A.1a})$$

$$F_2(H, M_e, \Theta) = (1 + n) \frac{\delta_2}{(\delta_2)_u}(H, M_e, \Theta) \alpha(H), \quad (\text{A.1b})$$

$$F_3(H, M_e, \Theta) = 1 - \frac{\delta_1}{\delta_2}(H, M_e, \Theta) + 2 \frac{\delta_4}{\delta_3}(H, M_e, \Theta), \text{ and} \quad (\text{A.1c})$$

$$F_4(H, M_e, \Theta) = \frac{\delta_2}{(\delta_2)_u}(H, M_e, \Theta) \left( 2\beta(H, M_e, \Theta) R e_{\delta_2}^{n-N} - \alpha(H) H^*(H, M_e, \Theta) \right), \quad (\text{A.1d})$$

together with the following terms:

$$\frac{\delta_1}{\delta_2}(H, M_e, \Theta) = \frac{H_{12}(H)}{\delta_2/(\delta_2)_u(H, M_e, \Theta)} + \mathcal{R} \frac{\gamma - 1}{2} M_e^2 (H^*(H, M_e, \Theta) - \Theta), \quad (\text{A.2a})$$

$$\frac{\delta_4}{\delta_3}(H, M_e, \Theta) = \mathcal{R} \frac{\gamma - 1}{2} M_e^2 \frac{H^*(H, M_e, \Theta) - \Theta}{H^*(H, M_e, \Theta)}, \quad (\text{A.2b})$$

$$\frac{\delta_2}{(\delta_2)_u}(H, M_e, \Theta) = \left( 1 + \mathcal{R} \frac{\gamma - 1}{2} M_e^2 (H^*(H, M_e, \Theta) - \Theta) (2 - H) \varphi_1(M_e) \right)^{-1}, \quad (\text{A.2c})$$

$$\beta(H, M_e, \Theta) = \beta_u(H) \chi(M_e, \Theta), \text{ and} \quad (\text{A.2d})$$

$$H^*(H, M_e, \Theta) = H (1 + (2 - H) \psi_1(M_e, \Theta)). \quad (\text{A.2e})$$

The heat transfer parameter was given as:

$$\Theta = \frac{T_{\text{rec}} - T_w}{T_{\text{rec}} - T_e}. \quad (\text{A.3})$$

While the previous expressions were independent of the state of the boundary layer, Walz distinguished the following terms for laminar and turbulent boundary layers.

### Laminar Flow

For laminar flow, the recovery factor was 0.85 and  $n = N = 1$ . The remaining variables were defined as followed:

$$\alpha(H) = 1.441(H - 1.515)^{0.66}, \quad (\text{A.4a})$$

$$\beta_u(H) = 0.1573 + 1.691(H - 1.515)^{1.637}, \quad (\text{A.4b})$$

$$H_{12}(H) = 4.03 - 4.183(H - 1.515)^{0.3945}, \quad (\text{A.4c})$$

$$\varphi_1(M_e) = 0.936 - 0.0572M_e, \quad (\text{A.4d})$$

$$\psi_1(M_e, \Theta) = 0.0114M_e(2 - \Theta)^{0.8}, \text{ and} \quad (\text{A.4e})$$

$$\chi(M_e, \Theta, \omega) = \left( \frac{1 + \frac{2}{3}\mathcal{R}\frac{\gamma-1}{2}M_e^2(1 - \frac{3}{4}\Theta)}{1 + \mathcal{R}\frac{\gamma-1}{2}M_e^2(1 - \Theta)} \right)^\omega. \quad (\text{A.4f})$$

### *Turbulent Flow*

For turbulent flow, the recovery factor was 0.88 and  $n = 0.268$ . The remaining variables were defined as followed:

$$\alpha(H) \approx 0.0566H - 0.0842, \quad (\text{A.5a})$$

$$\beta_u = 0.0056, \quad (\text{A.5b})$$

$$N = 0.168, \quad (\text{A.5c})$$

$$H_{12}(H) = 1 + 1.48(2 - H) + 104(2 - H)^{6.7}, \quad (\text{A.5d})$$

$$\varphi_1(M_e) = 1 - 0.0719M_e + 0.00419M_e^2, \quad (\text{A.5e})$$

$$\psi_1(M_e, \Theta) = 0.0114M_e(2 - \Theta)^{0.8}, \text{ and} \quad (\text{A.5f})$$

$$\chi = 1. \quad (\text{A.5g})$$

In this work the variable  $\omega$  was fixed constant at 0.7.

### A.3 Calibration Curves

In the following the polynomial curves used for calibrating mass flow and pressure data are given.

#### *Intake Throttle*

The polynomial used for the throttle calibration (equation (6.8)) is reprinted below:

$$\dot{m}_{\text{corr}} = \dot{m} (k_0 + k_1 A_{Q4} + k_2 A_{Q4}^2 + k_3 A_{Q4}^3 + k_4 A_{Q4}^4 + k_5 A_{Q4}^5 + k_6 A_{Q4}^6). \quad (\text{A.6})$$

The cross sectional area  $A_{Q4}$  varied with throttle ratio, and was therefore directly calculated from the streamwise position of the throttle's inner conical part. During this work  $A_{Q4}$  had to be given in mm, while the constants below were used:

$$k_0 = 0.96445, \quad (\text{A.7a})$$

$$k_1 = 8.9257 \times 10^{-6} \text{ mm}^{-1}, \quad (\text{A.7b})$$

$$k_2 = 1.7249 \times 10^{-8} \text{ mm}^{-2}, \quad (\text{A.7c})$$

$$k_3 = -1.2685 \times 10^{-11} \text{ mm}^{-3}, \quad (\text{A.7d})$$

$$k_4 = 3.3185 \times 10^{-15} \text{ mm}^{-4}, \quad (\text{A.7e})$$

$$k_5 = -3.7077 \times 10^{-19} \text{ mm}^{-5}, \text{ and} \quad (\text{A.7f})$$

$$k_6 = 1.5174 \times 10^{-23} \text{ mm}^{-6}. \quad (\text{A.7g})$$

#### *Pressure Rake*

Static pressure data at the rake was calibrated if the corresponding Mach number was  $> 1.5$ . From the uncorrected pressure  $p$ , a corrected pressure  $p_{\text{corr}}$  was calculated with the uncorrected Mach number  $M$ :

$$p_{\text{corr}} = \frac{p}{(c_0 + c_1 M + c_2 M^2 + c_3 M^3 + c_4 M^4)}. \quad (\text{A.8})$$

This corrected pressure was then used in equation (6.3) to determine a corrected Mach number. The steps above were repeated until converged results were reached. During this work the constants below were

used for the calibration polynomial:

$$c_0 = 0.96393, \tag{A.9a}$$

$$c_1 = 3.9648 \times 10^{-2}, \tag{A.9b}$$

$$c_2 = -1.9886 \times 10^{-2}, \tag{A.9c}$$

$$c_3 = 7.1212 \times 10^{-3}, \text{ and} \tag{A.9d}$$

$$c_4 = -4.5455 \times 10^{-4}. \tag{A.9e}$$

**A.4 Mesh Analysis – Additional Plots**

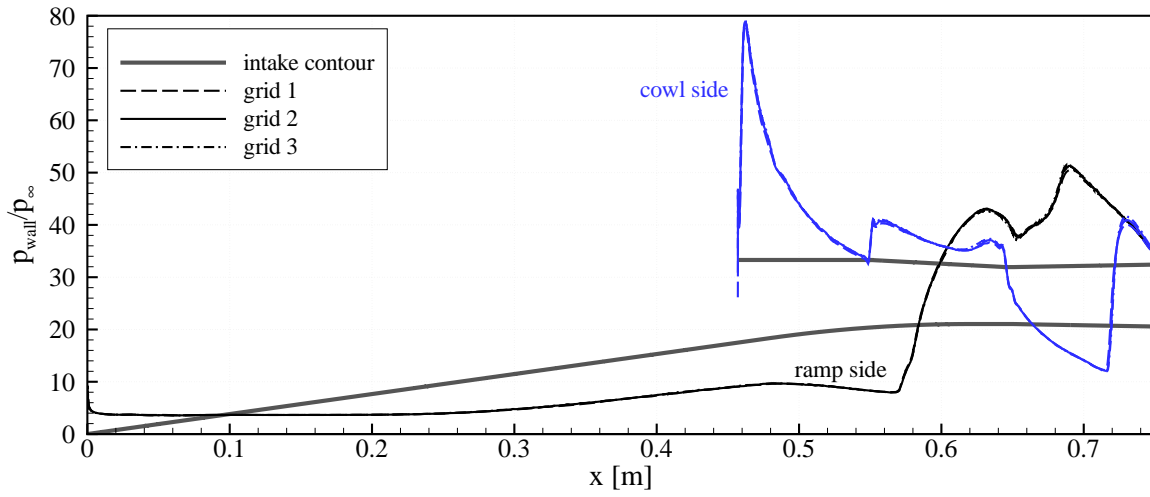


**Figure A.1: Influence of mesh size on wall pressure.**

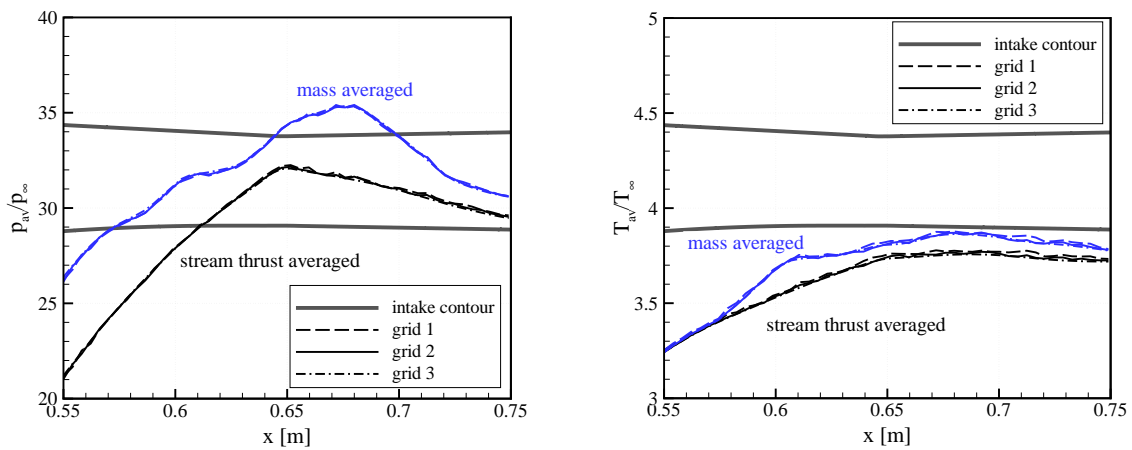
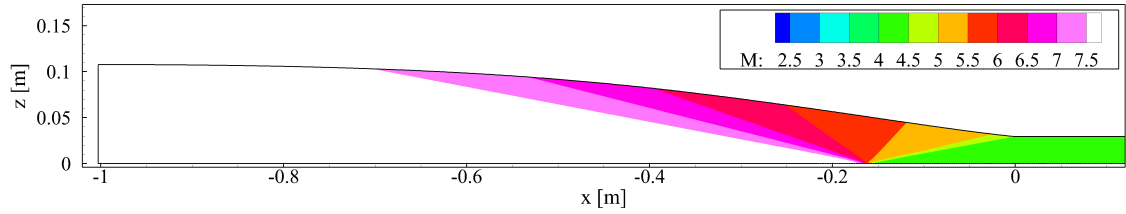


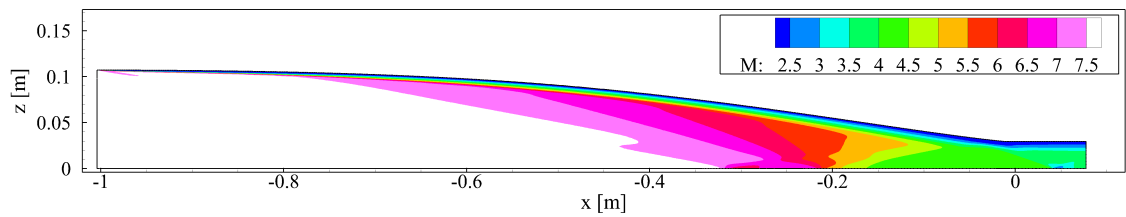
**Figure A.2: Influence of mesh size on average pressure (left) and average temperature (right).**

### A.5 Viscous Effects – Axisymmetric Contour Plots

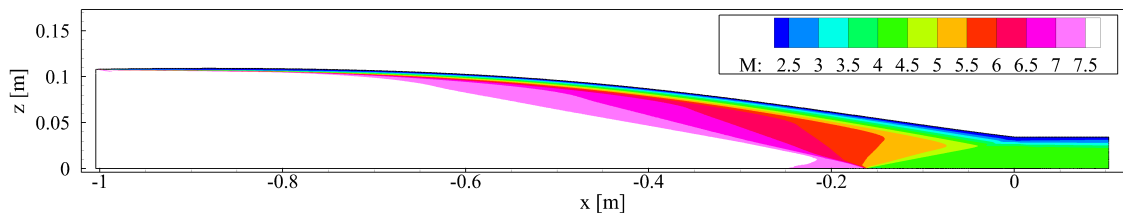
#### *Busemann Flow*



(a) no viscous correction, Euler solution



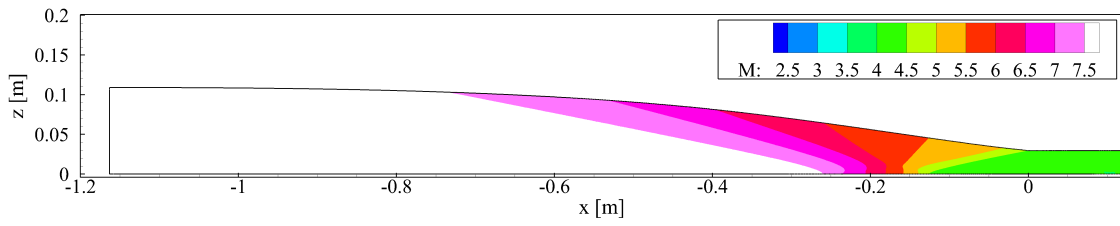
(b) no viscous correction, RANS solution



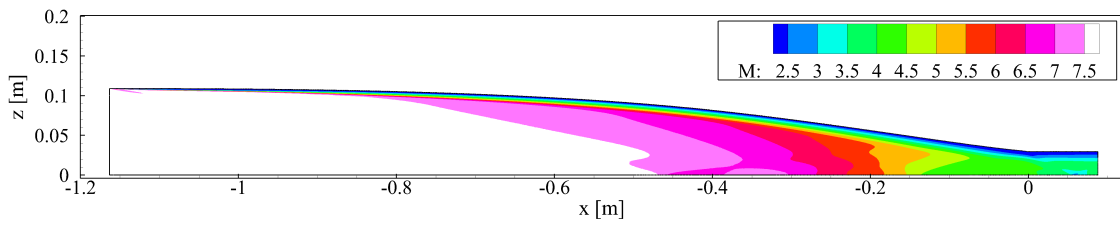
(c) with viscous correction, RANS solution

**Figure A.3: Axisymmetric Busemann contour plots without truncation.**

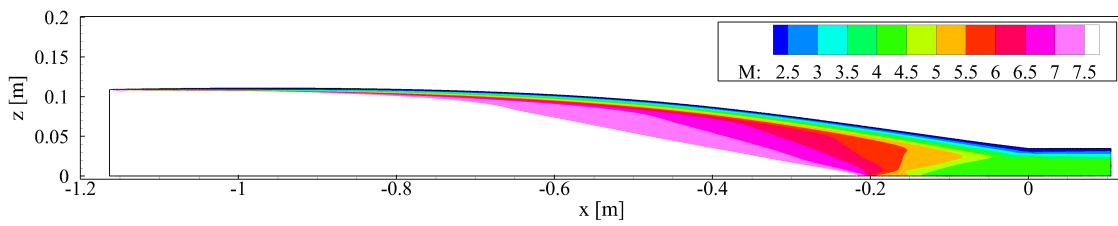
*Reversed Nozzle Flow*



(a) no viscous correction, Euler solution



(b) no viscous correction, RANS solution



(c) with viscous correction, RANS solution

**Figure A.4: Axisymmetric reversed nozzle contour plots without truncation.**



## A.6 ST Configurations – Cross-Stream Parameters

Analogous to figure 7.28, in which normalized pressures are plotted, normalized temperature and Mach number profiles are plotted below for the different streamline traced configurations.

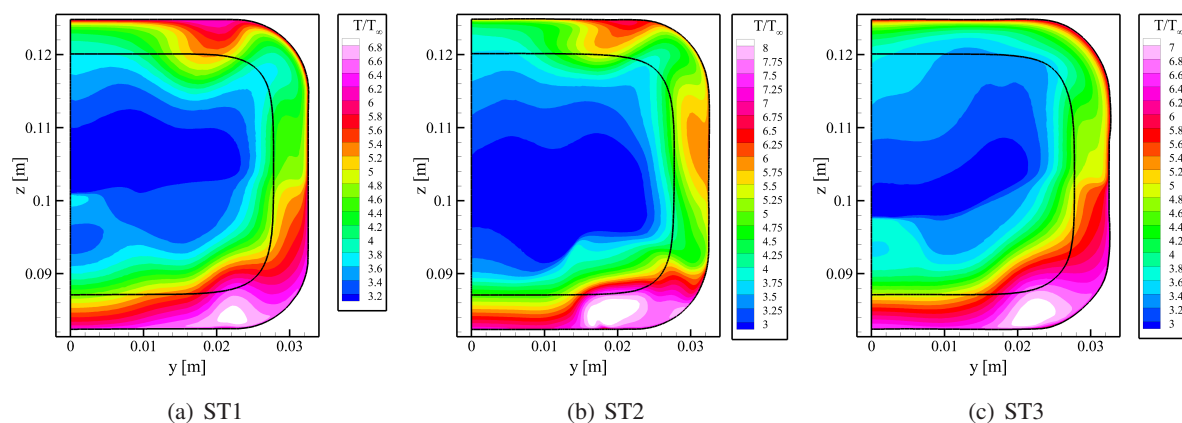


**Figure A.5: Normalized temperature on cross sectional planes of ST1, ST2, and ST3 configuration for Mach 8, extracted from CFD at  $x = 0.722$  m.**

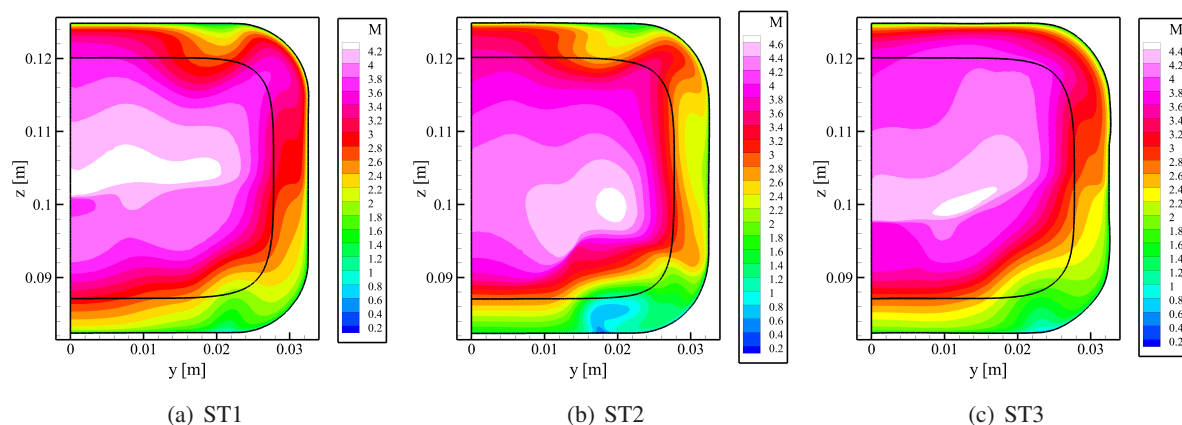


**Figure A.6: Mach number on cross sectional planes of ST1, ST2, and ST3 configuration for Mach 8, extracted from CFD at  $x = 0.722$  m.**

### A.7 3D-GRK Configuration – Cross-Stream Parameters

Analogous to figure 7.51, in which normalized pressures are plotted, normalized temperature and Mach number profiles are plotted below for the different self-starting 3D-GRK configurations.

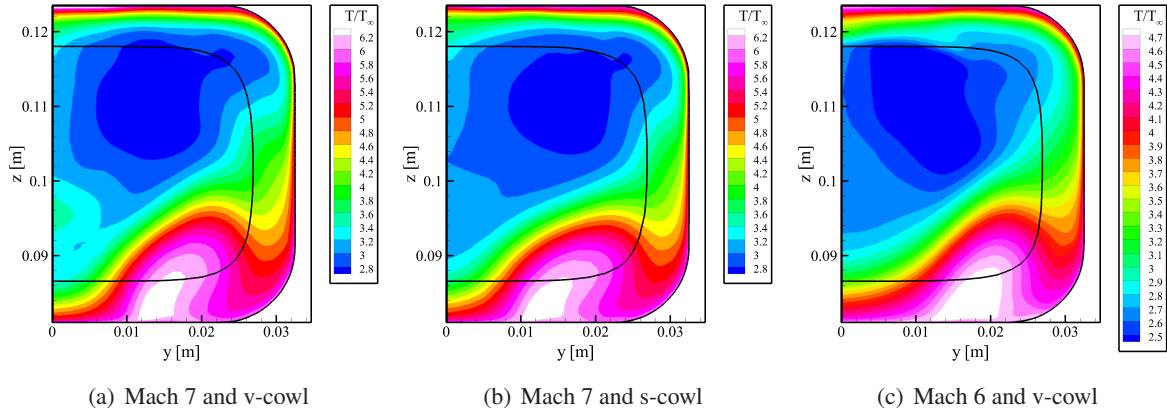


**Figure A.7: Normalized temperature on cross sectional planes, extracted from CFD at  $x = 0.722$  m.**

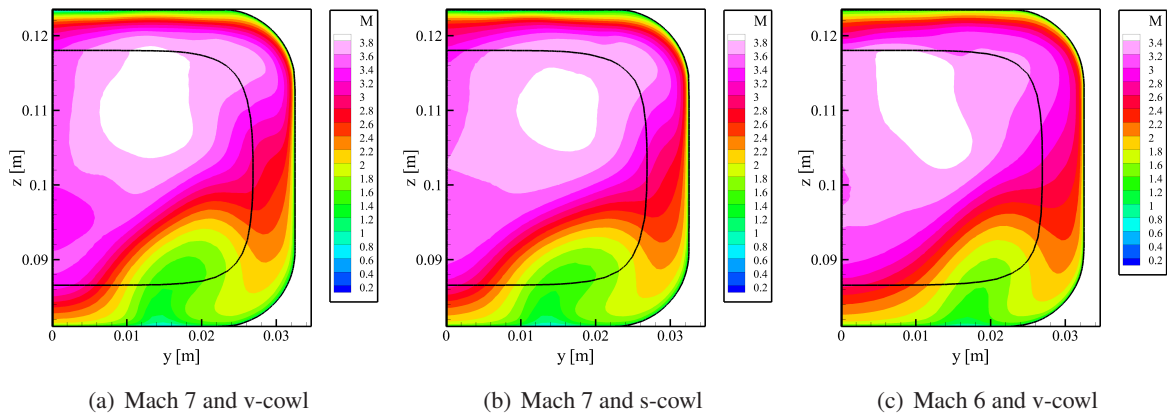
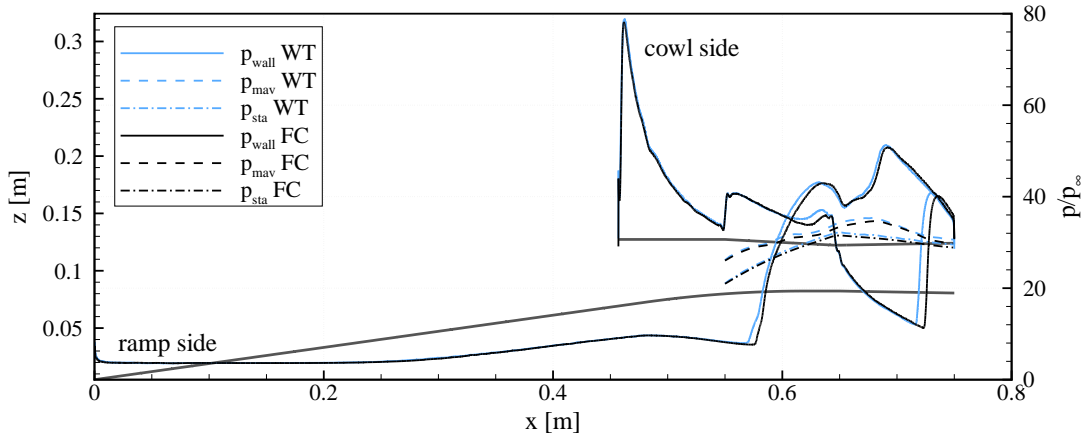


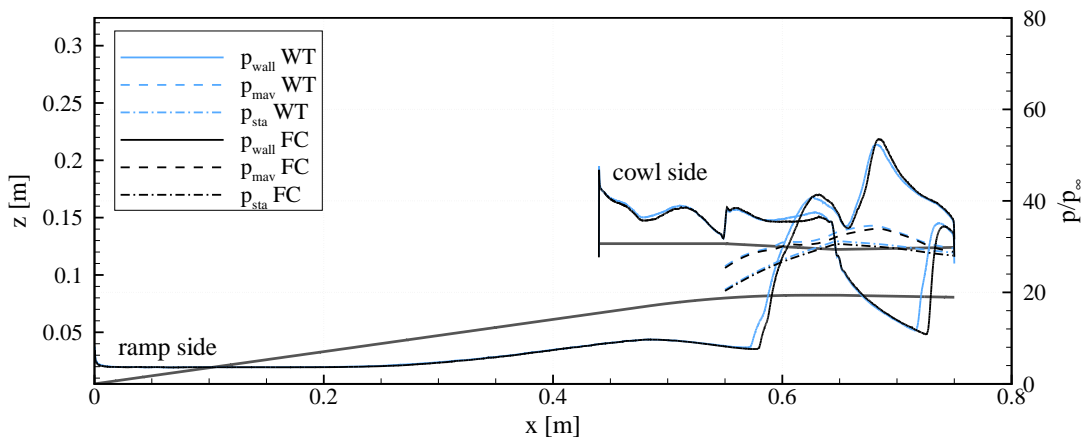
**Figure A.8: Mach number on cross sectional planes, extracted from CFD at  $x = 0.722$  m.**

### A.8 Comparison of Flight and Wind Tunnel Conditions

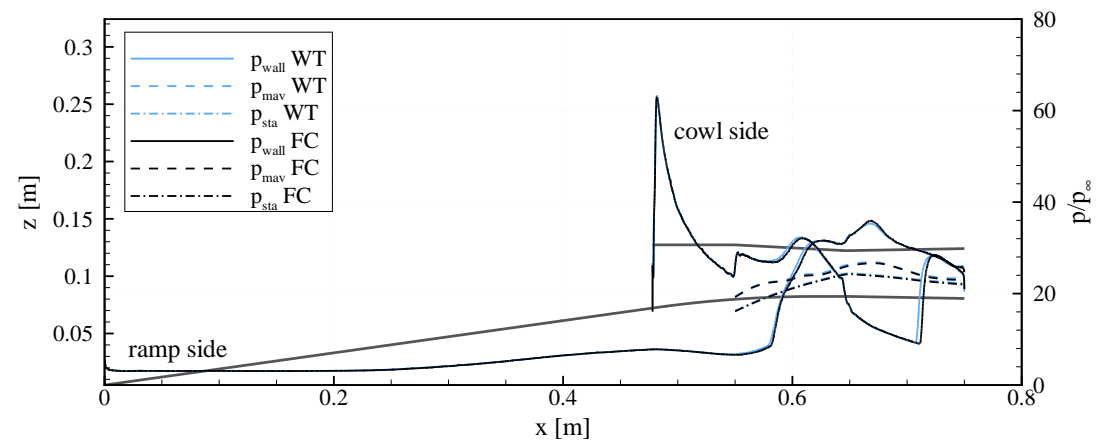
For the 3D-GRK intake the self-starting configurations were extrapolated to flight conditions (section 7.6.4). Normalized wall and average pressures for the different conditions are shown below.



(a) Mach 7 configuration with v-shaped cowl



(b) Mach 7 configuration with straight cowl



(c) Mach 6 configuration with v-shaped cowl

**Figure A.9: Comparison of numerical data for Wind Tunnel (WT) and Flight Condition (FC).**



## Bibliography

- [1] R. Abgrall, J.-A. Désidéri, R. Glowinski, and M. Mallet. *Hypersonic Flows for Reentry Problems - Volume III*. Springer Verlag, Berlin, Heidelberg, 1992.
- [2] J. D. J. Anderson. *Modern Compressible Flow*. McGraw Hill, New York, 1990.
- [3] J. D. J. Anderson. *Hypersonic and High-Temperature Gas Dynamics, Second Edition*. AIAA Education Series, Reston, Virginia, 2006.
- [4] J. D. J. Anderson. *Fundamentals of Aerodynamics, Fourth Edition*. McGraw Hill, Boston, 2007.
- [5] J. D. J. Anderson. *Introduction to Flight, Seventh International Edition*. McGraw Hill, Singapore, 2012.
- [6] T. Arens, F. Hettlich, C. Karpfinger, U. Kockelkorn, K. Lichtenegger, and H. Stachel. *Mathematik*. Spektrum Akademischer Verlag, Heidelberg, 2008.
- [7] M. Atak, J. Larsson, G. Gassner, and C.-D. Munz. DNS of a Flat-Plate Supersonic Boundary Layer Using the Discontinuous Galerkin Spectral Element Method. In *44th AIAA Fluid Dynamics Conference*, number 2014-3078, 2014.
- [8] R. A. Baurle and R. L. Gaffney. The Art of Extracting One-Dimensional Flow Properties from Multi-Dimensional Data Sets. In *45th Aerospace Sciences Meeting and Exhibit*, number 2007-0639, 2007.
- [9] R. A. Baurle and R. L. Gaffney. Extraction of One-Dimensional Flow Properties from Multidimensional Data Sets. *Journal of Propulsion and Power*, 24(4):704–714, 2008.
- [10] A. M. Berkowitz, C. L. Kyriss, and A. Martellucci. Boundary Layer Transition Flight Test Observations. In *AIAA 15th Aerospace Sciences Meeting*, number 77-125, 1977.
- [11] F. S. Billig. Design and Development of Single-Stage-to-Orbit Vehicles. *John Hopkins APL Technical Digest*, 11(3):336–352, 1990.
- [12] F. S. Billig. Supersonic Combustion Ramjet Missile. *Journal of Propulsion and Power*, 11(6):1139–1146, 1995.
- [13] F. S. Billig, R. A. Baurle, C.-J. Tam, and S. Wornom. Design and Analysis of Streamline Traced Hypersonic Inlets. *9th International Space Planes and Hypersonic Systems and Technologies Conference*, 1999.
- [14] F. S. Billig and L. S. Jacobsen. Comparison of Planar and Axisymmetric Flowpaths for Hydrogen Fueled Space Access Vehicles. In *39th Joint Propulsion Conference and Exhibit*, pages 1–12, 2003.
- [15] F. S. Billig and A. P. Kothari. Streamline Tracing: Technique for Designing Hypersonic Vehicles. *Journal of Propulsion and Power*, 16(3):465–471, 2000.
- [16] F. S. Billig and D. M. V. Wie. Efficiency Parameters for Inlets Operating at Hypersonic Speeds. In *International Society of Air Breathing Engines*, number 7047, pages 118–130, 1987.

- [17] M. A. Bolender, J. T. Staines, and D. J. Dolvin. HIFiRE 6: An Adaptive Flight Control Experiment. In *50th AIAA Aerospace Sciences Meeting*, number 2012-0252, Nashville, Tennessee, USA, 2012.
- [18] K. G. Bowcutt. Multidisciplinary Optimization of Airbreathing Hypersonic Vehicles. *Journal of Propulsion and Power*, 17(6), 2001.
- [19] K. G. Bowcutt. A Perspective on the Future of Aerospace Vehicle Design. In *12th AIAA International Space Planes and Hypersonic Systems and Technologies Conference*, number 2003-6957, 2003.
- [20] K. G. Bowcutt, J. D. J. Anderson, and D. Capriotti. Viscous Optimized Hypersonic Wavers. In *AIAA 25th Aerospace Sciences Meeting*, number 87-0272, 1987.
- [21] K. G. Bowcutt, A. Paull, D. J. Dolvin, and M. K. Smart. HIFIRE : An International Collaboration to Advance the Science and Technology of Hypersonic Flight. In *28th International Congress of the Aeronautical Sciences*, 2012.
- [22] R. R. Boyce, S. C. Tirtrey, L. Brown, M. Creagh, and H. Ogawa. SCRAMSPACE: Scramjet-based Access-to-Space Systems. In *17th AIAA International Space Planes and Hypersonic Systems and Technologies Conference*, number 2011-2297, pages 1–9, 2011.
- [23] A. Busemann. Die achsensymmetrische kegelige Überschallströmung. *Luftfahrtforschung*, 19(4):137–144, 1942.
- [24] T. Cain. Ramjet Intakes. Technical Report RTO-EN-AVT-185, 2011.
- [25] W. Y. K. Chan, S. A. Razzaqi, M. K. Smart, and D. J. Wise. Freejet testing of the 75%-Scale HIFiRE 7 REST Scramjet Engine. In *19th AIAA International Space Planes and Hypersonic Systems and Technologies Conference*, number 2014-2931, pages 1–20, 2014.
- [26] L. L. Cronvich. A Numerical-graphical method of characteristics for axially symmetric isentropic flow. *Journal of the Aeronautical Sciences*, 15(3):155–162, 1948.
- [27] E. T. Curran. The Use of Stream Thrust Concepts for the Approximate Evaluation of Hypersonic Ramjet Engine Performance. Technical Report AD-769 481, 1973.
- [28] E. T. Curran. Scramjet Engines: The First Forty Years Introduction. *Journal of Propulsion and Power*, 17(6):1138–1148, 2001.
- [29] E. T. Curran and S. N. B. Murthy. *Scramjet Propulsion (Progress in Astronautics and Aeronautics)*. AIAA, Reston, Virginia, 2001.
- [30] E. R. V. Driest. Turbulent Boundary Layer in Compressible Fluids. *Journal of Spacecraft and Rockets*, 18(3):145–160, 1951.
- [31] E. R. V. Driest. The Problem of Aerodynamic Heating. In *National Summer Meeting, IAS*, 1956.
- [32] A. Durant, A. Thierry, J. B. Edelman, B. C. Chynoweth, and S. P. Schneider. Mach 6 Quiet Tunnel Laminar to Turbulent Investigation of a Generic Hypersonic Forebody. In *20th AIAA International Space Planes and Hypersonic Systems and Technologies Conference*, pages 1–24, 2015.
- [33] S. Emami, C. A. Trexler, A. H. Auslender, and J. P. Weidner. Experimental Investigation of Inlet-Combustor Isolators for a Dual-Mode Scramjet at a Mach Number of 4 of. *NASA Technical Paper*, 3502, 1995.

- [34] A. K. Flock and A. Gülhan. Experimental Investigation of the Starting Behavior of a Three-Dimensional SCRamjet Intake with a Movable Cowl and Exchangeable Cowl Geometry at Different Mach Numbers. *19th AIAA International Space Planes and Hypersonic Systems and Technologies Conference*, (2014-2934):1–12, 2014.
- [35] A. K. Flock and A. Gülhan. Experimental and Numerical Performance Analysis of a Self Starting, Three-Dimensional SCRamjet Intake. In *20th AIAA International Space Planes and Hypersonic Systems and Technologies Conference*, number 2015-3680, Glasgow, 2015.
- [36] A. K. Flock and A. Gülhan. Experimental Investigation of the Starting Behavior of a Three-Dimensional Scramjet Intake. *AIAA Journal*, 53(9):2686–2693, 2015.
- [37] A. K. Flock and A. Gülhan. Viscous Effects and Truncation Effects in Axisymmetric Busemann SCRamjet Intakes. In *53rd Aerospace Sciences Meeting*, number 2015-0108, pages 1–15, 2015.
- [38] A. K. Flock and A. Gülhan. Viscous Effects and Truncation Effects in Axisymmetric Busemann Scramjet Intakes. *AIAA Journal*, 54(6):1881–1891, 2016.
- [39] A. K. Flock, J. C. Riehm, and A. Gülhan. Axisymmetric SCRamjet Engine Design and Performance Analysis. In *20th AIAA International Space Planes and Hypersonic Systems and Technologies Conference*, number 2015-3628, pages 1–11, Glasgow, 2015.
- [40] U. Gaisbauer, B. Weigand, and M. I. Yaroslavtsev. Wind Tunnel Testing of a Scramjet Propulsion System. *International Conference on the Methods of Aerophysical Research*, (2014-174):1–10, 2014.
- [41] T. J. Goldberg and J. N. Hefner. Starting Phenomena for Hypersonic Inlets with Thick Turbulent Boundary Layers at Mach 6. *Nasa Technical Note*, (D-6280), 1971.
- [42] A. Grainger, S. C. Tirtey, R. R. Boyce, S. Paris, and G. Paniagua. Starting Mechanisms for High Contraction Ratio Hypersonic Inlets. In *7th European Symposium on Aerothermodynamics*, 2011.
- [43] P. Gruhn and A. Gülhan. Experimental Investigation of a 3d Stream-Traced Air-Inlet for a Scramjet Engine. In *Space Propulsion 2014*, 2014.
- [44] J. Häberle. *Untersuchungen zum externen und internen Strömungsfeld eines Scramjet Triebwerkseinlaufs bei unterschiedlichen Betriebspunkten*. PhD thesis, Universität Stuttgart, 2009.
- [45] J. Hank, J. Murphy, and R. Mutzman. The X-51A Scramjet Engine Flight Demonstration Program. *15th AIAA International Space Planes and Hypersonic Systems and Technologies Conference*, (2008-2540):1–13, 2008.
- [46] D. R. Hartree. On an Equation Occurring in Falkner and Skan’s Approximate Treatment of the Equations of the Boundary Layer. *Proc. Camb. Phil. Soc.*, 33(Part II):223–239, 1937.
- [47] W. H. Heiser and D. T. Pratt. *Hypersonic Airbreathing Propulsion*. AIAA Education Series, Washington D.C., 1994.
- [48] R. Hermann. *Supersonic Inlet Diffusers and Introduction to Internal Aerodynamics*. Minneapolis-Honeywell Regulator Company, Minneapolis, Minnesota, 1956.
- [49] E. H. Hirschel. *Basics of Aerothermodynamics*. Springer, Berlin, Heidelberg, 2005.
- [50] O. M. Hohn. *Auslegung und Charakterisierung eines dreidimensionalen Scramjet-Einlaufs mit hohem Verdichtungsverhältnis und variabler Innenkontraktion*. PhD thesis, Universität Stuttgart, 2014.

- [51] M. S. Holden, M. MacLean, T. P. Wadhams, and E. P. Mundy. Experimental Studies of Shock Wave/Turbulent Boundary Layer Interaction in High Reynolds Number Supersonic and Hypersonic Flows to Evaluate the Performance of CFD Codes. In *40th Fluid Dynamics Conference and Exhibit*, number 2010-4468, pages 1–23, 2010.
- [52] M. S. Holden, T. P. Wadhams, and M. MacLean. Measurements in Regions of Shock Wave/Turbulent Boundary Layer Interaction from Mach 4 to 10 at Flight Duplicated Velocities to Evaluate and Improve the Models of Turbulence in CFD Codes. In *44th AIAA Fluid Dynamics Conference*, 2014.
- [53] K. R. Jackson, M. R. Gruber, and S. Buccellato. Mach 6-8+ Hydrocarbon-Fueled Scramjet Flight Experiment: The HIFiRE Flight 2 Project. *Journal of Propulsion and Power*, 31(1):36–53, 2015.
- [54] L. S. Jacobsen, C.-J. Tam, R. Behdadnia, and F. S. Billig. Starting and Operation of a Streamline-Traced Busemann Inlet at Mach 4. In *42nd AIAA/ASME/SAE/ASEE Joint Propulsion Conference & Exhibit*, number 2006-4508, pages 1–19, 2006.
- [55] T. J. Juliano, R. L. Kimmel, S. Willems, A. Gülhan, and R. M. Wagnild. HIFiRE-1 Boundary-Layer Transition: Ground Test Results and Stability Analysis. In *53rd Aerospace Sciences Meeting*, number 2015-1736, pages 1–16, 2015.
- [56] A. Kantrowitz and C. duP. Donaldson. Preliminary Investigation of Supersonic Diffusers. *National Advisory Committee for Aeronautics*, 1945.
- [57] R. L. Kimmel, D. Adamczak, K. Berger, and M. Choudhari. HIFiRE-5 Flight Vehicle Design. *40th Fluid Dynamics Conference and Exhibit*, pages 1–17, 2010.
- [58] M. Konopka, M. Meinke, and W. Schröder. Large-Eddy Simulation of Shock/Cooling-Film Interaction. *AIAA Journal*, 50(10):2102–2114, 2012.
- [59] M. Konopka, M. Meinke, and W. Schröder. Large-Eddy Simulation of Shock-Cooling-Film Interaction at Helium and Hydrogen Injection. *Physics of Fluids*, 25(10):106101, 2013.
- [60] L. G. Loitsianski. *Laminare Grenzschichten*. Akademie-Verlag, Berlin, 1967.
- [61] A. Mack and V. Hannemann. Validation of the Unstructured DLR-TAU-Code for Hypersonic Flows. In *32nd AIAA Fluid Dynamics Conference and Exhibit*, number 2002-3111, 2002.
- [62] A. J. Matthews, T. V. Jones, and T. M. Cain. Design and Test of a Hypersonic Isentropic-Spike Intake with Aligned Cowl. *Journal of Propulsion and Power*, 21(5), 2005.
- [63] C. R. McClinton. X-43 - Scramjet Power Breaks the Hypersonic Barrier Dryden Lectureship in Research for 2006. In *44th AIAA Aerospace Sciences Meeting and Exhibit*, number 2006-1, pages 1–19, 2006.
- [64] F. R. Menter, M. Kuntz, and R. Langtry. Ten Years of Industrial Experience with the SST Turbulence Model. *Heat and Mass Transfer*, 4, 2003.
- [65] P. W. Merlin. *Design and Development of the Blackbird*. AIAA Library of Flight, Reston, Virginia, 2008.
- [66] W. Merzkirch. *Flow Visualization*. Academic Press, London, UK, 1974.
- [67] J. Mo, J. Xu, R. Gu, and Z. Fan. Design of an Asymmetric Scramjet Nozzle with Circular to Rectangular Shape Transition. *Journal of Propulsion and Power*, 30(3):812–819, 2014.



- [68] S. Mölder and E. J. Szpiro. Busemann Inlet for Hypersonic Speeds. *AIAA Journal*, 3(8):1303–1304, 1966.
- [69] S. Mölder, E. V. Timofeev, and R. B. Tahir. Flow Starting in High Compression Hypersonic Air Inlets by Mass Spillage. In *40th AIAA/ASME/SAE/ASEE Joint Propulsion Conference & Exhibit*, number 2004-4130, pages 1–16, 2004.
- [70] F.-J. Niezgoda. Der Hyperschallwindkanal H2K des DLR in Köln-Porz. Technical Report 2001-01, Deutsches Zentrum für Luft- und Raumfahrt, Cologne, 2001.
- [71] N.N. *U.S. Standard Atmosphere*. U.S. Government Printing Office, NASA-TM-X-74335, Washington D.C., USA, 1976.
- [72] G. Norris. High-Speed Strike Weapon To Build On X-51 Flight. *Aviation Week and Space Technology*, page n.a., 2013.
- [73] G. Norris. X-51A Waverider Achieves Goal On Final Flight. *Aviation Week and Space Technology*, page n.a., 2013.
- [74] H. Ogawa, A. L. Grainger, and R. R. Boyce. Inlet Starting of High-Contraction Axisymmetric Scramjets. *Journal of Propulsion and Power*, 26(6):1247–1258, 2010.
- [75] H. Ogawa, S. Mölder, and R. R. Boyce. Effects of Leading-Edge Truncation and Stunting on Drag and Efficiency of Busemann Intakes for Axisymmetric Scramjet Engines. *JSME Technical Journal*, 8(2):186–199, 2013.
- [76] P. H. Oosthuizen and W. E. Carscallen. *Compressible Fluid Flow*. McGraw Hill, New York, 1997.
- [77] K. Oswatitsch. Pressure Recovery for Missiles with Reaction Propulsion at High Supersonic Speeds. *National Advisory Committee for Aeronautics*, 1944.
- [78] C. Peebles. *Road to Mach 10 - Lessons Learned from the X-43A Flight Research Program*. AIAA Library of Flight, Reston, Virginia, 2008.
- [79] D. M. Peterson, R. R. Boyce, and V. Wheatley. Simulations of Mixing in an Inlet-Fueled Axisymmetric Scramjet. *AIAA Journal*, 51(12):2823–2832, 2013.
- [80] S. Z. Pinckney. An Improved Static Probe Design. *AIAA Journal*, 12(4):562–564, 1973.
- [81] D. Preller and M. K. Smart. Scramjets for Reusable Launch of Small Satellites. In *20th AIAA International Space Planes and Hypersonic Systems and Technologies Conference*, number 2015-3586, pages 1–23, 2015.
- [82] M. L. Rasmussen. Waverider Configurations Derived from Inclined Circular and Elliptic Cones. *Journal of Spacecraft and Rockets*, 17(6):537–545, 1980.
- [83] B. Reinartz and U. Gaisbauer. Numerical Investigation of 3D Intake Flow. *17th AIAA International Space Planes and Hypersonic Systems and Technologies Conference*, (2011-2351):1–12, 2011.
- [84] J. C. Riehmer. *Aerothermodynamische Analysis eines Scramjet-Flugexperiments*. PhD thesis, RWTH Aachen, 2015.
- [85] J. C. Riehmer, E. Rabadan, A. Guelhan, and B. Weigand. Experimental and Numerical Investigations of a Scramjet Model Tested in the H2K Blow Down Wind Tunnel at Mach 7. *19th AIAA International Space Planes and Hypersonic Systems and Technologies Conference*, (2014-2933):1–14, 2014.

- [86] M. E. Roberts, M. K. Smart, and M. A. Frost. HIFiRE 7: Design to Achieve Scientific Goals. In *18th AIAA/3AF International Space Planes and Hypersonics Systems and Technologies Conference*, number 2012-5841, Tours, France, 2012.
- [87] T. Rolim and F. Lu. Design and Stream Thrust Analysis of a Scramjet Engine for Acceleration Mission from 2 to 3 km/s. In *51st AIAA Aerospace Sciences Meeting*, number 2013-0120, pages 1–16, 2013.
- [88] J. A. Schetz and R. D. W. Bowersox. *Boundary Layer Analysis Second Edition*. AIAA Education Series, Reston, Virginia, 2011.
- [89] H. Schlichting. *Grenzschicht-Theorie*. Verlag G. Braun, Karlsruhe, 1965.
- [90] L. Schweikart. The Quest for the Orbital Jet: The National Aero-Space Plane Program. Technical Report Volume III, Air Force Historical Studies Office, Washington D.C., USA, 1998.
- [91] C. Segal. *The Scramjet Engine*. Cambridge University Press, New York, 2009.
- [92] J. M. Simmons and E. H. Weidner. Design of Three-Dimensional Scramjet Inlets for Hypersonic Propulsion. In *2nd National Space Engineering Symposium*, 1986.
- [93] M. Sippel. SpaceLiner - A Visionary Concept of an Ultra Fast Passenger Transport under Investigation in FAST20XX. In *16th AIAA International Space Planes and Hypersonic Systems and Technologies Conference*, number 2009-7439, pages 1–9, 2009.
- [94] M. Sippel and J. Klevanski. Preliminary Definition of Supersonic and Hypersonic Airliner Configurations. In *14th AIAA/AHI Space Planes and Hypersonic Systems and Technologies Conference*, number 2006-7984, pages 1–17, Reston, Virginia, 2006. American Institute of Aeronautics and Astronautics.
- [95] M. K. Smart. Design of Three-Dimensional Hypersonic Inlets with Rectangular-to-Elliptical Shape Transition. *Journal of Propulsion and Power*, 15(3):408–416, 1999.
- [96] M. K. Smart. Optimization of Two-Dimensional Scramjet Inlets. *Journal of Aircraft*, 36(2):430–433, 1999.
- [97] M. K. Smart. Experimental Testing of a Hypersonic Inlet with Rectangular-to-Elliptical Shape Transition. *Journal of Propulsion and Power*, 17(2):276–283, 2001.
- [98] M. K. Smart. Scramjets. *The Aeronautical Journal*, -(3219):605–619, 2007.
- [99] M. K. Smart. How Much Compression Should a Scramjet Inlet Do? *AIAA Journal*, 50(3):610–619, 2012.
- [100] M. K. Smart and M. R. Tetlow. Orbital Delivery of Small Payloads Using Hypersonic Airbreathing Propulsion. *Journal of Spacecraft and Rockets*, 46(1):117–125, 2009.
- [101] M. K. Smart and C. A. Trexler. Mach 4 Performance of Hypersonic Inlet with Rectangular-to-Elliptical Shape Transition. *Journal of Propulsion and Power*, 20(2):288–293, 2004.
- [102] J. Steelant. Sustained Hypersonic Flight in Europe: Technology Drivers for LAPCAT II. pages 1–8, 2001.
- [103] J. Steelant, T. Langener, F. D. Matteo, K. Hannemann, and J. C. Riehmer. Conceptual Design of the High-Speed Propelled Experimental Flight Test Vehicle HEXAFLY. In *20th AIAA International Space Planes and Hypersonic Systems and Technologies Conference*, number 2015-3539, 2015.

- 
- [104] E. J. Stephen, S. R. Hoenisch, C. J. Riggs, M. L. Waddel, T. McLaughlin, and M. A. Bolender. HIFiRE 6 Unstart Conditions at Off-Design Mach Numbers. In *53rd Aerospace Sciences Meeting*, number 2015-0109, 2015.
- [105] B. Sun and K.-Y. Zhang. Empirical Equation for Self-Starting Limit of Supersonic Inlets. *Journal of Propulsion and Power*, 26(4), 2010.
- [106] B. Sun, K.-Y. Zhang, C.-P. Wang, and X.-S. Wu. Investigation on a Streamtraced Hypersonic Busemann Inlet. *Aerospace Engineering*, 224:57–63, 2009.
- [107] E. V. Timofeev, R. B. Tahir, and S. Mölder. On Recent Developments Related to Flow Starting in Hypersonic Air Intakes. In *15th AIAA International Space Planes and Hypersonic Systems and Technologies Conference*, number 2008-2512, pages 1–9, 2008.
- [108] K. Triesch and E.-O. Krohn. Verwendung von Kegeldüsen zur Drosselung und Durchsatzmessung bei Überschalleinläufen. Technical Report DVL R - IB-39113-83-A-04, Cologne, Germany, 1984.
- [109] C. Tropea, A. L. Yarin, and J. F. Foss. *Handbook of Experimental Fluid Mechanics*. Springer, Berlin, Heidelberg, 2007.
- [110] X. Veillard, R. Tahir, E. Timofeev, and S. Mölder. Limiting Contractions for Starting Simple Ramp-Type Scramjet Intakes with Overboard Spillage. *Journal of Propulsion and Power*, 24(5):1–8, 2008.
- [111] A. Walz. *Strömungs- und Temperaturgrenzschichten*. Verlag G. Braun, Karlsruhe, 1966.
- [112] B. Weigand and U. Gaisbauer. An Overview on the Structure and Work of the DFG Research Training Group GRK 1095: "Aero-Thermodynamic Design of a Scramjet Propulsion System". In *16th AIAA International Space Planes and Hypersonic Systems and Technologies Conference*, number 2009-7276, 2009.
- [113] F. M. White. *Viscous Fluid Flow, Second Edition*. McGraw Hill, New York, 1991.
- [114] D. M. V. Wie. Scramjet Inlets. In E. T. Curran and S. N. B. Murthy, editors, *Scramjet Propulsion*, pages 447–511. Progress in Astronautics and Aeronautics, 2000.
- [115] D. M. V. Wie, F. T. Kwok, and R. F. Walsh. Starting Characteristics of Supersonic Inlets. In *32nd Joint Propulsion Conference*, number 96-2914, 1996.
- [116] D. M. V. Wie and S. Mölder. Applications of Busemann Inlet Designs for Flight at Hypersonic Speeds. *AIAA Journal*, 1992.
- [117] Y.-N. Yu. A Summary of Design Techniques for Axisymmetric Hypersonic Wind Tunnels. Technical Report 35, NATO AGARD, 1958.
- [118] Z. Zhao and W. Song. Effect of Truncation on the Performance of Busemann Inlet. *Modern Applied Science*, 3(2):168–171, 2009.
- [119] M. J. Zucrow and J. D. Hoffman. *Gas Dynamics Volume I*. John Wiley and Sons, New York, 1976.



## Index

- 3D-GRK intake, 66, 116
- Adiabatic flow, 41
- Area weighted average, 81
- Averaging, 80
- Boundary layer equations, 46
- Busemann flow field, 52
- Calorically perfect gas, 41
- Contraction ratio, 29
- DLR-TAU software system, 76
- Empirical starting limit, 62
- FORTRAN, 51
- H2K wind tunnel, 72
- Half-stretching approach, 54
- HIFiRE, 27
- Ideal gas, 41
- Intake design tool, 51
- Intake starting, 30, 38, 62, 111
- Integral method, 46
- Isentropic flow, 42
- Kantrowitz criterion, 38
- Kinetic energy efficiency, 29
- Leading edge truncation, 33, 54, 83
- Mass capture ratio, 29
- Mass-flow-weighted average, 81
- Mass-weighted average, 81
- MDO, 25
- Mesh generation, 76
- Mesh sensitivity, 76
- Method of characteristics, 44
- Navier-Stokes equations, 45
- One-dimensional post analysis, 77
- Performance parameter, 29
- Pressure rake, 72
- Quasi one-dimensional flow, 41
- Rear side truncation, 34, 55, 88
- Rechenverfahren II, 49
- Research Training Group, 23
- Reversed nozzle flow field, 53
- Schlieren imaging, 74
- Semi-empirical starting limit, 62
- Shock relations, 42
- Specific impulse, 24
- SSTO, 25
- ST1 intake, 68, 103
- ST2 intake, 68, 105
- ST3 intake, 70, 107
- Standard atmosphere, 41
- Static pressure ratio, 29
- Static temperature ratio, 29
- Stream thrust averaging, 81
- Streamline tracing, 35, 56
- Taylor McColl equations, 43
- Throttle system, 74
- Total pressure recovery, 29
- Total temperature ratio, 29
- Truncation effects, 33
- Viscous effects, 35, 57, 92
- X43A, 25
- X51A, 26



## Curriculum Vitae

Andreas Konrad Flock

---

Place of Birth Schweinfurt, Germany

Date of Birth 9. June 1987

E-mail mail@aflock.de

---

- 2011 – present **Research Assistant**, German Aerospace Center (DLR), Cologne, Germany  
Research in the field of: supersonic/hypersonic flow, SCRam/Ramjet engines, aerodynamic vehicle design.
- 2006 – 2011 **Diplom-Ingenieur** (Dipl.-Ing.) Mechanical Engineering, Karlsruhe Institute of Technology (KIT), Karlsruhe, Germany  
Focus I: Gas and steam turbines; Focus II: Material science and lightweight materials; Additional Elective: Jet-engines and cooling of highly stressed gas turbine components.
- 2011 **Diploma Thesis**, Purdue University, West-Lafayette, IN, USA  
Setting up an experiment and evaluating the results for further investigation of the secondary atomization process of liquid droplets using a phase discriminating PIV system.
- 2010 **Pre-Diploma Thesis**, Karlsruhe Institute of Technology (KIT), Karlsruhe, Germany  
Programmed interface layer behaviour of granular microstructure contact utilizing FORTRAN; integrated it into ABAQUS software to perform finite element analysis of results.
- 2008 – 2009 **Internship**, Andreas Stihl AG, Waiblingen, Germany  
Measured performance parameters of a chainsaw combustion engine on a test block; wrote Visual Basic programs for advanced data-processing.
- 2009 **Exchange Student** with the Global Engineering Alliance for Research and Education (GEARE), Purdue University, West-Lafayette, IN, USA
- 2008 **Internship**, Angiotech Manan Medical, Wheeling, IL, USA  
Provided test support for electrochemical grinding machines producing biopsy needles; sized and dimensioned biopsy needle moulds to ensure proper quality control.
- 1997 – 2006 **Abitur**, Celtis Gymnasium, Schweinfurt, Germany  
Majors: Mathematics, Physics.
-